

**Designing carbon fibre-reinforced composites with improved structural retention on exposure to heat/fire**

**Francesca Louise McKenzie**

**A thesis submitted in partial fulfilment of the requirements of the  
University of Bolton for the degree of Doctor of Philosophy**

**School of Engineering | University of Bolton, UK**

**April 2023**

## **Declaration of Authorship**

I declare that the work described in this PhD thesis has not been previously presented in any form to the University or to any other institutional body, whether for assessment or for other purposes. Except for any referenced cited in this work, I confirm that the intellectual content of the work is the result of my own original research and of no other person.

Signed.....

Date.....

## **Acknowledgements**

First and foremost I would like to thank my supervisor Professor Baljinder Kandola, for believing in me and the continual encouragement, support and guidance to complete this PhD. Without her this would not have been possible.

Secondly, Professors Richard Horrocks and John Ebdon, who shared their wealth of expertise, provided advice and feedback on my work. I have been very fortunate to learn from them.

I would also like to express my gratitude to the technical staff at the University of Bolton, Dr John Milnes and Ail Sharhani, who always remained patient and ready to help with all the practical parts of this project.

At DSTL, Dr Emmajane Erskine and Dr Kevin Denham who have always shared ideas, provided constant enthusiasm, and their input from an industry perspective has been of the utmost of value.

I have enjoyed being part of the Fire Group at Bolton University and I would like to thank the many postdocs, PhD and visiting students, including Dr Bartosz Weclawski, Dr Chen Zhou and Annan Xiang who readily shared their knowledge, trained me on laboratory equipment and provided general encouragement throughout this PhD process.

And finally, my mother and sister who always believed I could complete a PhD and motivated me to return to science and academia. I am very lucky to have such a supportive family.

## **Funding**

I am grateful to the Defence Science and Technology Laboratory, UK, for the financial support.

## Abstract

Carbon fibre-reinforced composites (CFRCs) are increasing in popularity due to their high strength-to-weight ratio and resistance to corrosion. However, when exposed to temperatures above 300°C, the polymer matrix within CFRCs decomposes and then starts burning, exposing carbon fibres to the surroundings. The residual carbon fibres being electrically conductive, may pose a hazard to the surrounding electronics. Moreover, at over 550°C the carbon fibres begin to oxidise. This can lead to fibre defibrillation which also poses significant harm to human health as broken fibres can be sharp enough to cut through human skin, and under 7µm these particles are considered respirable where on inhalation they can cause damage to the trachea and lungs.

While considerable work has been carried out on assessing the effect of heat/fire on degradation of the composite resin (matrix) and CFRCs themselves, there are limited studies on identifying the damage to carbon fibres within CFRCs and the hazards posed by the exposed damaged carbon fibres. This study examined the damage caused by high temperatures, radiant heat and flames on carbon fibres and CFRCs, and the effects on their physical properties. A methodology was developed to study and quantify the structural damage to carbon fibres and CFRCs after exposure to a range of heat/fire conditions. These included thermogravimetric analysis (up to 900°C in nitrogen and air atmospheres), the tube furnace (450°C–900°C), cone calorimeter (35kWm<sup>-2</sup> to 75kWm<sup>-2</sup>) and a propane burner (116kWm<sup>-2</sup>) to simulate jet fuel fire conditions. Residual fibres were removed from different parts of the CFRCs and the physical properties were studied, such as fibre diameter reduction, change in electrical conductivity and decrease in tensile strength. It was found that at heat fluxes  $\geq 60\text{kWm}^{-2}$  oxidation of the carbon fibres occurred. After 10min exposure to the propane flame, fibres in direct contact with the flame showed signs of internal oxidation.

The aim of this PhD project was to also improve the structural retention of CFRCs on exposure to heat/fire so that the structural integrity is maintained and the carbon fibres are not exposed to the environment. To address this, the following approaches were undertaken:

- Modification of the resin by adding flame retardants and nanoparticles in order to reduce the flammability of CFRCs, improve the mechanical integrity of the char and its adherence to



the fibre. Flame retardants included ammonium polyphosphate, resorcinol bis-(diphenyl phosphate), 9,10-dihydro-9-oxa-10-phosphaphenanthrene 10-oxide, and the nano-additives, nano-clay, layered double hydroxide and carbon nano-tubes. Cone calorimeter testing at  $75\text{kWm}^{-2}$  showed that the addition of 15wt% ammonium polyphosphate resulted in large char formation and adherence to fibres in the underlying plies, which resulted in less oxidation to these carbon fibres. The addition of layered double hydroxides and carbon nano-tubes on the other hand caused pitting on fibres.

- Provide heat protection to carbon fibres within CFRCs by the inclusion of high performance fibrous veils/woven fabrics of aramid, basalt, E-glass, polyphenylene sulphide and Kevlar. The inclusion of the woven E-glass resulted in a notable reduction in the percentage of carbon fibre oxidised. However, the volatiles produced during the decomposition of Kevlar and PPS sensitised the carbon fibre to oxidation, causing it to occur more rapidly and at a lower temperature.
- Using high temperature chemical coatings to individually coat carbon fibres prior to making the CFRCs. Ceramic compounds (silica, alumina and zirconia), chosen as coating materials because of their high thermal stability, were applied by different processes. The most promising coatings included alumina and silica formed via sol-gel process and polysiloxane deposited during plasma exposure. Tows coated in these chemicals underwent heat testing in a tube furnace where those coated with alumina maintained the largest fibre diameters. While polysiloxane coating provided oxidation protection up to  $600^{\circ}\text{C}$ , after which cracks in the coating were observed. This was attributed to the mechanical mismatch of the polysiloxane coating and the carbon fibre.

## Nomenclature

APP	Ammonium polyphosphate
Al <sub>2</sub> O <sub>3</sub>	Aluminium oxide
BN	Boron nitride
CC	Control composite
CF	Carbon fibre
CFRC	Carbon fibre-reinforced composite
CNT	Carbon nano-tubes
CO	Carbon monoxide
CO <sub>2</sub>	Carbon dioxide
CVD	Chemical vapour deposition
DOPO	9, 10-dihydro-9-oxa-10-phosphaphenanthrene-10-oxide
DTG	Differential thermogravimetric
EDX	Energy dispersive X-ray spectroscopy
FO	Flame-out time
FRs	Flame retardants
GO	Graphene oxide
HNO <sub>3</sub>	Nitric Acid
LDH	Layered double hydroxide
N <sub>2</sub>	Nitrogen
NaAlO <sub>2</sub>	Sodium aluminate
NC	Nano-clay
PAN	Polyacrylonitrile
PS	Polysiloxane
PPS	Polyphenylene sulphide
RDP	Resorcinol bis-(diphenyl phosphate)
SEM	Scanning electron microscope
SiO <sub>2</sub>	Silicon dioxide
TGA	Thermogravimetric analysis
TGA-FTIR	Thermogravimetric analysis coupled with Fourier transfer infrared spectroscopy
TTI	Time-to-ignition
wt%	Weight percentage
ZrO <sub>2</sub>	Zirconium dioxide

## Contents

Chapter 1. Introduction and literature review .....	1
1.1 Introduction .....	1
1.2 Carbon fibre and CFRCs .....	2
1.2.2 Manufacturing Process of carbon fibres from polyacrylonitrile (PAN) .....	6
1.3 Effect of heat and fire on carbon fibre .....	8
1.3.1 Effect of heat and atmosphere on thermal stability of carbon fibres .....	8
1.3.3 Effect of heat and fire on mechanical properties of carbon fibres .....	11
1.3.4 Electrical properties of carbon fibres and CFRCs.....	14
1.4 Structural performance of CFRC under heat and fire .....	15
1.5 Structural performance of carbon fibres in CFRC under heat and fire .....	17
1.5.1 Health concerns of released fibres .....	19
1.6 Improving structural retention of carbon fibres in CFRCs: Use of flame-retardants to reduce CFRC combustion .....	21
1.6.1 Thermal degradation of epoxy resins .....	21
1.6.2 Condensed-phase flame retardants.....	22
1.6.3 Gas-phase flame retardants .....	25
1.6.4 Silicon-based flame retardants .....	26
1.7 Improving structural retention of carbon fibres in CFRCs: Carbon fibre surface coatings	27
1.7.1 Types of materials used for carbon fibre surface coatings.....	27
1.7.2 Size removal and activating the carbon fibre surface prior to coating.....	29
1.7.3 Methods to apply coatings to carbon fibres .....	31
1.8 Methods to improve structural retention of carbon fibres in CFRCs: Inclusion of other fibres for protection of carbon fibres .....	33
1.8.1 Behaviour of high temperature resistant fibres .....	34
1.8.2 Behaviour of high temperature resistant fibre-reinforced composites.....	36
1.8.3 Behaviour of hybrid composites when exposed to high heat fluxes .....	39
1.9 Summary .....	41
1.10 Aims and objectives .....	42
1.11 Thesis structure .....	42

1.12. References .....	44
Chapter 2. Materials and experimental techniques .....	56
2.1 Introduction .....	56
2.2 Materials.....	56
2.2.1 Carbon Fibre .....	56
2.2.2 Resin.....	57
2.2.3 Flame retardants .....	57
2.2.4 Non-woven fibrous veils .....	58
2.3 Preparation of composites .....	58
2.3.1 Resin infusion .....	59
2.3.2 Hand lay-up and vacuum bagging.....	59
2.3.3 Composites with nano-additives .....	60
2.3.4 Preparation of composites with veils .....	61
2.4 Exposure to different high temperature environments.....	63
2.4.1 Thermogravimetric Analysis.....	63
2.4.2 Tube furnace.....	64
2.4.3 Cone Calorimetry .....	64
2.4.4 Propane burner test.....	65
2.5 Carbon fibre analysis.....	67
2.5.1 Scanning Electron Microscopy .....	67
2.5.2 Mass density.....	68
2.5.3 Electrical conductivity .....	69
2.5.4 Tensile testing .....	72
2.6 Surface coating of carbon fibres .....	73
2.6.1 Preparation of carbon fibre surface prior to coating .....	73
2.6.2. Surface coating by dip coating method.....	73
2.6.3 Coating by the sol-gel process .....	74
2.6.4 Silica nano-particle deposition as sizing.....	78
2.6.5. Silica deposition by chemical vapour deposition.....	79
2.7 References .....	80
Chapter 3. Effects of heat, irradiance and flames on carbon fibre tows .....	82

3.1 Effects of thermal exposure under oxidative and inert atmospheres on carbon fibres and fibre tows.....	82
3.2 Effect of temperature on carbon fibres under oxidising and inert atmospheres .....	82
3.3 Effect of heat on carbon tows under oxidising and inert atmospheres .....	86
3.4 Effect of heat/fire on carbon fibres exposed to radiant heat in air .....	96
3.5 Effect of flames on carbon fibres exposed to premixed propane/air flames.....	99
3.6 Comparison with other PAN-based carbon fibres .....	103
3.7 Conclusions .....	107
3.8 References .....	109
Chapter 4: Effects of heat and fire on carbon fibre properties in fire retarded carbon-fibre reinforced composites .....	110
4.1 Introduction .....	110
4.2 Thermal stability of CC and components in air and nitrogen atmospheres .....	111
4.3 Effect of heat/fire on properties of CC and carbon fibre within CC.....	114
4.3.1 CCs exposed to radiant heat and the effects on carbon fibres: Cone calorimetric experiments (fluxes of 35, 50, 60 and 75kWm <sup>-2</sup> ).....	114
4.3.2 CCs exposed to jet fire conditions and the effects on carbon fibres: Propane burner experiments (116kWm <sup>-2</sup> ).....	122
4.4 Carbon fibre-reinforced composites with flame retardants and nano-additives .....	127
4.4.1 TGA studies (thermal stability) of CCs containing flame retardants and nano-additives .....	127
4.4.2 CCs containing flame retardants/nano-additives exposed to radiant heat and the effects on carbon fibre: cone calorimetric experiments.....	129
4.4.3 Electrical conductivity of CCs before and after exposure to radiant heat.....	139
4.4.4 Mechanical properties of carbon fibres after cone exposure (75kWm <sup>-2</sup> , 600s) .....	145
4.4.5 Analysis of char residue adhered on carbon fibres from cone exposed CC_APP composites.....	147
4.4.6 Effect of char residue on carbon fibre's electrical conductivity .....	156
4.5 Effect of jet fire on CCs with additives: Propane burner experiments .....	157
4.5.1 Effects of exposure time on damage to carbon fibres within CC with added flame retardants and nano-additives.....	157

4.5.2 Effects of propane flame on carbon fibres within CC with added flame retardants and nano-additives .....	157
4.5.3 Identification of damage to carbon fibres within composites with additives exposed to a propane flame for 5 minutes .....	159
4.5.4 Electrical resistivity of carbon fibres after propane burner testing ( $116\text{kWm}^{-2}$ , 300s)..	167
4.5.5 Mechanical properties of carbon fibres from composites after propane burner testing ( $116\text{kWm}^{-2}$ , 300s) .....	169
4.6 Conclusions .....	171
4.7 References .....	174
Chapter 5. Effects of high performance fibre inclusion in composites on thermal stability of carbon fibres.....	179
5.1 Introduction .....	179
5.2 Characterisation of veils.....	179
5.2.1 Physical properties of veil material.....	179
5.2.2 Thermal stability of veil/fabric materials .....	182
5.2.3 TGA-FTIR of the aramid, Kevlar and PPS .....	184
5.2.4 TGA of 50/50 wt% of carbon and veil fibres.....	186
5.2.5 Hybrid composite geometries and shear strengths.....	191
5.3 Cone calorimetric testing of composites at $75\text{kWm}^{-2}$ .....	194
5.3.1 Effect on structural coherence and morphological properties.....	194
5.3.2 Effect on burning parameters: time-to-ignition, flame-out time and residual mass .....	200
5.3.3 Effect of veils on properties of residual carbon fibres .....	202
5.4 Discussion on inclusion of veils in CC .....	210
5.5 Conclusions .....	212
5.6 References .....	214
Chapter 6. Surface modification of carbon fibres for improved structural retention on exposure to fire .....	217
6.1 Introduction .....	217
6.2 Characterisation of activated carbon fibre surface prior to coating .....	218
6.3 Characterisation of carbon fibre surfaces, modified by thermal barrier coatings .....	220
6.3.1. Inorganic coatings deposited by dip coating .....	221

6.3.2 Inorganic coatings deposited by sol-gel technology .....	224
6.3.3 Silica nano-particles deposited as sizing.....	229
6.3.4 Polysiloxane (PS) film, deposited by chemical vapour deposition of hexamethyldisiloxane (HMDSO).....	230
6.3.5 Discussion: thermal and oxygen barrier coatings on carbon fibres .....	231
6.4 Evaluation of thermal and oxidation protection efficiency of coatings .....	234
6.5 Mechanical properties of the coated fibres after exposure to heat.....	240
6.6 Electrical properties of the coated fibres after exposure to heat .....	245
6.7 Conclusions .....	247
6.8 References .....	250
Chapter 7. Conclusions .....	254
7.1 Development of a methodology to study and quantify structural damage to carbon fibres under a range of heat/fire conditions (Chapter 3). .....	255
7.1.1 Overall conclusions.....	255
7.1.2 Discussion .....	255
7.2 Modification of the resin in the CCs with the addition of flame retardant additives in order to increase cross-linking, reduce carbon fibre exposure, and promote the formation of char and its adherence to carbon fibres when the CCs are subjected to heat/fire (Chapter 4). .....	258
7.2.1 Overall conclusions.....	258
7.2.2 Discussion .....	258
7.3 Introduction of high-temperature material layers within the carbon fibre layers to improve the structural retention of carbon fibres within CCs (Chapter 5).....	263
7.3.1 Overall conclusions.....	263
7.3.2 Discussion .....	263
7.4 Modification of the carbon fibres prior to making the CCs so that the carbon fibres will not defibrillate and oxidise when exposed to heat/fire (Chapter 6) .....	268
7.4.1 Overall conclusions.....	268
7.4.2 Discussion .....	268
7.5 Limitations and recommendations for future research .....	271
7.6 References .....	273

## List of Figures

Figure 1.1. Breakdown of CFRCs parts in commercial aircrafts [10].	3
Figure 1.2. Breakdown of industries using CFRC and that predicted usage for 2024 [12].	4
Figure 1.3. Tensile modulus plotted against tensile strength for pitch and PAN-based carbon fibres [18].	6
Figure 1.4. PAN-based carbon fibre manufacturing process [19].	7
Figure 1.5. Separation of cost elements in the manufacture of carbon fibre from PAN [22].	8
Figure 1.6. Mass loss-temperature curves for the carbon fibre heated in air or nitrogen determined using TGA at the heating rate of 20°C/min [23].	9
Figure 1.7. Effect of temperature and heating time on the mass loss of carbon fibre in air T700S [23].	10
Figure 1.8. Diameter reduction and pitting on carbon fibre surface after exposure to 600°C for two hours [25].	11
Figure 1.9. (a) Fibre modulus for heat treatments in air or nitrogen (b) Young's modulus at different mass losses of carbon fibre when heated in air with calculated relationship and diagram illustrating the two-layer structure of carbon fibre [23].	12
Figure 1.10. (a) Weibull strength of fibres held at various temperatures for 30min or 2h (b) Estimated flaw size leading to failure at the same conditions as (a) [23].	13
Figure 1.11. Electrical resistivity ( $\sigma$ ) against temperature for a (a) PAN-based and (b) rayon based fibre [34].	14
Figure 1.12. Stress-displacement curves for CFRP held at various temperatures for 5min [43].	17
Figure 1.13. Diameter of fibres recovered from fire testing [48] with the original fibre diameter distribution [54].	21
Figure 1.14. Thermal degradation of DGEBA-based epoxy resin [9].	22
Figure 1.15. TGA in nitrogen and air for glass fibre reinforced epoxy composites containing 5 to 20wt% of APP or MPP [62].	24
Figure 1.16. TGA in air of uncoated carbon fibres and those coated with SiC/SiO <sub>2</sub> [79].	28
Figure 1.17. TGA in air of uncoated carbon fibres and those coated with BN [86].	28



Figure 1.18. SEM images of carbon fibres with different surface treatments: (a) untreated, (b) air-treated, and (c) gamma-radiated [105].	30
Figure 1.19. SEM images of (a) uncoated carbon fibres (b) SiO <sub>2</sub> coated CF SiC/SiO <sub>2</sub> coated CF and (d) surface cross-section of coated CF [79].	32
Figure 1.20. TGA in air for basalt, E-glass and carbon fibres [122].	35
Figure 1.21. Temperature–time profiles measured at the hot surface, middle region and cold surface of the (a) basalt fibre composite and (b) glass fibre composite when exposed to the heat flux of 25 and 50kWm <sup>-2</sup> . The dashed and solid curves are the measured and calculated trends [123].	37
Figure 1.22. Time to ignition at different heat fluxes for polyester laminates reinforced with woven or chopped glass fibres [132].	38
Figure 1.23. Schematic lay-up of hybrid laminates [120].	40
Figure 1.24. Mass loss versus time curves for laminates at 50kWm <sup>-2</sup> [120].	41
Figure 2.1 CC_APP preparation by hand lay-up	60
Figure 2.2. Schematics of the two configurations used to place veils in the composites.	61
Figure 2.3. SEM images of cross-sections of composites with veils.	63
Figure 2.4. Schematic of tube furnace with nitrogen flow.	64
Figure 2.5. Composite sample for cone calorimeter testing.	65
Figure 2.6. (a) Thermocouple setup (b) Temperatures recorded by thermocouples over 150s.	66
Figure 2.7. (a) Propane burner set up, and (b) Composite and graphite plate.	67
Figure 2.8. Graph of mass against tow length where the gradient is used to calculate the density.	69
Figure 2.9. Completed measured sample using the two probe method for measuring electrical conductivity.	70
Figure 2.10. Diagram of conductivity tests for CFRC.	71
Figure 2.11. Cards used for single fibre tensile tests.	72
Figure 2.12. TGA of silica sol after being held at different temperatures for 2h.	76
Figure 2.13. TGA of alumina sol after being held at different temperatures for 400°C for 2h.	77
Figure 2.14. TGA of alumina sol after being held at different temperatures for 400°C for 2h.	78
Figure 2.15. Atmospheric-pressure jet plasma of HMDSO carried by argon gas.	79
Figure 3.1. TGA graph of TR30S carbon fibre in nitrogen.	83

Figure 3.2. SEM images of (a) CF (b) Carbon fibre held at 500°C in a nitrogen atmosphere for 60min (c) EDX analysis of fibre from (b).....	84
Figure 3.3. The XPS results of T300 fibre from [3].....	85
Figure 3.4. TG curves in air and nitrogen, and first derivative of the mass loss curve in air for TR30S carbon fibre. ....	86
Figure 3.5. SEM of carbon fibres held for 1h in nitrogen (a) 500°C and (b) 700°C. ....	87
Figure 3.6. Carbon fibre tow held at 600°C for 60min - broken into several pieces. ....	90
Figure 3.7. Carbon fibre held in air at (a) 500°C for 1h with magnified pits (b) 500°C for 2h. ....	91
Figure 3.8. Graph of fibre diameter held at 500°C against time. ....	92
Figure 3.9. Graph of fibre diameter against temperature for fibres held for 30min. ....	93
Figure 3.10. Figure 3.10. Carbon fibre held for 30min in the tube furnace in air at a) 500°C b) 550°C c) 600°C d) 650°C. ....	94
Figure 3.11. Log of resistivity against temperature. ....	95
Figure 3.12. TR30S Carbon fibre after cone testing at 75kWm <sup>-2</sup> for 600s. ....	97
Figure 3.13. TR30S Carbon fibre after exposure to the propane burner for 1min and related EDX results. ....	99
Figure 3.14. Carbon fibres after exposure of fabrics to the propane burner for 1, 3, 5 and 10min. ....	102
Figure 3.15. SEM images of various PAN- based carbon fibres (a) TR30S (b) T300 (c) T800HB (d) AS4. ....	103
Figure 3.16. TGA curves for four different PAN-based fibres in air. ....	104
Figure 3.17. Isothermal TGA results for holding each fibre at 700°C in air. ....	105
Figure 3.18. T800HB fibre after (a) 2h at 500°C (b) 1h at 550°C in air. ....	107
Figure 4.1. TGA and DTG graphs of epoxy resin in nitrogen and air. ....	112
Figure 4.2. TGA of resin, carbon fibres, CC and the calculated curve (Calc. CC) in air atmosphere. ....	113
Figure 4.3. Schematic of CC cross-section with plies labelled. ....	116
Figure 4.4. Digital images of cross-sections of CC tested at 35kWm <sup>-2</sup> and 50kWm <sup>-2</sup> . ....	116
Figure 4.5. Image of the CC under the cone at t = 420s at 60kWm <sup>-2</sup> . ....	117
Figure 4.6. SEM images of (a) Surface (b) Individual fibres (c) Single carbon fibre from P1 after 600s exposure to 35kWm <sup>-2</sup> . ....	117

Figure 4.7. SEM images of carbon fibres removed from different plies after 600s exposure to various heat fluxes. Blue arrows indicate large areas of oxidation along striations. ....	118
Figure 4.8. Fibre from (a) P1 CC exposed to $75\text{kWm}^{-2}$ with spark ignition (b) EDX of fibre from P1 identifying only carbon. ....	119
Figure 4.9. CF fragments from P1 exposed to $75\text{kWm}^{-2}$ with spark ignition for 20min .....	121
Figure 4.10. CF from P8 exposed to $75\text{kWm}^{-2}$ with spark ignition for 20min. ....	121
Figure 4.11. Schematic of mounted CC and propane flame. ....	122
Figure 4.12. SEM of CF from CC at P1, T1 tested for (a) 3min (b) 5min and (c) 10min. ....	124
Figure 4.13. SEM images of fibre cross-sections removed from (a) CF, (b) P1 cone tested at $75\text{kWm}^{-2}$ 600s, (c) P1, T1 propane burner after 5min. ....	125
Figure 4.14. (a) Digital image of the propane/oxygen flame used in this work and (b) concentration of oxygen (o) and hydrogen ( $\square$ ) radicals at distance from the flame source, taken from [12]. ....	126
Figure 4.15. Chemical structures of the flame retardants. ....	128
Figure 4.16. TGA of CC, CC_APP, CC_DOPO, CC_RDP. ....	128
Figure 4.17. SEM images of fibres removed from the composite and of P1 and P8/10 after exposure to $75\text{kWm}^{-2}$ for 600s. ....	133
Figure 4.18. EDX analysis of char adhered on P8 of CC_APP, CC_DOPO and CC_RDP. ....	135
Figure 4.19. TGA responses of residual fibres removed from (a) P1 and (b) P8/10 plies from all exposed composites. ....	136
Figure 4.20. TGA responses of residual fibres removed from P1 and P8/10 of composites for (a) CC control, (b) CC_APP, (c) CC_DOPO, (d) CC_RDP, (e) CC_LDH, CC_NC .....	137
Figure 4.21. Electrical conductivity guide of components in CCs [29]. ....	139
Figure 4.22. Impurity concentration of the PAN-based fibres used Hexcel AS4, IM7 and HM63 detected with Neutron Activation Analysis [33]. ....	143
Figure 4.23. Fibre diameter vs Tensile Strength for fibres removed from ply P1 after cone testing at $75\text{kWm}^{-2}$ for 600s. ....	147
Figure 4.24. (a) SEM image and EDX maps showing the elements (b) carbon, (c) oxygen and (d) phosphorus on fibres from P8 CC_APP after cone testing at $75\text{kWm}^{-2}$ . ....	148

Figure 4.25. (a) SEM image and EDX maps showing the elements (b) carbon, (c) oxygen and (d) phosphorus in the loose char previously attached to P8 CC_APP after cone testing at $75\text{kWm}^{-2}$ .....	149
Figure 4.26. SEM images of CF from P8 CC_APP after ultrasound cleaning with different solvents.....	150
Figure 4.27. Cross-sections of fibres from Figure 4.26. ....	151
Figure 4.28. EDX maps showing the elements (a) carbon (b) oxygen and (c) phosphorus after cleaning fibres from P8 of CC_APP with toluene. ....	151
Figure 4.29. (a) SEM image, EDX maps showing the elements (b) carbon, (c) oxygen (d) phosphorus and (e) sodium after cleaning fibres from P8 CC_APP with 5wt% NaOH.....	152
Figure 4.30. Images showing the breakdown of solid epoxy char with 15wt% APP over 2h.....	153
Figure 4.31. Residue covered CF from P8 CC_APP after cone testing and 2 hours in $80^{\circ}\text{C}$ nitric acid. ....	154
Figure 4.32. (a) SEM image, EDX maps showing the elements (b) carbon (c) oxygen and (d) phosphorus after 2 hours in $80^{\circ}\text{C}$ nitric acid.....	154
Figure 4.33. TGA in air of residual carbon fibres from P8 CC_APP after various cleaning processes. ....	155
Figure 4.34. Digital photographs of composites after exposure to propane flame for 5min. .	157
Figure 4.35. SEM images of fibres removed from P1 at T1, T2, and T3 of composites with phosphorus-containing flame retardants after 5min.....	162
Figure 4.36. SEM and EDX of CC_RDP from P1, T3. ....	163
Figure 4.37. Fibres removed from P8 of CC and CC with phosphorus-containing flame retardants after 5min. ....	164
Figure 4.38. (a) Digital image, EDX from Ply P1 of (b) CC_LDHD (c) CC_NC. ....	164
Figure 4.39. SEM images of fibres from the difference piles at position T1 for CC_NC, CC_LDHD and CC_GO, along with fibres furthest from the flame at P10, T3.....	166
Figure 4.40. SEM images of fibres from CC_CNT at P1, T1 and P10, T3. ....	167
Figure 4.41. Fibre diameter vs tensile strength for fibres removed from P1 after propane burner testing at $116\text{kWm}^{-2}$ for 300s.....	171
Figure 5.1. SEM images of veils/fabrics taken at the same magnification. ....	181

Figure 5.2. TGA responses of (a) aramid, Kevlar and PPS under air 100ml/s at 20°C/min, and (b) basalt and glass fibre taken from [11]. .....	182
Figure 5.3. TGA and DTG curves of (a) aramid (b) Kevlar and (c) PPS, in air 100ml/s at 20°C/min. ....	183
Figure 5.4. FTIR spectra of evolved gases during TGA experiments of aramid and Kevlar at 576°C and 600°C, respectively. ....	185
Figure 5.5. FTIR spectra of evolved gases during TGA experiments of PPS in air at temperatures (a) 392°C, (b) 524°C and (c) 642°C.....	185
Figure 5.6. TGA curves in air of fibres from veils, carbon fibre (CF), 50/50wt% mixtures and calculated average 50/50wt% curve from the individual components. Fibres from veils used were (a) aramid, (b) Kevlar (c) PPS.....	187
Figure 5.7. DTG in air of fibres from veil fibre/carbon fibre (CF), 50/50wt% mixtures and calculated average 50/50wt% curve from the individual components. Fibres from veils used were (a) aramid, (b) Kevlar, (c) PPS.....	188
Figure 5.8. The two configurations of hybrid layers in CCs.....	191
Figure 5.9. Digital images of composites from configuration 1 after testing at 75kWm <sup>-2</sup> . ....	194
Figure 5.10. Comparisons of untested and the third aramid layer in CC_Ar_3 after cone calorimeter testing .....	195
Figure 5.11. Comparisons of untested and layers of basalt in CC_Bs_3 after cone calorimeter testing. ....	196
Figure 5.12. Comparisons of untested and layers of E-glass in CC_Gl_3 after cone calorimeter testing. ....	197
Figure 5.13. Comparisons of unexposed and layers of woven E-glass in CC_Wo-Gl_3 after cone calorimeter testing. ....	198
Figure 5.14. SEM images of where the weave crosses over in each hybrid layer. ....	199
Figure 5.15. EDX analysis of carbon fibres removed from ply P6 (P6) of CC_Wo-Gl_3. ....	199
Figure 5.16. EDX analysis of carbon fibres removed from ply P6 of CC_PPS_3. ....	200
Figure 5.17. (a-g) Graphs of carbon fibre diameters removed from different plies versus ply number.....	204
Figure 5.18. SEM images of carbon fibres removed from ply P1 after heat testing.....	205

Figure 5.19. SEM images of carbon fibres removed from ply P8 after heat testing. Pits circled.	206
Figure 5.20. SEM images of carbon fibres removed from P1, P3 and P6 of CC_PPS_3.	209
Figure 6.1. EDX of (a) CF (b) desized CF.	218
Figure 6.2. SEM images of desized CF followed by (a) HNO <sub>3</sub> or (b) plasma treatment, (c-d) EDX analysis of fibre in (b) and (c).	220
Figure 6.3. SEM images of CF-NaAlO <sub>2</sub> (a) after oven drying at 80°C for 12h, (b) EDX of fibre in (a), (c) fibres from (a) after 3.5h in nitrogen at 900°C.	221
Figure 6.4. (a) TGA curves for the CF and CF-NaAlO <sub>2</sub> , (b) DTG responses for the fibres in (a).	222
Figure 6.5. SEM images (a) CF-BN, (b) CF-BN-U and (c) TGA of CF and coated fibres in air.	224
Figure 6.6. Schematic of the reaction during sol-gel process to form SiO <sub>2</sub> [16].	225
Figure 6.7. SiO <sub>2</sub> coated (a) sized CF, (b) de-sized and treated with HNO <sub>3</sub> CF, (c) EDX of the coated fibre in (b).	226
Figure 6.8. (a) Cross-section of CF-Al <sub>2</sub> O <sub>3</sub> and (b) EDX analysis CF-Al <sub>2</sub> O <sub>3</sub> .	227
Figure 6.9. Structure of sol, where the complex = R(COO <sup>-</sup> ) <sub>n</sub> [18].	228
Figure 6.10. Carbon fibre coated with (a) ZrO <sub>2</sub> and complex, (b) ZrO <sub>2</sub> and (c) EDX analysis of carbon fibres from (b).	228
Figure 6.11. SEM images of coated CF with (a) sizing and (b) emulsified sizing, and (c) EDX of the carbon fibre coated with the emulsified epoxy nano-SiO <sub>2</sub> .	230
Figure 6.12. EDX analysis of (a) a single spherical particles and (b) over a larger area on the coated carbon fibre surface.	231
Figure 6.13. Tensile strength of carbon fibres after different surface treatments [10].	232
Figure 6.14. Coated carbon fibre diameters after being held for (a) Varying lengths of times at 500°C (b) Varying temperatures for 0.5h.	236
Figure 6.15. . SEM images of the CF and coated fibres held a different temperatures for varying times.	239
Figure 6.16. SEM images of CF-PS after exposing at (a) 550°C 1h and (b-c) 600°C 0.5h.	240
Figure 6.17. Stress-strain curves for (a) CF and coated fibres, after holding at (b) 500°C for 1h, (c) 500°C for 2h and (d) 550°C for 1h.	242

Figure 7.1. Summary of carbon fibres diameters after being exposed to different heat sources for varying times. Orange circles and blue squares represent heating in tube furnace, red boxed in a cone calorimeter and purple boxed in a jet fire with propane burner. ....	257
Figure 7.2. Schematic of CC. ....	259
Figure 7.3. The two configurations of hybrid layers in CC. ....	263

## List of Tables

Table 1.1. Taken from [54] summarising the aerodynamic sizes of particles which humans could inhale. ....	20
Table 1.2. LOI values of epoxy resins containing different wt% of APP.....	24
Table 1.3. Fibre properties [122].....	34
Table 1.4. Chemical composition of a basalt fibre used [122,124] compared to an E-glass fibre taken from [125].....	34
Table 1.5. Results from cone calorimeter for composites tested at $50\text{kWm}^{-2}$ [134].....	38
Table 1.6. EDX results of chemical composition of residue on basalt fibres after testing at $35\text{kWm}^{-2}$ [135]. ....	39
Table 2.1. Physical and mechanical properties of different carbon fibres [1-4]. ....	57
Table 2.2. Veil densities.....	58
Table 2.3. Summary of additives used and composite manufacturing method. ....	61
Table 2.4. Summary of composites with veils with fabric and resin ratios. ....	62
Table 3.1. Summary of tube furnace experiments carried out on carbon fibre tows in air. ....	88
Table 3.2. Electrical resistivity for fibres held for 30min. ....	94
Table 3.3. Tensile test results for CF after different heat treatments.....	96
Table 3.4. Summary of results for CF test under the cone and tube furnace. ....	98
Table 3.5. Average temperature recorded by the thermocouples and fibre diameters.....	101
Table 3.6. Results of Tube Furnace experiments on different PAN-based fibres.....	106
Table 4.1. TGA data for samples shown in Figure 4.3 in air, as well as in nitrogen.....	113
Table 4.2. Results for CC tested for 600s and varying heat fluxes. ....	115
Table 4.3. Mean fibre diameters ( $\mu\text{m}$ ) removed from different plies of CC after exposure to cone calorimeter.....	119
Table 4.4. Comparison of the mean electrical resistivity fibre from different plies after exposure to $75\text{kWm}^{-2}$ with spark ignition. ....	120
Table 4.5. Fibre diameters removed from different plies and distance from the flame of CC at varying exposure times. ....	123
Table 4.6. TGA data for samples shown in Figure 4.16 in air.....	129
Table 4.7. Residual mass of CC exposed to $75\text{kWm}^{-2}$ .....	130



Table 4.8. Mean fibre diameters after exposure to $75\text{kWm}^{-2}$ for 600s. ....	132
Table 4.9. Electrical conductivities of composites with additives. ....	140
Table 4.10. Mean electrical resistivity of CF from different plies of composites exposed to $75\text{kWm}^{-2}$ .....	142
Table 4.11. Mean tensile strength and modulus for CF from Ply1, removed from composites, exposed to $75\text{kWm}^{-2}$ . ....	145
Table 4.12. Density of solvents used in ultrasound bath.....	150
Table 4.13. Mean electrical resistivity of carbon fibre after ultrasound cleaning with different solvents.....	156
Table 4.14. FO and residual mass of composites exposed to $116\text{kWm}^{-2}$ 300s.....	158
Table 4.15. Mean CF diameters removed from different plies within the composites after exposure to propane flame for 5min. ....	160
Table 4.16. Mean electrical resistivity of CF at T1, from different plies of composites exposed to $116\text{Wm}^{-2}$ . ....	168
Table 4.17. Mean tensile strength and modulus for CF removed from composites after heat testing ( $116\text{kWm}^{-2}$ , 300s).....	169
Table 5.1. Veil densities and approximate melting points. ....	180
Table 5.2. EDX element composition. ....	181
Table 5.3. Characteristic parameters of the thermal decomposition from TGA curves. ....	183
Table 5.4. Characteristic parameters of the thermal decomposition from TGA and DTG curves. ....	189
Table 5.5. Physical properties of composites.....	192
Table 5.6. Shear strength of composites from short beam shear tests. ....	193
Table 5.7. Composition of composites and resulting cone calorimeter results after $75\text{kWm}^{-2}$ for 600s. ....	201
Table 5.8. Carbon fibre diameters measured after exposure to $75\text{kWm}^{-2}$ for 600s. ....	203
Table 5.9. Electrical resistivity results for carbon fibres removed from P1. ....	210
Table 6.1. Characteristic parameters of the thermal decomposition from TGA and DTG curves. ....	222
Table 6.2. wt% loss of CF and coated carbon fibres held in the tube furnace for varying temperatures and times.....	234

Table 6.3. Diameters of CF and coated carbon fibres after being held in the tube furnace for varying temperatures and times. ....	236
Table 6.4. Tensile strength and modulus of CF and coated carbon fibres after heat testing in the tube furnace. ....	241
Table 6.5. Percentage tensile strength loss of the fibres with respect to the untested fibres. .	243
Table 6.6. Electrical resistivity of CF and coated carbon fibres after heat treatments in the tube furnace. ....	245
Table 7.1. Comparison of the properties of ply P1 carbon fibres after heat and fire testing. .	262
Table 7.2. Physical properties of composites. ....	264
Table 7.3. Summary of results for CC with additional veils/fabric layer after heat testing (75kWm <sup>-2</sup> for 600s). ....	267
Table 7.4. Summary of results for CF and coated fibres. ....	271

## **Chapter 1. Introduction and literature review**

### **1.1 Introduction**

The use of carbon fibre, predominantly used in carbon fibre-reinforced composites (CFRCs) is on the rise due to their high strength-to-weight ratio. Combined with their resistance to corrosion, CFRCs are rapidly replacing many metals and are particularly attractive to the aerospace and automotive industries. While in general CFRCs have high heat resistance, when exposed to temperatures above the glass transition temperature (180-230°C depending on the resins), the organic resin matrix softens and above 300°C starts decomposing, resulting in loss of the mechanical properties of the CFRC. At even higher temperatures the resin ignites and at over 550°C in an oxidative environment, oxidation of the carbon fibres begins to occur [1]. They are largely used in the aerospace industry, where situations with high heat, and impact to an aeroplane, could arise. The combustion of composites in such a situation can lead to the release of broken fibres, which could be aurally transported given their low weight. These released fibres pose hazards. Firstly, they may interfere with surrounding electrical equipment and pose health concerns if inhaled. Secondly, Moreton [2] first raised the idea of electrical hazards due to the release of carbon fibres into the atmosphere in 1979. It was believed the predominance of fibres shorter than 3mm in length had a marked effect upon the susceptibility of electrical equipment to the fibres [3]. It was reported that material containing carbon fibre was accidentally introduced into the Union Carbide incinerator in Fostania, Ohio. The released fibres were transported by winds to an electricity sub-station half a mile away causing a blackout. Furthermore, broken fibres can also be sharp enough to cut through human skin, and when under 7µm these particles are considered respirable where on inhalation they can causes damage to the trachea and lungs [4].

The focus of this work is to further examine the damage caused by high temperature, radiant heat and flames on carbon fibres and the effects on their physical properties, including fibre diameter reduction and electrical conductivity. The aim is also to improve the structural retention of CFRCs on exposure to heat/fire so that the structural integrity is maintained and the carbon fibres are not exposed to the environment. With this in view, in this chapter a

comprehensive literature review has been covered, including the existing literature related to effects of extreme heat/fire and oxidising environment on carbon fibre used as a reinforcing fibre in carbon fibre-reinforced composites (CFRCs) in terms of changes in physical, morphological and mechanical properties. The combustion behaviour of CFRCs and whether during combustion any carbon fibres are exposed or released in the environment, and their potential hazards, have also been reviewed. In addition, methodologies that researchers have used to reduce the flammability of CFRCs and/or protect the carbon fibres, including the addition of flame-retardants and the use of fibre coatings and hybrid layers, have been discussed.

## **1.2 Carbon fibre and CFRCs**

The history of carbon fibre spans back over 150 years, with significant manufacturing process improvements made in the last 50 years to produce fibres with an excellent strength-to-weight ratio. In 1879 Thomas Edison used cellulose-based carbon fibre filaments in the first light bulbs to be heated by electricity. However, commercial fibre only became available in 1958 in the form of rayon based precursor fibres made by Bacon [5]. In the 1960s Shindo at the Agency of Industrial Science and Technology in Japan, produced the first polyacrylonitrile (PAN) precursor carbon fibres that had 55wt% carbon content and were manufactured at a reduced cost than those produced previously [6]. In 1963 British scientists Watt, Phillips, and Johnson designed a manufacturing process to make even stronger carbon fibres [7], which were used by Rolls Royce in their jet engines. Since then, various types of carbon fibre from different precursors have entered industry and as a standard, carbon fibres now contain at least 92wt% carbon with a diameter of 5-10 $\mu$ m [8], with significantly increased tensile strength and modulus than those produced in the 1960s.

As production costs continue to decrease, the demand for carbon fibre increases, where the majority of carbon fibre is used in carbon fibre polymer composites. Composites typically consist of two or more components that have very different physical and chemical properties and remain physically separate and distinct from each other. In the case of CFRCs, this includes a soft and weaker resin matrix with a strong carbon fibre reinforcement distributed through it. The matrix protects, supports and transfers loads across the fibre. This results in a lightweight

material with improved mechanical strength which the components would not have individually. The resins used are divided into two types - thermoplastic or thermosetting. Thermoplastic resins harden when cooled but do not cross-link and can be re-moulded when heated to their melting point. Thermoset resins however, most often used in composites, cross-link during curing and once cured the composite cannot return to its original state. These resins are divided into unsaturated polyester (usually used with glass fibre composites because of their low cost and good mechanical strength), vinyl ester (midrange mechanical performance properties and greater water and chemical resistance - typical applications are in marine and corrosive environments) and epoxy resins (bi-, tri- or tetra functional) which are mainly used in CFRCs. These use a hardener (called a curing agent) to set. Depending on the hardener used, the curing time and temperature can be relatively low. Epoxy resins are extremely versatile and usually have increased adhesive strength and mechanical properties compared to other polymer resin types [9]. The overall properties of the CFRCs can depend on the carbon fibres used, the type of polymer used (epoxy resin, vinyl ester, unsaturated polyester), and additives to the polymer matrix.

The use of CFRCs is currently dominated by the aerospace industry for making parts of the aircraft structure due to their high strength-to-weight ratios. Demand for CFRCs is expected to increase due to growth in both military and commercial aerospace sectors. Currently 50% of the Boeing 787 Dreamliner structure is made of CFRCs, along with key aircraft components, such as the outer wing flaps and vertical tail plates. These are shown in the images in Figure 1.1 taken from [10].

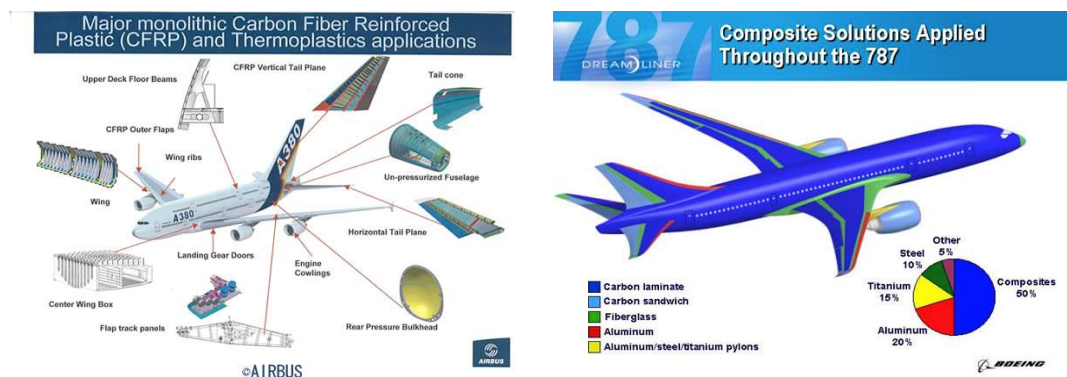


Figure 1.1. Breakdown of CFRCs parts in commercial aircrafts [10].

Use in the automotive industry is also expected to increase with the desire for fuel-efficient vehicles. Reduced weight of vehicle parts results in improved energy efficiency. Currently 55% of total volume in production of a modern car consisted of steel parts with some potentially being replaced with CFRCs [11]. Figure 1.2 shows the breakdown of industries using CFRC and those predicted for 2024.

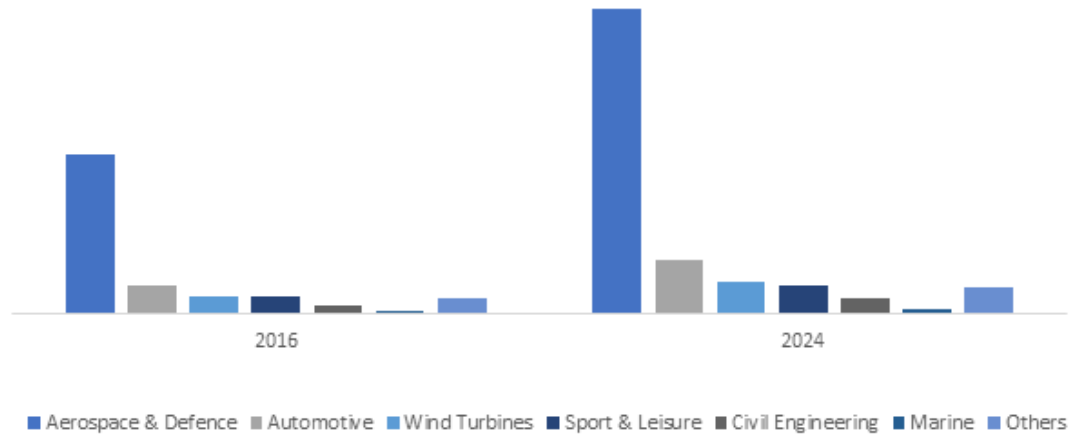


Figure 1.2. Breakdown of industries using CFRC and that predicted usage for 2024 [12].

### 1.2.1 Carbon fibre production and properties

Carbon fibres consist of graphene sheets in a hexagonal pattern with Van der Waals forces between them. Depending upon the precursor used these planes may have different structures. The tensile modulus is connected to the orientation of these planes where the more highly orientated they are the higher their tensile modulus [13]. Depending on modulus, strength, final heat treatment and precursor material, carbon fibres are placed into the following categories. Carbon fibres tensile modulus [14]:

- Standard modulus (< 265 GPa)
- Intermediate modulus (265-320 GPa)
- High modulus (320-440 GPa)
- Ultra-high modulus (>440 GPa)

Final heat treatment temperatures for carbon fibres are classified into [14]:

- Type-I, high-heat-treatment carbon fibres (HTT), where final heat treatment temperature should be above 2000°C and can be associated with high-modulus type fibre.
- Type-II, intermediate-heat-treatment carbon fibres (IHT), where final heat treatment temperature should be around or above 1500°C and can be associated with high-strength type fibre.
- Type-III, low-heat-treatment carbon fibres, where final heat treatment temperatures not greater than 1000°C. These are low modulus and low strength materials.

Carbon fibre polymer precursors are typically separated into three types: rayon-based, polyacrylonitrile (PAN)-based and pitch-based. PAN-based are the most widely used, accounting for 90% of the current carbon fibres produced [15]. Rayon-based fibres are rarely produced today, and pitch-based fibres (the term covers isotropic and anisotropic mesophase pitch) are considered a niche product. Pitch-based fibres have a higher degree of orientation than PAN-based ones resulting in pitch-based fibres having a higher modulus and greater electrical and thermal conductivity along the fibre direction. Because of their more graphitic structure they can reach a tensile modulus of over 1000GPa [16]. PAN-based fibres on the other hand, have a more complex structure compared to pitch-based, which results in higher tensile strengths as the structure hinders crack propagation [17]. A comparison of the available modulus range is given in Figure 1.3. Due to the high processing costs of pitch-based fibres, significantly higher than that of PAN-based fibres, there are a limited number of producers.

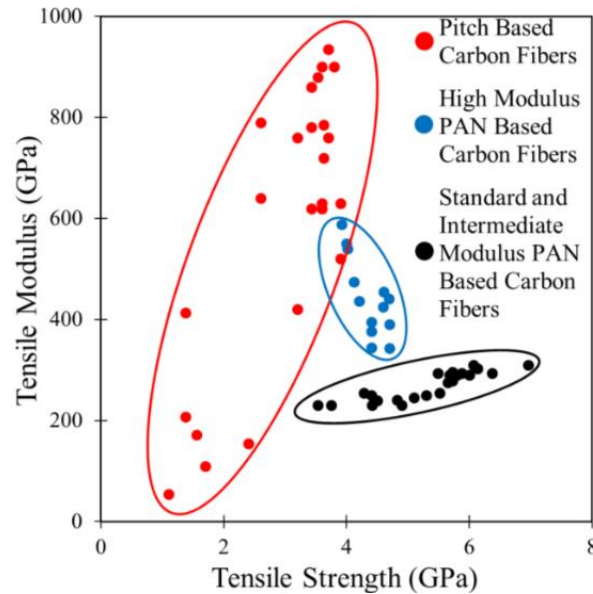


Figure 1.3. Tensile modulus plotted against tensile strength for pitch and PAN-based carbon fibres [18].

### 1.2.2 Manufacturing Process of carbon fibres from polyacrylonitrile (PAN)

The manufacturing process of carbon fibres involves several steps [19]:

**Polymerisation** – the initial stage of precursor fibre production. This can be emulsion or suspension polymerisation in which acrylonitrile, the monomer of PAN, is polymerised using catalysts and reactants to produce PAN.

**Spinning** – the polymer is converted into fibres. This can be done through melt, dry, wet or gel spinning. Immediately after spinning the precursor fibre is stretched, so that the polymer chains are aligned and filaments approach the chosen diameter. This process also determines the internal atomic structure of the fibres.

**Stabilisation** – this step involves chemically altering the fibres. They are heated to 200-400°C under tension in air and an oxidation process occurs. In the case of PAN-based carbon fibres, the polymerised linear polyacrylonitrile molecules form a thermally stable, rigid so-called ladder structure.



Carbonisation – the thermally stable fibres are further heated in an inert atmosphere, to 1000-3000°C under tension for several minutes. This removes non-carbon atoms, such as, hydrogen, oxygen and nitrogen, and increases the carbon content causing the remaining carbon atoms to bond closer together forming an ordered structure. The final carbonisation temperature and tension play key roles in influencing the carbon fibre’s mechanical properties. The overall fracture of carbon fibres is often attributed to a flaw within the fibre [20]. These flaws can occur during the carbonisation stage. If carried out too fast, the evolution of volatiles, such as, CO<sub>2</sub>, CO, CH<sub>4</sub>, H<sub>2</sub>, interrupt the structure development and leave defects. Yet if carried out too slowly, too much nitrogen is lost at this early stage, resulting in pore formation [21]. However, the chances of this occurring during the manufacturing process are low. It is more likely the voids are due to contaminating particles in the precursor, which react with the carbon at high temperatures and vaporise [21].

Surface treatment and sizing – a thin coating, typically a polymer is applied to the surface of carbon fibres to make them easier to handle and use in chosen applications.

These manufacturing steps are shown pictorially for the PAN precursor carbon fibres in Figure 1.4.

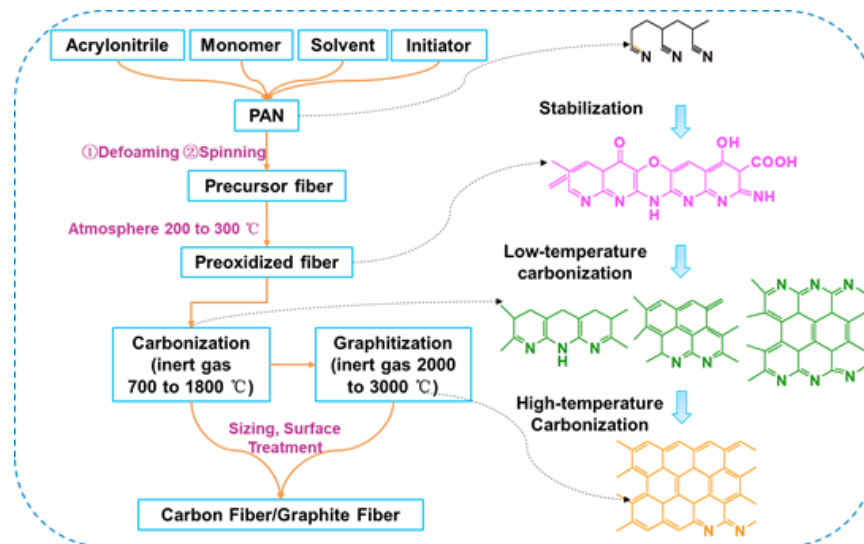


Figure 1.4. PAN-based carbon fibre manufacturing process [19].

A breakdown of the costs involved in manufacturing PAN-based carbon fibre is given in Figure 1.5, where the cost of the precursor accounts for over 50% of the manufacturing costs.

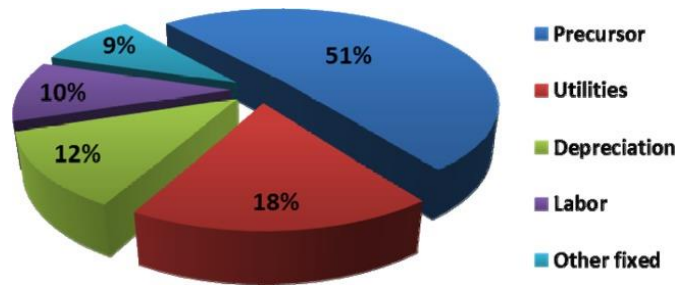


Figure 1.5. Separation of cost elements in the manufacture of carbon fibre from PAN [22].

### 1.3 Effect of heat and fire on carbon fibre

#### 1.3.1 Effect of heat and atmosphere on thermal stability of carbon fibres

Carbon fibres are very stable in an inert environment (e.g. nitrogen) up to 2000°C, where they become even stronger due to loss of any remaining functional groups/impurities left during processing. In air atmosphere however, above 550°C they start losing mass and the fibre diameters decrease due to surface oxidation [1]. The effect of oxygen concentration also plays a large role in carbon fibre oxidation.

Feih and Mouritz [23] reported that when heating T700 carbon fibres during TGA in both air and nitrogen atmospheres there was a small mass loss (0.8%) over the temperature range of 300–500°C. This was attributed to the decomposition of the polymer sizing on fibre surfaces. In nitrogen there was no further mass loss. In air, a large mass loss was seen between 500–950°C due to oxidation of carbon. The results are shown in Figure 1.6. Further SEM analysis of the fibres also found for those heated in nitrogen had no change in fibre diameter.

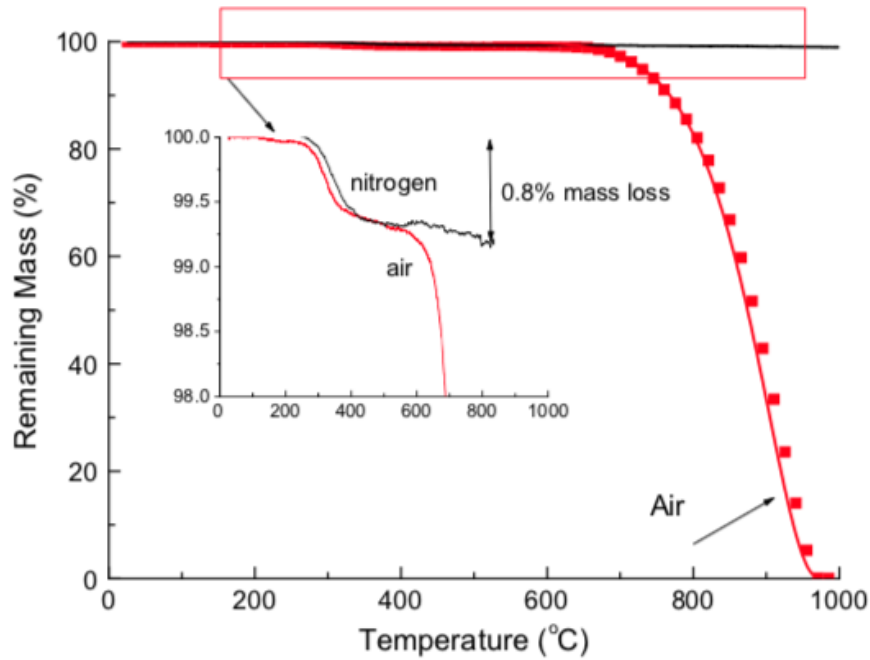
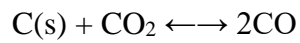
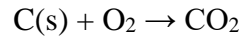


Figure 1.6. Mass loss-temperature curves for the carbon fibre heated in air or nitrogen determined using TGA at the heating rate of 20°C/min [23].

In theory, the oxidation is controlled by these reactions:



The third reaction is referred to as the “Boudouard reaction”, which determines the ratio of CO<sub>2</sub> to CO. Below 700°C mainly CO<sub>2</sub> is produced and above 700°C mainly CO [1].

### 1.3.2 Mass loss and reduction in fibre diameter

In air, carbon fibre mass loss begins to occur at temperatures above 500-550°C and with increased temperature the rate of mass loss also increases. This was also seen by Feih and Mouritz [23] when they conducted isothermal TGA tests at temperatures from 500°C to 650°C (Figure 1.7(a)) on T700S PAN-based carbon fibres. Extended heating at these temperatures

would result in complete oxidation of the carbon fibre (and hence no residual mass). At elevated temperatures this has been observed to occur within minutes. Su et al. [24] observed that at 850°C the oxidation of the carbon fibres to its gaseous products was complete within a few minutes.

Feih and Mouritz [23] also have reported a correlation between mass loss and fibre diameter as shown in Figure 1.7(b), where theoretical relationship for fibres held at temperatures from 500°C to 700°C is also plotted. These results suggest there is uniform diameter reduction of the fibres due to surface oxidation between these temperatures.

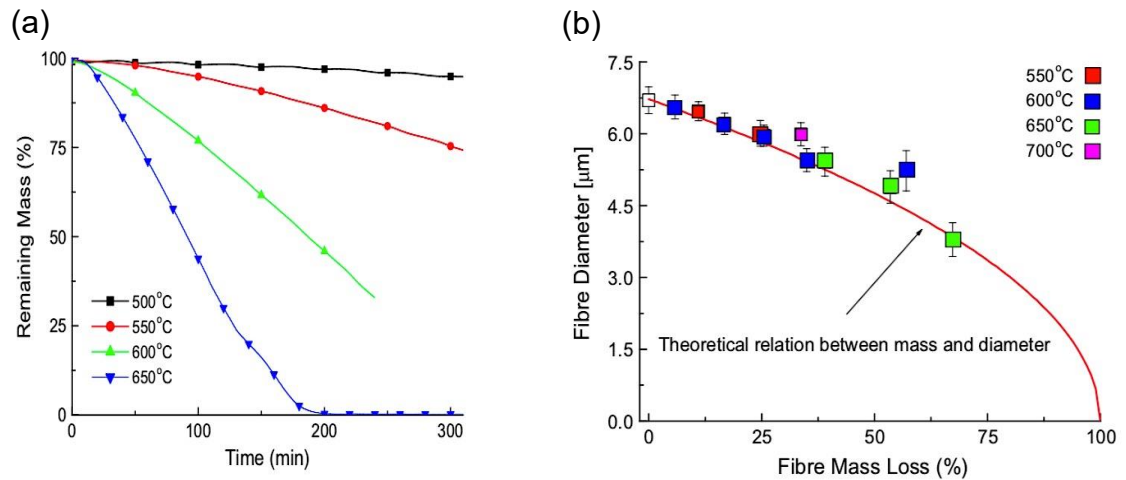


Figure 1.7. Effect of temperature and heating time on the mass loss of carbon fibre in air T700S [23].

In another study Feih et al. [25] suggested that impurities in the fibres could increase the rate of mass loss. These impurities lead to surface pitting, where micro-pores and porosity develop at different rates, causing the active surface to change. The presence of very small amounts of elements such as, platinum or sodium, could cause localised acceleration of oxidation and result in pitting on the fibre surface (Figure 1.8) [25]. This idea was also tested by Yin et al. [26] when they used an alumina boat to contain their carbon fibres in a furnace. Areas with increased carbon fibre oxidation were observed in areas in contact with the boats. They theorised it was due to impurities in the alumina, e.g.  $\text{Na}_2\text{O}$  which upon heating reacts with oxygen to become sodium peroxide, which can react with carbon.

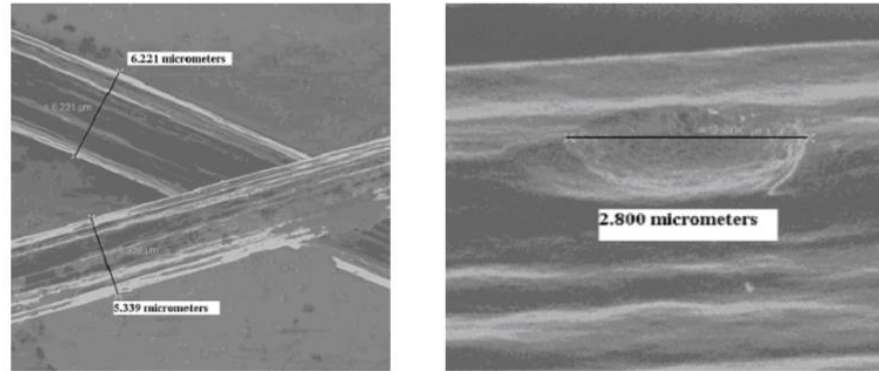


Figure 1.8. Diameter reduction and pitting on carbon fibre surface after exposure to 600°C for two hours [25].

This may also explain why the oxidation process is not the same for each grade of carbon fibre, even if the same precursor is used. Trumbauer et al. [27] studied the oxidation behaviours of PAN-based standard modulus T300R and intermediate modulus IM7 fibres up to 1000°C. Between 400°C to 950°C both fibres displayed different oxidation behaviours – the T300R carbon fibres oxidised along the axis from the end of the fibre, whereas the IM7 showed uniform oxidation over the fibre surface. The rate of oxidation also differed, where that of the T300R fibre steadily decreased because of the fibre mass loss, yet the oxidation rate of the IM7 fibres increased until 35% burn-off had occurred and then steadily decreased.

### 1.3.3 Effect of heat and fire on mechanical properties of carbon fibres

As discussed above, carbon fibres oxidise at higher temperatures in oxygen containing environments, where there is mass loss due to surface oxidation. Their oxidation behaviour restricts use in high temperature environments, typically above 500°C for carbon fibres and 200°C when used in epoxy composites.

#### *Effect on fibre modulus*

Heating carbon fibres in an oxygen-free atmosphere such as nitrogen or a vacuum, does not result in a change in the elastic modulus [25, 28]. However, when heating in air as oxidation

occurs it has been found that the modulus decreases (Figure 1.9(a)). The lack of change in modulus when heated in oxygen absent environments suggests that temperature solely is not responsible for the increase in fibre stiffness seen in air. Therefore, fibre modulus is most likely related to the mass loss due to surface oxidation observed in air. Feih and Mouritz [23] found a two-stage relationship between mass loss and Young's modulus for carbon fibres heated in air. During the first stage, fibre modulus decreased proportionally to mass loss until 35% loss. The second stage showed no change in modulus with increasing mass loss. This behaviour was credited to the non-heterogeneity of the PAN-based carbon fibre cross-sectional microstructure. Initially there is surface oxidation of the carbon fibre, where the microstructure of the outer surface of the carbon fibres are reported to consist of the crystalline planes with a high degree of preferred orientation along the fibre axis which are responsible for the fibre's stiffness. The second stage is oxidation of the lower modulus core. This structure is most likely brought about during the thermal stabilisation stage where oxygen diffuses into the core of the precursor fibres [29]. In Figure 1.9(b) a simplified version of the two-layer structure is presented for demonstration purposes only. In reality the boundary between the layers would not be well-defined but a complex structure changing over a small distance. The line plotted is of the predicted relationship from models in [23] based on their 2-layer (skin-core) model. This skin-core heterogeneity was also reported in [30, 31].

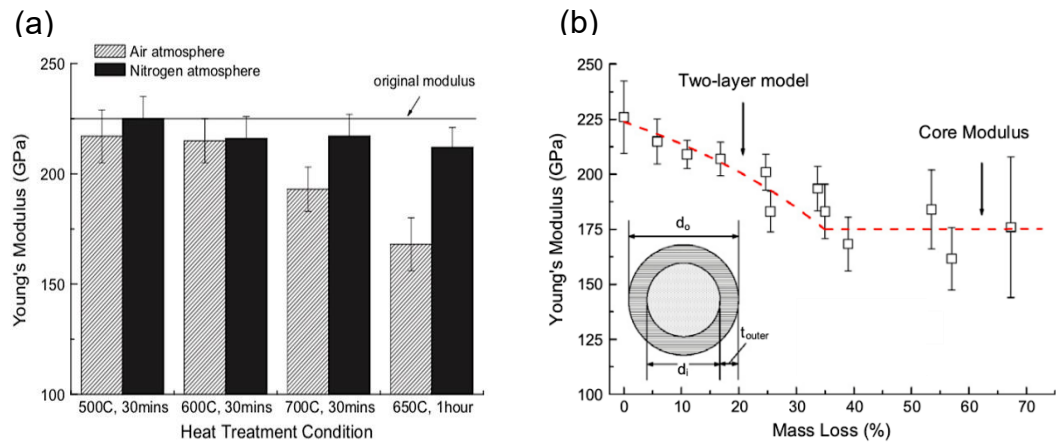


Figure 1.9. (a) Fibre modulus for heat treatments in air or nitrogen (b) Young's modulus at different mass losses of carbon fibre when heated in air with calculated relationship and diagram illustrating the two-layer structure of carbon fibre [23].

### *Effect on fibre strength*

The results from [23] shown in Figure 1.10(a) which records the effect of temperature on fibre strength (obtained using a two-parameter Weibull strength distribution from [31] in air after holding fibre bundles at temperatures from room temperature to 700°C for both 30 minutes and 2h in a furnace. Above 400°C fibre strength began to decrease until 600°C and increased exposure time in this range resulted in greater loss of fibre strength. After 700°C for 2h the fibre had fully oxidised. It was further reported that fibre strength was most likely controlled by a single critical defect, yet SEM images were unable to identify it. Instead, using the results for fibre strength and assuming it is a surface flaw, they predicted flaw size and this is given in Figure 1.10(b).

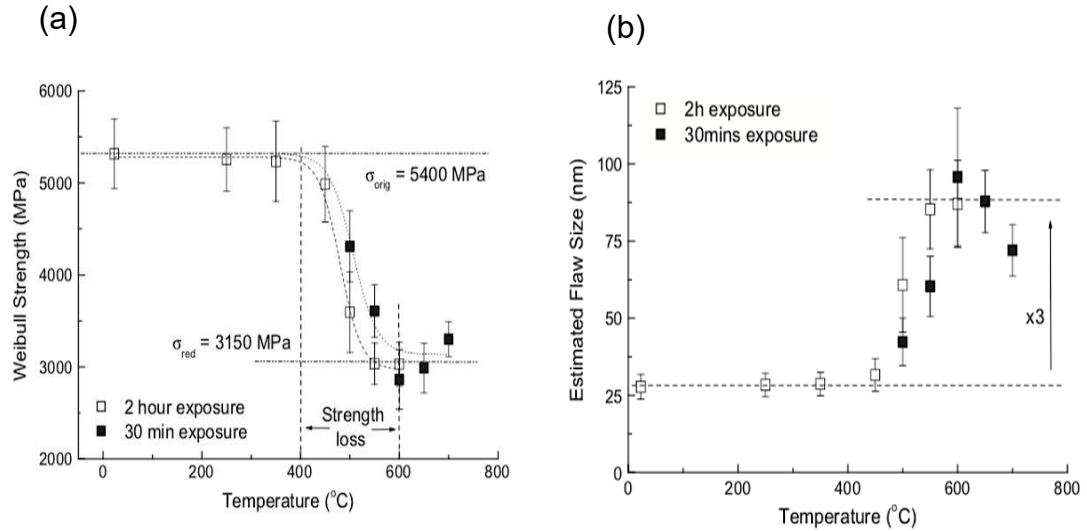


Figure 1.10. (a) Weibull strength of fibres held at various temperatures for 30min or 2h (b) Estimated flaw size leading to failure at the same conditions as (a) [23].

Li and Xian [32] conducted single PAN- based fibres (TC36S) tensile tests on carbon fibres, holding the fibres in air for 30 minutes at temperatures varying from room to 700°C and found similar results. Between room temperature and 400°C, the tensile strength only decreased slightly, even at 500°C it was within error of that at room temperature, but at higher temperatures the tensile strength reduced significantly. At 700°C within 30 minutes the carbon fibre had fully oxidised and single-fibre measurements could not be taken.

### 1.3.4 Electrical properties of carbon fibres and CFRCs

Carbon fibres are electrically conductive. This can be a drawback and in some applications glass fibres cannot be replaced with carbon fibres due to their conductivity. Electrical resistance has been found to vary between different carbon fibres, even those from the same precursor. Furthermore, resistance is dependent on the individual fibre diameter to the extent that electrical impedance measurements have even been used to determine the fibre diameter. Furthermore, impedance was also found to be directly proportional to the length of the carbon fibre [33].

Sauder et al. [34] investigated the relationship between high temperatures (up to 2000°C in a vacuum) and conductivity of PAN-based and rayon-based carbon fibres. Electrical conductivity was found to be temperature dependent - as the temperature increased, so did the electrical conductivity. While low temperature data was not recorded, they believed this trend follows that of an extrinsic semiconductor. At low temperatures conduction is ruled by impurities (extrinsic conductivity), while at high temperatures the thermal energy is enough to induce electronic transitions. The electrical conductivity of rayon-based fibres was more affected by temperature than the PAN-based fibres. This is seen in Figure 1.11(a-b). They put this down to the fibre's microstructure and the orientation of the basal planes being parallel to the fibre axis.

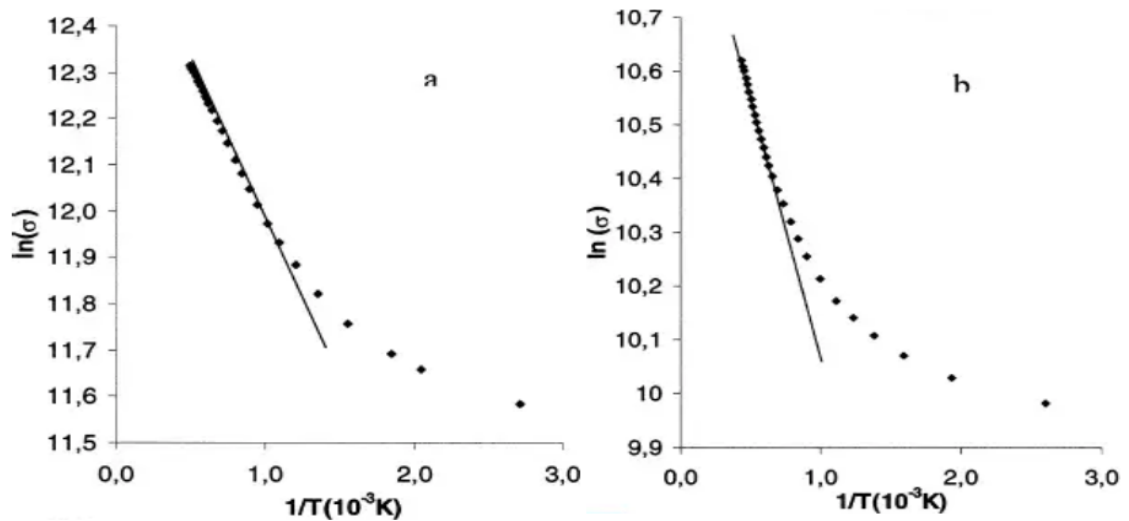


Figure 1.11. Electrical resistivity ( $\sigma$ ) against temperature for a (a) PAN-based and (b) rayon based fibre [34].



Owston [35] measured the resistance of single carbon fibres under different mechanical strains. Initially no relationship between strain and electrical resistance was observed, but as the strain increased above 0.1%, the resistance increased linearly. He attributed this to the fibre's microstructure where the fibrils inside the fibre came into greater contact as the strain increased.

While carbon fibres are conductive, the polymer matrix of CFRCs is an insulator. This means the electrical resistivity of CFRCs is significantly higher than carbon fibres. While most metals have a resistivity of around  $10^{-8}\Omega\text{m}$ , the CFRCs resistivity is 1000 times higher than that [36]. This is because of the polymer matrix. For example, epoxy has a resistivity from  $10^{11}\Omega\text{m}$  to  $10^{13}\Omega\text{m}$  due to the lack of free electrons to conduct [37]. CFRCs consist of an insulating polymer layer on the surface, an insulating polymer, and conductive carbon fibres inside. These differences cause CFRCs to be anisotropic along the layers of the composite. Conductivity is greatest along the fibre direction, which means CFRCs have better conductivity in the longitudinal direction compared to the through-thickness direction. There are many experimental methods to measure the electrical properties of CFRCs, including the four-probe method [36], induction [38, 39] and electrical impedance tomography [40]. The electrical conductivity also strongly depends on the fibre volume in the CFRCs. The higher the volume of carbon fibres the more conductive it is. Adding conductive filler to the resin can increase electrical conductivity. For example, Wentzel and Sevostianov [41] added graphene to the epoxy in unidirectional CFRCs which significantly increased the composite's electrical conductivity.

#### **1.4 Structural performance of CFRC under heat and fire**

When subjecting a CFRC to increased temperatures below the resin matrix's glass transition temperature,  $T_g$  (typically 80-120°C) the CFRC will not be significantly affected and will maintain the same appearance. Only slight changes in its mechanical properties, such as reduction in strength and stiffness, will occur. However, above its glass transition temperature dramatic changes in mechanical properties occur. The resin changes from a glassy to a rubbery

state, causing a considerable reduction of both strength and stiffness. Further heating or fire results in structural failure and complete loss of mechanical properties.

Using the T700 carbon fibre, Feih and Mouritz [23] tested carbon fibre epoxy laminate strips under the cone calorimeter at 35 and 50kWm<sup>-2</sup> heat fluxes while also applying a tensile load. From recording the temperature on the laminate's front and back surface during the test and comparing with TGA, it was found to go through the following stages; softening of the resin as it reach its glass transition temperature, followed by decomposition of the resin matrix, on the surface facing the cone heater, which then fully extended through the thickness of the laminate over time with the resin decomposing into volatile gasses and char (this was also theorised in an earlier paper [42]). The temperature of the back face of the laminate at 35kWm<sup>-2</sup> was not high enough for complete decomposition of the resin. However, it had lost the majority of its strength. Even after 4 minutes, it was found that the laminate was still able to bear an applied stress (below a threshold limit) due to the carbon fibres. Ultimate failure of the laminate was therefore due to fibre breakage.

Wang et al. [43] studied the mechanical properties of pultruded carbon fibre-reinforced polymer (CFRP) plates from 20°C to 700°C. Heat was applied by a furnace and the CFRP loaded until fracture in a tensile testing machine. While recording the surface temperature of the CFRP as it was heated (100°C/min rate), they saw two temperature spikes – the first at 350°C due to the epoxy resin igniting and then at 600°C, as the carbon fibres oxidised and so released heat. Similar observations were made on tests done at Sandia National Labs [44] where CFRCs were exposed to a jet flame. Two peaks in heat released were measured, one consistent with flaming combustion and the later one believed to be due to fibre oxidation.

Wang et al. [43] tested tensile properties of CFRCs after holding the samples at various temperatures for 5 minutes. The stress-displacement curves are given in Figure 1.12. Samples held from 22°C to 520°C showed a linear relationship up to failure. But for those held at 625°C and 706°C the relationship was no longer temperature dependent and the relationship became nonlinear at higher stresses. This was attributed to loss of fibre strength following oxidation.

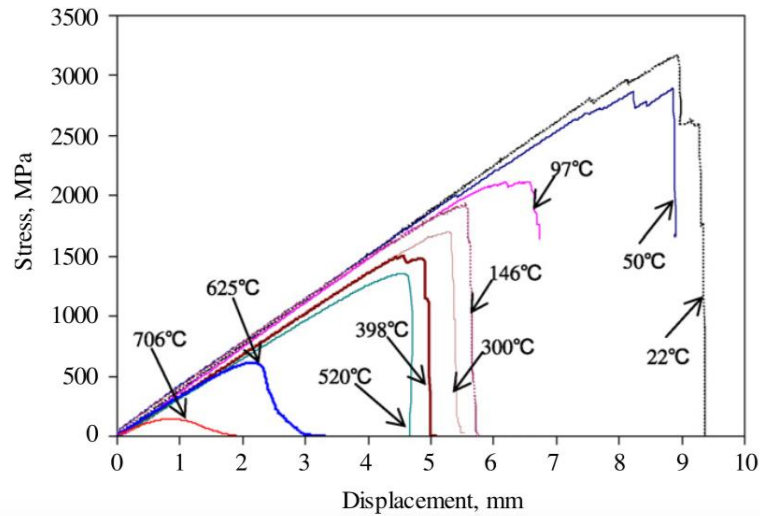


Figure 1.12. Stress-displacement curves for CFRP held at various temperatures for 5 minutes [43].

These authors separated the CFRPs' failure mode by exposure temperature. Those held at low temperatures, from 22-50°C failed primarily by brittle fracture. From 96-308°C, failure was located in the furnace region, leading to softening and gasification of the epoxy resin matrix and then fibre breakage. From 395 to 625°C, little or no epoxy remained on the samples and remaining fibres they were fully flexible before testing. At 706°C all epoxy had burnt and over 50% of the fibre had oxidised and failure was due to fibre breakage.

However, Di Modica et al. [45] conducted compression tests using a loading frame and propane burner to examine the fire response of CFRCs, it was found that compression failure was resin dependent and the thickness of the laminate played a significant role in time-to-failure.

### 1.5 Structural performance of carbon fibres in CFRC under heat and fire

Bell [3] has conducted the early testing in the period 1970s to 1980s and has reviewed most of the work prior to that on the release of carbon fibres from burning composites used in airplanes, as part of a NASA program. This was concerned with the effect of released carbon fibres on surrounding electrical equipment. The scale of the tests included large-scale outdoor fire tests, chamber tests and those on a laboratory bench scale. In this programme, several large-scale fire

tests were carried out by the US Army at Dugway Proving Ground to determine the concentration of carbon fibres released from exposing carbon fibre epoxy composites to fire. One such test included exposing 45kg of carbon fibre epoxy composite to a jet fuel fire for 20 minutes. On examining the collected pieces they found single fibres along with clusters of fibres and even intact fragmented pieces of the CFRCs. The proportion of single fibres released was 0.23% of the original fibre content [3]. Of the collected fibres during these tests, the mean diameter was 4.2 $\mu$ m, significantly reduced from the 7 $\mu$ m of the original fibre. Given the flame temperature reached over 900°C in air, many of the carbon fibres had fully oxidised during the test. Another large-scale test at China Lake studied the effect of both burning (with either a propane or jet JP-5 fuel burner) and impact (using explosives) on CFRCs components, including recreations of a 737 spoiler and a DC10 rudder. Both fire and impact was to simulate a real-life plane crash situation. A 1mm mesh was used to collect the fibres, with the length of fibre collected ranging from 1-5mm. As such low numbers of fibres were collected (0.008-0.010% of the original mass) results were not conclusive.

In fire chamber tests at Lowell, USA, NASA studied the release of carbon fibre due to burning composites with a combination of gas and radiant heating (to simulate the conditions of a jet-fuel fire) using strips close to 50 x 125mm. The air-to-fuel ratios ranged from 6:1 to 20:1 and showed that carbon fibres oxidised quicker when more oxygen was present. Furthermore, this NASA programme found that for thin composites with impact – such as with explosives – increased the number of single fibres released from the burning composite. This was highlighted in the Dahlgren burner chamber tests, in which after just burning a carbon fibre epoxy composites (0.1m<sup>2</sup> and 6.4mm thick) resulted in 0.01-0.2% of single fibres released, but when combined with explosive impact, this increased to 15-20% of fibres. Another of the chamber tests with impact was at Ames, Redwood, USA where large CFRCs samples of 0.3m<sup>2</sup> were exposed to a burner for up to 20 minutes and impacted with a weight using a drop tower, only 0.1% of the carbon fibres were collected with lengths 0.5-3mm.

In laboratory-scale tests done later in 1997 by the US Coast Guard, who used a cone calorimeter at 50 and 75kWm<sup>-2</sup> on 100x100mm graphite/epoxy composites [46], the composites were burned completely and the released fibres collected. They were characterised using SEM. The

fibre diameters ranged between 0.5-9 $\mu\text{m}$  in diameter (mean 2.5 $\mu\text{m}$ ) and between 3-210 $\mu\text{m}$  in length (mean 52 $\mu\text{m}$ ).

### **1.5.1 Health concerns of released fibres**

While inhalation of smoke during the early stages of composite combustion can cause short-term health problems, such as difficulty in breathing, it is the fibre fragments which have been highlighted as a more dangerous long-term hazard to human health.

Real life crash site data have highlighted the hazards that first responders faced on a crash site in Denmark of a Harrier GR5 containing carbon fibre epoxy composites. Results showed, that even after the fire had been extinguished, and while wearing personal protective equipment, some suffered from eye and skin irritations, as well as breathing difficulties [47].

This showed the two major health concerns of exposure to carbon fibres resulting from the combustion of CFRCs. The first is irritation to skin and eyes. The seriousness of this would depend on the size of the fibre and their stiffness, where fibre diameters of at least 4-5 $\mu\text{m}$  are required to cause such irritation [48]. The second is their potential inhalation. There have been studies on the deposition of fibre particles in the human respiratory passage [49, 50]. Due to difficulties in human trials, casts and airway passage replicas, along with numerical models are typically used to measure the amount of fibre entering the respiratory system. While the size of the fibre is important, flow rate and the inertia of the fibres play major roles, where impaction is credited as the principal deposition mechanism [51].

Researchers also found that the deposition efficiency of fibres is less than that of spherical particles [51, 52]. Using human nasal models, glass fibres with a diameter of 1  $\mu\text{m}$  were shown to deposit in the human nasal cavity [53]. They attributed this to the fibres aspect ratio having an effective aerodynamic diameter similar to spherical particles. In [51] studying carbon fibres of diameter 3.66  $\mu\text{m}$ , the inertia of the fibres played a larger role. Those with high inertia were deposited in the nasal airway but those with low inertia passed through the nasal airway and could potentially enter the lungs.

Mourtiz [54] summarised the aerodynamic sizes of particles which humans could inhale and these are given in Table 1.1. The aerodynamic diameter assumes the fibre to be spherical. Fibres over 50 $\mu\text{m}$  in length are typically not inhaled because their weight causes them not to stay airborne long. Airborne fibres carried in smoke are more likely to be 7 to 50 $\mu\text{m}$ , however, on the chance some are inhaled, they would be trapped at entry points (nose and throat) and expelled through coughing and sneezing. The work concluded that aerodynamic diameters between 0.7 to 7 $\mu\text{m}$  pose the greatest risk because if inhaled they could be deposited in the alveoli of the lungs, leading to haemorrhages. As reported in [54] fibre diameters of the most concern are around 2 to 3.5 $\mu\text{m}$ .

Table 1.1. Taken from [54] summarising the aerodynamic sizes of particles which humans could inhale.

Aerodynamic Diameter	Effect
>50 $\mu\text{m}$	Usually not in air long enough to be inhaled.
~ 7-50 $\mu\text{m}$	Particles in this size range are often large enough to be caught by nose and throat, and are often ejected by coughing or sneezing. Usually filtered out by the nose, although can be deposited in cilia or airways.
0.7 – 7 $\mu\text{m}$ (respirable dust)	This particle size range presents the greatest hazard. They are small enough to reach the lungs when inhaled, yet large enough to remain in the lungs when we breathe out. Deposited in the lower bronchioles and alveoli.
<0.5 $\mu\text{m}$	Usually remain airborne and are exhaled.

The resulting carbon fibre particle sizes from a burn test of a carbon fibre epoxy composite, were defined by Gandhi et al. [48]. Using the data in Table 1.1 as a guideline for which sizes can be inhaled and comparing it to the graph in Figure 1.13, around 60% of the fibres collected are small enough to be inhaled and cause potential damage to the alveoli.

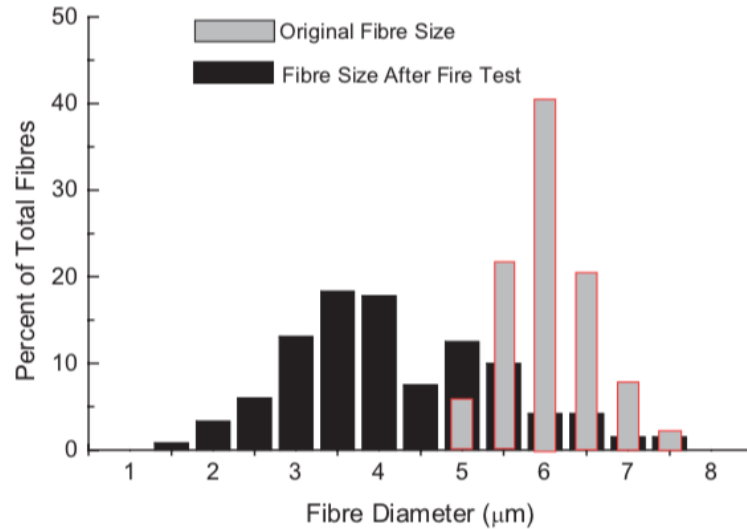


Figure 1.13. Diameter of fibres recovered from fire testing [48] with the original fibre diameter distribution [54].

## 1.6 Improving structural retention of carbon fibres in CFRCs: Use of flame-retardants to reduce CFRC combustion

### 1.6.1 Thermal degradation of epoxy resins

When CFRCs are exposed to heat the resin begins to break down at around 150°C, at higher temperatures it then ignites and burns. Hence to reduce its combustion the resin is typically modified [55-57]. In this section decomposition of the resin and the effect of different flame-retardants (FRs) has been summarised.

The combustion properties of CFRCs depend on the type of resin used, as well as the curing agent, curing process and cross-linking density. Resins are divided into two types - thermoplastic or thermosetting as stated previously. The most common type of resins used in the aerospace industry are thermoset epoxy resins, particularly the glycidyl-based epoxy resins, where the diglycidyl ether of bisphenol-A (DGEBA) takes up 75% of the epoxy resin market [9]. Figure 1.14 shows the two-step thermal degradation of a cured epoxy DGEBA resin. Up to around 400°C dehydration of the resin predominantly occurs with the formation of a polyaromatic structure and release of H<sub>2</sub>O and H<sub>2</sub>. The following stage is a thermo-oxidative

reaction, when the carbonaceous residue is completely decomposed [9, 58]. To measure the flammability and thermal stability of cured resins, limiting oxygen index (LOI), UL-94 test, and thermogravimetric analysis (TGA) methods are often used.

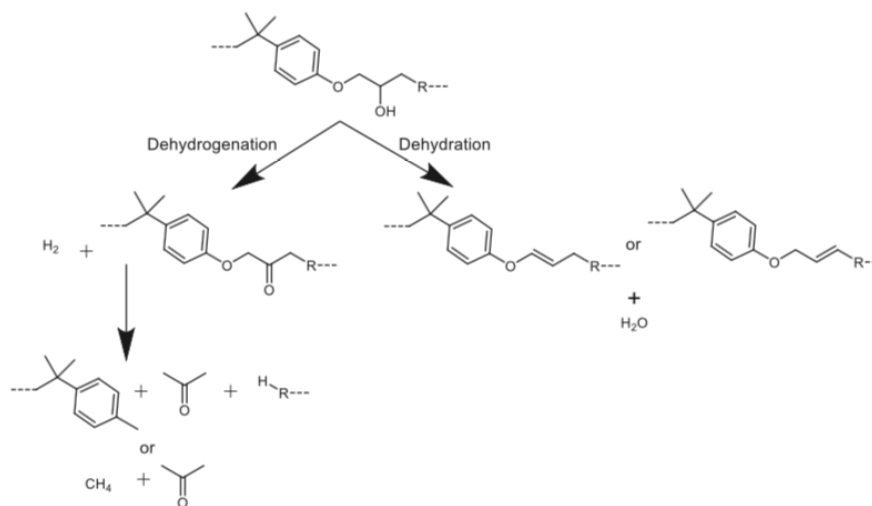


Figure 1.14. Thermal degradation of DGEBA-based epoxy resin [9].

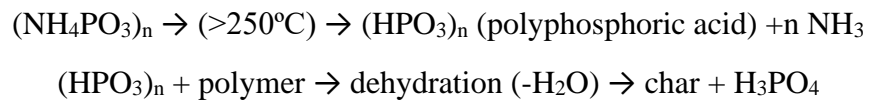
To improve their resistance to heat/fire, the resin matrix can be modified with FRs. This is done either by structural modification of the resin, where elements with flame retardant functions are introduced directly into the molecular structure of epoxy resin or hardener (reactive), or by adding flame retardant chemicals (additives) to the resin at the preparation stage (before adding the hardener) [9]. In both cases the FRs chosen can either work by gas-phase and/or the condensed-phase.

### 1.6.2 Condensed-phase flame retardants

Condensed-phase flame retardants work by reacting with the polymer during pyrolysis and promote char formation. These are usually phosphorus based FRs, with those commonly used in epoxy including the inorganic phosphates - ammonium polyphosphate (APP), melamine phosphate (MP) and melamine polyphosphate (MPP). Other condensed-phase phosphorus FR, such as red phosphorus and metal phosphates are less compatible with epoxy resins. Their inclusion results in phase dispersion and separation, hindering the resins' curing and reducing its mechanical properties [59]. As inorganic phosphates thermally break down, anhydrides of



phosphoric and related acids are produced which catalyse the dehydration reaction [60]. These reactions lead to cross-linking and carbonised structures. This char layer provides a protective barrier to oxygen, pyrolysis gases, thermal feedback, smoke and products of incomplete combustion. For example, when a resin containing the flame retardant APP is exposed to heat/fire, it decomposes into polymeric phosphoric acid and ammonia. The polyphosphoric acid reacts with hydroxyl groups in the epoxy to form a non-stable phosphate ester. This is followed by the dehydration of the phosphate ester. Char forms as an insulating layer, stopping any more decomposition of the resin [61].



Matykiewicz [62] studied the inclusion of varying amounts (5 to 20wt%) of APP and MPP to glass fibre-reinforced epoxy composites. They conducted TGA in both air and nitrogen on the samples, which is shown in Figure 1.15 (where they used to acronym PNA for MPP) [62]. In nitrogen, for all composites with added FR, there was a two-step decomposition, as opposed to the one step for the sample without FR (the control labelled ASET). These two steps are due to the breakdown of the APP (as described above) and MPP. The production of char also accounts for the greater residual mass of the composites with FR. In the presence of oxygen, there is a two-step decomposition for ASET, this additional step is due to the oxidation of the char residue. Those containing FRs showed the same trend as in nitrogen but also had a third step due to char oxidation which resulted in less residue remaining, compared to in nitrogen (with the except of 20APP).

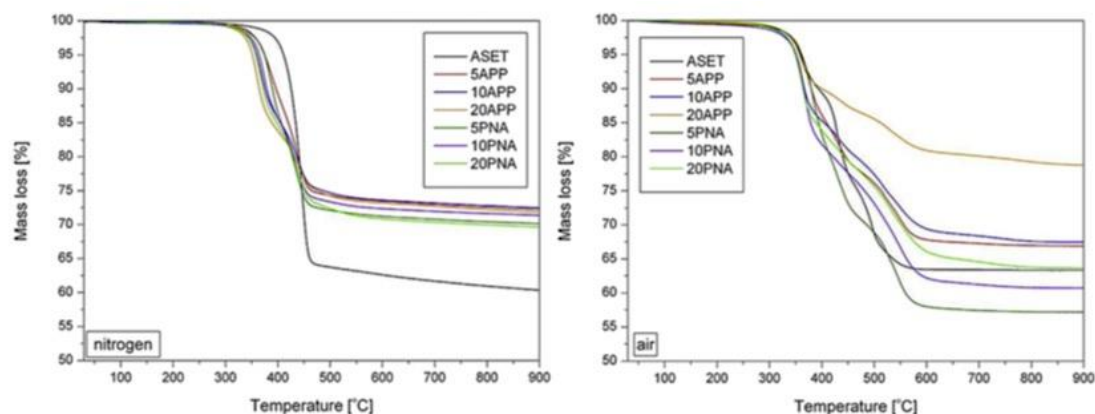


Figure 1.15. TGA in nitrogen and air for glass fibre reinforced epoxy composites containing 5 to 20wt% of APP or MPP [62].

LOI experiments which measure the minimum percentage of oxygen required to sustain flaming combustion, show that by adding as low as 5wt% APP to a DGEBA resin (with a low molecular weight polyamide curing agent) increased its LOI from 19.6 to 27.1 vol%. A summary of epoxy/APP mix and their resulting LOI values is given in Table 1.2.

Table 1.2. LOI values of epoxy resins containing different wt% of APP.

Content of APP (wt%)	LOI Values (vol%)*			
	Ref [60]	[62]	[63]	[64]
0	19.6	25.9	25.5	20.2
5	27.1	29.1	-	26.8
10	-	29.7	30	29.3
20	-	30.1	38	41

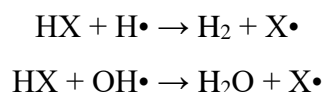
\*The uncertainty of measurements for LOI is  $\pm 0.5$  vol%

Son et al. [63] carried out cone calorimeter measurements at  $30\text{kWm}^{-2}$  on  $100\text{mm} \times 100\text{mm} \times 3\text{mm}$  samples of epoxy resin with 10 and 20wt% APP. They found the inclusion of APP increased TTI and decreased peak heat release rate. These results indicated that APP promoted char formation and therefore improved the thermal stability of epoxy at high temperatures. Zhang et al. [65] used samples of DGEBA epoxy resin with phosphorus-based FRs APP and

PEPA (1-oxo-4-hydroxymethyl-2,6,7-trioxa-1-phosphabicyclo[2.2.2] octane) at  $50\text{kWm}^{-2}$ . They also found the TTI was increased for all samples with added FRs, with the inclusion of APP resulting in the longest delay. The HRR curves showed the control epoxy, after ignition burnt quickly with a sharp peak in peak heat release rate, p-HRR, but the inclusion of 2.9wt% APP increased this. PEPA, also found to work in the condensed phase however, significantly reduced the p-HRR and this was attributed to char forming ability.

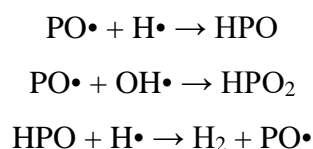
### 1.6.3 Gas-phase flame retardants

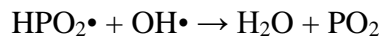
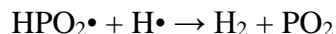
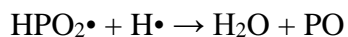
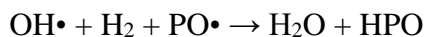
Gas-phase FRs operate by inhibiting the oxidation reactions (and hence flame propagation). They trap free high energy radical species (e.g.  $\text{H}\cdot$  and  $\text{OH}\cdot$ ) which evolve as the resin breaks down. These are typically halogenated species containing chlorine and bromine as they can react with these radicals, interrupting the radical chain mechanism of the combustion. This is shown in the following where X can be either Cl or Br:



Tetrabromobisphenol-A (TBBA) is a common halogen FR used mainly in printed circuit boards. But while these are very effective flame retardants, there are many environmental concerns surrounding them which has led them to being phased out in recent years [66].

Some organophosphorus flame retardants also work in the gas phase. The most common contain phosphinate, phosphonate and phosphate ester groups [67]. Those that work in the gas-phase, behave similarly to halogenated FRs but with the  $\text{PO}\cdot$  radicals trapping free radicals within the flame chemistry. While there are many reactions occurring during combustion, below are those governing the gas phase action of phosphorus-based additives [9]:





The phosphonate 9,10-dihydro-9-oxa-10-phosphaphenanthrene-10-oxide (DOPO) has been reported to work in the gas-phase, where there have been many studies on its ability as a flame extinguisher in epoxy resin. DOPO reacts with the epoxy monomer via its reaction of its P-H group. Given this reaction, the mechanical properties of the cured epoxy could be affected, which has led researchers to increase its reactive functionality [9].

#### 1.6.4 Silicon-based flame retardants

There are also silicon-based flame retardants which include siloxanes and polysiloxanes, along with nano-particles - silicates, silsesquioxanes and silica. They work in the condensed phase by forming a physical barrier on the resin surface to impede the flow of oxygen and other volatiles.

They were often used in combination with other FRs but more recently their uses as nano-particles are being explored. Of the silsesquioxanes, polyhedral oligomeric silsesquioxanes (POSS) has been studied frequently. At its core it has the thermally stable Si-O-Si bond, and on the surface it has various functional groups with particle diameters ranging from 1 to 3nm [2, 59]. While on its own its flame retardancy effect has been modest, it is often used as additive with another FR additive or modified with a FR chemical. For example, there are numerous reports on modification of POSS with DOPO [68, 69].

Other nanoparticles include layered silicates which are also called nanoclays. These include, the cationic and organofunctionalised montmorillonites (MMT) and anionic layered double hydroxides (LDH). Nano-clays work in composites by forming a surface physical shield during thermal decomposition. The shield is made up of inorganic nanoparticles remaining after the polymer has decomposed, and usually following the migration of nanoparticles to the top layer [70]. This barrier reduces the release of the volatiles and acts as a heat shield to re-radiate heat

from an external heat source. Other nanoparticles that can work in a similar way, include graphene oxide and carbon nano-tubes [9]. All are typically added to the epoxy in concentrations below 10wt% due to difficulties in dispersion but where they appear to be most effective.

### **1.7 Improving structural retention of carbon fibres in CFRCs: Carbon fibre surface coatings**

The surfaces of carbon fibres can be modified prior to making the composite. A high temperature resistant coating may protect the fibres by preventing exposure to the environment, and therefore they would not oxidise as readily during heat exposure. As carbon fibres have a large surface area to volume ratio, this can be exploited, thus making an oxidation barrier on the surface of individual fibres a viable approach.

#### **1.7.1 Types of materials used for carbon fibre surface coatings**

Applying ceramic compounds as coatings to carbon fibres has been shown to improve their oxidation resistance. At very high temperatures, the carbon atoms bond with otherwise inactive species to form interfibrillar bonds. For example, silicon carbide (SiC) is stable in air up to 1000°C. These coatings act as an effective heat barrier and include carbides (SiC, TiC) [71] nitrides (BN) [72] oxides (SiO<sub>2</sub>) [73] and metal oxides (Al<sub>2</sub>O<sub>3</sub>, MgO, and ZrO<sub>2</sub>) [74-76].

Silicon-containing coatings can improve the oxidation protection to carbon fibres. Hao et al. [77] found coating carbon fibre in SiC increased the initial oxidation temperature by 90°C compared to those not coated. Gallyamova et al. [78] found when conducting isothermal tests at 600°C that the weight loss carbon fibre was almost double that of the same fibres coated with SiO<sub>2</sub>. Yang et al. [79] demonstrated much greater oxidation protection by preparing a SiO<sub>2</sub> coating with dispersed SiC nanoparticles. The TGA results (Figure 1.16) shows the SiC/SiO<sub>2</sub> coated carbon fibres began to lose mass at 900°C, with 57wt% still remaining at 1400°C, while the original fibre had fully oxidised by 850°C.

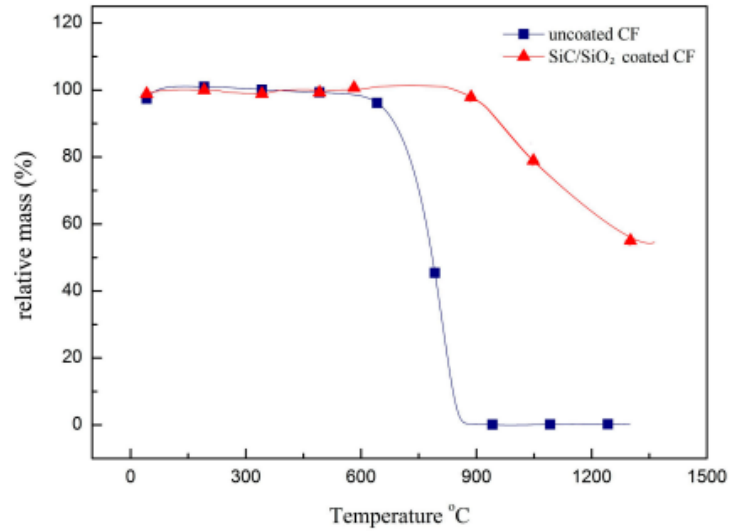


Figure 1.16. TGA in air of uncoated carbon fibres and those coated with SiC/SiO<sub>2</sub> [79].

Titanium nitride (TiN) [80, 81], aluminium nitride (AlN) [82] and boron nitride (BN) [83-85], have all been used to coat carbon fibres, due to their low densities and high thermal conductivities. Xu et al. [86] coated carbon fibres with BN nanosheets. TGA results (Figure 1.17) showed that the oxidation of the uncoated fibres began to oxidise at around 500°C and were fully oxidised 740°C (only 1wt% remaining), yet for those coated with BN, oxidation began around 640°C up to 850°C.

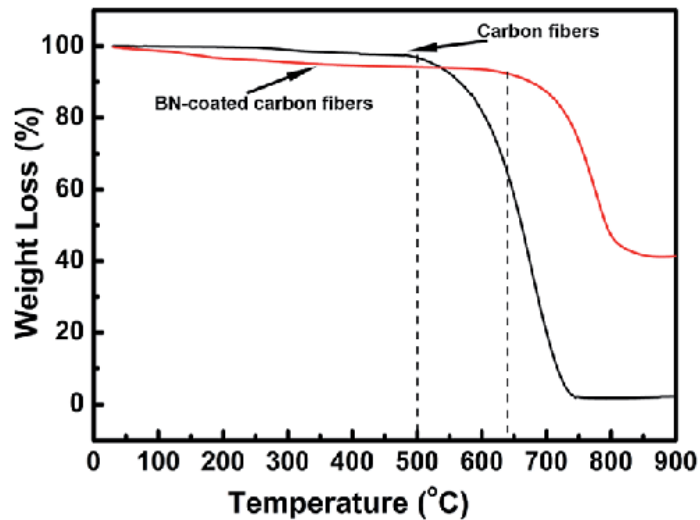


Figure 1.17. TGA in air of uncoated carbon fibres and those coated with BN [86].

Zhang et al. [81] noted that while trying to apply TiN coatings on carbon fibres, the oxygen-containing functionalities on the fibre surface introduced an oxide component to the coating and the TiN coating provided little oxidation protection. Yet when using TiC, more promising results have been observed. Fibres have been coated with TiC/Ti<sub>2</sub>AlC mixtures using an in-situ reaction in a molten salt bath, and the TiC/Ti<sub>2</sub>AlC coatings provided protection to carbon fibres in static air up to 800°C [87]. However, while these coatings provided the fibres with good protection from oxidation, Wang et al. [88] found that *in-situ* growth of the TiC/Ti<sub>2</sub>AlC coatings introduced surface defects and damaged the fibre, decreasing its mechanical properties. Constantin et al. [89] used the molten salt process to react titanium, chromium and carbon fibre to form a multilayer carbide coating consisting of Cr<sub>3</sub>C<sub>3</sub>, TiC and Cr<sub>3</sub>C<sub>2</sub> layers, which protected the fibre at temperatures as high as 1200°C.

### **1.7.2 Size removal and activating the carbon fibre surface prior to coating**

The final stage of carbon fibre production is called sizing as mentioned previously. This is where a thin coating, typically a polymer, is applied to the individual fibres in order to protect them from damage when they are later handled or woven into a fabric. However, when applying other coatings to the fibre, the sizing can be detrimental to the adhesion of the coating. For example, when Qiu et al. [90] applied a graphene coating to fibres, the sizing affected the uniformity of the coatings, where the graphene coatings on the as-received sized carbon fibres samples adhered less than that on the desized samples. Hence, the commercial sizing needed to be removed. Methods used to do this include, the use of acetone [91, 92], nitric acid (HNO<sub>3</sub>) [93] and plasma [94], as well as heating above size volatilisation temperatures [95]. Removal of the sizing can be confirmed with TGA, X-ray photoelectron spectroscopy and atomic force microscope. Sometimes TGA is not sensitive enough to detect if the entire sizing agent has been removed, so XPS is used to identify the difference in chemical composition on the surface before and after desizing [96].

Once the sizing has been removed, the surface activation energy needs to be increased, to promote chemically active functional groups, to help a coating bond to the fibre surface. The different methods for this fall into two groups - ‘wet’ chemical or ‘dry’ application. While the

vast majority of literature on carbon fibre coatings concerns increasing their adhesion to resins, it also provides some insight into material preparation and different coating methods. Wet chemical methods include using concentrated, strong liquid acids such as  $\text{HNO}_3$ . These corrode the fibre surface which introduces pores and voids, thus improving the fibre/matrix interlocking [97]. However, the fibre strength may be reduced as pits and micro-voids are also introduced into the fibre. On using 65-68%  $\text{HNO}_3$ , Tiwari et al. [98] found that while the use of  $\text{HNO}_3$  was initially beneficial, after a treatment time of 90 minutes, the benefits of greater fibre adhesion to the resin matrix were outweighed by the loss of fibre strength. Alternatively, anodic oxidation takes advantage of the carbon fibres' electrical conductivity and in suitable electrolyte baths they act as anodes and a potential may be used to release oxygen and increase its local concentration on the fibre surface [99]. Typical electrolytes include nitric acid, sulfuric acid, sodium chloride, potassium nitrate, sodium hydroxide and ammonium hydroxide [100].

Dry oxidative treatments are normally performed with air, oxygen and  $\text{CO}_2$  at low or elevated temperature. Such treatments include plasma which uses an ionized gas containing electrons, radicals, ions or molecules to create active sites and attach functional groups on the surface of carbon fibres. Typical gases used for plasma treatment on carbon fibres include air, oxygen, nitrogen and argon, where all have been shown to increase carbon fibre surface roughness and an increase in functional group concentrations [101-104]. In addition to plasma, high energy irradiation can displace atoms on the fibre surface, thereby creating active sites for bonding with other groups. Wan et al. [105] used gamma radiation to treat the surface of PAN-based carbon fibres and recorded a higher content of carboxyl groups on the fibre surface, as well as surface roughening (Figure 1.18).

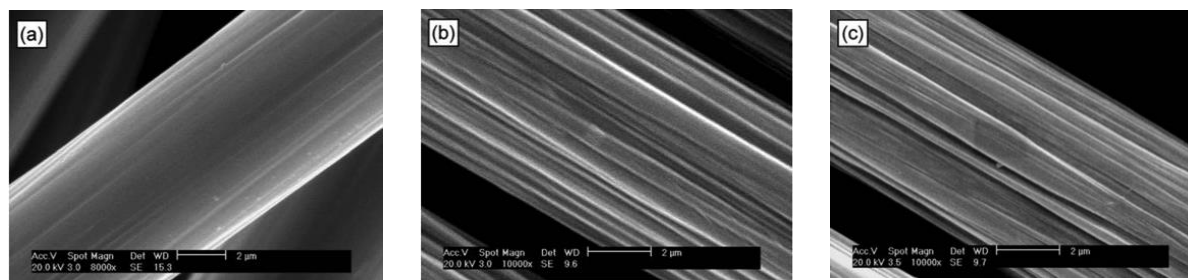


Figure 1.18. SEM images of carbon fibres with different surface treatments: (a) untreated, (b) air-treated, and (c) gamma-radiated [105].



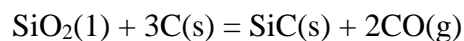
### 1.7.3 Methods to apply coatings to carbon fibres

Chemical vapour deposition (CVD) is a common method to apply surface coatings on to carbon fibres [106, 107]. CVD is a broad term to describe the use of chemical reactions to deposit a material on surfaces. It uses volatile chemical compounds to carry the material to the deposition zone, where it undergoes another chemical reaction to form a solid coating. Unfortunately, this process usually requires often hazardous and expensive chemicals, such as methyltrichlorosilane and hydrogen, which limits its use on a large scale.

Another drawback of CVD is the high temperatures required during the process. Hackl et al. [108] found that a deposition temperature of 950°C only deposited a 15nm SiC coating on carbon fibres. When coating pitch-based carbon fibres with a layer of SiC using CVD, Emig et al. [109] found that a layer of 50nm was not sufficient to provide protection against oxidation. The same was true for a SiC layer of 100nm with a porous structure. Significant carbon fibre oxidation protection was only noted for layers above 150nm with a smooth surface.

The sol-gel method is increasing in popularity as it has a faster deposition rate and is more cost effect than CVD. The sol-gel method uses a precursor solution (sol) of a metal or carbon with oxide groups which cross-link via a polycondensation reaction to form a polymer (gel). Sol-gel method gives the user greater control over the coating purity and can be done at low temperatures.

The preparation of silicon dioxide (SiO<sub>2</sub>) or silica gels through this method involves the hydrolysis and condensation of silicon alkoxy derivatives (typically tetraethyl orthosilicate (TEOS)) with an acid catalyst [110]. Furthermore, at temperatures above 1640°C, silica can react with the carbon fibres to produce silicon carbide (SiC):



Carbon fibres coated with SiO<sub>2</sub> and SiC using the sol-gel method have shown improved oxidation stability up to 800°C [111]. However, the thickness of the coating must also be

considered because, if too thick, it can affect the fibre strength which is why sol-gel coatings are typically only around several hundred nm. SEM images taken from [79] and given in Figure 1.19 show a sol-gel  $\text{SiO}_2$  coating and that including SiC nano particles.

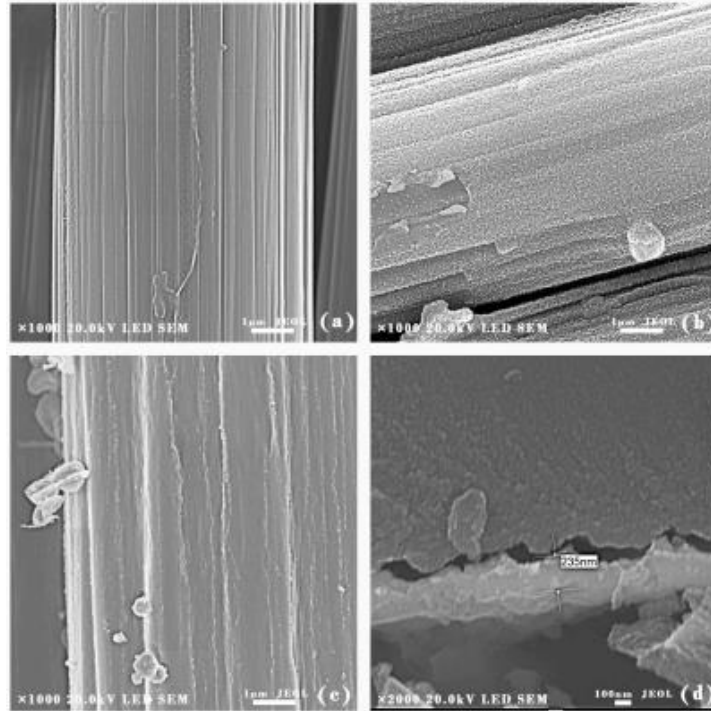


Figure 1.19. SEM images of (a) uncoated carbon fibres (b)  $\text{SiO}_2$  coated CF (c)  $\text{SiC/SiO}_2$  coated CF and (d) surface cross-section of coated CF [79].

During the process, the sol concentration can affect the thickness of the coating as shown by Xia et al. [112] who used  $\text{SiC/SiO}_2$  coatings and found that increasing the sol concentration from 1wt% to 4wt% increased the carbon oxidation fibre and the temperature at which oxidation occurred. For example, using the 4wt% concentration delayed oxidation by  $250^\circ\text{C}$  compared to the uncoated carbon fibre. However, at 5wt% there was a rapid decrease in oxidation protection, which they attributed to the coating spallating.

Other ceramics formed via the sol-gel process include aluminium oxide ( $\text{Al}_2\text{O}_3$ ) [113,114], or alumina. This is a non-reactive, amorphous white ceramic with excellent thermal properties. Here aluminium isopropoxide was hydrolysed with water below its boiling point. An acid was added to the solution acting as a catalyst to form a gel. Given that this process involves

hydrolysis, many hydroxyl groups formed from water absorbed in the coating and so further heat treatment is required to remove these. Zirconium dioxide ( $\text{ZrO}_2$ ) or zirconia is usually made by the hydrolysis of zirconium alkoxide in water with an acid catalyst [76]. Often the precursor is zirconyl chloride ( $\text{ZrOCl}_2 \cdot 8\text{H}_2\text{O}$ ) which is dissolved in HCl. This is followed by a condensation process to produce Zr-O-Zr polymer. When subjected to a heat treatment, the organic groups are removed, leaving just the  $\text{ZrO}_2$  gel [115]. Alternatively, titanium dioxide ( $\text{TiO}_2$ ) which uses titanium isopropoxide ( $\text{Ti}(\text{OC}_3\text{H}_7)_4$ ) as a precursor [116] can be synthesised but this has not been used as often as silica and alumina for coatings.

The formation of nitrides can often require very high temperatures, for example, Kim et al. [82] found that in order to form the Al-N bonds and remove the Al-O when heating  $\text{Al}_2\text{O}_3$  in nitrogen, a heat treatment of at least  $1700^\circ\text{C}$  was required. While there are lower temperature alternatives to forming AlN, such as using ammonium chloride as an additive [117] and high energy ball milling [118], these would be difficult to use to form coatings on individual fibres or tows. The formation of BN coating does not require many chemicals, initially using only boric acid and usually an alcohol source. However, it then requires heating in a nitrogen atmosphere and for the nitridation to occur to form BN at temperatures above  $1200^\circ\text{C}$  [83,84]. In order to lower this temperature, ammonia ( $\text{NH}_3$ ) gas has been added, as well as the use of urea [85], which both act as promoters and additional sources of nitrogen.

### **1.8 Methods to improve structural retention of carbon fibres in CFRCs: Inclusion of other fibres for protection of carbon fibres**

There are many naturally occurring inorganic and synthetic fibres with resistance to high temperatures. Amongst inorganic fibres, glass is the most commonly used reinforcing fibre in composites, another example being basalt fibre. Amongst synthetic fibres, the so-called high temperature and fire resistant aromatic structures para-aramid (e.g. Kevlar) and meta-aramid (e.g. Nomex) are often used in flame retardant clothing [119] as well as in composites [120]. By including such fibre layers in composites, it is hoped that they will protect the carbon fibres at high temperatures. A review of these fibres and their high temperature behaviours is covered below.

### 1.8.1 Behaviour of high temperature resistant fibres

While seen in section 1.6.1 that ceramics have been used to coat carbon fibre for oxidation protection, the use of ceramic fibre is not yet widespread, with glass and basalt fibres being commonly included in polymer composites. E-glass is the most popular type of glass fibre to include [121]. Originally, the production of E-glass was for electrical insulation products (hence the “E” in E-glass). Similar to carbon fibre, these are used in fibre tows and the fibre diameters are usually less than 20 $\mu$ m. While E-glass fibre is significantly cheaper than carbon fibre by weight, carbon fibre is stronger and has a superior strength-to-weight ratio [122].

Basalt fibre is made from volcanic rock and has been of interest to researchers. Like E-glass it is an insulator, lower in cost and more resistant to corrosion [123]. However, basalt fibres are stronger and stiffer than E-glass and are made in a cheaper production process, using no additives and low processing energy [123]. Table 1.3 gives a comparison of the fibre properties (data taken from [122]) and Table 1.4 the fibre chemical compositions.

Table 1.3. Fibre properties [122].

Reinforcing Fiber	Linear density [tex]	Fiber diameter [ $\mu$ m]	Density [g/cm <sup>3</sup> ]	Tensile strength (manufacturer) [MPa]	Tensile modulus (manufacturer) [GPa]
Basalt	1200	13–20	2.6	2850	90
E-Glass	2400	17	2.45	2450	80
Carbon	800	7	1.8	4900	230

Table 1.4. Chemical composition of a basalt fibre used [122,124] compared to an E-glass fibre taken from [125].

\ Element Fiber \	Na <sub>2</sub> O [wt%]	MgO [wt%]	Al <sub>2</sub> O <sub>3</sub> [wt%]	SiO <sub>2</sub> [wt%]	K <sub>2</sub> O [wt%]	CaO [wt%]	TiO <sub>2</sub> [wt%]
Basalt	2.8	4.9	19.4	51.8	2.5	7.7	2.1
E-glass	0.30	0.54	11.86	58.25	0.43	21.09	0.41

Both types of fibres have good oxidation resistant properties, with operating temperature limits of 650°C for basalt and 460°C for E-glass, and softening points of 960°C for Basalt and 850°C for E-glass [126]. Figure 1.20 shows TGAs of Basalt, E-Glass and carbon fibre in air. Unlike carbon fibre, Basalt and E-Glass do not loose mass to oxidation at high temperatures.

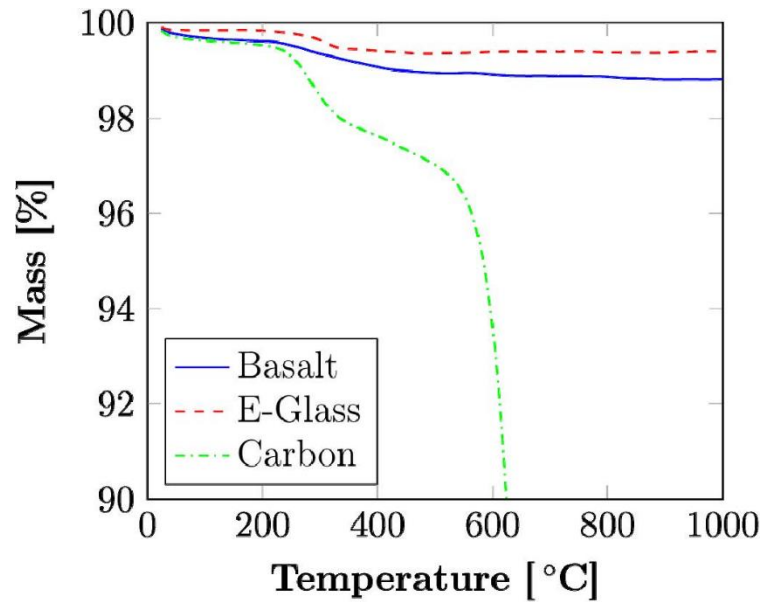


Figure 1.20. TGA in air for basalt, E-glass and carbon fibres [122].

Aramid fibres decompose in air at temperatures close to 500°C [127]. They are available in both meta and para form. Investigating para-aramid fibres, Perepelkin et al. [128] found it to be adequately resistant to thermal oxidation in air between 400-450°C, with a 4% mass loss above 490-500°C.

Semi-crystalline thermoplastics, such as polyphenylene sulphide (PPS) and polyether ether ketone (PEEK) are typically used as the resin in high performance CFRCs. Compared to epoxy resins, these materials have been shown to reduce TTI, the smoke density and the peak heat release rate [54]. They are temperature resistant up to around 250°C [129] because of their respective aromatic structures. However, recently they have been used as fibres. Using meltblown spinning, PPS filaments can have diameters of around 20µm, and recently Fan et al. [130] produced these by electro spinning with diameters down to under 8µm. Both materials have then be woven into fabrics. Normal commercial PEEK fibre is 34µm in diameter.

### 1.8.2 Behaviour of high temperature resistant fibre-reinforced composites

On modelling the tensile strength of glass-fibre polymer composites in fire Feih et al. [131] found, as with CFRCs, at high temperatures there is thermal softening and then decomposition, with eventual combustion of the resin matrix. However, unlike carbon fibres which oxidise, glass fibres begin to soften. This means that under tensile loading, the composites failure is due to the thermal softening and eventual rupture of the fibres.

Bhat et al. [123] exposed both basalt and glass reinforced composites to heat fluxes of 25 and 50kWm<sup>-2</sup> and recorded the temperature on the front and back face of the composites using thermocouples. Neither of the composites combusted at 25kWm<sup>-2</sup>. However, at 50kWm<sup>-2</sup>, the basalt fibre composite heated up faster than the glass fibre composite. This was put down to the higher thermal emissivity of basalt ( $\varepsilon = 0.92$  at 20°C for basalt composite, while for glass composite  $\varepsilon = 0.65$  at 20°C), which also explains why the basalt reinforced composite ignited. Figure 1.21 shows a higher temperature recorded by the thermocouples for the basalt fibre composite. When exposed to 50kWm<sup>-2</sup>, this resulted in quicker ignition of the basalt fibre composite as the material decomposed more rapidly, releasing in a greater number of volatiles than the glass fibre laminate.

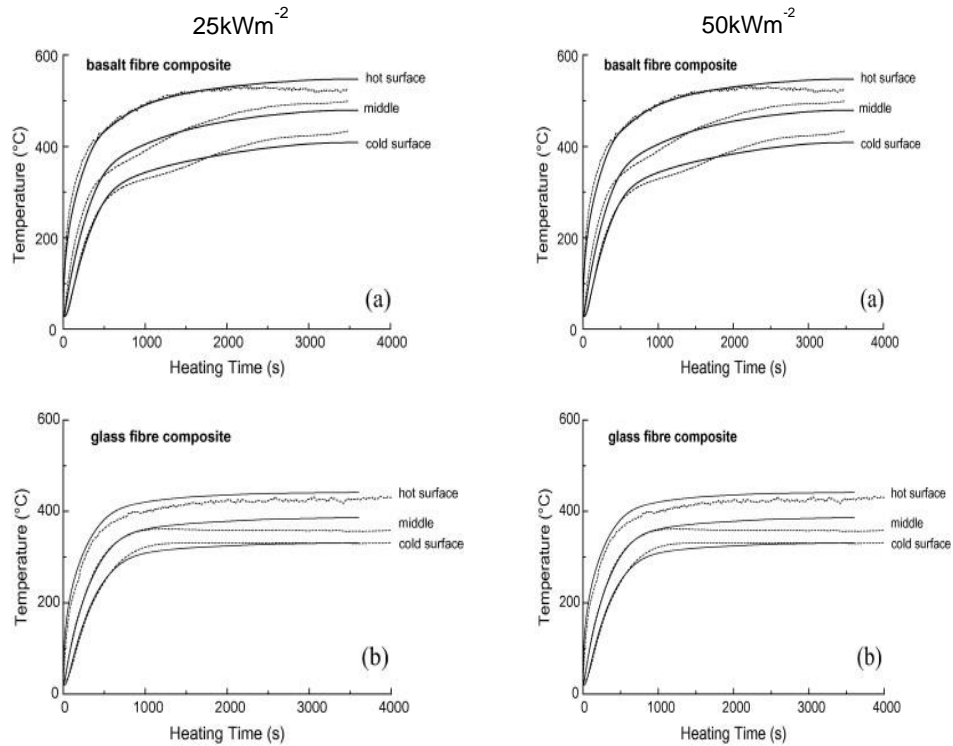


Figure 1.21. Temperature–time profiles measured at the hot surface, middle region and cold surface of the (a) basalt fibre composite and (b) glass fibre composite when exposed to the heat flux of 25 and  $50 \text{ kWm}^{-2}$ . The dashed and solid curves are the measured and calculated trends [123].

Fibres such as glass and basalt are inert up until temperatures over  $1000^\circ\text{C}$  [54]. However, sizing and emulsion binder are applied to fibres at the final stage of production, this makes them easier to handle in composite manufacturing. This sizing is usually a polymer accounting for 1 to 2wt% of the final fibre [19]. When heat is applied it will thermally decompose releasing volatiles. Given that it only contributes a very small weight percentage of the composite it does not usually have a notable effect on ignition properties such as TTI [54].

However, Mouritz [54], noted that in other reinforcement types e.g. chopped strand mats, much more polymer binding agent is used to bind the chopped strands, and this would have a greater effect on ignition properties. Taken from [132] with data from [133] are the TTI for two glass/polyester composites as plots versus heat flux in Figure 1.22. The resin and glass fibres (with sizing) were the same but in different forms. One used woven glass fabric and the other chopped. The chopped glass fibre mat contains additional emulsion binder to hold it together. The graph shows reduced values of TTI for the chopped glass composite, particularly apparent

at lower heat fluxes. This was attributed to the flammable volatiles produced when the binder decomposed.

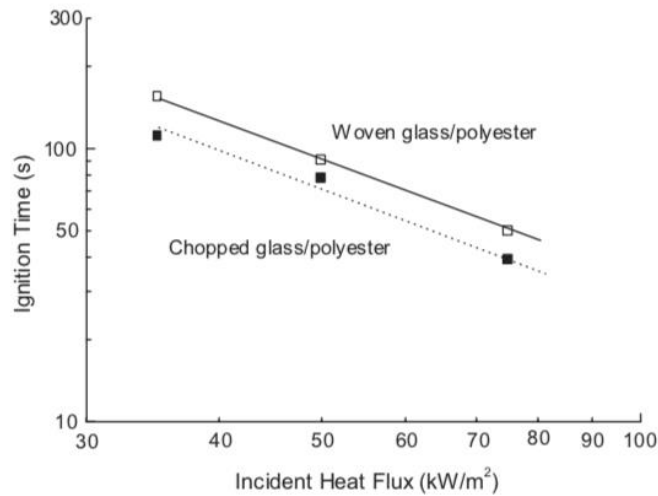


Figure 1.22. Time to ignition at different heat fluxes for polyester laminates reinforced with woven or chopped glass fibres [132].

Kandola et al. [134] exposed epoxy composite laminates containing different reinforcement to the cone calorimeter at  $50\text{kWm}^{-2}$ . The results are given in Table 1.5, where carbon (b) has a reinforcing fibre area density just over twice that of the carbon (a) sample. The carbon fibre samples had the lowest and highest TTI values and this was due to the area density differences of these fabrics. Both carbon fibre samples had a shorter burn time than the glass samples. However, while the aramid sample had a lower peak heat release, it also had a significantly longer burn time compared to all the other samples, as well as a greater total heat released.

Table 1.5. Results from cone calorimeter for composites tested at  $50\text{kWm}^{-2}$  [134].

Sample	TTI (s)	Burn time (s)	PHRR (kw/m <sup>2</sup> )	THR (mJ/m <sup>2</sup> )	E <sub>c</sub> (MJ/kg)	Mass residue at 300s (%)
1.Glass	34	194	373	20.7	20.9	71
2.Carbon (a)	25	150	413	21.1	18.9	62
3.Carbon (b)	53	146	264	17.9	20.1	78
4.Aramid	31	542	295	40.6	22.0	37



### 1.8.3 Behaviour of hybrid composites when exposed to high heat fluxes

Mazur et al. [135] investigated the behaviour of hybrid composites consisting of polyamide 6 with chopped basalt and carbon fibres. These basalt and carbon fibres were added in 5/5 wt%, 7/7 wt%, and 10/10 wt% ratio respectively. As expected, the inclusion of these fibres (even in the lowest amount) significantly increased the strength and modulus of the composites compared to just polyamide 6. The samples were tested under the cone calorimeter at  $35\text{kWm}^{-2}$  with spark ignition. The inclusion of basalt and carbon fibres reduced the heat release rate and because they had taken the place of polyamide 6, they reduced the number of volatiles emitted during the test. Also, the remaining char residue was much increased.

SEM and EDX were used to examine the microstructure of the samples after cone testing. Mazur et al [135], found evidence of a flame-retardant mechanism, whereby residue was found on the remaining basalt fibres. EDX revealed the surface chemical composition was characteristic of the elements used to make the thermally stable basalt e.g., oxides -  $\text{SiO}_2$ ,  $\text{Al}_2\text{O}_3$ ,  $\text{CaO}$ ,  $\text{MgO}$ , listed in Table 1.6. The authors also believed the chopped basalt made a physical shield on the surface of composite, thereby reducing the heat-transfer rate to sub-surface layers.

Table 1.6. EDX results of chemical composition of residue on basalt fibres after testing at  $35\text{kWm}^{-2}$  [135].

Element	Concentration, wt%		
	PA6/5B5C	PA6/7B7C	PA6/10B10C
C	5.178	5.128	5.005
O	36.139	42.658	43.440
Na	1.232	0.871	1.924
Mg	1.166	1.617	1.362
Al	9.327	8.492	8.311
Si	29.837	26.850	27.206
K	1.777	1.144	1.322
Ca	6.714	6.553	4.866
Ti	0.832	0.696	0.542
Fe	6.742	4.932	5.177
Cu	1.054	1.059	0.845
Total	100.000		

PA6: Polyamide 6.

Ambigai and Prabhu [136] investigated thermal properties of glass-carbon/epoxy hybrid composites. They carried out TGAs analyses in air at 20°C/min on the individual glass and carbon fibre composites, as well as the 50/50 glass-carbon fibre composites, and found the hybrid composite to be slightly more thermally stable than the other individual fibre-containing composites (decomposition began at 280°C, as opposed to 270°C and 275°C for the glass and carbon composites respectively).

Kandola et al. [120] exposed a series of epoxy composite laminates including hybrid glass/carbon and glass/aramid in different arrangements to the cone calorimeter at 50kWm<sup>-2</sup>. The arrangement for these hybrids is given in Figure 1.23.

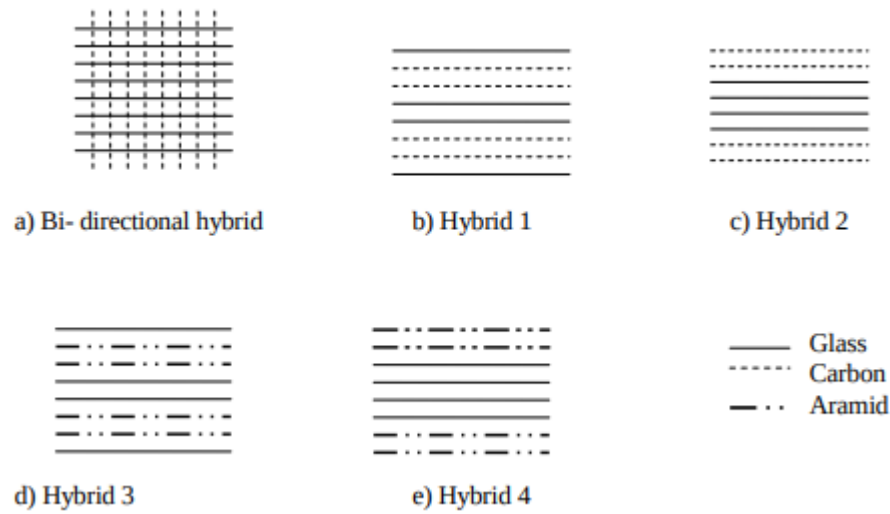


Figure 1.23. Schematic lay-up of hybrid laminates [120].

Their results showed aramid fibre had the greater decomposition; this also remained true when it was included in the hybrid composites. However, it had the lowest peak heat release rate. The graphs in Figure 1.24 show the mass loss curves over 300s of exposure to the cone (a) for composites with one material and (b) hybrid composites. Both hybrids 1 and 2 (of glass and carbon fibre) have similar mass losses after 100s, with hybrid 1, with glass plies on the outside of the composite, having 4% more mass remaining. The bidirectional sample lost the most mass but this was attributed to its higher resin content.

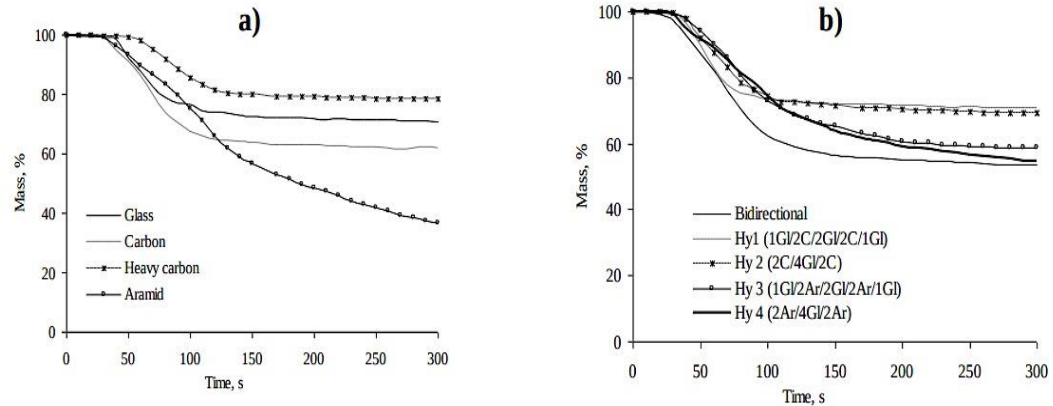


Figure 1.24. Mass loss versus time curves for laminates at  $50\text{kWm}^{-2}$  [120].

## 1.9 Summary

The majority of carbon fibres currently produced are PAN-based. At high temperatures in a nitrogen atmosphere, the only mass loss of the fibres is due to the removal of the polymer sizing. However, in air, carbon fibres lose mass to surface oxidation at around  $550^{\circ}\text{C}$ . Different grades of PAN-based carbon fibre have also been shown to oxidise at different rates and temperatures. Oxidation of carbon fibres causes changes in fibre diameter, tensile strength and modulus, electrical conductivity, as well as visual changes to the fibre surface morphology.

Researchers have used the addition of flame-retardants in the CFRCs matrix to promote the formation of char and/or delay ignition. While much work has been done on this, it is generally with regard to protecting the resin and CFRC, and there is less research on how different flame-retardants and char promoters protect the individual carbon fibres within the composites.

While carbon fibres have been successfully coated with high temperature resistant materials, many coating methods, such as CVD and the formation of nitrate coatings, require expensive chemicals and/or extremely high temperatures. A low-cost alternative needs to be explored. Furthermore, there is little information on how coated carbon fibres behave in CFRCs, for example, their adhesion to the resin.

### 1.10 Aims and objectives

**Aim:** To improve the structural retention of carbon fibre-reinforced composites on exposure to heat/fire so that the structural integrity is maintained and the carbon fibres are not exposed to the environment.

**Objectives:**

- To develop a methodology to study and quantify structural damage to carbon fibres under a range of heat/fire conditions.
- To develop carbon fibre-reinforced composites with improved structural retention.
- To modify the carbon fibres prior to making the composites so that the carbon fibres will not defibrillate and oxidise when exposed to heat/fire.

### 1.11 Thesis structure

**Chapter 1. Introduction and Literature Review:** This comprises of a comprehensive literature review on carbon fibre, the effects of temperature on carbon fibre and CFRCs, and the concerns of released fibres. Also included are methods to improve structural retention of CFRCs and carbon fibres, including the use of flame retardants to reduce CFRC combustion, carbon fibre surface coatings and the inclusion of hybrid layers in CFRCs to provide heat protection to the carbon fibres.

**Chapter 2. Materials and experimental techniques:** This chapter details the materials and experimental techniques used in this project.

**Chapter 3. Effects of heat, irradiance and flames on carbon fibre tows:** This chapter covers the effect of atmosphere, as well as various heat sources on the oxidation of carbon fibre tows. To simulate different temperature environments, thermogravimetric analysis, a tube furnace, cone calorimeter and propane burner techniques were used. The carbon fibres were then examined for fibre diameter reductions, surface damage and change in electrical and mechanical properties.

**Chapter 4. Effects of heat and fire on carbon fibre properties in fire retarded carbon-fibre reinforced composites:** This chapter covers the effects of heat and fire on CFRCs. The CFRCs' resin matrix was modified with flame retardants and nano-particles in order to improve the mechanical integrity of the char and its adherence to the fibre. After various heat and fire testing, residual fibres were removed from the CFRCs and their properties examined to determine if the inclusion of additive to the matrix had the desired effect.

**Chapter 5. Effects of high performance fibre inclusion in composites on thermal stability of carbon fibres:** Hybrid layers were placed within the CFRC in two different configurations. These layers consisted of aramid, basalt, E-glass and polyphenylene sulphide nonwoven fibrous arrays or veils. CFRCs with hybrid layers were then exposed to the cone calorimeter at  $75\text{kWm}^{-2}$  for 600s and the residual fibres removed for analysis to determine the effect of including these layers on the oxidation of the carbon fibres within the composite.

**Chapter 6. Surface modification of carbon fibres for improved structural retention on exposure to fire:** This chapter describes the coating of individual carbon fibres with a number of heat resistant materials prior to introducing them into a CFRC. Focusing on surface activation of the carbon fibre, the use of high temperature ceramic materials as coatings was prioritised and the oxidation protection these coatings provided to the fibre at high temperatures assessed.

**Chapter 7. Conclusions:** This chapter summarises the work conducted in the previous chapters and arrives at the overall conclusions, as well as suggesting possible future work.

## 1.12 References

- [1] Yin, Y., Binner, G. P., Cross, T. E., Marshall, S. J., The oxidation behaviour of carbon fibres J Mater Sci, 29, pp. 2250-2254, (1994).
- [2] Moreton, R., RAE. MRCC/79/44. Materials Department. Electrical hazards due to the release of carbon fibres into the atmosphere, (1979).
- [3] Bell, V. L., NASA Report N80-29431. Potential release of fibres from burning carbon composites, (1980).
- [4] Inthavong, K., Mouritz, A. P., Dong, J., & Tu, J. Y., Inhalation and deposition of carbon and glass composite fibre in the respiratory airway. Journal of Aerosol Science, 65, pp. 58–68, (2013).
- [5] Bacon, R., Growth, Structure, and Properties of Graphite Whiskers, Journal of Applied Physics 31, 283,, (1960).
- [6] Shindo, A., Studies on Graphite Fiber, Rept. No. 317, Gov't. Ind. Res. Inst., Osaka; also J. Ceram. Assoc. Japan 69, C195, (1961).
- [7] Johnson, W., Phillips, L. N., Watt, W., UK Patent 1 110 791 (1968).
- [8] Huang X .S., Fabrication and Properties of Carbon Fibers, Materials, 2 pp. 2369-2403, (2009).
- [9] Kandola, B. K., Magnoni, F., Ebdon, J. R., Flame retardants for epoxy resins: Application-related challenges and solutions, Vinyl and Additive Technology, Volume 28, Issue 1, (2022).
- [10] Airbus, accessible here: <https://www.carbonfiber.gr.jp/english/field/craft.html>
- [11] Ahmad, H., Markina, A. A., Porotnikov, M. V., Ahmad, F., A review of carbon fiber materials in automotive industry, IOP Conf. Ser.: Mater. Sci. Eng. 971 032011, (2020).
- [12] GMI2180, Carbon Fibre Composites Market Size By End-Use (Aerospace, Automotive, Wind Turbines, Sport & Leisure, Civil Engineering, Marine), By Matrix Material (Polymer [Thermosetting, Thermoplastics], Carbon, Ceramic, Metal, Hybrid), Industry Analysis Report, Regional Outlook, Growth Potential, Price Trends, Competitive Market Share & Forecast, 2017 – 2024, Oct 2017
- [13] Johnson, D. J., Structure property relationships in carbon fibers. J. Phys. D: Appl. Phys. 20(3), 287–291, (1987).

- [14] Bhatt, P., Goe, A., Carbon Fibres: Production, Properties and Potential Use. *Mat.Sci.Res.India*;14(1), (2017).
- [15] Nunna, S., Blanchard, P., Buckmaster, D., Davis, S., Naebe, M., Development of a cost model for the production of carbon fibres, *Heliyon*, Volume 5, Issue 10, (2019).
- [16] Huson, M. G., Structure and Properties of High-Performance Fibers, High-performance pitch-based carbon fibers, *Woodhead Publishing Series in Textiles* Number 187, p32, (2016).
- [17] Naito, K., Yang, J. M. Tanaka, Y., Kagawa, Y., The effect of gauge length on tensile strength and Weibull modulus of polyacrylonitrile (PAN)-and pitch-based carbon fibers, *Journal of Materials Science*, Vol. 47 Issue 2, p632-642, (2012).
- [18] Newcomb, B. A., Processing, structure, and properties of carbon fibers, *Composites Part A: Applied Science and Manufacturing*, Volume 91, Part 1, (2016).
- [19] Xu, Y., Liu, Y., Chen, S., Ni, Y., Current overview of carbon fiber: Toward green sustainable raw materials, *BioRes.* 15(3), 7234-7259, (2020).
- [20] Reynolds, W. N., Moreton, R., Some factors affecting the strength of carbon fibres, *Philos Trans*, 294, p.11, (1980).
- [21] Burnay, S. G., Sharp, J. V., Defect structure of PAN-based carbon fibres, *Journal of Microscopy*, Volume 97, Issue 1-2, pp. 153-163, (1973).
- [22] Baker, D. A., Rials, T. G., Recent advances in low-cost carbon fiber manufacture from lignin, *Journal of Applied Polymer Science*, Vol 130, issue, 2, pages 713-728, (2013).
- [23] Feih, S. and Mouritz, A. P., Tensile properties of carbon fibres and carbon fibre–polymer composites in fire, *Composites Part A: Applied Science and Manufacturing*, Volume 43, Issue 5, (2012).
- [24] Su, F., Huang, P., Li, T., Yao, R., Oxidation of Carbon Fibre and its Effect on Mechanical Properties, *21st International Conference on Composite Materials*, (2017).
- [25] Feih, S., Manatpon, K., Mathys, Z., Gibson, A. G., Mouritz, A. P., Strength degradation of glass and fibers at high temperatures *J Mater Sci*, 44, pp. 392-400, (2009).
- [26] Yin, Y., Binner, J. G. P., Cross, T. E., The Oxidation Behaviour of Carbon Fibres, *Journal of Material Science* 29 pp. 2250-2254, (1994).
- [27] Trumbauer, E. R., Hellmann, J. R., Jones, L., E., Oriented microchannel membranes via oxidation of carbon-fiber-reinforced glass composites, *Carbon*, Volume 30, Issue 6, pp. 873-882, (1992).

- [28] Sauder, C., Lamon, J., Pailier, R., The tensile behavior of carbon fibers at high temperatures up to 2400 °C, *Carbon*, Volume 42, Issue 4, Pages 715-725, (2004).
- [29] Morita, K., Murata, Y., Ishitani, A., Murayama, K., Ono, T., Nakajima, A. Characterisation of commercially available PAN (polyacrylonitrile)-based carbon fibres. *Pure Appl Chem* 58:455–68, (1986).
- [30] Cao, S., Wang, X., Wu, Z., Evaluation and prediction of temperature-dependent tensile strength of unidirectional carbon fiber-reinforced polymer composites. *Journal of Reinforced Plastics and Composites*. 30(9):799-807, (2011).
- [31] Khalili, A. and Kromp, K., Statistical properties of Weibull estimators. *J Mater Sci*, ;26:6741–52, (1991).
- [32] Li, C. and Xian, G., Experimental investigation of the microstructures and tensile properties of polyacrylonitrile-based carbon fibers exposed to elevated temperatures in air. *Journal of Engineered Fibers and Fabrics*, 14, (2019).
- [33] Dandy, L., Oliveus, G., Wood, J., Jenkins, M., Leeke, G., Counting carbon fibres by electrical resistance measurement, *Composites: Part A*, 68, pp. 276-281, (2015).
- [34] Sauder, C., Lamon, J., Pailier, R., Thermomechanical properties of carbon fibres at high temperatures (up to 2000 °C), *Composites Science and Technology*, Volume 62, Issue 4, Pages 499-504, (2002).
- [35] Owston, C. N., Electrical properties of single carbon fibres, *Journal of Physics D: Applied Physics*, Volume 3, Number 11, (1970).
- [36] Abid, R., Electrical Characterisation of Aerospace Grade Carbon-Fibre Reinforced Polymers, PhD thesis, Cardiff School of Engineering, (2015).
- [37] Thiagarajan, C., Smart Characterisation of damage in carbon fibre reinforced composites under static and fatigue loading conditions by means of electrical resistivity measurements, PhD thesis, Cranfield University, (1996).
- [38] Hoshikawa, H and Koyama, K., A New Eddy Current Probe with Minimal Liftoff Noise and Phase information On Discontinuity Depth, *Mater. Eval.* 61, pp 423-427, (2003).
- [39] Gros, X. E. and Lowden, W., Electromagnetic testing of composite materials, *Insight*, 37, 4, pp. 290-293, (1995).
- [40] Schueler, R., Damage detection in CFRP by electrical conductivity mapping, *Composites Science and Technology*, Volume 61, Issue 6, pp. 921-930, (2001).



- [41] Wentzel, D and Sevostianov, I., Electrical conductivity of unidirectional carbon fiber composites with epoxy-graphene matrix, *International Journal of Engineering Science*, Volume 130, pp.129-135, (2018).
- [42] Mouritz, A. P and Mathys, Z., Post-fire mechanical properties of glass-reinforced polyester composites, *Composites Science and Technology*, Volume 61, Issue 4, Pages 475-490, (2001).
- [43] Wang, K., Young, B., Smith, S. T., Mechanical properties of pultruded carbon fibre-reinforced polymer (CFRP) plates at elevated temperatures. *Engineering Structures*, 33(7), 2154-2161, (2011).
- [44] Brown, A. L., Dodd, A. B., Pickett, B. M., Intermediate Scale Composite Material Fire Testing, *Proceedings of the ASME 2011 International Mechanical Engineering Congress & Exposition IMECE2011 November 11-17, 2011, Denver, Colorado, USA*.
- [45] Modica, P. D., Kotsikos, G., Gibson, A. G., Fire behaviour of carbon fibre composites under load, *ECCM16 – 16<sup>th</sup> European conference on composites materials*, Seville, Spain, 22-26 June 2014.
- [46] Clougherty, E., Gerren, J., Greene, J., Haagensen, D., Zalosh, R. G., Graphite Fiber Emissions From Burning Composite Helicopter Components, Draft Report, United States Coast Guard, Department of Transportation. (1997).
- [47] Royal Air Force Institute of Community and Occupational Medicine. Environmental Health Department. Report No. ICOM/12/91. April 1991. Final report on hazards associated with the crash of a Harrier GR5 aircraft on the Island of Moors in Denmark - October 1990.
- [48] Gandhi, S., Lyon, R., Speitel, L., Potential Health Hazards from Burning Aircraft Composites, *Journal of Fire Science* volume 17, issue 1, page(s): 20-41, (1999).
- [49] Wang, Z., Hopke, P.K., Ahmadi, G., Cheng, Y., Baron, P.A., Fibrous particle deposition in human nasal passage: The influence of particle length, flow rate, and geometry of nasal airway, *Journal of Aerosol Science*, Volume 39, Issue 12, pp. 1040-1054, (2008).
- [50] Cavallo, D., Campopiano, A., Cardinali, G., Casciardi, S., Simone, P. D., Kovacs, D. et al. Cytotoxic and oxidative effects induced by man-made vitreous fibers (MMVFs) in a human mesothelial cell line. *Toxicology*, 201, 219–229, (2004).
- [51] Su, W. C., & Cheng, Y. S., Deposition of fiber in the human nasal airway. *Aerosol Science and Technology*, 39, 888–901, (2005).

- [52] Beeckmans, J. M., Deposition of ellipsoidal particles in the human respiratory tract. In: T. Mercer, P. E. Morrow, & W. T. Dtrober (Eds.), *Assessment of airborne particles II*: Springfield, (1972).
- [53] Dandy, L., Oliveus, G., Wood, J., Jenkins, M., Leeke, G., Counting carbon fibres by electrical resistance measurement, *Composites: Part A*, 68, pp. 276-281, (2015).
- [54] Mourtiz, A. P., *Fire Properties of Polymer Composite Materials* (2006)
- [55] Levchik, S. V., Weil, E. D., Thermal decomposition, combustion and flame-retardancy of epoxy resins—a review of the recent literature, *Polymer International*, Volume 53, Issue 12, pp 1901-1929, (2004).
- [56] Levchik, S., Piotrowski, A., Weil, E., Yao, Q, New developments in flame retardancy of epoxy resins, *Polymer Degradation and Stability*, Volume 88, Issue 1, Pages 57-62, (2005).
- [57] Jain, P., Choudhary, V., Varma, I. K., Flame Retarding Epoxies with Phosphorus, *Journal of Macromolecular Science, Part C*, 42:2, 139-183, (2002).
- [58] Kandola, B. K., Biswas, B., Price, D., Horrocks, A. R., Studies on the effect of different levels of toughener and flame retardants on thermal stability of epoxy resin, *Polym. Degrad. Stab.* 2010, 95, 144, (2010).
- [59] Rabe, S., Chuenban, Y., Schartel, B., Exploring the Modes of Action of Phosphorus-Based Flame Retardants in Polymeric Systems. *Materials (Basel)*, 10(5): 455, (2017).
- [60] Wang, J-W., Wang, D-Y., Liu, Y., Ge, X-G., Wang, Y-X., Polyamide-enhanced flame retardancy of ammonium polyphosphate on epoxy resin, *Applied Polymer Science*, Volume 108, Issue 4, pages 2644-2653, (2008).
- [61] Kishore, K, and Mohandas, K., Mechanistic studies on the action of ammonium phosphate on polymer fire retardancy, *Combustion and Flame*, Volume 43, Pages 239-242, (1981).
- [62] Matykiewicz, D., Przybyszewski, B., Stanik, R., Czulak, A., Modification of glass reinforced epoxy composites by ammonium polyphosphate (APP) and melamine polyphosphate (PNA) during the resin powder molding process, *Composites Part B: Engineering*, Volume 108, Pages 224-231, (2017).
- [63] Song, L., Wu, K., Wang, Y., Wang, Z., Hu, Y., Flammability and Thermo-Oxidative Decomposition of Epoxy Resin Containing Ammonium Polyphosphate and Metallic Oxide, *Journal of Macromolecular Science, Part A*, 46:3, 290-295, (2009).

- [64] Riahipour, R., Alizadeh Sahraei, A., Van de Werken, N., Tehrani, M., Abrinia, K. and Baniassadi, M., Improving flame-retardant, thermal, and mechanical properties of an epoxy using halogen-free fillers. *Science and Engineering of Composite Materials*, Vol. 25 (Issue 5), pp. 939-946, (2018).
- [65] Zhang, W., He, X., Song, T., Jiao, Q., Yang, R., The influence of the phosphorus-based flame retardant on the flame retardancy of the epoxy resins. *Polymer Degradation and Stability*, 109 , 209-217, (2014).
- [66] Hull, T. R., Law, R. J., Bergman, A., Chapter 4 - Environmental Drivers for Replacement of Halogenated Flame Retardants, Editor(s): Constantine D. Papaspyrides, Pantelis Kiliaris, *Polymer Green Flame Retardants*, Elsevier, Pages 119-179, (2014).
- [67] Papaspyrides, C. D. and Kiliaris, P. *Polymer Green Flame Retardants*, Elsevier, Amsterdam, Netherlands, (2014).
- [68] Zhang, Y., Fang, Y., Zheng, K., Lin, W., Huang, Z., Xie, G., Wang, X., An Improved Synthesis of DOPO-POSS, *Organic Preparations and Procedures International*, 54:4, 380-385, (2022).
- [69] Zhang, W., Li, X., Yang, R., Novel flame retardancy effects of DOPO-POSS on epoxy resins, *Polymer Degradation and Stability*, Volume 96, Issue 12, Pages 2167-2173, (2011).
- [70] Kalali, E. N., Wang, X., Wang, D-Y., Functionalized layered double hydroxide-based epoxy nanocomposites with improved flame retardancy and mechanical properties, *J. Mater. Chem. A*, 3, 6819-6826, (2015).
- [71] Wang, Y., Zhou, B., Wang, Z., Oxidation protection of carbon fibers by coatings, *Carbon*, Volume 33, 4, pages 427-433, (1995).
- [72] Xu, Z., Chen, Y., Li, W., Li, J., Yu, H., Lui., Wu., G., Yang, T., Luo, L., Preparation of boron nitride nanosheet-coated carbon fibres and their enhanced antioxidant and microwave-absorbing properties, *RSC Advances*, Issue 32, 17944-17949, (2018).
- [73] Wang, J., Lin, W., Yan, X., Wu, X., Wu, F., Yang, Y., Preparation and microstructure of Al<sub>2</sub>O<sub>3</sub>-SiO<sub>2</sub>-TiO<sub>2</sub> coating on three-dimensional braided carbon fiber by sol-gel technology, *Materials & Design*, Volume 89, Pages 928-932, (2016).
- [74] Tang, Y. P., Deng, Y. D., Zhang, K., Liu, L., Wu, Y.T., Hu, W. B., Improvement of interface between Al and short carbon fibers by  $\alpha$ -Al<sub>2</sub>O<sub>3</sub> coatings deposited by sol-gel technology, *Journal of Applied Polymer Science*, Volume 70, pp. 177-183, (1998).

- [75] Xie, Y., Sherwoof, M. P. A., Coatings of Aluminum Oxide and Magnesium Oxide on Carbon Fiber, *Surfaces Chem. Mater.*, 6 (5), pp 650–657, (1994).
- [76] Li, S., Zhang, Y.M., Zhou, Y. F., Preparation and characterization of sol–gel derived zirconia coated carbon fiber, *Surface and Coatings Technology*, Volume 206, Issue 23, Pages 4720-4724, (2012).
- [77] Hao, J., Li, J., Shi, W., Tan, Y., Ding, X., Antioxidant Coating Composed of SiC on Carbon Fibers by Chemical Vapor Reaction, *J. Ceram. Sci. Technol.*, 09 [4] 465-470 (2018).
- [78] Gallyamova, R., Galyshev, S., Musin, F., Dokichev, V., Thermal stability of the carbon fibers with SiO<sub>2</sub> coating, *MATEC Web Conf.*, 298, 00090, (2019).
- [79] Yang, G., Huang, Z., Wang, X., Wang, B., Fabrication and Anti-Oxidation Ability of SiC-SiO<sub>2</sub> Coated Carbon Fibers Using Sol-Gel Method. *Materials (Basel)*, 11(3):350, (2018).
- [80] Popovska, N., Gerhard, H., Wurm, D., Poscher, S., Emig, G., Singer, R.F., Chemical vapor deposition of titanium nitride on carbon fibres as a protective layer in metal matrix composites, *Materials & Design*, Volume 18, Issues 4–6, Pages 239-242, (1997).
- [81] Zhang, J., Hector, A.L., Soulé, S., Zhang, Q., Zhaob, X., Effects of ammonolysis and of sol–gel titanium oxide nitride coating on carbon fibres for use in flexible supercapacitors, *J. Mater. Chem. A*, 6, 5208-5216, (2018).
- [82] Kim, H.H., Lee, Y.S., Chung, D.C., Kim, B.J., Studies on Preparation and Characterization of Aluminum Nitride-Coated Carbon Fibers and Thermal Conductivity of Epoxy Matrix Composites. *Coatings*. 7(8):121, (2017).
- [83] Badakhsh, A., Han, W., Jung, S. C., An, K. H., Kim, B. J., Preparation of Boron Nitride-Coated Carbon Fibers and Synergistic Improvement of Thermal Conductivity in Their Polypropylene-Matrix Composites. *Polymers*, 11(12), (2019).
- [84] Das, M., Basu, A.K., Ghatak, Amish, S., Joshi, G., Carbothermal synthesis of boron nitride coating on PAN carbon fiber, *Journal of the European Ceramic Society*, Volume 29, Issue 10, Pages 2129-2134, (2009).
- [85] Wei, Y., Huang, X., Du, Z., Cheng, Y., Synthesis of BN coatings on carbon fiber by dip coating, *Volume 49, Issue 3*, Pages 177-181, (2017).
- [86] Xu, Z., Chen, Y., Li, W., Li, J., Yu, H., Liu, L., Wu, G., Yang, T., Luo, L., Preparation of boron nitride nanosheet-coated carbon fibres and their enhanced antioxidant and microwave-absorbing properties, *RSC Adv.*, 8, 17944, (2018).

- [87] Li, M., Wang, K., Wang, J., Long, D., Liang, Y., He, L., Huang, F., Du, S., Huang, Q., Preparation of TiC/Ti<sub>2</sub>AlC coating on carbon fiber and investigation of the oxidation resistance properties, *Journal of the American Ceramic Society*, Volume 101, Issue 11, Pages 5269-5280, (2018).
- [88] Wang, K., Li, Mian., Liang, Y., Wang, J., He, L., Du, S., Huang, Z., Huang, Q., Interface modification of carbon fibers with TiC/Ti<sub>2</sub>AlC coating and its effect on the tensile strength, *Ceramics International*, Volume 45, Issue 4, p4661-4666, (2019).
- [89] Constantin, L., Fan, L., Mouey, P., Roger, J., Cui, B., Silvain, J., Lu, Y.F., Spontaneous Formation of Multilayer Refractory Carbide Coatings in a Molten Salt Media, *Proceedings of the National Academy of Sciences*, Volume 118., Issue 18, (2021).
- [90] Qiu, J., Li, J., Yuan, Z., Zeng, H., Chen, X., Surface Modification of Carbon Fibres for Interface Improvement in Textile Composites, *Applied Composite Materials*, 25, 853-860, (2018).
- [91] Zhang, X., Fan, X., Tan, C., Li, H., Zhu, Y., Li, X., Yu, L., Interfacial microstructure and properties of carbon fiber composites modified with graphene oxide. *ACS Appl. Mater. Interfaces*. 4(3), 1543–1552, (2012).
- [92] Afzal, F. I., Saha, M. C., Altan, M. C., Effect of Sizing Removal Method and POSS Coating on Flexural Properties of Carbon Fiber Epoxy Composites, *Proceedings of the ASME 2013 International Mechanical Engineering Congress and Exposition. Volume 9: Mechanics of Solids, Structures and Fluids*. San Diego, California, USA. November 15–21, V009T10A080. ASME, (2013).
- [93] Li, Y., Guo, L., Wany, Y., Li, H., Song, Q., A novel multiscale reinforcement by in-situ growing carbon nanotubes on graphene oxide grafted carbon fibers and its reinforced carbon/carbon composites with improved tensile properties. *Journal of Materials Science & Technology*. 32(5), 419–424, (2016).
- [94] Kim, J., Han, J. H., Hong, S., Kim, D., Park, S., Wee, J., Yang, K. S., Kim, Y., Effect of plasma surface modification on pullout characteristics of carbon fiber-reinforced cement composites, *Carbon Trends*, Volume 3, (2021).
- [95] Kiss, P., Glinz, J., Stadlbauer, W., Burgstaller, C., Archodoulaki, V., The effect of thermally desized carbon fibre reinforcement on the flexural and impact properties of PA6,

PPS and PEEK composite laminates: A comparative study, *Composites Part B: Engineering*, Volume 215, 108844, (2021).

[96] Stojcevski, F., Hilditch, T. B., Gengenbach, T. R., Henderson, L. C., Effect of carbon fiber oxidization parameters and sizing deposition levels on the fiber-matrix interfacial shear strength, *Composites Part A: Applied Science and Manufacturing*, Volume 114, Pages 212-224, (2018).

[97] Li, J., The effect of surface modification with nitric acid on the mechanical and tribological properties of carbon fiber-reinforced thermoplastic polyimide composite. *Surface and Interface Analysis* 41(9):759-63, (2019).

[98] Tiwari, S., Bijwe, J., Panier, S., Tribological studies on polyetherimide composites based on carbon fabric with optimized oxidation treatment, *Wear*, Volume 271, Issues 9–10, Pages 2252-2260, (2011).

[99] Xin, L., Changling, Y., Yonggen, L., Contrastive study of anodic oxidation on carbon fibers and graphite fibers. *Applied Surface Science*, 258(10), 4268-4275, (2012).

[100] Bismarck, A., Kumru, M., Springer, J., Simitzis, J., Surface properties of PAN based carbon fibers tuned by anodic oxidation in different alkaline electrolyte systems. *Applied Surface Science*;143(1):45-55, (1999).

[101] Liu, Z., Tang, C., Chen, P., Yu, Q., Li, W., Modification of carbon fiber by air plasma and its adhesion with BMI resin, *RSC Adv*, 4, 26881-26887, (2014).

[102] Tiwari, S, Sharma, M., Panier, S., Mutel, B., Mitschang, P., Bijwe, J., Influence of cold remote nitrogen oxygen plasma treatment on carbon fabric and its composites with specialty polymers. *J Mater Sci*, 46, (4), 964–974, (2011).

[103] Lin, J., Sun, C., Min, J., Wan, H., Wang, S., Effect of atmospheric pressure plasma treatment on surface physicochemical properties of carbon fiber reinforced polymer and its interfacial bonding strength with adhesive, *Composites Part B: Engineering*, Volume 199, 108237, (2020).

[104] Vinodhini, J., Sudheendra, K., Balachandran, M., Bhowmik, S., Influence of argon plasma treatment on carbon fibre reinforced high performance thermoplastic composite. *High Performance Polymers*, 33(3):285-294, (2021).

- [105] Wan, Y.Z., Wang, Y.L., Huang, Y., Effect of surface treatment of carbon fibers with gamma-ray radiation on mechanical performance of their composites. *J Mater Sci* 40, 3355–3359, (2005).
- [106] Archer, N. J., Chemical vapour deposition, *Physics in Technology* 10 152, (1979).
- [107] Dharmi, T. L., Bahl, O. P., Awasthy, B. R., Oxidation-resistant carbon-carbon composites up to 1700 °C, *Carbon*, Volume 33, Issue 4, Pages 479-490, (1995).
- [108] Hackl, G., Gerhard, H., Popovska, N., Coating of carbon short fibers with thin ceramic layers by chemical vapor deposition, *Thin Solid Films*, Vol 513, Issues 1-2, 217–222, (2006).
- [109] Emig, G., Popovska, N., Schoch, G., Chemical vapour deposition of silicon carbide on mesophase pitch-based carbon fibres, Volume 241, Issues 1–2, Pages 361-365, (1993).
- [110] Mujiyanti, D.R., Surianthy, M.D., Junaidi, A. B., The Initial Characterization of Nanosilica From Tetraethylorthosilicate (TEOS) with The Addition Polivynil Alcohol by Fourier Transform Infra Red, *IOP Conf. Ser.: Earth Environ. Sci.* 187 012056, (2018).
- [111] Yang, G., Huang, Z., Wang, W., Wang, B., Fabrication and Anti-Oxidation Ability of SiC-SiO<sub>2</sub> Coated Carbon Fibers Using Sol-Gel Method. *Materials*. 11(3), 350, (2018).
- [112] Xia, K., Lu, C., Yang, Y., Preparation of anti-oxidative SiC/SiO<sub>2</sub> coating on carbon fibers from vinyltriethoxysilane by sol–gel method, *Applied Surface Sciece*, 265, pp. 603-609, (2012).
- [113] Zhang, Y. D., Su, X. J., Hou, G. L., Guo, F., Anti-Oxidation Behavior of Alumina Coating on Carbon Fibre by Sol-Gel Method. In *Advanced Materials Research*, Vols. 79–82, pp. 819–822, Trans Tech Publications, (2009).
- [114] Tang, Y., Deng, Y., Zhang, K., Liu, L., Wu, U., Hu, W., Improvement of interface between Al and short carbon fibers by  $\alpha$ -Al<sub>2</sub>O<sub>3</sub> coatings deposited by sol–gel technology, *Ceramics International*, Volume 34, Issue 7, Pages 1787-1790, (2008).
- [115] Li, S., Zhang, Y. M., Zhou, Y. F., Preparation and characterization of sol–gel derived zirconia coated carbon fiber, *Surface and Coatings Technology*, Volume 206, Issue 23, Pages 4720-4724, (2012).
- [116] Kartini I, Meredith P, Zhao X. S, Costa J. C, Lu G.Q., A two-step sol-gel method for synthesis of nanoporous TiO<sub>2</sub>. *J Nanosci Nanotechnol*;4(3):270-4, (2004).
- [117] Kato, T and Sugawara, K., Low-Temperature Synthesis of Aluminum Nitride by Addition of Ammonium Chloride *ACS Omega* 4 (12), 14714-14720, (2019).

- [118] Rounaghi, S.A., Eshghi, H., Rashid, A.R.K, Khaki, J.V., Khoshkhoo, M.S., Scudino, S., Eckert, J., Synthesis of nanostructured AlN by solid state reaction of Al and diaminomaleonitrile, *Journal of Solid State Chemistry*, Volume 198, Pages 542-547, (2013).
- [119] Pandit, P., Singha, K., Kumar, V., Maity, S., Chapter 16 - Advanced flame-retardant agents for protective textiles and clothing, Editor(s): Shahid ul-Islam, Bhupendra Singh Butola, In *The Textile Institute Book Series, Advances in Functional and Protective Textiles*, Woodhead Publishing, Pages 397-414, (2020).
- [120] Kandola, B. K., Horrocks, A. R., Rashid, M. R., Effect of Reinforcing Element on Burning Behaviour of Fibre-Reinforced Epoxy Composites, in *Recent Advances of Flame Retardancy of Polymeric Materials*, Ed. M.Lewin; proceedings of the 17th conference, Business Communication Company, Stamford, Conn. (2006).
- [121] Zweben, C. H., Composites: Overview, Editor(s): Franco Bassani, Gerald L. Liedl, Peter Wyder, *Encyclopedia of Condensed Matter Physics*, Elsevier, Pages 192-208, (2005).
- [122] Kessler, E., Gadow, R., Straub, J.. Basalt, glass and carbon fibers and their fiber reinforced polymer composites under thermal and mechanical load, *AIMS Materials Science*, 2016, 3(4): 1561-1576, (2016).
- [123] Bhat, T., Chevali, V., Liu, X., Feih, S., Mouritz, A. P., Fire structural resistance of basalt fibre composite, *Composites Part A: Applied Science and Manufacturing*, Volume 71, Pages 107-115, (2015).
- [124] Gadow, R. and Weichand, P., Novel intermediate temperature ceramic composites, materials and processing for siloxane based basalt fiber composites. *Key Eng Mater* 611: 382–390, (2014).
- [125] Deak, T. and Czigany, T., Chemical composition and mechanical properties of basalt and glass fibers: a comparison. *Text Res J* 79: 645–651, (2009).
- [126] Sarasini, F., Tirillò, J., Seghini, M., C., Influence of thermal conditioning on tensile behaviour of single basalt fibres, *Composites Part B: Engineering*, Volume 132, Pages 77-86, (2018).
- [127] Kevlar® aramid fiber technical guide, DuPont, (2017)
- [128] Perepelkin, K. E., Andreeva, I. V., Pakshver, E. A., Morgoeva, I. Y., Thermal Characteristics of Para-Aramid Fibres. *Fibre Chemistry* 35, 265–269, (2003).



- [129] Guo, Y., Bradshaw, R. D., Isothermal physical aging characterization of Polyether-ether-ketone (PEEK) and Polyphenylene sulfide (PPS) films by creep and stress relaxation. *Mech Time-Depend Mater* 11, 61–89, (2007).
- [130] Fan, Z-Z., He, H-W., Yan, X., Zhao, R-H., Long, Y-Z., Ning, X., Fabrication of Ultrafine PPS Fibers with High Strength and Tenacity via Melt Electrospinning. *Polymers*; 11(3):530, (2019).
- [131] Feih, S., Mouritz, A. P., Mathys, Z., Gibson, A., Tensile strength modelling of glass fiber-polymer composites in fire. *Journal of Composite Materials*, 41(19), 2387–2410, (2007).
- [132] Mouritz, A. P., Mathys, Z., Gibson, A. G., Heat release of polymer composites in fire, *Composites Part A: Applied Science and Manufacturing*, Volume 37, Issue 7, Pages 1040-1054, (2006).
- [133] Brown, J. R. and Mathys, Z., Reinforcement and matrix effects on the combustion properties of glass reinforced polymer composites. *Composites*; 28A:675-681, (1997).
- [134] Kandola, B. K., Myler, P., Kandare, E., Herbert, K., Rashid, M.R., Fire and Mechanical Behaviour of Hybrid Composite Laminates, 8th International Conference on Textile Composites (TEXCOMP-8), Nottingham, UK, 16-18 Oct (2006).
- [135] Mazur, K., Kuciel, S., Salasinska, K., Mechanical, fire, and smoke behaviour of hybrid composites based on polyamide 6 with basalt/carbon fibres. *Journal of Composite Materials*; 53(28-30):3979-3991, (2019).
- [136] Ambigai, R. and Prabhu, S., Analysis on mechanical and thermal properties of glass-carbon/epoxy based hybrid composites, *IOP Conf. Ser.: Mater. Sci. Eng.* 402 012136, (2018).

## **Chapter 2. Materials and experimental techniques**

### **2.1 Introduction**

This chapter covers the materials and experimental techniques used in this project. Several grades of carbon fibres were sourced and characterised for their physical properties. One out of these, TR30S (Mitsubishi-Rayon Pyrofil), was used to make carbon fibre-reinforced composites (CFRCs). To understand the effects of heat and fire on the carbon fibre tows and/or CFRCs were exposed to various heat sources, including: thermogravimetric analysis, a tube furnace, a cone calorimeter and a propane burner. Detailed microscopy of the fibre surface was carried out using a scanning electron microscopy and chemical compositions acquired using energy dispersive X-ray spectroscopy. Characterisation of the as-received and heat exposed carbon fibre included measurements of fibre diameter, mass density, electrical resistivity and tensile strength.

Also outlined in this chapter are the materials used to modify the CFRCs, including the addition of flame-retardants to the resin matrix, as well as the inclusion of veils within the CFRCs plies. The chemical methods used to coat the individual fibres are also outlined, including both sol-gel processes and the use of plasma.

### **2.2 Materials**

#### **2.2.1 Carbon Fibre**

Four commercially available polyacrylonitrile (PAN)-based carbon fibres of different grades and fabric compositions were sourced:

- TR30S (Mitsubishi-Rayon Pyrofil), 200gsm 2x2 twill weave 3K carbon fibre, sourced from East Coast Fibreglass Supplies, UK.
- T300 (Toray) 198gsm 2x2 twill weave 3K carbon fibre, sourced from Toray Composite Materials America, Inc.
- T800HB (Toray), 6K twisted yarn, sourced from Toray Composite Materials America, Inc.
- AS4 (Hexcel), 12K twisted yarn, sourced from Hexcel Corporation, UK.

Carbon fibres are grouped by their modulus and for commercial PAN-based carbon fibres these are: Standard (known as ‘High strength’) <265GPa, Intermediate 265 - 320GPa, High 320 - 440GPa, Ultra high >440GPa.

Physical and mechanical properties of these fibres as provided by manufacturer are given in Table 2.1.

Table 2.1. Physical and mechanical properties of different carbon fibres [1-4].

Fibre Type	Filament diameter/ $\mu\text{m}$	Tensile Strength/MPa	Modulus/GPa	Chemical composition: carbon
TR30S (Mitsubishi)	7	4120	235	-
T300 (Toray)	7	3530	230	<93%
T800HB (Toray)	5	5490	294	>96%
AS4 (Hexcel) (unsized)	7.1	4447	231	94%

### 2.2.2 Resin

The epoxy matrix system consisted of epoxy resin component Bis Phenol A EPILOK 60-822 and curing agent amine based CURAMINE 32-790 NT. Both were provided by Bitrez Ltd, Wigan, UK.

### 2.2.3 Flame retardants

The following fire retardants were used:

- Ammonium polyphosphate, APP (Antiblaze MC, Rhodia)
- Resorcinol bis-(diphenyl phosphate), RDP (Chemtura)
- 9,10-Dihydro-9-oxa-10-phosphaphenanthrene 10-oxide, DOPO (EMPA Materials Science and Technology)

The following nanoparticles were used:

- Nano clay, octadecyl ammonium ion-modified montmorillonite clay, Nanomer I.30E (Nanocor Inc. China)).
- Layered double hydroxide, LDH (Prolabin-Tefarm, Perugia, Italy).
- Graphene oxide (William Blythe, Accrington, UK).
- Carbon nano-tubes (Tuball 301, OCSiAL Luxembourg) Single wall carbon nano-tubes (SWNT).

#### 2.2.4 Non-woven fibrous veils

Veils listed in Table 2.2 were used as extra layers along with carbon fibres 200gsm 2x2 twill weave to prepare CFRCs and were sourced from TechnoFire, Technical Fibres LTD, UK. These veils were selected as they had a low mass density, and would minimally affect the CFRC's mechanical properties. An additional two woven veils were supplied by Easy Composites, UK, including a satin 300g 2x2 twill weave Kevlar® cloth with a thickness of 0.47mm, manufactured by Dupont. All veils selected had low electrical conductivity and would not increase the CFRC's overall conductivity.

Table 2.2. Veil densities.

Veil	Mass density/gm <sup>-2</sup>
Aramid	14
Basalt	15
E-glass	17
Polyphenylene sulphide (PPS)	20
Woven glass	25
Kevlar	300

### 2.3 Preparation of composites

An outline of the composite preparation procedures are given below and generally they were prepared via resin infusion and hand lay-up methods. Each composite measured 300mm x 300mm and comprised 8 carbon fibre plies.

### **2.3.1 Resin infusion**

Resin infusion is a popular method to make void-free composites, when liquid resin is drawn through stacks of dry fabric using a vacuum pump. An aluminium plate was covered with polymer film and the fabric plies laid on top of each other. A so-called “peel ply” was placed both underneath and on top of the fabric to provide a uniform finish to both sides. Extruded polypropylene mesh was placed on the top layer to assist the flow of resin into the laminate during the resin infusion process. A spiral coil provided medium flow infusion while evenly distributing the resin flow.

Once the vacuum connectors and resin feed were in place, the setup was covered with polymer film and sealed. Resin and hardener were measured out in a 100:38 weight ratio. For the specific composite composition CC\_RDP, because the flame retardant RDP is a liquid, 15wt% of liquid RDP was added to resin and mechanically stirred for 15min before the hardener was included. This mixture was mechanically stirred for a further 10min before degassing for several minutes in a vacuum oven. The vacuum pump drew the resin through the sample and was held under vacuum for 24h at ambient temperature before transferring to an oven at 80°C for 8h for post curing.

### **2.3.2 Hand lay-up and vacuum bagging**

Due to the larger particle size of the solid APP and DOPO flame retardants, resin infusion was not possible so hand lay-up method was used. An aluminium plate was prepared with polymer films and Easy-Lease release spray. 15wt% of APP powder was added to the resin. This was mechanically stirred for 15min before the hardener was added, stirred again and degassed in a vacuum oven. The resin/APP mixture was applied equally to each carbon fibre layer using a roller. Each coated later was placed on top of each other, until all layers were evenly coated. The whole assembly was covered in breather cloth acting as a soaker/bleeder cloth, wrapped in polymer film and sealed, as shown in Figure 2.1. The set up was connected to a vacuum of 1 bar for 24h at room temperature, then post cured under vacuum at 80°C for 8h.

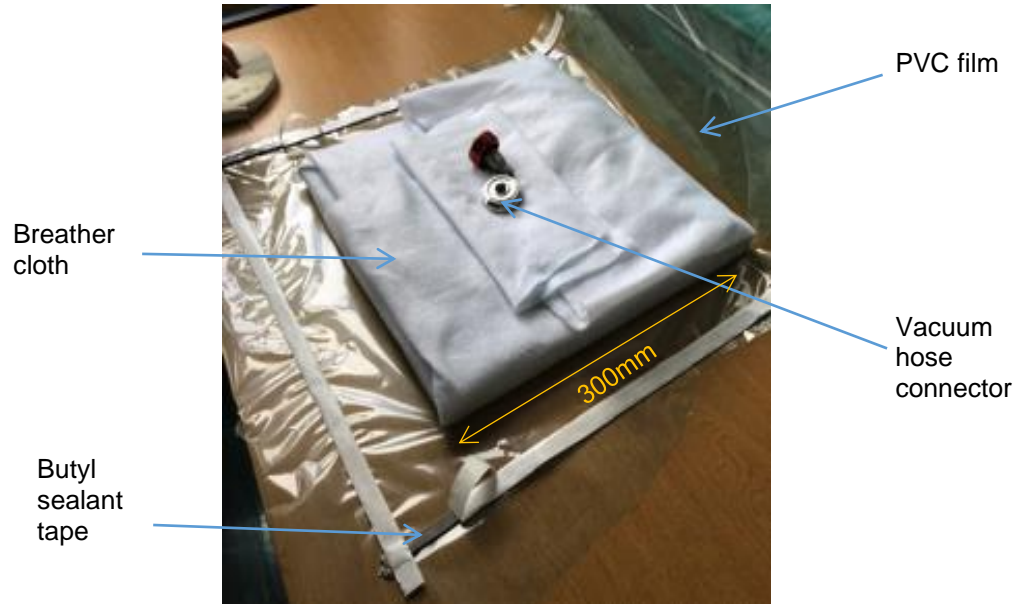


Figure 2.1 CC\_APP preparation by hand lay-up

The flame retardant DOPO had to be dissolved before adding to the resin. First it was crushed with a mortar and pestle. Once in a powdered form the DOPO was added to 100ml of chloroform (99+%, Thermo Scientific), then heated on a hot plate to 40°C and mechanically stirred for 1h until the DOPO had fully dissolved. The solution was heated to 65°C (above the boiling point of chloroform (61.2°C)) until all the chloroform had evaporated. It was then cooled down to 40°C (where it still remained in a liquid form), added to the resin and mechanically stirred for 5min at 40°C. The composite was then prepared in the same way as for CC\_APP.

### 2.3.3 Composites with nano-additives

Composites CC\_NC, CC\_LDH, CC\_GO and CC\_NT were sourced from another PhD project [5] and had been made by resin infusion using the same carbon fibre and resin as in this project. For CC\_GO and CC\_NT the additives were mixed with the epoxy resin by a high shear mixing method (turbo-mixer) at Bitrez Ltd before resin infusion. A detailed account of the manufacture of these composites is given in [5]. The composites and manufacturing methods are given in Table 2.3.

Table 2.3. Summary of additives used and composite manufacturing method.

Composite	Additive	Mass % of additive	Manufacture method	Supplied from other project [5]
CC	None	N/A	Resin infusion	
CC_APP	Ammonium polyphosphate	15	Hand lay-up	
CC_DOPO	9,10-Dihydro-9-oxa-10-phosphaphenanthrene 10-oxide	15	Hand lay-up	
CC_RDP	Resorcinol bis(diphenyl phosphate)	15	Resin infusion	
CC_NC	Nano clay, octadecyl ammonium ion-modified montmorillonite clay	5	Resin infusion	✓
CC_LDH	Layered double hydroxide	5	Resin infusion	✓
CC_GO	Graphene oxide	0.5	Resin infusion	✓
CC_NT	Carbon nano-tubes	1	Resin infusion	✓

#### 2.3.4 Preparation of composites with veils

The veils were placed in two configurations shown in Figure 2.2. The first had only a veil placed on the top surface of the composite, while the second also incorporated two more veils within the plies of the composites.

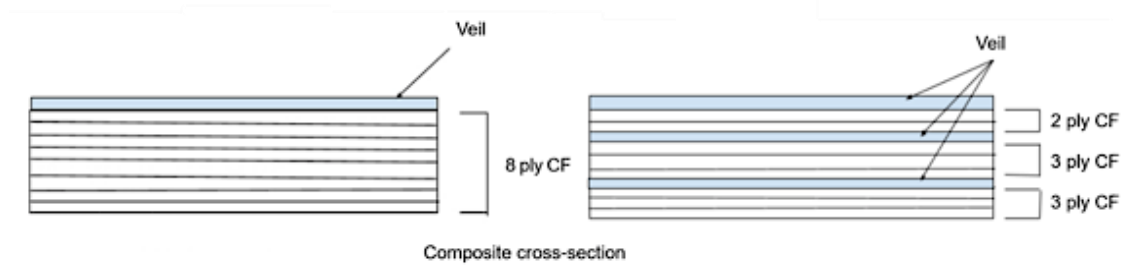


Figure 2.2. Schematics of the two configurations used to place veils in the composites.

As for CC all composites with veils were made via resin infusion as outlined in Section 2.3.1. The carbon fibre and veils were weighed before making the composite and the final composite weighed again. Using equation [2.1] the fibre wt%, and therefore the resin wt% in the composite could be calculated (Table 2.4).

$$Fibre\ wt\% = \left( \frac{mass\ of\ carbon\ fibre + veils}{mass\ of\ composite} \right) \times 100 \quad [2.1]$$

Table 2.4. Summary of composites with veils with fabric and resin ratios.

Composite	Veil/fabric	No. Added veils	Mass fraction %			Thickness, mm
			Veil/fabric	Carbon fibre	Resin	
CC	-	-	-	65.7	34.3	2.08
CC_Ar_1	Aramid	1	0.4	46.4	53.3	1.79
CC_Ar_3	Aramid	3	1.3	54.0	44.6	2.05
CC_Bs_1	Basalt	1	0.8	62.2	37.0	1.88
CC_Bs_3	Basalt	3	2.1	53.8	44.1	1.97
CC_Gl_1	E-glass	1	0.6	66.5	32.9	1.79
CC_Gl_3	E-glass	3	1.6	58.4	40.0	2.05
CC_Wo-Gl_1	E-glass	1	0.9	59.5	39.6	1.91
CC_Wo-Gl_3	E-glass	3	3.7	52.1	44.2	2.19
CC_PPS_1	PPS	1	0.6	48.2	51.2	2.55
CC_PPS_3	PPS	3	1.8	57.2	41.0	2.07
CC_Kv_1	Kevlar	1	-	-	-	2.49

Higher magnification SEM images were taken of several cross-sections and are given in Figure 2.3. Voids in CC\_PPS\_3 were seen but the overall adhesion between the carbon fibre/PPS veil appeared to be adequate.



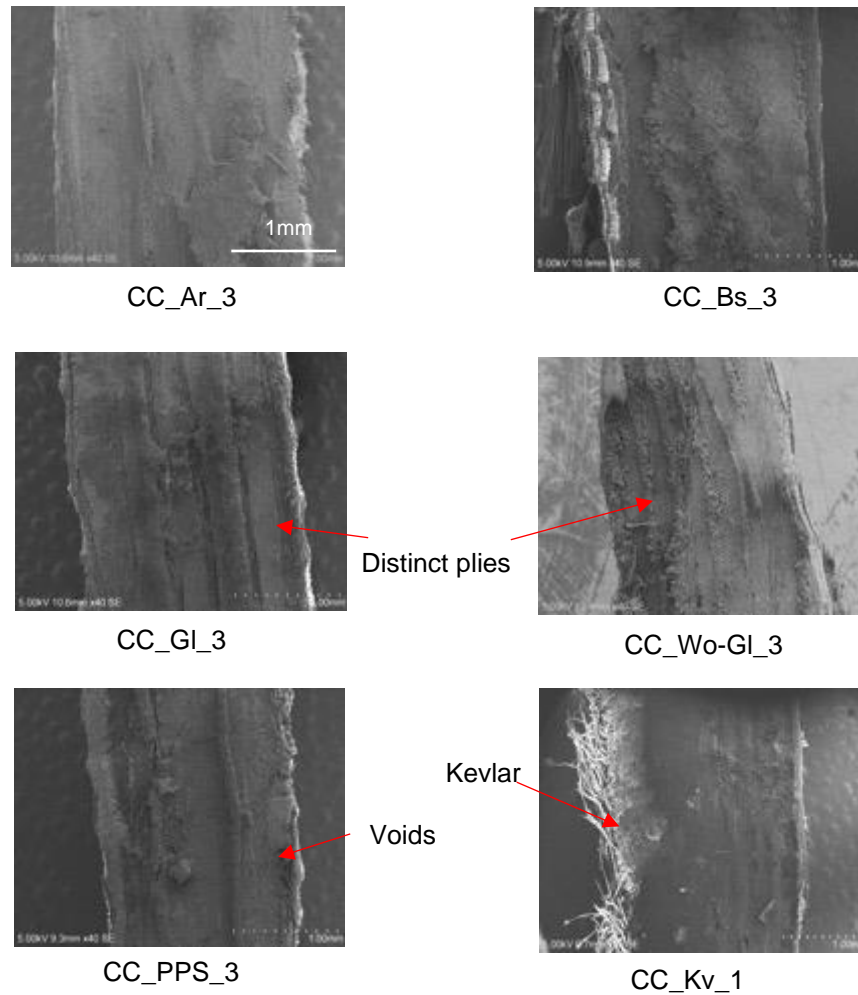


Figure 2.3. SEM images of cross-sections of composites with veils.

## 2.4 Exposure to different high temperature environments

### 2.4.1 Thermogravimetric Analysis

Measurements were carried out on a TA instruments Q500 Thermogravimetric Analyser, using sample masses between 2–8mg in a platinum pan, heated from ambient temperature to 1,000°C at a heating rate of 20°C/min. Both air and nitrogen gases were used (depending on the experiment) each at a flow rate of 100ml/min.

### 2.4.2 Tube furnace

In order to remove sizing from carbon fibres, as well as to subject them to varying temperatures, a tube furnace was used. This is an electrical heating apparatus which can be used at controlled temperatures as shown in Figure 2.4.

Carbon fibre tows were held within a 25mm internal diameter quartz tube. The tube furnace was left for 40min for the selected temperature to stabilise. The sample was then placed in the middle of the constant temperature heat zone. Depending on the experiment, the tube furnace was used at temperatures from 150°C to 900°C with samples exposed under static air or nitrogen atmosphere at a constant flow rate of 100ml/min.

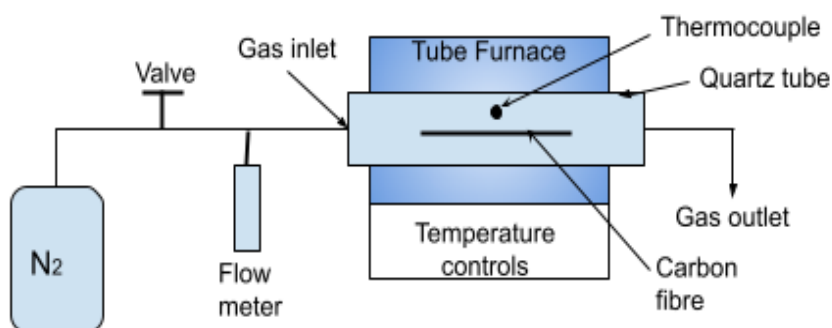


Figure 2.4. Schematic of tube furnace with nitrogen flow.

### 2.4.3 Cone Calorimetry

The cone calorimeter was used in the horizontal configuration in accordance with the standard ISO 5660 [6]. Heat fluxes from 35kWm<sup>-2</sup> to 75kWm<sup>-2</sup> were applied, with and without spark ignition.

The set up was modified from ISO 5660 in that rectangular samples of 25mm x 100mm (instead of 100mm x 100mm) were used, as the cone calorimeter acted only as a source of heat in these experiments. The sample was weighed before being wrapped in aluminium foil (24µm thick) to negate edge effects. A typical prepared sample and holder are shown in Figure 2.5.



Figure 2.5. Composite sample for cone calorimeter testing.

At each selected incident heat flux, a K-type thermocouple was placed on the composites surface at the beginning of the test and the temperature recorded. A stopwatch was used to record time-to-ignition and flame-out. After the experiment finished, the sample was removed and left to cool before being removed from the foil and weighed.

#### **2.4.4 Propane burner test**

In order to carry out fire testing on carbon fibres and carbon fibre composites under more realistic fire conditions, a small-scale propane burner set up was used. The propane burner test was initially based on the bench test [7] and then further developed at the University of Newcastle by Gibson et al [8]. It conforms to two standards. First, ISO 2685:1998(E) [9] which is a burner test to determine the resistant of equipment and structures within a “fire zone”. And the second, FAR 25.856(b):2003 [10], an insulation burn through test used to evaluate the burn through resistance characteristics of thermal and acoustic insulation material when exposed to a high-intensity open flame.

Composite samples and fibre strips were mounted in a 250mm x 250mm graphite plate with a placement holder in the centre of 25mm x 100mm x 3mm. This was used so that edge effects of the composite were negated. Kaowool ceramic fibre was used to insulate the plate. The plate was placed vertically in a steel holder at 1.4m above the ground (see Figure 2.6(a)). The sample was held in place using a nickel alloy wire. This wire was also used to attach K-type

thermocouples to the top, middle and bottom of the sample, at a distance of 10mm in front of the sample. The plate also had a small 2mm diameter hole was drilled through the middle of it to allow a 1.5mm K-thermocouple to be placed on the cold, rear surface of the sample. However, due to the thin samples used in this thesis (maximum composite thickness of 2.8mm) and the force of the propane gas flame, this thermocouple was pushed out and lost contact with the cold surface and gave a reading of the graphite plate temperature. Hence, this reading was not used and instead the front three K-thermocouples were recorded (Figure 2.6(b)).

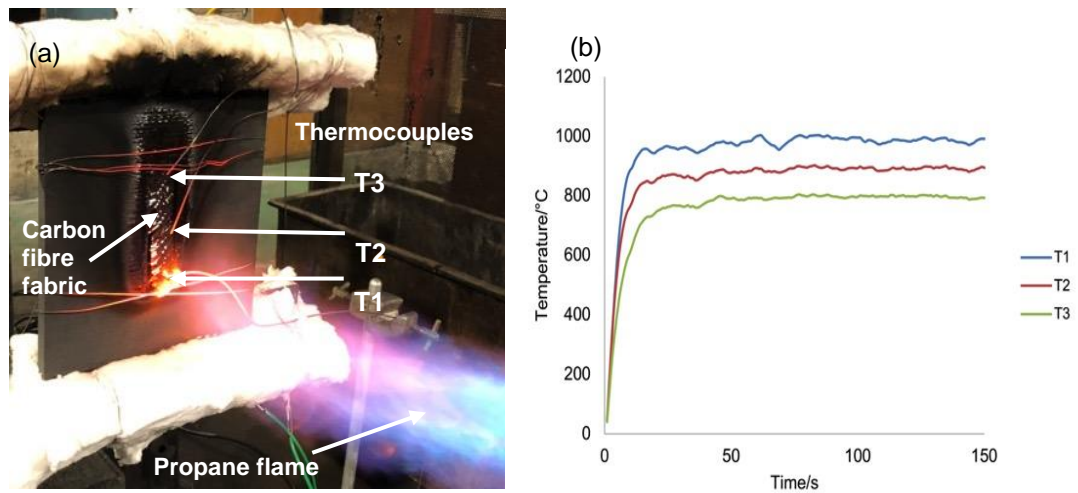


Figure 2.6. (a) Thermocouple setup (b) Temperatures recorded by thermocouples over 150s.

The propane burner (Bullfinch No. 1270) was directed horizontally to the bottom section of the sample so that when testing the composites, the flame effect from ignition of the lower part of the composite could be studied as it rose vertically up the sample (Figure 2.7(b)). The burner diameter was 63.5mm and it was positioned 350mm from the sample plate (Figure 2.7(a)). The propane burner gas pressure was adjusted until the bottom thermocouple located 10mm in from of the sample hot face, recorded 1,000°C. According to previous work [10], this set up corresponds to a heat flux of 116kWm<sup>-2</sup>. This condition was kept the same throughout the experiment to maintain a constant heat flux.

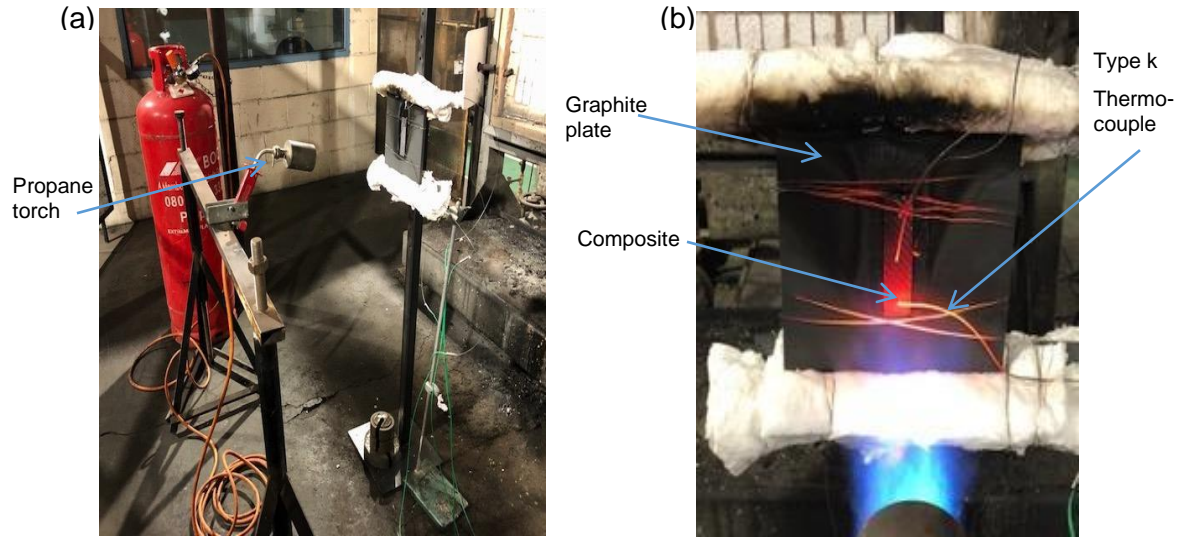


Figure 2.7. (a) Propane burner set up, and (b) Composite and graphite plate.

## 2.5 Carbon fibre analysis

### 2.5.1 Scanning Electron Microscopy

A Hitachi S-3400 scanning electron microscope was used to obtain all SEM images. As carbon fibre is conductive, no gold coating was required. Small pieces of a sample were placed on adhesive carbon tape attached to an aluminium SEM stub. The samples were then positioned on a stage in the chamber of the SEM with a working distance of around 10mm from the sample and voltages of 5eV to 20eV depending on the sample. Magnification ranged from x100 to x10,000.

Following the ISO standard 11567:2018 [11] to determine the diameter of carbon fibre, at least ten fibres from the same bundle were imaged on the SEM and measured using the on-screen measurement tool. A mean of these measurements was taken and this value used.

Attached to the SEM is an Energy dispersive X-ray spectroscopy (EDX) analysis accessory (Oxford instruments) with INCA software, which provided elemental and chemical analysis of samples.

### 2.5.2 Mass density

In order to compare the carbon fibre to the specification given by the manufacturer, their mass densities were calculated. Due to the low mass of carbon fibres and difficulties in accurately measuring it without specialist equipment, a length of tow of 3,000 fibres was removed from the weave and used in the calculations.

From SEM measurements the average diameter of fibre was measured and assuming it is circular, the cross-sectional area (A) for a single fibre is found using  $A=\pi r^2$ , where r is the fibre radius. By multiplying this by 3,000 the cross-sectional area for a tow can be estimated. The tow was then repeatedly cut and the mass recorded, and using equation [2.2], the mass density was obtained:

$$M = (N\rho A)L + M_0 \quad [2.2]$$

where:

M is the mass of the tow,

N is the number of individual fibres in a tow,

$\rho$  is the mass density,

A is the cross-sectional area,

L is the length of the tow,

$M_0$  is the tare weight of the measurement

The graph of mass versus tow length is shown in Figure 2.8, from which the slope, 0.0019g/cm enables the density,  $\rho$ , to be calculated.

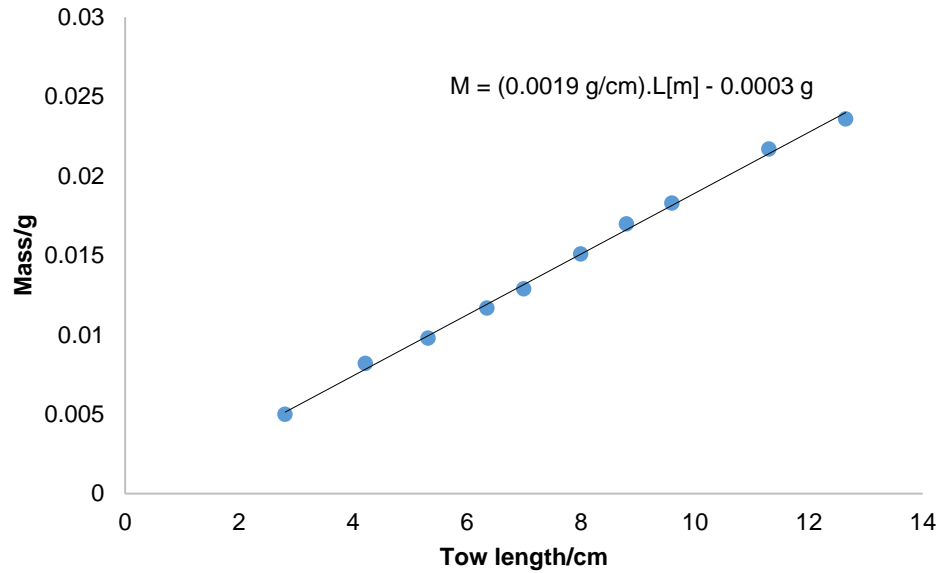


Figure 2.8. Graph of mass against tow length where the gradient is used to calculate the density.

### 2.5.3 Electrical conductivity

#### 2.5.3.1 Single fibre resistivity

Single fibre electrical tests were used instead of testing fibre tows because within the tow individual fibres can make contact at various points and this has the potential to lead to erroneous results depending on the tension of the tow.

Electrical conductivity of a single fibre can be measured by means of resistance probes, where either the two probe or four probe methods are used. Here an adapted two probe method was used. Individual carbon fibres were held straight and taut on a plastic slide using Loctite super glue. Contacts were made at each fibre end (typically 10cm apart) with small drops of silver conductive epoxy (MG Chemicals). A digital multimeter (RS PRO IDM93N) measured the terminal resistance between two electrical contacts. The contacts were reduced incrementally and the resistance measured (see Figure 2.9). At least five fibres from the same tow were selected in order to calculate an error in measurements.

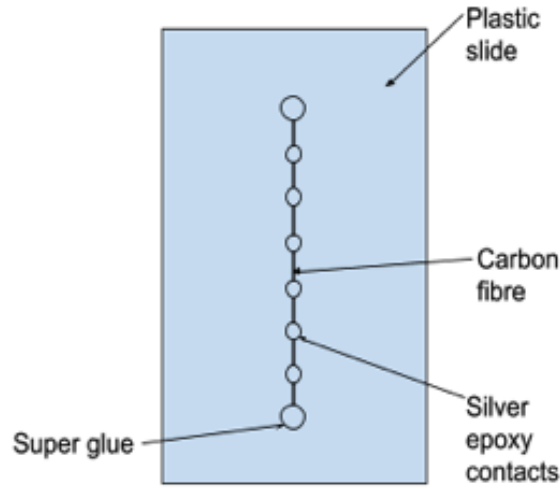


Figure 2.9. Completed measured sample using the two probe method for measuring electrical conductivity.

The measured two terminal resistance ( $R$ ) is related to the distance between the contacts ( $L$ ) by:

$$R = \left( \frac{\rho_{el}}{A} \right) L + R_c \quad [2.3]$$

where:

$\rho_{el}$  is the electrical resistivity,

$A$  is the fibre cross-section,

$R_c$  is the contact resistance

From a known current ( $I$ ) and voltage ( $V$ ), using Ohm's law the resistance ( $R$ ) can be calculated using:

$$V = IR \quad [2.4]$$

The cross-section of a carbon fibre was assumed to be circular and using the diameter measure on a scanning electron microscope, the area was obtained from  $A = \pi r^2$ , where  $r$  is the fibre radius.



### 2.5.3.2 CFRC resistivity

CFRCs were cut using a bandsaw into 25mm x 100mm rectangles and rinsed in acetone to remove any dust. The thickness of the sample was measured using a micrometre.

A two-probe set up was used to measure the resistance of the CFRC specimens. The points of contact were painted with silver conductive epoxy (MG Chemicals) to create a smooth conductive surface. Copper plates were positioned using spring clamps (Figure 2.10) in order, to apply a repeatable contact pressure to all specimens. Measurements were made on an insulating PTFE plate.

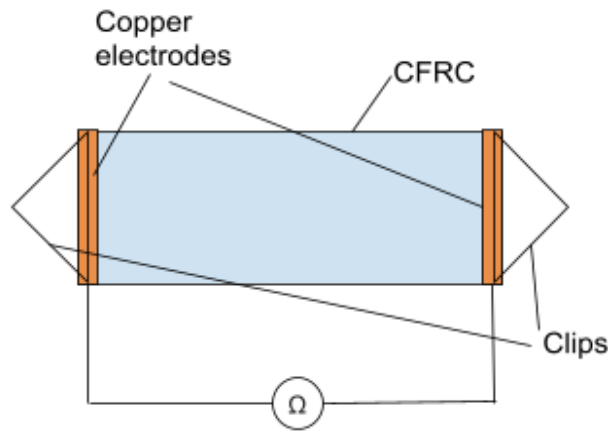


Figure 2.10. Diagram of conductivity tests for CFRC.

The current was injected via the copper plates and the DC resistance measured between them using a digital multimeter (RS PRO IDM93N). The conductivity,  $\sigma$ , of the composites were measured in the same direction:

$$\sigma = \frac{L}{RA} \quad [2.5]$$

where:

L is the distance between contacts,

R is the resistance of the composite rectangle,

A is the area of the electrodes

In general, the conductivity of the through thickness of the composite was found to be significantly less than the longitudinal conductivity, because the longitudinal direction is dominated by the carbon fibre properties. As this project is interested in the fibre properties, only the longitudinal conductivity was measured.

#### 2.5.4 Tensile testing

Tests were performed on the Instron Testing System 3369 with a 1N load cell. Single fibre specimens were made according to BS ISO11566 [12]. A minimum of 20 test specimens for each sample were produced so there were at least 20 measurements for each result reported. This provided enough results to calculate a mean with errors.

Single fibres were carefully removed from tows using tweezers and placed on prepared card mounts with slots cut into them (Figure 2.11). The fibre was attached to the cards using adhesive tape, with a drop of adhesive to the fibre at each end to ensure the fibre was secure to the card.

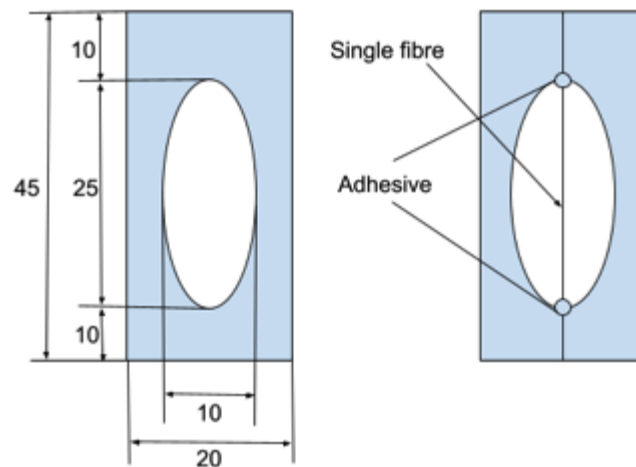


Figure 2.11. Cards used for single fibre tensile tests.

The specimen cards were clamped in the mounting grips and aligned with the loading axis. Both sides of the card were cut with scissors, care being to ensure the fibre did not break. A crosshead speed was set to 0.8mm/min on all tests. Due to the fragility of the carbon fibres, specimens failed within or at the grips occasionally occurred and these were discarded.

## **2.6 Surface coating of carbon fibres**

### **2.6.1 Preparation of carbon fibre surface prior to coating**

#### **2.6.1.1. Removal of sizing and activation of carbon fibre surfaces**

Prior to coating fibres the sizing was removed and the surface chemically activated. Carbon fibre tows were removed from the relevant woven fabric and heated at 450°C in a tube furnace in a nitrogen atmosphere for 1.5h to remove the polymer sizing. Fibres were then placed in concentrated nitric acid (HNO<sub>3</sub> 68% Fisher Scientific, UK) for 2h at 80°C to chemically activate the surface. Finally fibres were rinsed with distilled water to remove any HNO<sub>3</sub> residue and dried in an oven at 60°C.

#### **2.6.1.2 Plasma treatment**

An atmospheric cold plasma fully described elsewhere [13] was used for surface activation treatment on carbon fibre. It consisted of a Surfatron Microwave cavity into which a plasma containment quartz tube was placed. This was connected to a microwave generator with an operating frequency of 2.45GHz and power output of 0 to 300W; for treatment of carbon fibre surfaces 190W was used. As carbon fibre is electrically conductive, a higher power output could result in sparking. Argon gas (99.99% purity) was used to initiate and generate the plasma at atmospheric pressure. It was set at a flow rate of 20l/min and a copper wire employed to ignite the argon plasma. A 10mm distance was maintained between the end of the quartz tube and the carbon fibres, which were treated by plasma sweeping along the tow for 5min.

### **2.6.2. Surface coating by dip coating method**

#### **2.6.2.1. Sodium aluminate (NaAlO<sub>2</sub>)**

In order to prepare sodium aluminate, 3g of sodium hydroxide (NaOH) was added to 70ml of deionized water and heated on a hotplate to 60°C. 1.5g of aluminium flakes were slowly added

to the solution. Any excess of aluminium flakes were removed using a 100-mesh filter. The carbon fibres tows were immersed in the solution for 15min and then oven dried 80°C for 12h. On selected fibre tows, a further heat treatment in a tube furnace in a nitrogen atmosphere for 3h at 900°C was carried out to remove any excess solvent.

#### **2.6.2.2 Boron nitride**

Boric acid ( $\text{H}_3\text{BO}_3$ , ACS reagent,  $\geq 99.5\%$ , Sigma-Aldrich, UK) was used as a precursor with 10g dissolved in 100ml of ethanol at 90°C and mechanically stirred for 1h. Carbon fibre tows were submerged in the solution for 30min and then removed and left to air dry for 18h, after which the tow was placed in a tube furnace in 100ml/s flowing nitrogen  $\text{N}_2$  (purity of 99.99%) for nitridation for 3h at 900°C.

Another solution was made using urea ( $\text{CH}_4\text{N}_2$ , ACS reagent, 99.0-100.5%, Sigma-Aldrich, UK) as an additional source of nitrogen. The boric acid solution was made as above but urea was added in a mass ratio of 1:1 with the  $\text{H}_3\text{BO}_3$ , before undertaking the same drying and nitridation process.

#### **2.6.3 Coating by the sol-gel process**

The sol-gel process involves two reactions – hydrolysis of the precursor and then polycondensation of the hydrolysed products to a ceramic-based structure. The metal precursor undergoes hydrolysis to produce a metal hydroxide solution, followed by condensation leading to the formation of three-dimensional gels, and then a final drying process. Metal oxide nanoparticles  $\text{SiO}_2$ ,  $\text{Al}_2\text{O}_3$  and  $\text{ZrO}_2$  were synthesised using this method.

##### **2.6.3.1 Silica ( $\text{SiO}_2$ ) coating**

Tetraethyl orthosilicate, (TEOS,  $\text{SiC}_8\text{H}_{20}\text{O}_4$  98% Thermo Scientific) was used as the silica source. The silica sol was prepared as follows:

TEOS, water and ethanol, in a molar ratio of 1:1:2.5, were mixed at room temperature for 1h. An additional 1mol distilled H<sub>2</sub>O was added, along with 2.5mol ethanol. 1M hydrochloric acid was then added dropwise (as a catalyst) until pH= 3 was obtained. This was further stirred for 1h until a nearly transparent sol was obtained. Carbon fibre tows (100mm in length, mass 16.2±0.2mg) was submerged in the sol for 5min and any excess solution on the fibre removed. The fibres were left to air dry at room temperature. The subsequent heat treatment of the dried sol coating was determined after the following investigation.

In order to fully evaporate the water and remove residual organic molecular fragments, further heat treatment was required. To determine the treatment to optimise this processing condition, the sol was left to dry at room temperature for 24h before examining by TGA in air (flow rate 100ml/min). TGA was only carried out on the sol and not the coated carbon fibre, so that any mass loss due to the coating would not be confused with mass loss of the carbon fibre. Figure 2.12 shows the TGA response of the sol after being held at various temperatures for 2h. All TGAs were carried out at 20°C/min and a gas flow rate of 100ml/min. ‘No heat’ stands for the solution being left to air dry only. It can be seen that with no heat treatment, up to 25% of the sol’s mass had evaporated after 400°C, indicating the sol had not been fully formed, with mass loss likely from the unreacted ethanol or water. Drying the sol in an oven at 150°C and 200°C still did not remove all the residual sol-gel products, as a mass loss of 15wt% up to 400°C was seen in the TGA response. However, when oven-dried at 400°C, the mass loss of the resulting sol was only 6% at 1000°C. The final heat treatment condition was at 700°C in a nitrogen atmosphere. This inert gas was used as at 600°C in air, carbon fibres oxidise. After 2h at 700°C in nitrogen the silica sol had completely formed and was heat resistant up to 1000°C. Carbon fibre tows were therefore coated with the silica sol and heat for 2h at 700°C in nitrogen.

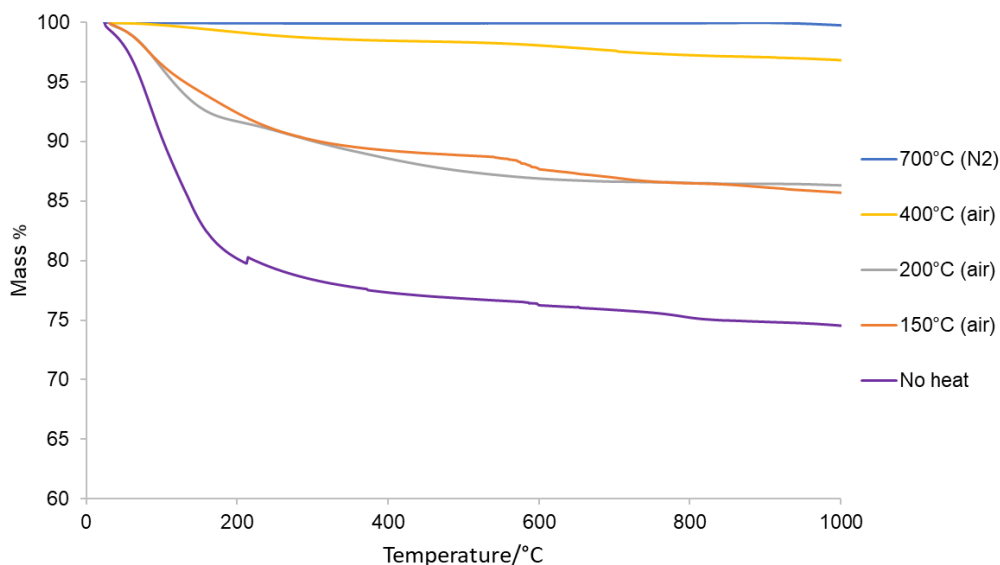


Figure 2.12. TGA of silica sol after being held at different temperatures for 2h.

### 2.6.3.2 Alumina ( $\text{Al}_2\text{O}_3$ )

Aluminium isopropoxide ( $\text{C}_9\text{H}_{21}\text{O}_3\text{Al}$ , 98% Thermo Scientific, UK) was used as the precursor to making an alumina coating. The alumina sol was prepared as follows: 0.1mol aluminium isopropoxide was added to 15mol distilled water. The water was preheated to  $85^\circ\text{C}$  and the solution stirred for 1h. 1M HCl (acting as a catalyst) was then added dropwise to adjust the solution until  $\text{pH} = 3$ . The solution was further stirred for 1h to produce a transparent sol. The fibres were immersed in the sol for 5min before being removed and left to air dry for 24h.

As with the silica sol, TGA experiments with just the alumina sol were carried out to find the heat treatment required to fully evaporate the water and remove organic fragments. The TGA responses in Figure 2.13 were recorded under the same condition as defined in Figure 2.12. Thus it was seen that a heat treatment of 2h at  $400^\circ\text{C}$  was sufficient to produce a cured alumina sol, which condition.

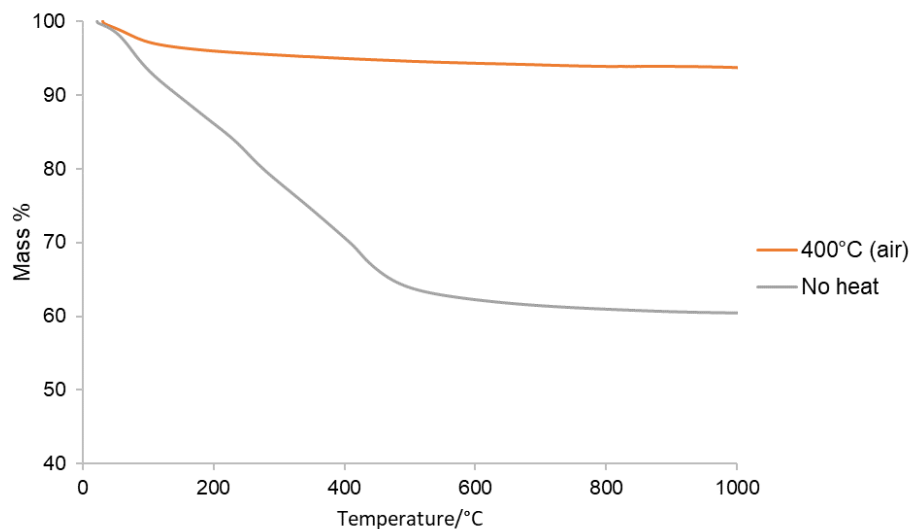


Figure 2.13. TGA of alumina sol after being held at different temperatures for 400°C for 2h.

### 2.6.3.3 Zirconia ( $\text{ZrO}_2$ )

Zirconyl chloride octahydrate ( $\text{ZrOCl}_2 \cdot 8\text{H}_2\text{O}$ , Thermo Scientific, UK) was used as the precursor to make a zirconia coating.  $\text{ZrOCl}_2 \cdot 8\text{H}_2\text{O}$  was dissolved in ethanol and distilled water in a molar ratio of 0.05:1:1. It was stirred at room temperature for 1h, nitric acid (acting as a catalyst) was then added drop wise until a pH= 2 was reached. Acetylacetone ( $\text{C}_5\text{H}_8\text{O}_2$ , Sigma-Aldrich, UK) was added in the same volume as nitric acid as it has been shown to act as a complexing agent [14,15]. The solution was stirred for another hour before the fibres were submerged in the sol for 10min before being removed and left to air dry for 24h.

To find the optimum heat treatment for this, TGA was carried out on the sol. Figure 2.14 shows that heating at 150°C for 2h showed a slight improvement in the coating's heat resistant properties, however, a heat treatment of at least 700°C for 2h (in nitrogen) resulted in the formation of temperature resistant zirconia coating stable up to 1000°C.

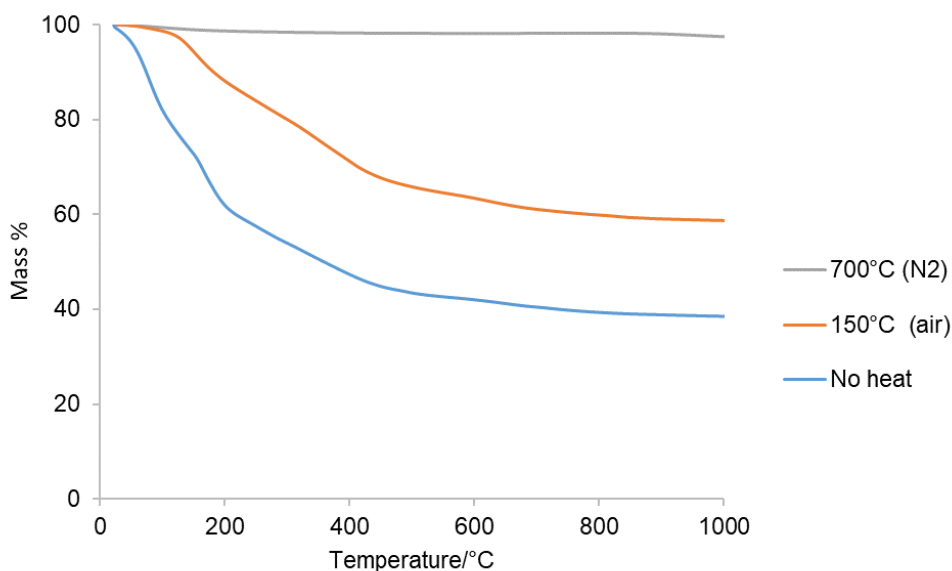


Figure 2.14. TGA of alumina sol after being held at different temperatures for 400°C for 2h.

#### 2.6.4 Silica nano-particle deposition as sizing

LUDOX® HS-40 colloidal silica (40wt% suspension in water, 12nm particle size) (Sigma-Aldrich, UK) was mixed with a silane coupling agent (3-glycidoxypopyl)trimethoxysilane, Sigma-Aldrich, UK), which was added dropwise (2ml total) and stirred with a magnetic stirrer. The epoxy resin component Bis Phenol A EPILOK 60-822, which was used to make composites in the previous chapters, was diluted with butanone in a volume ratio of 100:20. The colloidal silica mixture was added to the diluted epoxy at a mass ratio of colloidal silica to epoxy resin at 3wt% as previously found to be optimum in [16,17]. The solution was magnetically stirred for 30min and then placed in an oven for 1h at 90°C to evaporate the water and volatilise the butanone. At this stage the resin hardener CURAMINE 32-790 NT was added to the resin mixture and stirred for 5min. As only small amount of solution (25ml) was made, degassing in a vacuum oven was not required. Yang et al. [17] found that forming an emulsion resulted in more uniformly distributed nano-SiO<sub>2</sub> particles in their epoxy sizing. To investigate this, an additional 25ml of solution was made with the emulsifier Polyoxyethylene Sorbitan Trioleate (Tween 85, Sigma Aldrich, UK) along with deionized water. Both were added dropwise until a visible change in the solution was observed. Carbon fibre tows were then dipped in the solutions for



2min and additional resin was removed by pressing and drawing slowly through two aluminium plates covered in peel ply. The sizing cured at 24h at room temperature, 8h at 80°C.

#### **2.6.5. Silica deposition by chemical vapour deposition**

The plasma equipment and treatment are described in Section 2.6.1.2. This equipment was also used to deposit a layer of HMDSO monomer on to the carbon fibre surface. Argon gas was again used as in has been seen to create a high degree of activation of hexamethyldisiloxane (HMDSO) in previous studies [13]. To incorporate the HMDSO monomer ( $C_6H_{18}OSi_2$  98% Sigma-Aldrich, UK), the argon gas passed through the HMDSO in its liquid state. A 10mm distance was maintained between the end of the quartz tube and the carbon fibre tow, which was treated by the argon-HMDSO plasma sweeping along the tow for 5min (Figure 2.15).



Figure 2.15. Atmospheric-pressure jet plasma of HMDSO carried by argon gas.

## 2.7 References

- [1] Mitsubishi Pyrofil datasheet, accessible here: [https://www.m-chemical.co.jp/en/products/departments/mcc/cfcm/product/\\_\\_icsFiles/afiedfile/2020/01/15/CFtow\\_Jan2020en.pdf](https://www.m-chemical.co.jp/en/products/departments/mcc/cfcm/product/__icsFiles/afiedfile/2020/01/15/CFtow_Jan2020en.pdf)
- [2] Toray T300 Standard Modulus Carbon Fibre data sheet, accessible here: <https://www.toraycma.com/page.php?id=661>
- [3] Toray T800HB Carbon Fibre data sheet, accessible here: <https://www.toraycma.com/page.php?id=661>
- [4] Hexcel AS4 Carbon Fibre data sheet, accessible here: <https://www.hexcel.com/Resources/DataSheets/Carbon-Fiber>
- [5] Chapple, R., Effect of Simultaneous impact and heat/Fire on carbon fibre reinforced composites containing nano-additives, PhD thesis, University of Bolton, UK, (2021).
- [6] ISO 5660-1:2015, Reaction-to-fire tests — Heat release, smoke production and mass loss rate — Part 1: Heat release rate (cone calorimeter method) and smoke production rate (dynamic measurement)
- [7] Tranchard, P., Samyn, F., Duquesne, S., Thomas, M., Estebe, B., Montes, J. L., Bourbigot, S., Fire behaviour of carbon fibre epoxy composites for aircraft: Novel test bench and experimental study, *Journal of Fire Sciences*, vol. 33, no. 3, pp. 247–266 (2015).
- [8] Gibson, A. G., Wan-Jusoh, W. N. B., Kotsikos, G., A propane burner test for passive fire protection (PFP) formulations containing added halloysite, carbon nanotubes and graphene' *Polymer Degradation and Stability*, 148, p 86-94, (2018).
- [9] ISO 2685:1998(E). Aircraft — Environmental test procedure for airborne equipment — Resistance to fire in designated fire zones. International Organization for Standardization, (1998).
- [10] FAR 25.856(b):2003. Title 14 code of Federal – test methods to determine the burnthrough resistance of thermal/acoustic insulation materials (Appendix F, Part VII).
- [11] ISO 11567:2018 Carbon fibre — Determination of filament diameter and cross-sectional area.
- [12] ISO 11566:1996 Carbon fibre — Determination of the tensile properties of single-filament specimens

- [13] Horrocks, A. R., Nazare, S., Masood, R., Kandola, B. K., Price, D., Surface modification of fabrics for improved flash-fire resistance using atmospheric pressure plasma in the presence of a functionalized clay and polysiloxane, Volume 22, Issue 1 Special Issue: Selected papers presented at the 10th International Symposium on Polymers for Advanced Technologies, Pages 22-29, (2010).
- [14] Dimitriv, O., Stambolova, I., Vassilev, S., Lazarova, K., Babeva, T., Mladenova, R., Surface and Morphological Features of  $\text{ZrO}_2$  Sol-Gel Coatings Obtained by Polymer Modified Solution, Materials Proceedings, 2(1), 6, (2020).
- [15] Georgieva, I., Danchova, N., Gutzov, S., Trendafilova, N., DFT modelling, UV-Vis and IR spectroscopic study of acetylacetone-modified zirconia sol-gel materials, J Mol Model 18:2409-2422, (2012).
- [16] Wang, C., Jiao, G-S., Peng, L., Zhu, B-L., Li, K-Z., Wang, J-L., Influences of surface modification of nano-silica by silane coupling agents on the thermal and frictional properties of cyanate ester resin, Results in Physics, Volume 9, Pages 886-896, (2018).
- [17] Yang, Y., Lu, C-H., Su, X-L., Wu, G-P., Wang, X-K., Effect of nano- $\text{SiO}_2$  modified emulsion sizing on the interfacial adhesion of carbon fibers reinforced composites, Materials Letters, Volume 61, Issue 17, Pages 3601-3604, (2007).

## **Chapter 3. Effects of heat, irradiance and flames on carbon fibre tows**

### **3.1 Effects of thermal exposure under oxidative and inert atmospheres on carbon fibres and fibre tows**

The first part of this study has examined the damage caused by high temperatures on carbon fibres as individual fibres and as tows and the effects on their physical properties. These included fibre diameter reduction, change in electrical conductivity and decrease in tensile strength, with the aim to provide further insight into potential hazards posed by exposed fibres after high heat situations.

A series of experimental techniques was used to simulate fires which radiate varying amounts of heat and temperatures, ranging from 400°C to 1100°C. Firstly, the effect of heat in a controlled environment was studied. TGA is an extremely accurate and controlled instrument to measure the mass loss of carbon fibre as temperature increases. This was performed in air or nitrogen, simulating environmental conditions where oxygen is present or absent respectively. However, it is limited by the small sample sizes (under 10mg). Tube furnaces on the other hand, allow larger samples, such as fibre tows to be exposed to high temperatures in air or nitrogen. To replicate real fire conditions using radiant heat fluxes, the cone calorimeter was used from 50kWm<sup>-2</sup> to 75kWm<sup>-2</sup>, where a heat flux of 50kWm<sup>-2</sup> simulates a standard house fire at the flashover condition. For situations where there is extremely high heat flux reaching 116kWm<sup>-2</sup> (close to what would be experienced in a jet fuel fire) a propane burner setup was used and the flame effects on carbon fibres studied.

### **3.2 Effect of temperature on carbon fibres under oxidising and inert atmospheres**

TR30S carbon fibres were heated in nitrogen at 20°C/min to 1050°C. Figure 3.1 shows a 1.2% initial mass loss due to the removal of the sizing, which begins to decompose at 200°C and is completely removed at 450°C. The manufacturer did not provide the chemical composition for this sizing. However, its behaviour at these temperatures would suggest it is an organic-based

polymer. Feih and Mouritz [1] also saw a similar mass loss of 0.8% in nitrogen during their TGA study of PAN T700 fibres. This was also attributed to removal of a polymer sizing.

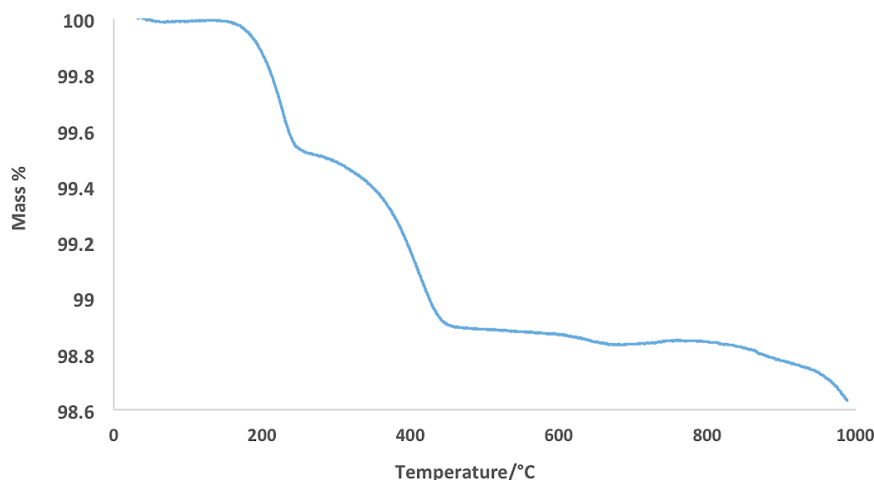


Figure 3.1. TGA graph of TR30S carbon fibre in nitrogen.

A second fibre sample was heated in a nitrogen atmosphere at 20°C/min until 500°C where they were held for 60min in order to see if high temperatures without the presence of oxygen could still cause surface damage to the carbon fibre, for example, pitting due to reactions of contaminating particles, which may have entered during fibre production [2]. Along with the as-received control carbon fibre (CF) (Figure 3.2(a)), Figure 3.2(b) shows that no such damage was evident with the surface remaining featureless apart from the same striations as seen on the CF. Although they were slightly more defined.

To confirm if the all the polymer sizing was removed, Energy-dispersive X-ray spectroscopy (EDX) was carried out. Typical sizing consists of carbon and hydrogen and a high oxygen content, from any epoxy resin content present. However, EDX was unable to detect hydrogen and so the presence of oxygen indicates the presence of any sizing remaining as seen in Figure 3.2(c). Only a trace amount of oxygen was detected. Indicating that the polymer sizing has been removed.

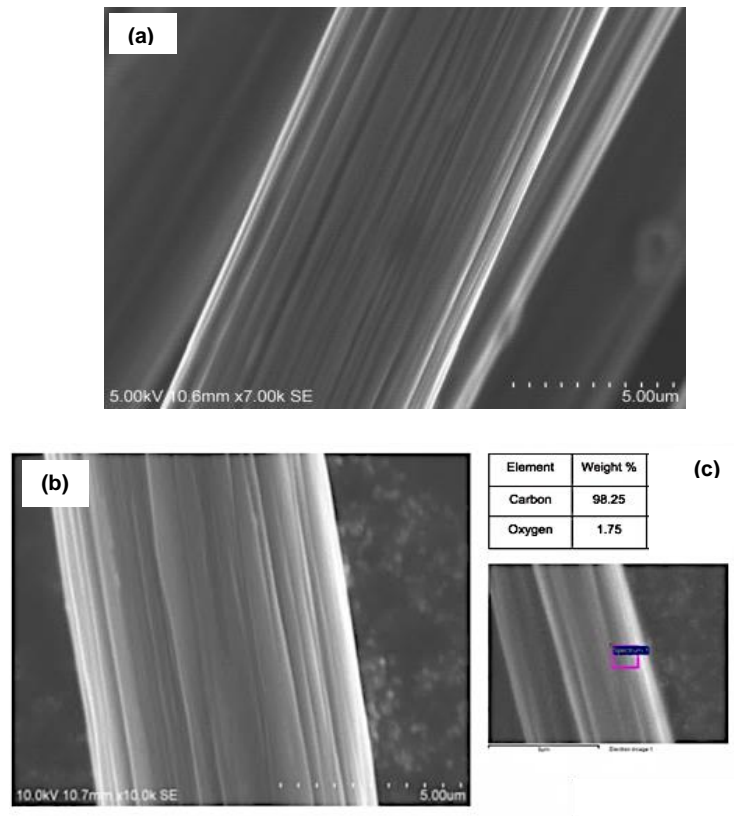


Figure 3.2. SEM images of (a) CF (b) Carbon fibre held at 500°C in a nitrogen atmosphere for 60min (c) EDX analysis of fibre from (b)

In a similar study, Li et al. [3] carried out oxidation tests in air for 1.5h on a similar PAN-based fibre, Toray T300, at 300°C, 400°C and 500°C. They used X-ray photoelectron spectrometry (XPS) to analyse the surface composition of the as-received and oxidised carbon fibres. The as-received fibres had a high oxygen content, which was expected due to the polymer sizing present. The fibres held at 300°C had the same oxygen content on the fibre surface, while at 400°C the oxygen content had decreased and at 500°C there was also a trace amount detected. Their XPS results are given in Figure 3.3.

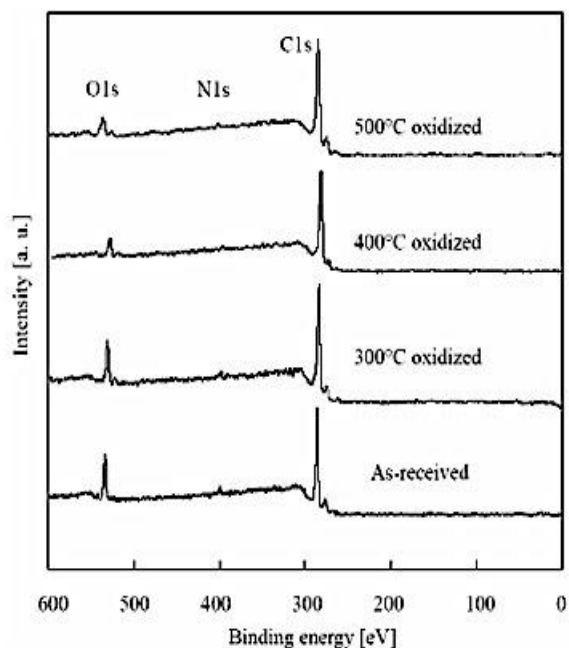


Figure 3.3. The XPS results of T300 fibre from [3].

A further sample of TR30S carbon fibres was heated in a TGA in an oxygen atmosphere (air) at 20°C/min from room temperature to 1050°C. Figure 3.4 shows that mass loss begins at 362°C but there is only a 1.6% total mass loss up until 500°C. This is due again to the loss of sizing as seen during TGA under nitrogen (Figures 3.1 and 3.2). Fibre mass loss continued to 820°C, after which the fibre has been fully oxidised into carbon dioxide.

The first derivative (DTG) curve also shown in Figure 3.4 has a very small peak at 267°C coinciding with the removal of the fibre sizing. The major mass loss peak commencing at about 500°C has been credited as predominantly a surface reaction of carbon oxidation, but between 750°C and 900°C, it is fully controlled by diffusion through pores [4]. This suggests that between 500°C to 750°C a mixture of both mechanisms could have been occurring, which is why the rate of oxidation increased.

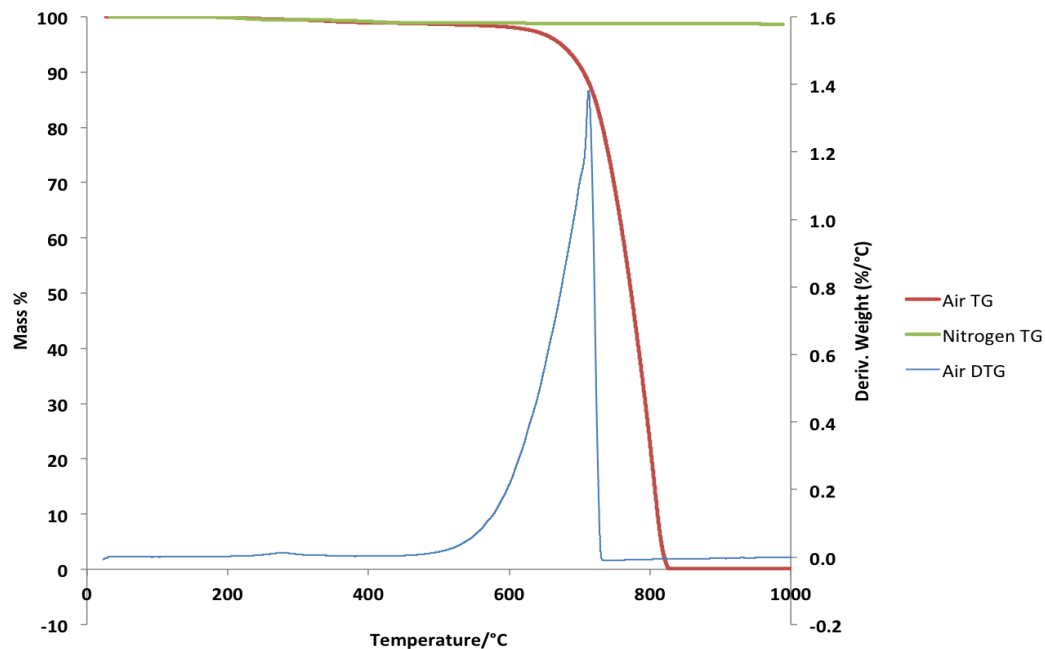


Figure 3.4. TG curves in air and nitrogen, and first derivative of the mass loss curve in air for CF.

### 3.3 Effect of heat on carbon tows under oxidising and inert atmospheres

In order to test carbon fibre tows at different constant temperatures, the tube furnace (Section 2.4.2) was used in air and nitrogen atmospheres.

Tows were held in a nitrogen atmosphere for 1h at 500°C and 1h at 700°C to identify the damage caused to carbon fibre without the presence of oxygen. After 1h at each temperature no reduction in carbon fibre diameter was observed (Figure 3.5(a-b)). The fibres also showed no signs of surface damage such as pitting or micro-cracks, and had a similar surface to the CF (Figure 3.2(a)).



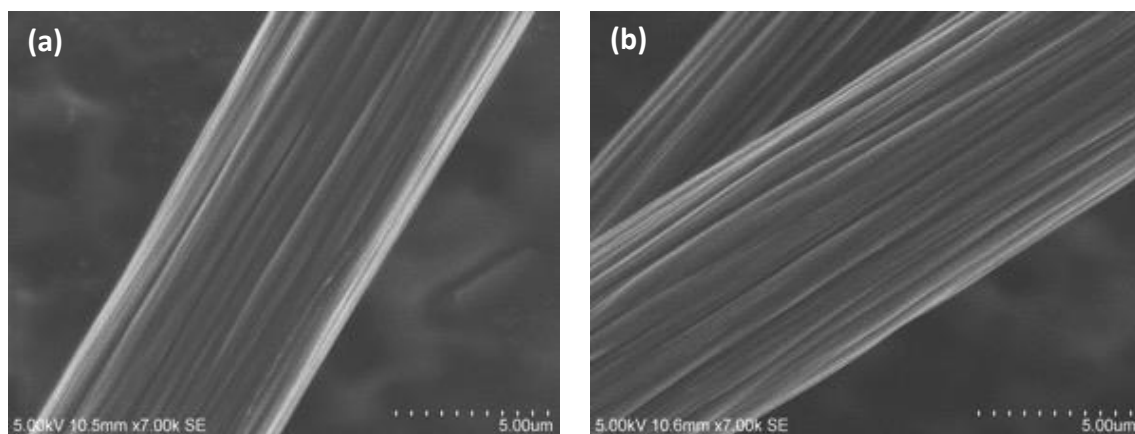


Figure 3.5. SEM of carbon fibres held for 1h in nitrogen (a) 500°C and (b) 700°C.

The benefit of using longer lengths of carbon fibre is that further analysis on the fibres can be carried out. A fibre tow was held at 450°C for 1.5h in a nitrogen atmosphere in order to remove the polymer sizing. After the tow had cooled to room temperature (20°C), single fibres were removed for electrical resistivity tests.

Electrical resistivity was measured (Section 2.5.3.1) along the fibre direction as  $(2.07 \pm 0.05) \times 10^{-5} \Omega\text{m}$ , and is in good agreement with that measured for the CF of  $(2.08 \pm 0.13) \times 10^{-5} \Omega\text{m}$ . This demonstrates that the polymer sizing, while an insulator, is such a thin coating that it has little or no effect on fibre conductivity. Also, it shows that in an inert atmosphere, 450°C is not a sufficient temperature to introduce defects into the fibre, which would have impeded the flow of electrons, thus increasing fibre resistivity.

TGA results in Figure 3.4 showed that oxidation of carbon fibres began around 550°C and were fully oxidised after 800°C. However, the heating rate used was 20°C/min and did not account for the possibility of oxidation of carbon fibres at lower temperatures over a longer period of time. In order to investigate this, carbon fibres tows were held in the tube furnace at 400°C for 60min as the lowest temperature and then increasing temperatures as given in Table 3.1.

Table 3.1. Summary of tube furnace experiments carried out on carbon fibre tows in air.

Temperature/°C	Time/min	Carbon fibre diameter/ $\mu\text{m}$	Observation
400	60	$7.68 \pm 0.23$	No change in fibre diameter
450	30	$7.63 \pm 0.17$	No change in fibre diameter
500	30	$7.13 \pm 0.15$	Small reduction in fibre diameter
500	60	$6.02 \pm 0.21$	Tow intact, further decrease in fibre diameter
500	120	$5.87 \pm 0.34$	Tow intact, decrease in fibre diameter and increase in surface damage
550	30	$6.57 \pm 0.28$	Tow intact, decrease in fibre diameter
550	60	$5.47 \pm 0.31$	Tow intact, decrease in fibre diameter
550	120	N/A	Tow broken in several places, little remaining
600	30	$5.26 \pm 0.32$	Tow intact, decrease in fibre diameter
600	60	N/A	Tow broken in several places, little remaining
600	120	N/A	Zero residue
650	30	$4.98 \pm 0.58$	Tow broken in several places
650	60	N/A	Zero residue

Carbon fibre diameter was used as an indication of oxidation instead of mass loss as carbon fibre oxidation is believed to be a surface-eroding phenomenon. Yin et al. [5] studied oxidation of fibres in air up to 860°C and found a linear relationship between fibre diameter and oxidation time. Furthermore, a previous study by Feih and Mourtiz [1] on Toray T700 PAN fibres in air, measured the diameter of 500 fibres tested at different temperatures and exposure times, over the same temperature range used in these tube furnace experiments (500°C to 700°C). They found a strong correlation between mass loss and carbon fibre diameter reduction.

As seen in Table 3.1, several tows (550°C for 120min, 600°C for 60min, 650°C for 30min) broke into several fragments (Figure 3.6), showing that the fibres did not all oxidise at the same rate over longer exposure times and high temperatures. There are two theories on why the breakages occurred. The first one considers that breakages occur at points of defects in the fibre. These act as activation sites, absorbing more oxygen and enlarging until the fibre weakens at that point and breaks. Defects may occur at the boundaries of ordered regions in the carbon fibre's ordered crystalline structure. Perret and Ruland [6] believed the microstructure of PAN-based fibres consist of stacks of parallel carbon atom ribbons or microfibrils. These ribbons have different contours which do not perfectly match when stacked, leading to nano-sized micropores in the structure.

The second is based on contaminant particles, such as sodium or Na<sub>2</sub>SO<sub>4</sub>, in the fibre which may also affect breakage. These impurities may be introduced during the spinning stage of fibre production. Higher concentrations of sodium reduce the fibre's thermo-oxidative resistance, as the Na<sub>2</sub>SO<sub>4</sub> and oxygen in the air could react with the carbon to produce carbon dioxide, SO<sub>2</sub> and Na<sub>2</sub>O [2]. But in practice this is unlikely as, manufacturers introduce steps to remove sodium sulphate during production. Although sodium could be present as a salt of itaconic acid which is used in a typical PAN precursor [7]. Gourdin [8] studied PAN fibres with different impurity contents by comparing the oxidation rates at 500°C with respect to the fibre sodium content and showed that those with the lowest sodium content experienced greater resistance to oxidation. This is similar to the conclusion of Zhang et al. [9] in that the percentage of sodium was responsible for the TGA shift to higher oxidation temperatures for high modulus PAN fibres compared to its mid-range modulus counterpart.



Figure 3.6. Carbon fibre tow held at 600°C for 60min - broken into several pieces.

In order to identify if impurities are present in the carbon fibre, starting at 400°C, fibres tows were held for 1h in air in the tube furnace. Again no reductions in fibre diameter or visible surface damage were seen as observed previously, also in Figure 3.5 under nitrogen conditions. From the TGA results, oxidation was not expected at 400°C. When the temperature was increased and fibres as tows were held at 500°C for 30min and 1h, a small reduction in diameter occurred during the first 30min of nearly half a micron, confirming that measurable carbon fibre surface oxidation occurred around 500°C.

After 1h, the results of localised surface oxidation were observed in that while the striations on the fibre surface remained, there were now irregularities and small pits present, which are labelled in Figure 3.7(a). Figure 3.7(b) shows a carbon fibre after being held at 500°C for 2h in air. There was a significant reduction in fibre diameter compared to the CF, but the tow remained intact. The striations became less visible, with the surface appearing smoother with distinct areas of surface oxidation.

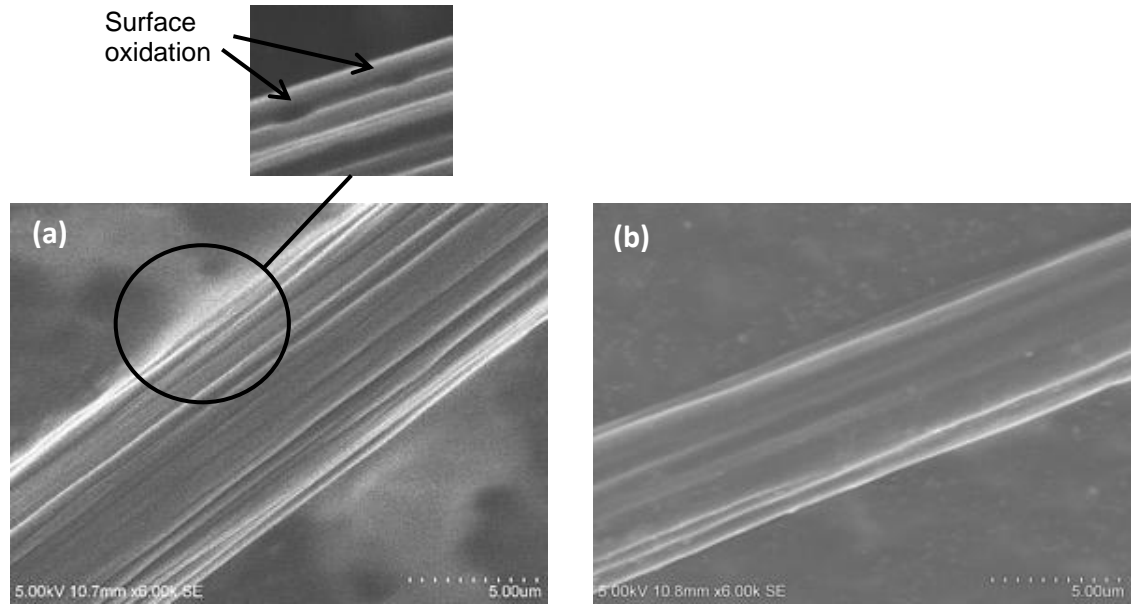


Figure 3.7. Carbon fibre held in air at (a) 500°C for 1h with magnified pits (b) 500°C for 2h.

Fibre diameters, after holding the fibre tow at 500°C for times up to 2h, are plotted in Figure 3.8. Over the first hour there is rapid oxidation where the fibre diameter decreased linearly with time. However, after 1h the reduction in fibre diameter slowed and was not directly proportional to time. This suggested that after an initial significant surface burn off, defects on the fibre surface led to the internal structure becoming exposed (an example is the grooves along the fibre in Figure 3.7(b)). Fibre diameters, after holding the fibre at 500°C for times up to 2h, are plotted in Figure 3.8. Over the first hour there is rapid oxidation where the fibre diameter decreased linearly with time. However, after 1h the reduction in fibre diameter slowed and was not directly proportional to time. This suggested that the fibre surface oxidised more readily than the interior carbon layers. Perhaps this is due to more impurities and voids located near the surface or a denser internal crystalline structure.

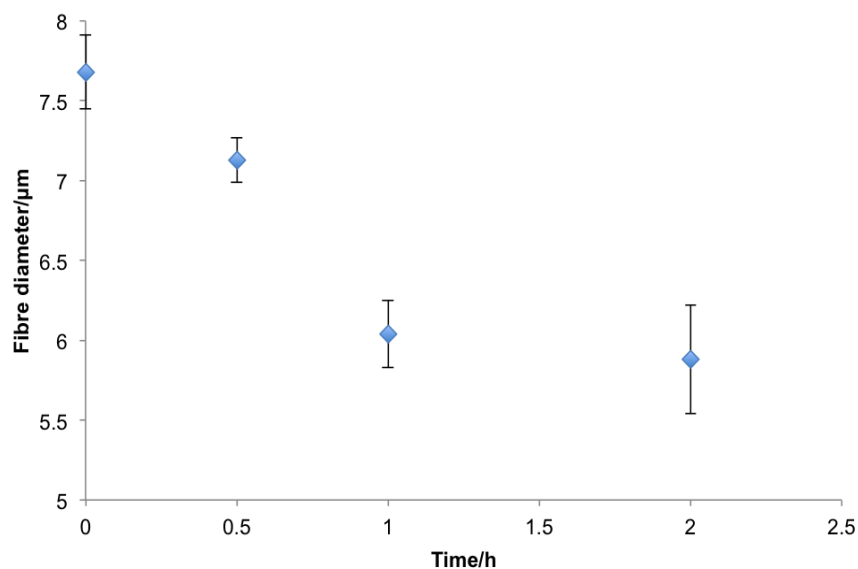


Figure 3.8. Graph of fibre diameter held at 500°C against time.

Subsequently, carbon fibre tows were also held for 30min at specific temperatures up to 700°C and their fibre diameters as a function of temperature are plotted in Figure 3.9. The relationship between fibre diameter and temperature appeared to be linear, with the measurement at 600°C a possible outlier. At the higher temperature of 700°C the fibre had left zero residue within 30min. At 450°C the diameter was within error that of the CF. As the temperature was increased and approached the TGA-derived, fibre oxidation start temperature (see Figure 3.4), the error also increased. The tow held at 650°C had oxidised into several fragments and fibre diameter was measured from the intact pieces.

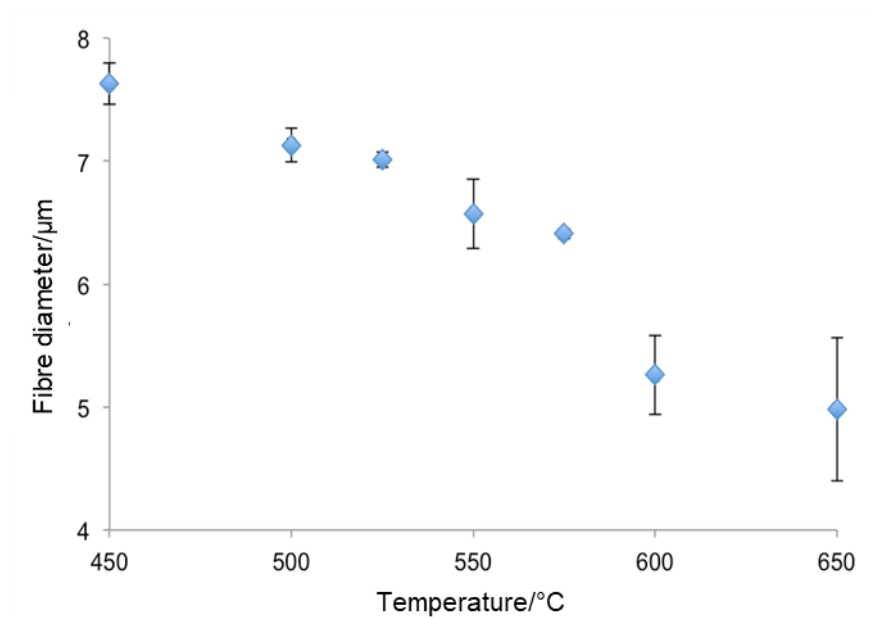


Figure 3.9. Graph of fibre diameter against temperature for fibres held for 30min.

Figure 3.10(a-d) shows SEM images of the surface morphologies of carbon fibres held at 500°C, 550°C, 600°C and 650°C for 30min in air at the same magnification. At 500°C the fibre surface is slightly rougher than the CF, due to the removal of the sizing. At 550°C and 600°C some of the striations remained but there was a more mottled and irregular surface texture, where the surface layer has been burnt off. The fibre diameter has also decreased and greater surface damage was observed. At 650°C there was further surface burn off and more irregular grooves along the fibre axis, as well as, significant reduction in fibre diameter, even causing the fibre to break into several fragments.

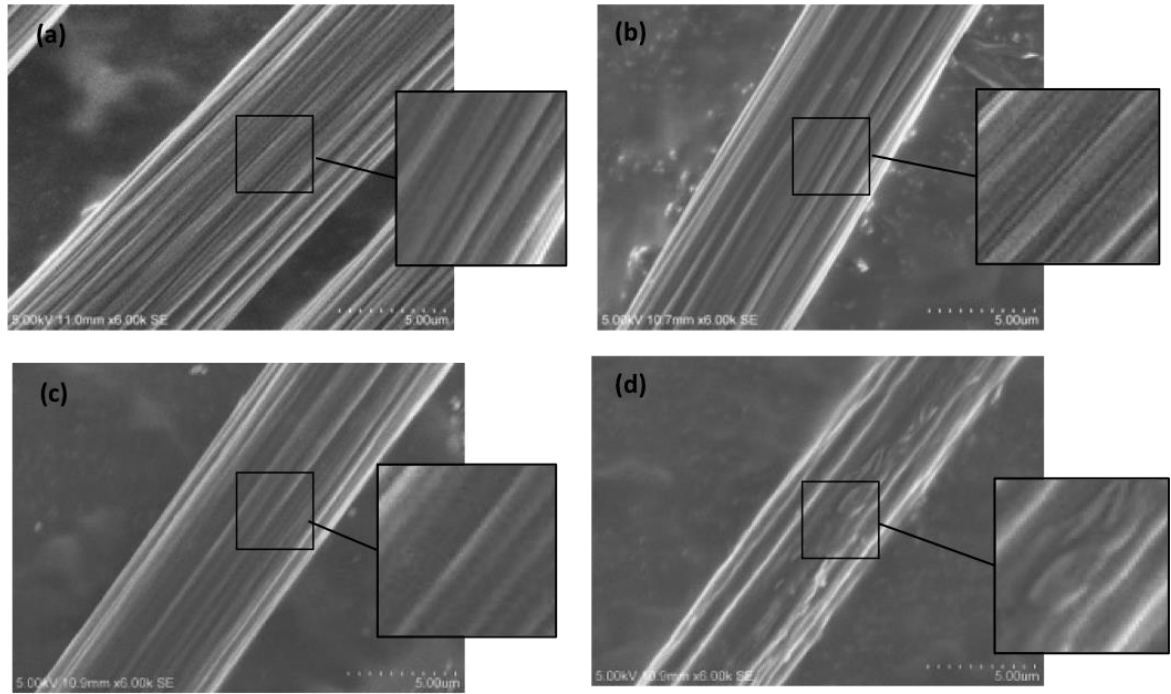


Figure 3.10. Carbon fibre held for 30min in the tube furnace in air at a) 500°C b) 550°C c) 600°C d) 650°C.

The intact tows from tube furnace experiments in air for 30min at 500°C, 525°C, 550°C, 575°C and 600°C were left to cool for 24h and single fibres removed to be measured for their electrical resistivity. Due to the amount of fibre breakage at 650°C, electrical resistivity could not be determined. The results are given in Table 3.2. The electrical resistivity for a fibre held at 500°C and 525°C was within error of the CF ( $2.08 \pm 0.13$ )  $\times 10^{-5} \Omega\text{m}$ . At 650°C, however, the fibre was too damaged to measure its resistivity.

Table 3.2. Electrical resistivity for fibres held for 30min.

Temperature, °C	Electrical resistivity, $\times 10^{-5} \Omega\text{m}$
CF	$2.08 \pm 0.13$
500	$1.66 \pm 0.38$
525	$1.82 \pm 0.34$
550	$2.35 \pm 0.22$
575	$5.38 \pm 0.16$
600	$16.31 \pm 0.71$



Figure 3.11 shows there was a linear relationship between the logarithm of the fibre resistivity and increasing temperature above 525°C. While at 500°C there was not enough oxidation of the fibre to significantly affect its electrical resistivity. Above 600°C, fibre oxidation left too little of the fibre to remain to perform single fibre electrical resistivity tests on and below 500°C there is no change in fibre resistivity.

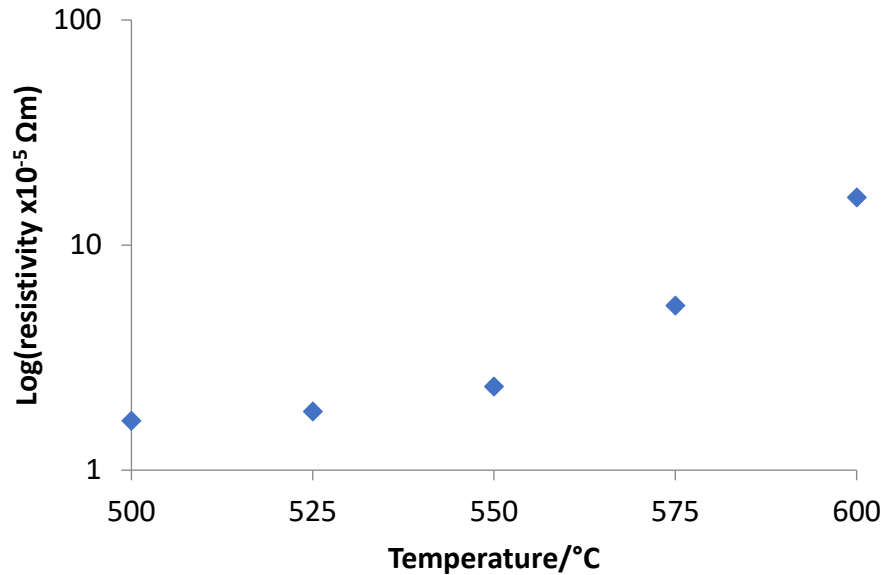


Figure 3.11. Log of resistivity against temperature.

Partially oxidised fibre resulting from heat testing at 600°C for 30min had increased electrical resistance by a factor of eight compared to the CF. However, on the scale of electrical resistance, this was almost a relatively negligible increase. For comparison, this fibre now had a resistance of  $10^{-4}$ , whereas glass is  $10^{12}\Omega\text{m}$ . However, oxidised fibres could still pose a threat to electrical circuits, especially as their diameter had reduced significantly from  $7.68 \pm 0.23\mu\text{m}$  to  $5.26 \pm 0.32\mu\text{m}$  with a percentage mass decrease of 33.8%, making the oxidised fibres smaller and lighter, and therefore easier to be aurally transported. The increase of fibre resistivity to  $(1.63 \pm 0.07) \times 10^{-4}\Omega\text{m}$  suggests that during oxidation at 600°C, some of the carbon fibre's original regular crystalline structure may have been lost in the areas where pitting was observed, and as further oxidation occurs at these sites, crystallinity in these areas is reduced.

Single fibre tensile tests (Section 2.5.4) were carried out. A selection of results for fibres tested in the tube furnace at different temperatures and times are given in Table 3.3.

Table 3.3. Tensile test results for CF after different heat treatments.

		Tensile strength, MPa	Tensile modulus, GPa
CF		$3877 \pm 136$	$237 \pm 4$
Temperature, °C	Time, min		
500	120	$1504 \pm 284$	$291 \pm 11$
550	60	$2180 \pm 130$	$147 \pm 9$

It was noted that the datasheet [10] of CF TR30S had the tensile strength as 4120 MPa. This is more than what was recorded in these tensile tests. However, the fibre diameter used here was that measured of  $7.68\mu\text{m}$  and not the  $7\mu\text{m}$  given in the data sheet.

The diameters of the fibres used in the tensile test calculations are given in Table 3.1. After 120min at  $500^\circ\text{C}$  the fibre had lost its sizing and had a significant amount of surface damage (Figure 3.10(b)), resulting in a 61.2% strength loss. The large error was expected due to the random locations of the stress concentrators, which had increased due to oxidation of the fibre. After 60min at  $550^\circ\text{C}$  the fibre experienced considerable oxidation and had a diameter within error of the other fibre (tested at  $500^\circ\text{C}$  for 120min). This fibre appears to have 56.2% of its residual tensile strength. However, its modulus had increased by 18.5%. For both tube furnace heat treatments, it was seen that fibre oxidation leads to a loss in tensile strength due to increased generation of flaws, increasing the chance of fibre breakage under a load.

### 3.4 Effect of heat/fire on carbon fibres exposed to radiant heat in air

The cone calorimeter was used to provide a constant controllable radiant heat flux. Instead of individual tows, as used in the tube furnace experiments, TR30S 2x2 twill weave fabric samples were exposed to the cone calorimeter. No load was applied to the fabric. The carbon fibre fabric was exposed from above to heat fluxes of  $50\text{kWm}^{-2}$  and  $75\text{kWm}^{-2}$  for 600s. At a heat flux of  $50\text{kWm}^{-2}$  a thermocouple on the surface of the carbon fibre recorded a temperature around

600°C. However, the fibre diameter remained within error of that measured for the CF and no reduction was seen. This indicated a heat flux of  $50\text{kWm}^{-2}$  over this time period was not high enough to cause noticeable fibre oxidation. While the fibres could have been exposed to the cone heater for longer than 600s, as there were no observable changes to the fibre, increasing the heat flux would be more effective than increasing the time held at  $50\text{kWm}^{-2}$ .

The experiment was repeated with the same setup as before but at  $75\text{kWm}^{-2}$  for 600s. A thermocouple on the surface of the carbon fibre recorded a temperature around 680°C. The mass of the fibre decreased by 57.2%. Using the density of the CF fibre of  $1.78\text{ g/cm}^3$ , and the mean fibres diameters in Table 3.4, if only surface oxidation occurred then the change in mass loss should have been 32.2%. This greater mass loss indicated that not only has surface oxidation occurred, but also diffusion of gases from oxidation within the fibre. No micro-cracks on the fibre surface were observed during microstructural analysis, but there was a loss of surface texture (Figure 3.12). Potentially nano sized pores already existing within the fibre had opened to allow diffusion of gases from inside the fibre.

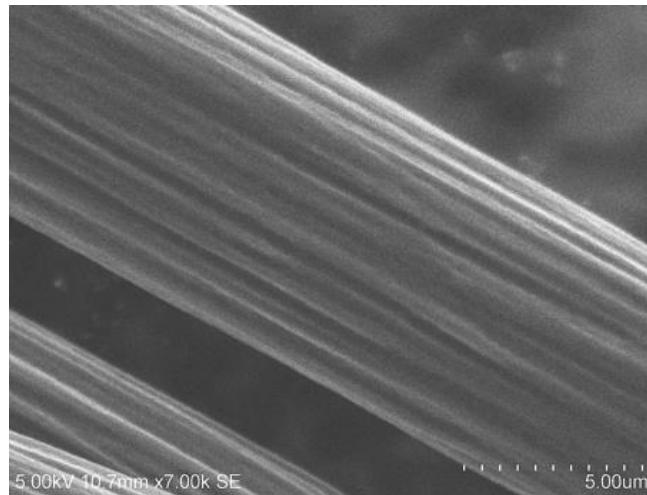


Figure 3.12. CF after cone testing at  $75\text{kWm}^{-2}$  for 600s.

The electrical resistivity of the fibre after exposure to the cone heater for 600s at  $50\text{kWm}^{-2}$  was  $(1.94 \pm 0.07) \times 10^{-5}\Omega\text{m}$ . This was within error of the electrical resistivity of the CF  $(2.08 \pm 0.13) \times 10^{-5}\Omega\text{m}$ . This, combined with no observed reduction in fibre diameter, confirmed that exposure

to a heat flux of  $50\text{kWm}^{-2}$  (over a period of 600s) was not great enough to cause significant carbon fibre oxidation.

At a heat flux of  $75\text{kWm}^{-2}$  the fibre resistivity increased to  $(5.12 \pm 0.12) \times 10^{-5}\Omega\text{m}$ , indicating that there was damage within the fibre, impeding the flow of electrons. However, the damaged fibre's resistivity was the same magnitude as before ( $10^{-5}$ ) and as discussed previously for in the tube furnace heat experiments, this still falls within the electrical resistivity generally found for carbon (graphite). Comparing results from exposing the carbon fibres to high heat flux (irradiance) in one direction via the cone calorimeter and fibres subjected to constant heat (TGA and tube furnace), showed interesting results. The same carbon fibre diameter reduction and a similar decrease in electrical conductivity was measured for carbon fibre tows placed in a tube furnace at  $500^{\circ}\text{C}$  for 2h. However, after 600s under the cone heater at  $75\text{kWm}^{-2}$ , the carbon fibre fabric lost 57.2% of its mass, while after 2h at  $500^{\circ}\text{C}$ , only 27.4% mass was lost. There was also significantly less surface damage on the carbon fibres tested under the cone heater (Figure 3.12) compared to that in the tube furnace (Figure 3.7(b)). This is summarised in Table 3.4.

Table 3.4. Summary of results for CF test under the cone and tube furnace.

		Mass loss %	Fibre diameter/ $\mu\text{m}$	Electrical resistivity/ $\Omega\text{m}$ $\times 10^{-5}$
CF		N/A	$7.68 \pm 0.23$	$2.08 \pm 0.13$
Heat flux, $\text{kWm}^{-2}$ 600s (10min)	50	1.3	$7.60 \pm 0.17$	$1.94 \pm 0.07$
	75	57.2	$5.88 \pm 0.43$	$5.12 \pm 0.12$
Tube furnace at $500^{\circ}\text{C}$ for 2h (120min)		27.4	$5.88 \pm 0.34$	$6.83 \pm 0.30$

Short-term exposure to high heat flux has resulted in greater carbon fibre mass loss, compared to longer exposure at lower temperatures. The cone element heater was  $863 \pm 1^{\circ}\text{C}$  throughout the experiment. It was seen in previous TGA/DTG experiments (Figure 3.4), under the

conditions used, the maximum rate of change of mass loss occurred at 782°C. The results from the cone calorimeter experiment further confirmed that there is a change in the carbon fibre oxidation mechanism from predominantly being a surface reaction to one above 750°C controlled by diffusion of gases (CO and CO<sub>2</sub>) through pores and defects in the fibre. This could explain the reduced surface damage seen in Figure 3.12 while a greater mass loss was recorded.

### 3.5 Effect of flames on carbon fibres exposed to premixed propane/air flames

Using a propane burner, the effects of extremely high heat flux (116kWm<sup>-2</sup>) and direct contact with a pre-mixed flame were studied. The set-up for this burner test is given in Section 2.4.4. Initially the carbon fibre fabric was exposed to the propane flame for 1min. The flame was directed at thermocouple T1 (see Figure 2.7(a), Section 2.4.4), which recorded the highest temperature (995°C) and had the greatest reduction in carbon fibre diameter by 0.87µm. The fibres on the periphery of the flame (T2 and T3) also showed reductions in fibre diameter. Fibres removed from the three sections showed the same smooth surface texture. However, fibres taken from T1 area also showed signs of pitting (Figure 3.13). These pits measured as around 0.3µm in diameter. EDX was used to identify if any of the contaminant particle remained but only carbon was detected so most likely any such particles were vaporised by the propane flame. A high magnification image of the pits is also given in Figure 3.13 along with the EDX results.

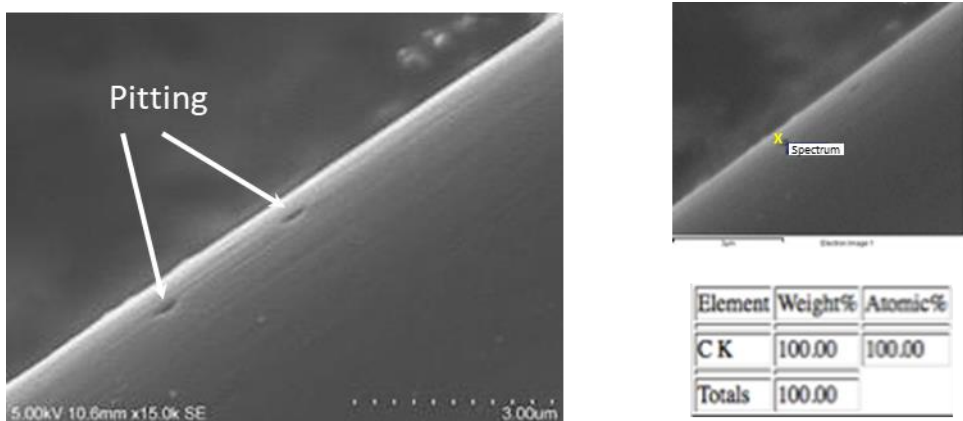


Figure 3.13. Carbon fibre after exposure to the propane burner for 1min and related EDX results.

The exposure time was then increased to 3min and again fibres in direct contact with the propane flame (T1) had the same smooth surface texture as that seen on the fibres exposed for 1min. Fibres removed from section T3, furthest from the flame, had a greater mean diameter than those exposed for 1min. SEM images also showed surface striations were still visible on the fibres removed from T2 and T3.

Fibres removed after 5min showed even greater fibre diameter loss compared to those from 3min exposure and fibres from the T1 zone had the greatest diameter reduction. Furthermore, large areas of surface oxidation were observed, far greater than the pits seen after 1min. This was attributed again to the flame reacting with contaminant particles present and leading to greater fibre oxidation in these areas. This effect was also seen after 10min, where fibres from T2 and T3 zones again showed smooth surface texture but with those at T1 experiencing a larger reduction in diameter and significant surface damage. Average temperatures recorded by the thermocouples and fibre diameters are given in Table 3.5. SEM images of fibres are given in Figure 3.14.

Table 3.5. Average temperature recorded by the thermocouples and fibre diameters.

		Mean fibre diameter/ $\mu\text{m}$
Control Fibre		$7.68 \pm 0.23$
Thermocouple zones	Average temperature recorded by thermocouple/ $^{\circ}\text{C}$	
1min		
T1	995	$6.81 \pm 0.08$
T2	861	$6.96 \pm 0.07$
T3	762	$6.88 \pm 0.07$
3min		
T1	973	$6.99 \pm 0.07$
T2	880	$6.97 \pm 0.08$
T3	787	$7.20 \pm 0.05$
5min		
T1	963	$6.79 \pm 0.05$
T2	811	$6.90 \pm 0.05$
T3	770	$7.01 \pm 0.06$
10min		
T1	959	$5.10 \pm 0.20$
T2	833	$7.17 \pm 0.06$
T3	771	$7.10 \pm 0.04$

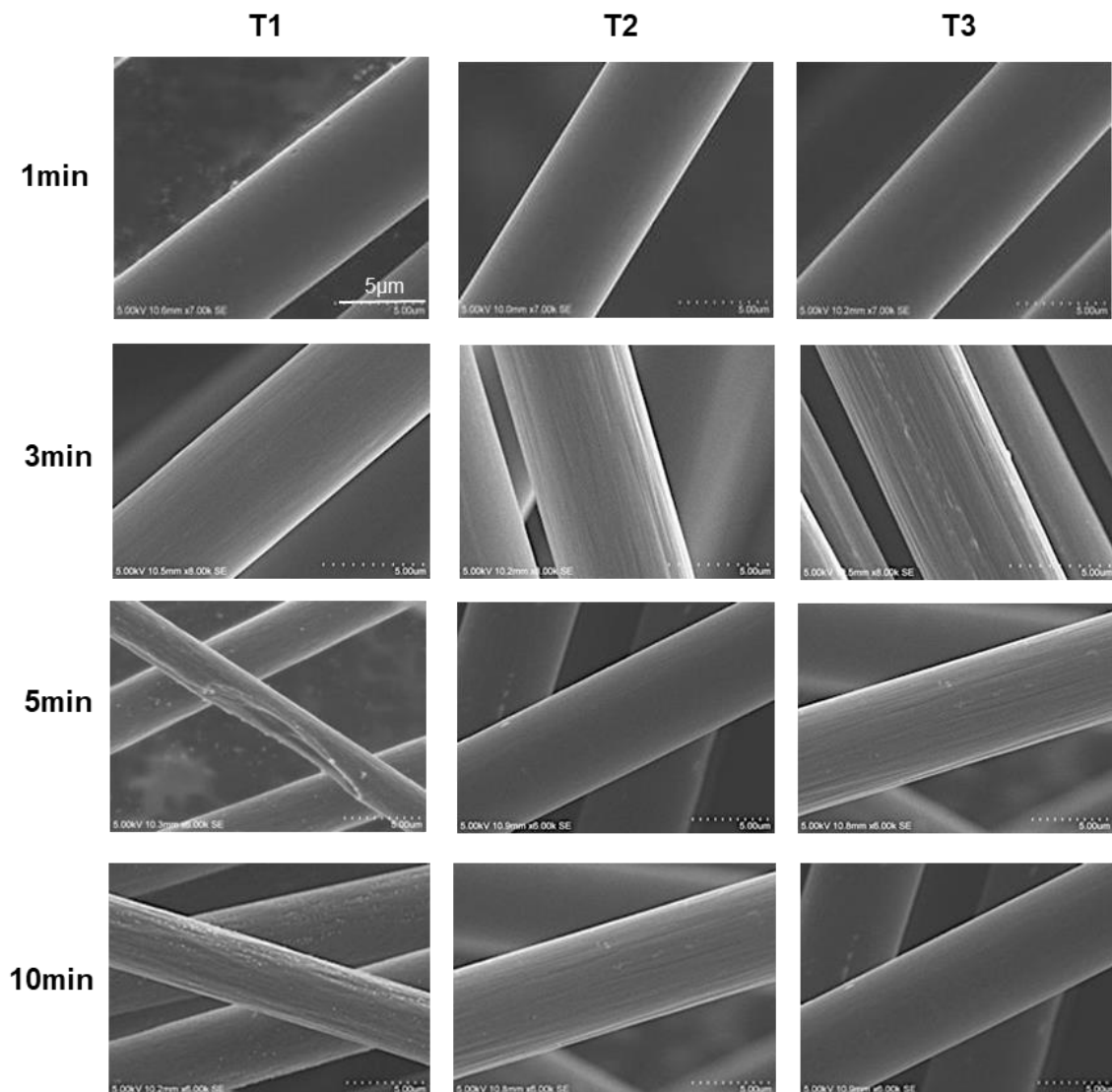


Figure 3.14. Carbon fibres after exposure of fabrics to the propane burner for 1, 3, 5 and 10min.

While there was typically only around 100°C difference recorded by the thermocouples between each zone (T1, T2, T3), these temperatures are in the critical oxidation region for this carbon fibre (TGA results in Figure 3.4 showed the greatest rate of oxidation occurred from temperatures between 700°C to 850°C). Over a period of 10min, this effect was seen to be the greatest with the fibre exposed to an average temperature of 959°C resulting in the highest amount of surface oxidation and damage.



### 3.6 Comparison with other PAN-based carbon fibres

To gain further understanding on the effects of heat on PAN-based carbon fibres, results of CF TR30S were compared to similar modulus fibres T300, a higher modulus fibre T800HB and AS4, which is a raw fibre without sizing. These are shown in Figure 3.15.

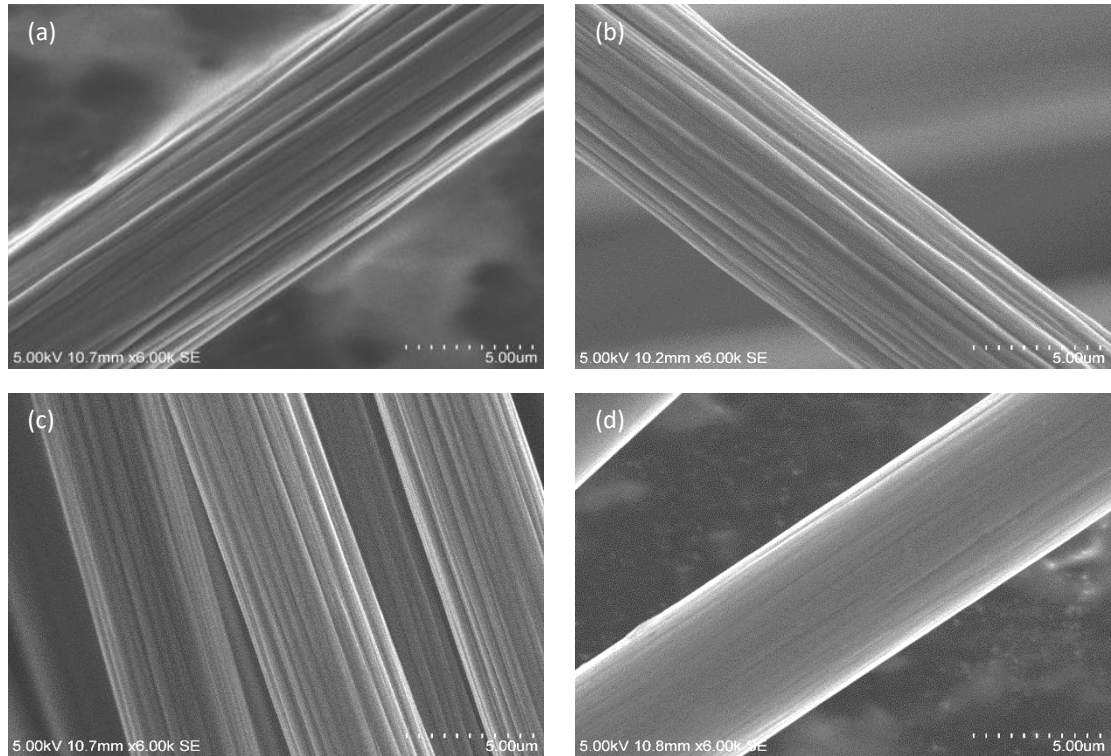


Figure 3.15. SEM images of various PAN-based carbon fibres (a) TR30S (b) T300 (c) T800HB (d) AS4.

The fibres were characterised using TGA. These are shown in Figure 3.16.

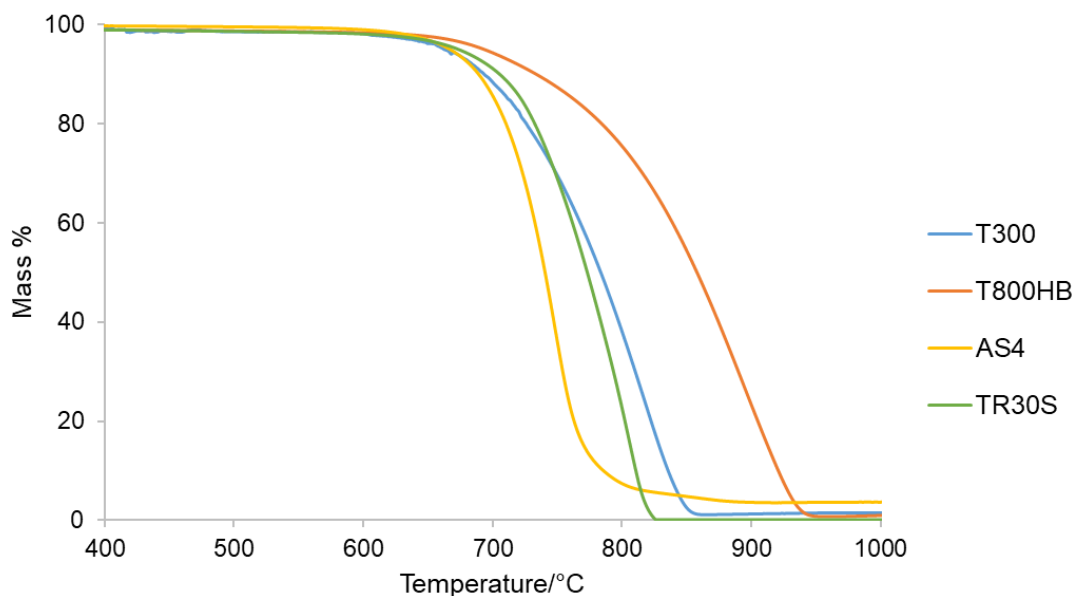


Figure 3.16. TGA curves for four different PAN-based fibres in air.

While all carbon fibres began to oxidise at around the same temperature (500°C to 600°C), the rate at which they oxidised varied. T800HB showed the greatest oxidation resistance while TR30S and T300 showed very similar mass loss curves. AS4 oxidised fastest, given that it had a slightly higher carbon content and a similar modulus to T300, it would be expected to fit the same mass loss curve as TR30S and T300. However, without a polymer sizing present it had less protection to the environment and perhaps over time had reacted with oxygen in the air, which might have sensitised it to further oxidation.

There are limited studies in the literature which compare TGA results of standard to intermediate or high modulus PAN-based fibres. Zhang et al [9] and Govorov et al [11] took standard modulus carbon fibres (Zhang et al, unknown manufacturer, Govorov et al, ZOLTEK PX35) and heat-treated them in a vacuum to 2600°C and 2800°C respectively, to increase the respective fibre moduli. Both found that the higher modulus fibre had less mass loss than the original fibre at the same temperature. Zhang et al attributed this to the amounts of metal (potassium and sodium) within the fibre, where due to heat treatments the high modulus fibre had a lower percentage of sodium present. However, Govorov et al [11] credited this to the crystalline structure of the fibre as the heat treatment had reduced fibre porosity and increased the degree

of graphitisation. Hence, they conclude that a reduction in lattice defects and disruptions in the fibre's uniform structure were the reason, rather than sodium ions.

In this study the oxidation resistance of intermediate modulus T800HB was further confirmed by carrying out isothermal TGA in air (flow rate 50ml/min). The fibres were heated from 23°C to 700°C, at a heating rate of 200°C/min, and then held at 700°C for 1h. The results are presented in Figure 3.17.

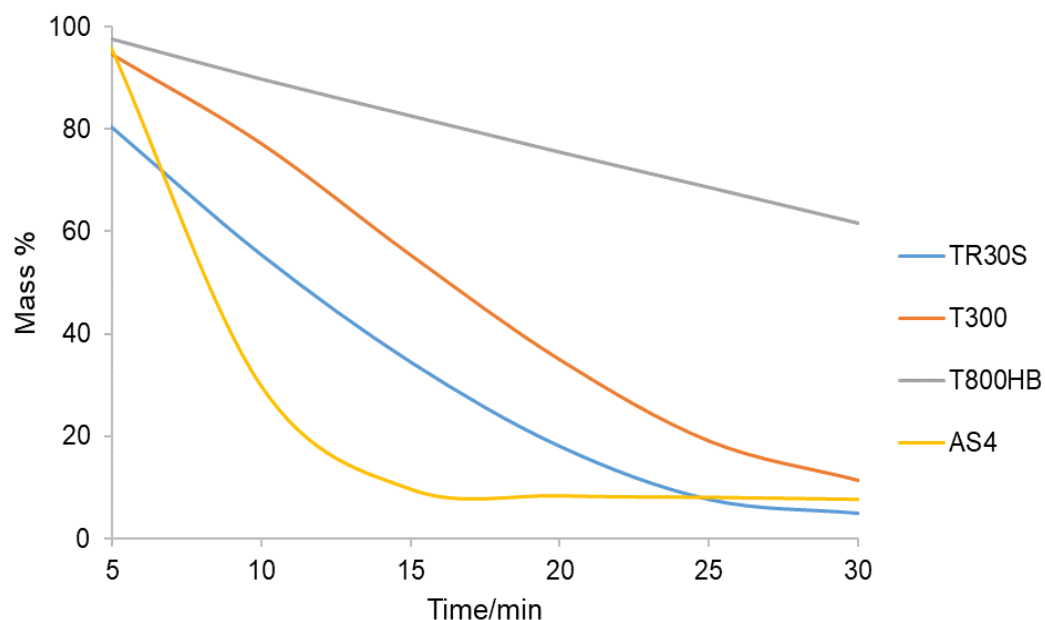


Figure 3.17. Isothermal TGA results for holding each fibre at 700°C in air.

The TR30S and T300 fibres again followed the same trend, with the percentage mass of the fibres decreasing linearly with time for the first 20min. As seen in the dynamic TGA curves in Figure 3.16, TR30S began to oxidise at a slightly lower temperature than the other fibres, but followed the same rate of oxidation as T300. The AS4 fibre was the least resistant to oxidation with a rapid mass loss after 10min, while the most resistant to oxidation was the T800HB with 61.5 wt% still remaining after 30min, as opposed to TR30S which had only 5wt% left.

To test larger samples, fibre tows of 7cm in length were placed in ceramic boats and placed in a tube furnace for varying times in static air, and weighed before and after exposure. After 500°C

for 0.5h, only a small amount of mass loss was recorded for all fibres. This mass loss also included that fraction from the sizing applied to the fibres (except for AS4). At 600°C for 0.5h T800HB showed little mass loss, this was expected due to its higher oxidation resistance seen from TGA results. At temperatures below 700°C AS4 displayed a higher oxidation resistance than TR30S and T300. The results are listed in Table 3.6.

Table 3.6. Results of Tube Furnace experiments on different PAN-based fibres.

Temperature/°C	Time/hr	Fibre type			
		TR30S	T300	T800HB	AS4
		% mass loss			
500	0.5	4.32	1.29	2.03	1.75
500	1	14.20	5.16	2.54	3.38
500	2	20.37	12.26	6.06	8.85
550	0.5	7.32	9.87	7.74	10.56
550	1	18.29	25.00	13.69	14.40
600	0.5	33.83	44.59	9.20	19.75

The results showed that different grades of PAN-based fibres have different oxidation properties. T800HB with the highest modulus and smallest fibre diameter, has superior oxidation resistant properties, which was attributed to its higher carbon content (>96%) and its increased crystalline graphic structure.

At temperatures below 700°C AS4 fibre showed a greater oxidation resistance compared to TR30S and T300 but above 700°C it oxidised faster than the other fibres. From the manufacturers' data sheets [10,12] fibres T300 and TR30S should have shown almost identical oxidation properties. They have similar fibre diameters and appeared to be identical as SEM images (Figure 3.15). While they do not have the same modulus (T300 – 230GPa and TR30S – 235GPa) they are both considered to be standard modulus fibres. Yet T300 showed slightly better oxidation resistance above 780°C, which was surprising as TR30S had the higher modulus.

T800HB fibres were analysed by SEM after exposing in the tube furnace for 1h at 550°C and 2h at 500°C, as shown respectively in Figures 3.18(a-b)

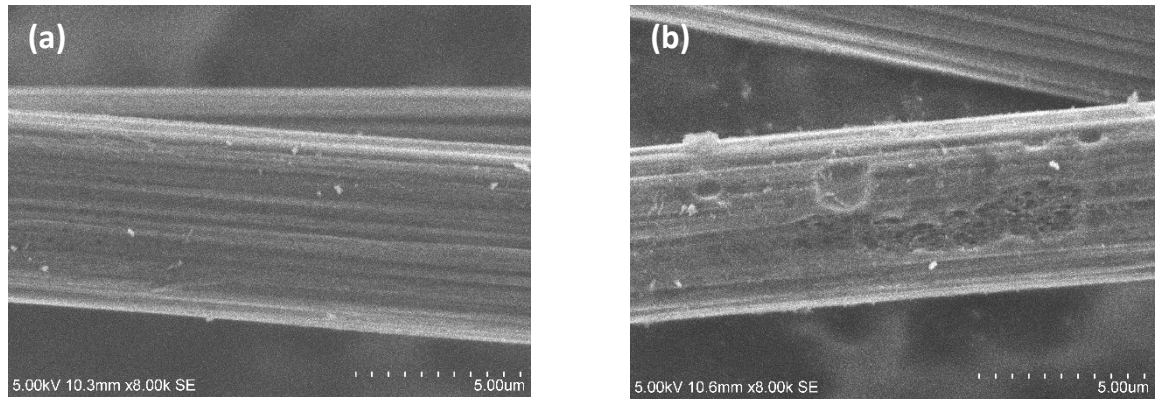


Figure 3.18. T800HB fibre after (a) 2h at 500°C (b) 1h at 550°C in air.

Significant surface burn-off and damage were observed for TR30S fibres also held at the temperatures for the same time period. However, on the T800HB fibres, the striations along the fibre had not been lost, and instead the surface damage was very localised with obvious signs of pitting (Figure 3.18(b)).

### 3.7 Conclusions

In this project TR30S was characterised and studied under a range of heat and fire conditions. Major conclusions drawn are:

- Exposing carbon fibre to high temperatures in a nitrogen atmosphere did not reduce fibre diameter but did remove the polymer sizing (above 450°C).
- TGA results showed that fibre oxidation began at 550°C with rapid oxidation between 700 and 850°C. Above 850°C the fibre was fully oxidised.
- Below an exposure time of 1h, carbon fibre diameter was found to be directly proportional to temperature.

- Electrical resistivity did not increase greatly with heat exposure and still remained within that of expected for carbon.
- Exposing carbon fibre to a heat flux in a cone calorimeter of  $50\text{kWm}^{-2}$  for 600s caused no significant fibre oxidation or change in electrical resistivity.
- At  $75\text{kWm}^{-2}$  heat flux for 600s, there was significant carbon fibre oxidation with the dominant mechanism suggested to be determined by the rate of diffusion of gases through pores and micro-structural defects.
- When exposed to higher heat flux of  $116\text{kWm}^{-2}$  and a direct flame, vaporisation of possible contaminant particles present created sites for localised oxidation.
- On comparing the oxidation behaviour of TR30S to carbon fibres with different modulus, the higher modulus carbon fibre (T800HB) was more oxidation resistant. This was attributed to its higher carbon content ( $>96\%$ ) and increased crystalline graphitic structure.

### 3.8 References

- [1] Feih, S. and Mouritz A. P., Tensile properties of carbon fibres and carbon fibre–polymer composites in fire, *Composites Part A Applied Science and Manufacturing* 43(5) 7, (2012).
- [2] Reynolds, W. N and Moreton, R., Some Factors Affecting the Strengths of Carbon Fibres [and Discussion], *Philosophical Transactions of the Royal Society of London. Series A, Mathematical and Physical Sciences*, vol. 294, no. 1411, pp. 451–461. (1980).
- [3] Li, B., Zhang, C., Cao, F., Wang, S., Cao, Y., Chen, B., Surface Oxidation of Carbon Fiber and its Influence on the Properties of Carbon Fiber Reinforced BN-Si<sub>3</sub>N<sub>4</sub> Composites, *Key Engineering Materials Vols*, 368-372 pp 901-904, (2008).
- [4] Rossberg M. Z. *Elektrochem.*, 60, 952, (1956)
- [5] Yin, Y., Binner, J. G. P., Binner, Cross, T.E., Marshall, S. J., The oxidation behaviour of carbon fibres, *Journal of Materials Science*, 29, 2250-2254, (1994).
- [6] Perret, R and Ruland, W., The Microstructure of PAN-Base Carbon Fibres, *J. Appl. Cryst*, 3, 525, (1970).
- [7] Morgan, P , *Carbon Fibers and Their Composites*, CRC Press, p828, (2005).
- [8] Gourdin, C., Ageing of carbon fibres of various origins, *SAMPE*, Bourdeaux, 49-61, Pct 17-20, (1983).
- [9] Zhang, X., Shen, Z., Tian, Y., Zhang, X., Zhang, W., Yang, Y., Zhang, X., Chen, H., Oxidation properties of high modulus carbon fiber, (2004)
- [10] Mitsubishi Pyrofil datasheet, accessible here: [https://www.m-chemical.co.jp/en/products/departments/mcc/cfcm/product/\\_icsFiles/afieldfile/2020/01/15/Cftow\\_Jan2020en.pdf](https://www.m-chemical.co.jp/en/products/departments/mcc/cfcm/product/_icsFiles/afieldfile/2020/01/15/Cftow_Jan2020en.pdf)
- [11] Govorov, A. V., Galiguzov, A. A., Tikhonov, N. A., Malakho, A. P., & Rogozin, A. D. Study of Different Types of Carbon Fiber Oxidation Kinetics. *Refractories and Industrial Ceramics*, 56(6), 605–609, (2016)
- [12] Toray T300 Standard Modulus Carbon Fibre data sheet, accessible here: <https://www.toraycma.com/page.php>

## **Chapter 4: Effects of heat and fire on carbon fibre properties in fire retarded carbon fibre-reinforced composites**

### **4.1 Introduction**

In Chapter 3 carbon fibres were subjected to a range of heat and fire conditions, and the resulting fibres analysed in terms of reduction in fibre diameter, surface damage and electrical and tensile properties. In this chapter the control carbon fibre-reinforced composites (defined from here onwards as the CCs) have been exposed to a range of heat and fire conditions and the properties of carbon fibres retrieved from different plies of the heat/fire damaged CCs have been assessed. The effect of flame retardants and nano-additives in CCs on the carbon fibre properties and how they act to reduce these hazards, have also been discussed.

The CC's resin was modified with different flame retardant additives in order to reduce flammability of the resin. The flame retardant additives were also expected to:

- Increase cross-linking during resin decomposition.
- Promote the formation of char.
- Increase char adherence to carbon fibres.
- Reduce carbon fibre exposure by encapsulating within char.

Phosphorus-containing flame retardants were selected as they have been shown to be effective in epoxy resins [1-3]. During the decomposition process, the high concentration of -OH groups in the epoxy can react with the phosphorus-containing products from flame retardants and undergo charring as opposed to producing combustible volatiles.

The following flame retardants were added to the resin:

- 15wt% Ammonium polyphosphate, APP (Antiblaze MC, Rhodia)
- 15wt% Resorcinol bis-(diphenyl phosphate), RDP (Chemtura)
- 15wt% 9,10-Dihydro-9-oxa-10-phosphaphenanthrene 10-oxide, DOPO (EMPA)



The following composites were made by resin infusion and given from another DSTL project [4]:

- 5wt% Nano clay, octadecyl ammonium ion-modified montmorillonite clay, Nanomer I.30E (Nanocor Inc. China))
- 5wt% Layered double hydroxide, LDH (Prolabin-Tefarm, Perugia, Italy)

By recovering fibres from different layers within the composite the effects of heat and fire on carbon fibres throughout the thickness of the composites were examined. This meant barrier effects of above layers, such as physical shielding or the impedance of oxygen flow to underneath layers, could be studied. During cone calorimetry and propane burner tests, the carbon fibres on the top surface were in direct contact with the flame and oxygen-rich air, hence were affected most. Whereas those underneath were contained in an atmosphere with restricted oxygen flow and volatiles produced by the decomposing resin. As a result, the fibres' physical and electrical properties were affected to a different extent through the thickness of the sample.

#### **4.2 Thermal stability of CC and components in air and nitrogen atmospheres**

Thermogravimetric analyses (TGA) of CC and its components (carbon fibre and resin) were carried out to understand the thermal stability of CC and its components in air and nitrogen. CC consisted of 8 plies with 34.5wt% epoxy resin and 65.5wt% carbon fibre. An 8mg piece of cured resin was also subjected to thermal analysis. The TGA of carbon fibres in nitrogen and air has already been discussed in detail in Chapter 3.

The TGA curves of epoxy resin, with the first derivatives of the mass loss with respect to temperature (DTG) overlaid, in air and nitrogen atmospheres are given in Figure 4.1. In nitrogen the epoxy resin lost only 1.8% mass up until 300°C, after which it underwent rapid mass loss until it was fully decomposed at 544°C with 14.5% residue mass remaining. In air, mass loss began at lower temperatures than in nitrogen but rapid degradation did not occur until after 300°C. However, in air there were two stages of decomposition (mass loss). The DTG (overlaid on the TGA in Figure 4.1) showed a peak at 367°C, corresponding to the first stage of stable carbonaceous residue (char) production. The second stage began at 492°C and occurred due to

oxidation of the char residue, with a maximum peak at 570°C. After 668°C only 2.9% residual mass remained.

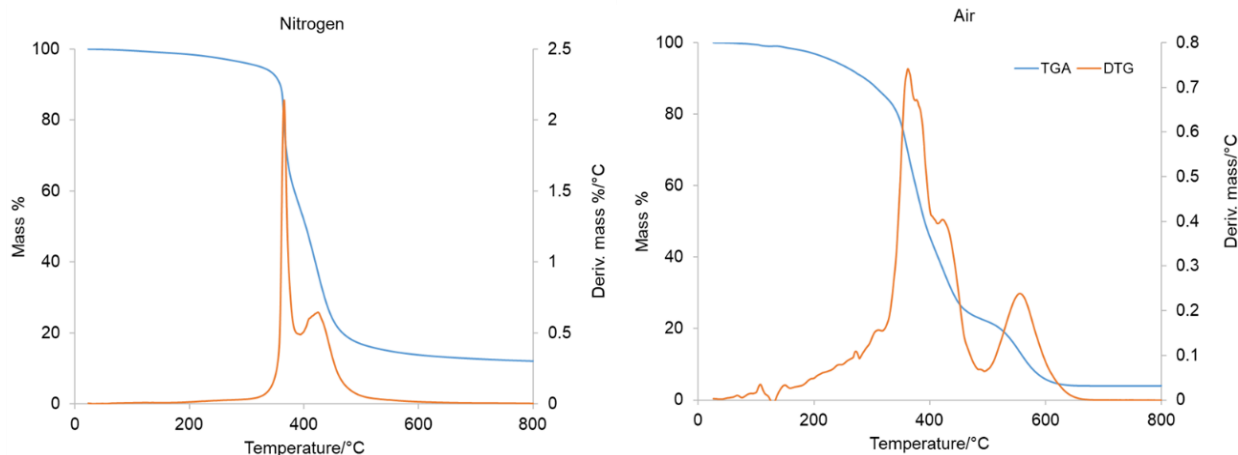


Figure 4.1. TGA and DTG graphs of epoxy resin in nitrogen and air.

Mass loss graphs of carbon fibre (TR30S), epoxy resin, CC, and the calculated curve for epoxy resin and carbon fibre mixture in the percentages 34.5wt% and 65.5wt% (as were present in the CC), are plotted in Figure 4.2 and important parameters derived from these TGA curves are given in Table 4.1. The curves for CC and that calculated from the weighted percentages of resin and fibre within the CC are in good agreement with each other, indicating that both components decomposed independently.

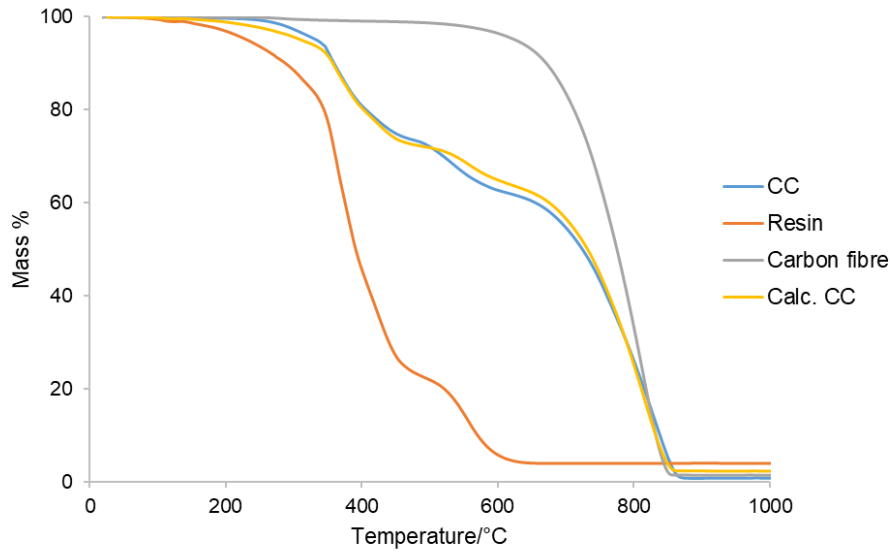


Figure 4.2. TGA of resin, carbon fibres, CC and the calculated curve (Calc.CC) in air atmosphere.

Table 4.1. TGA data for samples shown in Figure 4.3 in air, as well as in nitrogen.

Atmosphere	Sample	T <sub>Onset</sub> , °C	T <sub>Max</sub> , °C	Mass remaining at 900°C, wt%
Air	Resin	232	658	2.9
	CC	334	895	0.8
	Carbon fibre	538	812	1.9
Nitrogen	Resin	324	544	14.5
	CC	316	558	50.6
	Carbon fibre	N/A	567	98.7

Note: T<sub>Onset</sub> = Temperature at which 5% mass loss occurs; T<sub>Max</sub> = Temperature at which all the mass has been lost and the residual mass is uniform

These results indicated that at and above 300°C the resin begins to degrade, and within a composite the coherence will be affected as the carbon fibres become exposed to the volatiles emitted from the resin. This is up until 544°C in nitrogen or 658°C in air, when the resin is completely oxidised and the carbon fibres are fully exposed. However, even though CC is thermally thin, there is still a temperature gradient, so this information cannot be directly related

to CC's behaviour in a fire. Furthermore, in a fire the atmosphere becomes vitiated and then after the fire it is an air atmosphere. Hence, fire testing is needed.

#### **4.3 Effect of heat/fire on properties of CC and carbon fibre within CC**

##### **4.3.1 CCs exposed to radiant heat and the effects on carbon fibres: Cone calorimetric experiments (fluxes of 35, 50, 60 and 75kWm<sup>-2</sup>)**

To examine the effect of irradiance on CCs, a cone calorimeter was used without spark ignition. The radiant heat was applied to one side of the 2.8mm thick 8-ply CC laminate samples. No load was applied and the cone's conical radiative heater was used to provide a constant heat flux.

For epoxy composites, Mouritz [5] reported the minimum heat flux required in a standard cone test (with spark ignition) for onset of combustion as  $\sim 13\text{kWm}^{-2}$ , whereas autoignition occurs at  $\sim 31.5\text{kWm}^{-2}$  [6]. Low incident heat fluxes, over the range 20 to  $50\text{kWm}^{-2}$  represent the initial development stages of a fire.  $35\text{kWm}^{-2}$  is used in the Federal Aviation Administration (FAA) regulations for the Ohio State University (OSU) calorimeter [7]. Fully developed fire results in heat fluxes  $>40\text{kWm}^{-2}$ , here the heat release rate and temperature of a fire is at a maximum.  $50\text{kWm}^{-2}$  is a room fire [5]. Heat fluxes above  $75\text{kWm}^{-2}$  represent fuel-related fires. Above  $100\text{kWm}^{-2}$  are post-flashover fires and those approaching that of a typical jet fuel fire [5], to simulate this condition a propane burner set-up has been used [8]. Using the relationship between type and stage of fire, and irradiance, the following heat fluxes were selected for the cone tests: 35, 50, 60 and  $75\text{kWm}^{-2}$ .

Rectangular samples of 25mm x 100mm were cut from the same CC. These sample sizes were used instead of the standard 100mm x 100mm as the intention was to not do the full cone calorimeter tests but to see the effects of heat on the carbon fibre. All composites auto-ignited. In order to see if spark ignition made any difference to the results, the experiment at  $75\text{kWm}^{-2}$  was repeated with spark ignition.

As well as measuring the incident heat flux, the temperature on the top surface of the composite (pre-ignition) was recorded using a thermocouple (Section 2.4.3). The results for time-to-ignition (TTI), flame-out time and residual mass are given in Table 4.2. After flame-out the surface fibres of CC were exposed to the radiant heat for the remainder of the test, keeping total exposure time from the beginning to the end as 600s, during which further fibre oxidation could occur. The TTI value of the CC tested with spark ignition and that without, were very similar, showing that self-ignition of CC at these high heat fluxes is just as dangerous as if there was an ignition source around. In order to calculate the carbon fibre percentage oxidised, it was assumed that all the resin had burnt before fibre oxidation.

Table 4.2. Results for CC tested for 600s and varying heat fluxes.

Heat flux/ $\text{kWm}^{-2}$	Approximate surface temperature, $^{\circ}\text{C}$	Time-to- ignition (TTI), s	Flame-out time, s	Residual mass, wt%	% of carbon fibre oxidised**
35	470	72	131	61.5	-
50	610	38	85	52.4	20.0
60	650	30	76	37.4	43.1
75	680	20	71	38.5	41.2
75*	680	23	91	39.9	39.1

Notes:\* = experiment with spark ignition;

\*\*Carbon fibre oxidised wt% =  $100 - (\text{residual mass} - \text{original resin})\text{wt}\%$

and % of carbon fibre oxidised =  $\frac{\text{Carbon fibre oxidised}}{\text{Original carbon fibre}}\text{wt}\%$

At over  $50\text{kWm}^{-2}$  carbon fibre oxidation occurred in all composites. Carbon fibre oxidation was similar for both spark and non-spark ignition at  $75\text{kWm}^{-2}$ .

Fibres were taken from different plies in CC, where ply 1 (P1) is on the surface exposed to the radiant heat and ply 8 (P8) is on the underneath surface. A schematic is in Figure 4.3.

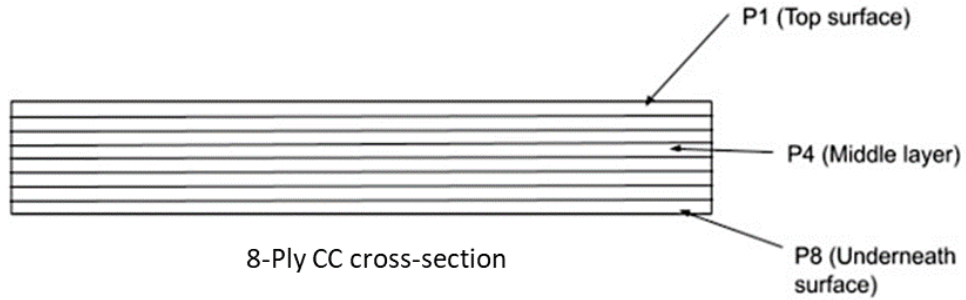


Figure 4.3. Schematic of CC cross-section with plies labelled.

Cross-sections of both CC tested at  $35\text{kWm}^{-2}$  and  $50\text{kWm}^{-2}$  appeared to be similar apart from plies P7 and P8. At  $35\text{kWm}^{-2}$  they were bonded to each other and more structurally intact, whereas at  $50\text{kWm}^{-2}$  all structural integrity provided by the resin had been lost and the plies had separated. Digital images of CC taken at the same magnification are given in Figure 4.4.

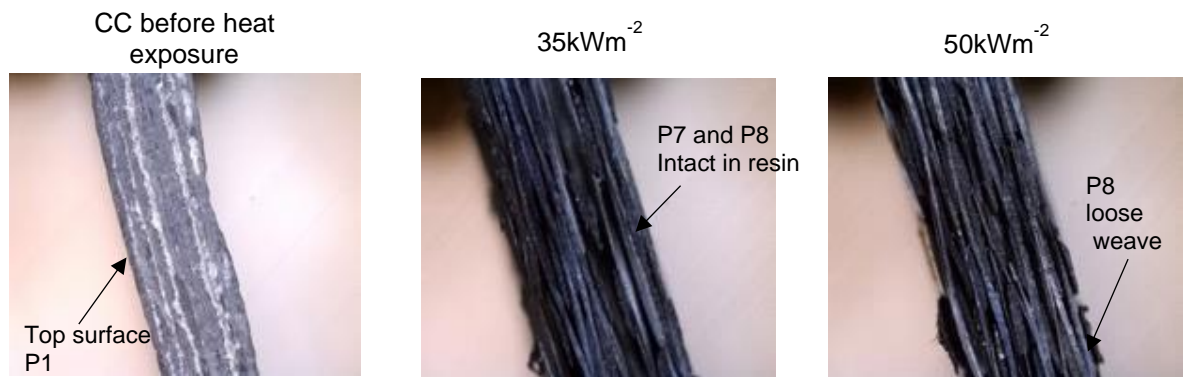


Figure 4.4. Digital images of cross-sections of CC tested at  $35\text{kWm}^{-2}$  and  $50\text{kWm}^{-2}$ .

During the cone calorimeter test at  $60\text{kWm}^{-2}$  and  $75\text{kWm}^{-2}$ , after flame-out, “glowing” of the carbon fibre was observed. This was not seen at  $35\text{kWm}^{-2}$  and  $50\text{kWm}^{-2}$ . These small areas of glow are labelled in Figure 4.5, which shows a digital photo of the CC under the cone calorimetric exposure at  $60\text{kWm}^{-2}$ . In previous reports this observation has been linked to the carbon fibre oxidising [9].

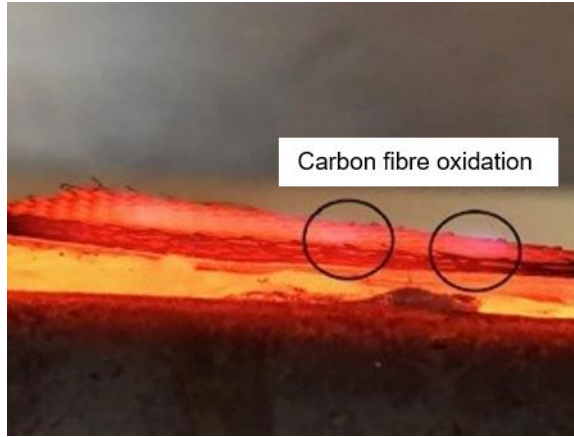


Figure 4.5. Image of the CC under the cone at  $t = 420\text{s}$  at  $60\text{kWm}^{-2}$ .

In order to see if this led to oxidation of the carbon fibres in CC, where possible, fibres were taken from plies P1, P4 and P8 and studied using SEM to identify reduction in fibre diameters and degrees of surface damage.

Figure 4.6(a) shows char over P1 for CC exposed at  $35\text{kWm}^{-2}$  for 600s. Fibres from P4 to P8 could not be examined as they were still embedded within unburnt resin and could not be removed. The SEM images in Figure 4.6(b and c) show char adhering to the fibres from P1. Large parts of the fibre are covered in char as well as encapsulating individual fibres. This char layer on the fibres was measured to be around  $3.5\mu\text{m}$  thick.

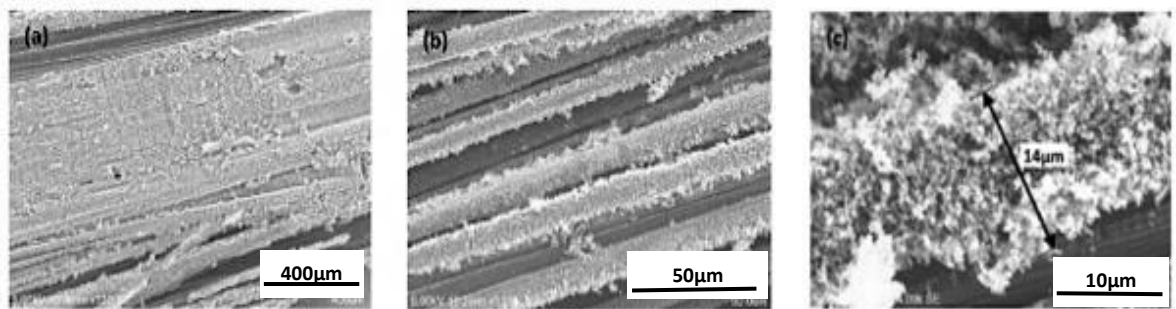


Figure 4.6. SEM images of (a) Surface (b) Individual fibres (c) Single carbon fibre from P1 after 600s exposure to  $35\text{kWm}^{-2}$ .

Fibres from P1 of CC exposed to  $50\text{kWm}^{-2}$  heat flux were examined under SEM and did not have any char deposits attached. The same was found for fibres taken from P4. The fibres had

clear striations with no signs of surface damage. However, the bottom layer P8 had char residue adhering to it. At  $60\text{kWm}^{-2}$  heat flux, significant damage to the fibres was observed on all plies. P1 showed large areas of oxidation and a loss of its original structure with uniform striations. Meanwhile on P4 there were clear signs of highly localised oxidation in the form of large pits. Fibres from P8 showed less localised areas of oxidation but the striations were more defined, indicating general surface oxidation had occurred. It also showed that the plies above protected those underneath, as the surface oxidation of the fibre is greater on above plies. Between heat fluxes  $50\text{kWm}^{-2}$  and  $60\text{kWm}^{-2}$ , there was a sizable increase in carbon fibre surface damage. At  $75\text{kWm}^{-2}$  no char or resin was found on the fibres and they had undergone severe surface oxidation. SEM images of fibres removed from different plies of CC after testing are given in Figure 4.7.

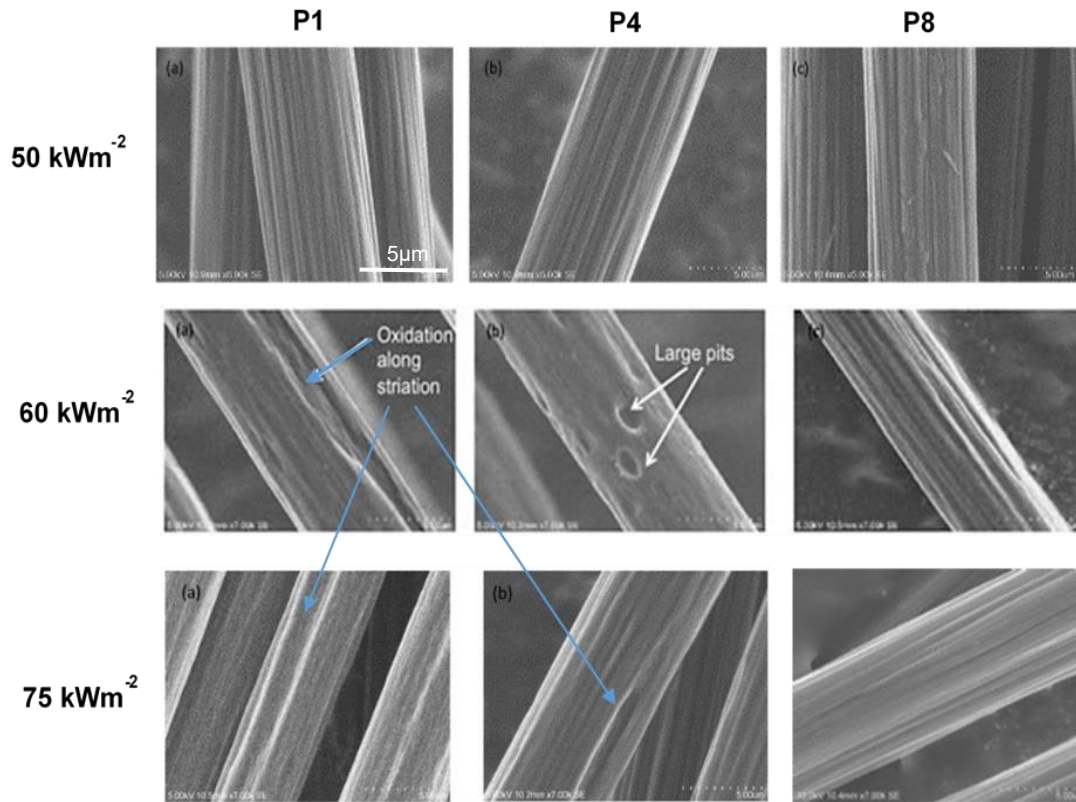


Figure 4.7. SEM images of carbon fibres removed from different plies after 600s exposure to various heat fluxes. Blue arrows indicate large areas of oxidation along striations.

EDX was carried out on fibres from ply P1 and only carbon was observed to be present (Figure 4.8 (a-b)). The absence of oxygen indicated that all the resin had pyrolytically volatilised.



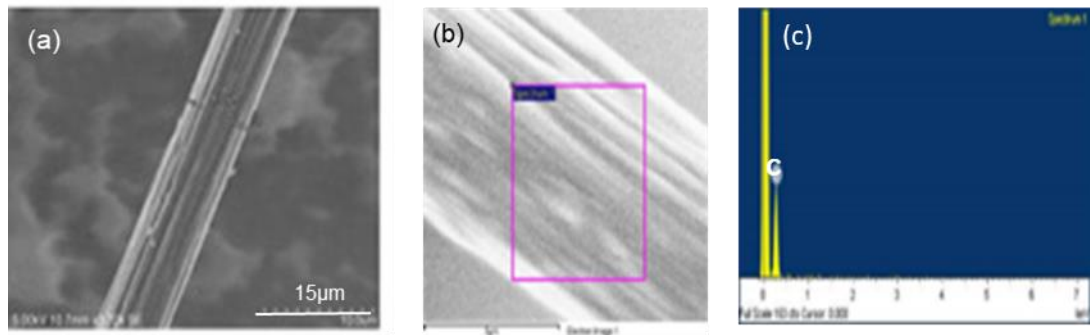


Figure 4.8. Fibre from (a) P1 CC exposed to  $75\text{kWm}^{-2}$  with spark ignition (b) Area used for EDX of fibre from P1 (c) EDX results identifying only carbon.

To quantify the levels of carbon fibre oxidation, the diameters of twenty five fibres were measured from SEM images. In Table 4.3 the mean diameters of fibres from different plies, and samples exposed to varying heat fluxes are given.

Table 4.3. Mean fibre diameters ( $\mu\text{m}$ ) removed from different plies of CC after exposure to cone calorimeter.

Ply	CF	Incident heat flux, $\text{kWm}^{-2}$				
		35	50	60	75	75*
P1	$7.68 \pm$	$7.43 \pm 0.10$	$7.35 \pm 0.12$	$6.19 \pm 0.13$	$6.12 \pm 0.32$	$5.89 \pm 0.11$
P4	0.23	$7.45 \pm 0.11$	$7.37 \pm 0.12$	$6.82 \pm 0.13$	$6.80 \pm 0.12$	$6.69 \pm 0.09$
P8		$7.46 \pm 0.12$	$7.37 \pm 0.09$	$6.57 \pm 0.12$	$6.72 \pm 0.22$	$6.65 \pm 0.11$

Note: \* = experiment with spark ignition

At  $35\text{kWm}^{-2}$  heat flux, the average fibre diameter remained within error similar to that of the CF, even those on ply P1, which were in contact with the flame. This is as expected as the thermocouple pre-ignition recorded a temperature of  $\sim 470^\circ\text{C}$  (Table 4.2) and at that temperature oxidation of carbon fibre was not expected according to TGA results (Section 3.2). At  $50\text{kWm}^{-2}$  there was a slight reduction in fibre diameter which appeared uniform in all plies.

Mean fibre diameter reduction for P4 and P8 for composites exposed to heat fluxes of  $60\text{kWm}^{-2}$  and  $75\text{kWm}^{-2}$  (with and without spark ignition) were within error of each other. For both composites, fibres removed from P1 showed more surface damage and diameter reduction than other plies. To understand if this damage due to oxidation had an effect on its properties, the electrical resistivity of carbon fibres from different plies of the most damaged CC (after exposure to  $75\text{kWm}^{-2}$  with spark ignition) were measured and are given in Table 4.4.

Table 4.4. Comparison of the mean electrical resistivity fibre from different plies after exposure to  $75\text{kWm}^{-2}$  with spark ignition.

		Resistivity, $\Omega\text{m}$ $10^{-5}$
Control carbon fibre		$2.08 \pm 0.13$
Ply	P1	$2.20 \pm 0.05$
	P4	$1.94 \pm 0.04$
	P8	$2.27 \pm 0.07$

As observed in Table 4.4, fibres from P1 were expected to have a greater resistivity as surface damage to the fibre was observed in the SEM images (Figure 4.7), which in theory should have impeded the flow of electrons. However, while the resistivity had increased, it was still within error of the CF. This further suggested that only localise surface oxidation had occurred, which did not penetrate into the fibres' internal structure. Mean resistivity of fibres removed from plies P4 and P8 were also within error of the CF.

Carbon fibres with an aerodynamic diameter between  $0.7$  to  $7\mu\text{m}$  are considered respirable and harmful to the trachea and lungs [10,11]. Particles under  $7\mu\text{m}$  in length were not observed after exposure of CC to  $75\text{kWm}^{-2}$  600s, so exposure time at this heat flux was doubled to 1200s (20min). The experiment was carried out under the same conditions as before, with spark ignition. Directly after the test had finished carbon tape was used to remove surface fibres from CC and these were then examined with SEM. Potentially respirable carbon particles of between  $4\mu\text{m}$  and  $7\mu\text{m}$  in length were found on P1 (Figure 4.9).

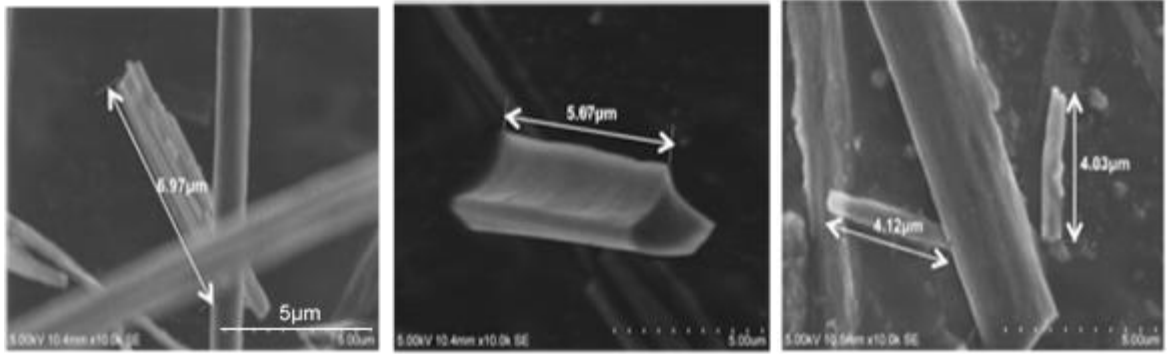


Figure 4.9. CF fragments from P1 exposed to  $75\text{kWm}^{-2}$  with spark ignition for 20min.

Intact but heavily oxidised fibres (pitting, loss of striations and grooves) remain in P8 (Figure 4.10). This further showed the barrier effect of the above-lying plies restricting oxygen flow to those underneath.

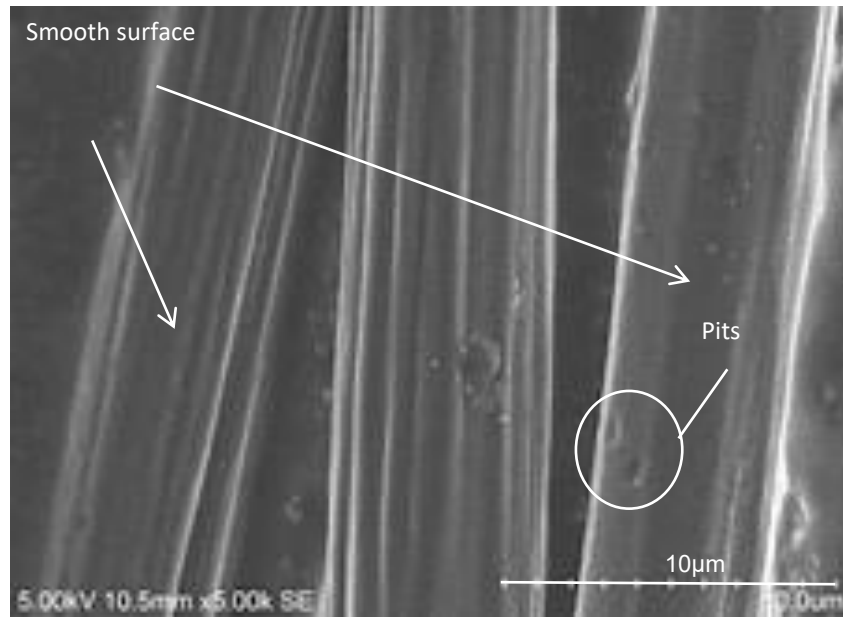


Figure 4.10. CF from P8 exposed to  $75\text{kWm}^{-2}$  with spark ignition for 20min.

#### 4.3.2 CCs exposed to jet fire conditions and the effects on carbon fibres: Propane burner experiments ( $116\text{kWm}^{-2}$ )

CCs were exposed to a propane/air mixed gas flame using the set up in [8], also described in Section 2.4.4. CCs were again cut to 25mm x 100mm strips. These were mounted in a graphite plate and exposed to the propane flame for 1, 3, 5 and 10min. The samples were removed from the plate immediately after the test and the plate cooled to room temperature before the next sample was tested. This set of experiments was conducted in order to:

- 1) Understand the effect of varying exposure times on the extent of damage to the CC and its component fibres.
- 2) Evaluate the damage to the CC in direct contact with the propane gas flame compared to those on the edge of the flame and the underneath side of the CC.

The propane flame with a heat flux of  $116\text{kWm}^{-2}$  was directed at the bottom third section of the CC, with thermocouples placed a few millimetres in front of it, in the lower, middle and upper third, to record the temperature in these sections. This is shown as a schematic in Figure 4.11, where the different plies of CC are labelled, along with the three thermocouples.

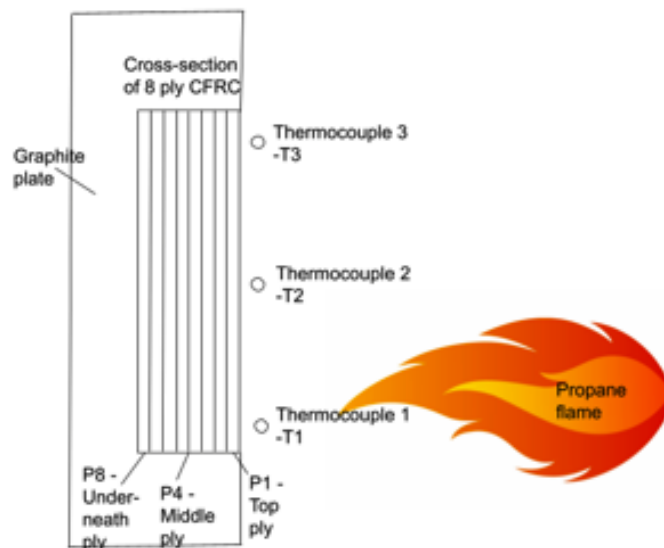


Figure 4.11. Schematic of mounted CC and propane flame.

The CC was exposed to the propane flame for 1, 3, 5 and 10min. Fibres were selected from different sections and plies of CC. After 1min exposure, the resin was still binding all the fibres together and individual fibres could not be removed. This was also the case for the CC after 3min exposure, with the exception of fibres at P1, T1 (in direct contact with the flame). Table 4.5 gives the mean fibre diameter for each exposure time.

Table 4.5. Fibre diameters removed from different plies and distance from the flame of CC at varying exposure times.

Thermocouple	Average temp recorded by thermocouple, °C	Mean Diameter, μm		
		P1	P4	P8
		3min		
T1	987	7.14 ± 0.17	-	-
		5min		
T1	993	6.79 ± 0.14	6.98 ± 0.22	6.96 ± 0.14
T2	866	7.28 ± 0.13	7.27 ± 0.13	7.28 ± 0.13
T3	785	7.31 ± 0.15	7.32 ± 0.16	7.38 ± 0.18
		10min		
T1	995	6.15 ± 0.13	7.07 ± 0.08	7.18 ± 0.12
T2	875	5.78 ± 0.07	6.95 ± 0.11	7.20 ± 0.12
T3	778	6.98 ± 0.08	7.16 ± 0.08	7.42 ± 0.09
CF diameter		7.68 ± 0.23μm		

\*‘Average’ temperature was taken over 5min from the temperatures recorded by each thermocouple

All fibres removed from P1, T1 underwent significant oxidation, particularly after 10min. Those removed from P8, T3 underwent the least amount of oxidation. This was because the

above carbon fibre plies and the surrounding graphite plate created a lower oxygen environment compared to the surface. SEM was used to identify any char remaining on the fibres and areas of localised surface damage. No char remained on the fibres from any ply after 5 and 10min. Furthermore, after 3min when in contact with a propane flame (with a temperature close to 1000°C) this was high enough to burn all resin from CC. While all fibres experienced surface oxidation, over 3 and 5min (Figures 4.12(a) and (b)), each fibre still maintained its inherent striations. At 5min, signs of localised surface damage appeared. While after 10min, large section of the surface had been removed, leaving fewer striations and severe reduction in fibre diameter (Figure 4.12(c)).

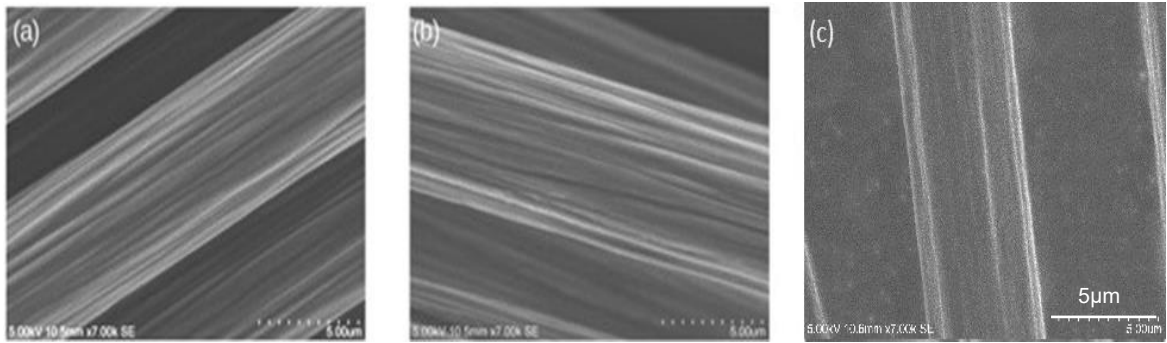


Figure 4.12. SEM of CF from CC at P1, T1 tested for (a) 3min (b) 5min and (c) 10min.

After 5min exposure, fibres removed from T2 and T3 had diameters within error of each other, with those from position T2 being slightly less on average than those from T3. This indicated that temperatures around approximately 775 to 875°C, over 5min, did not result in an increase in oxidation. After a 10min exposure more significant oxidation was seen to fibres in all sections of P1. However, those removed from P8 were within error of those after 5min. Again, this was attributed to the above fibres reducing the flow of oxygen to the underlying ply.

The fibres were cut with a sharp blade and held vertically under the SEM using a cross-section holder. The SEM images of these fibre cross-sections are given in Figure 4.13, including a CF and P1 of the CC tested under the cone calorimeter at  $75\text{kWm}^{-2}$  for comparison.

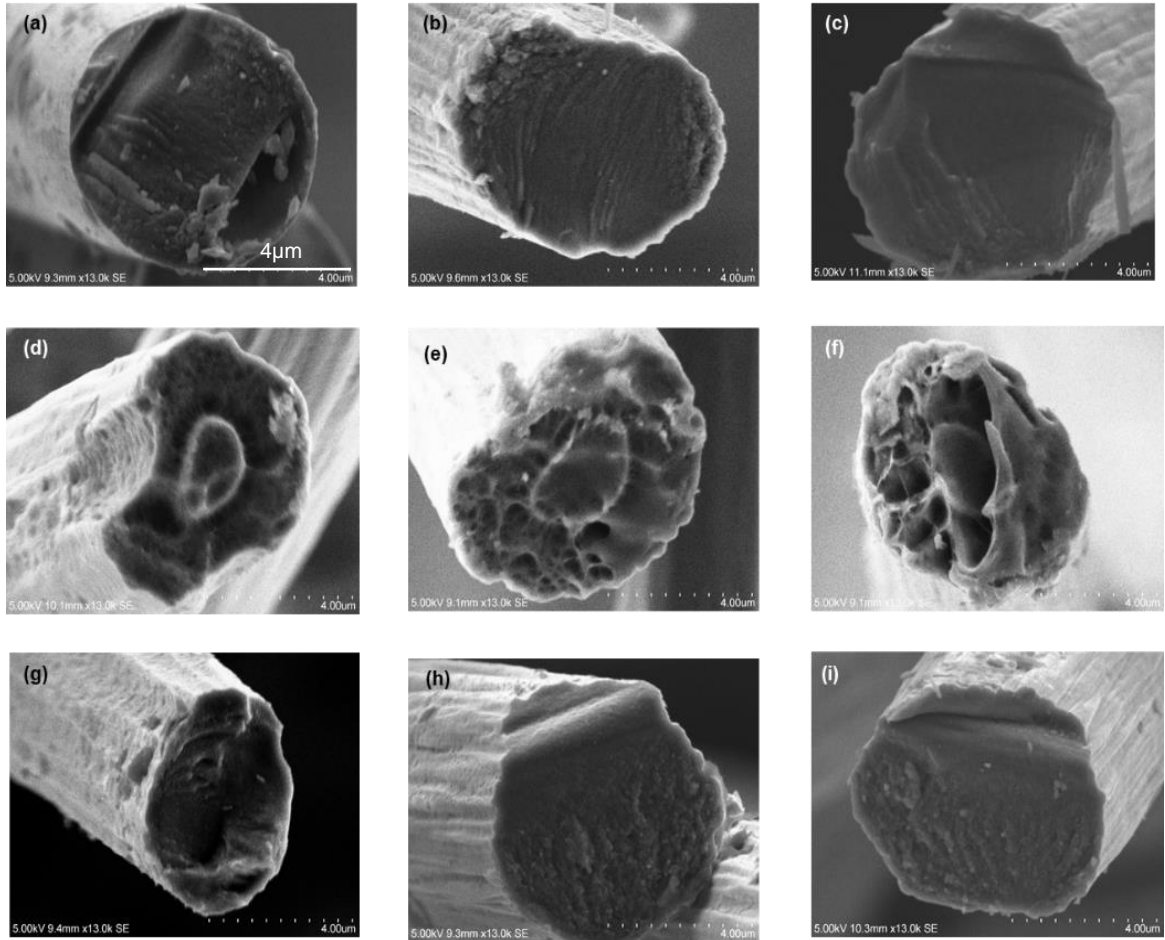


Figure 4.13. SEM images of fibre cross-sections removed from (a) CF, (b) P1 cone tested at  $75\text{kWm}^{-2}$  600s, (c) P1, T1 propane burner after 5min. After propane burner exposure for 10min from (d-f) P1, T1 (g) P1, T2 (h) P1, T3 (i) P8, T1.

The CF showed a distinct circular cross-sectional shape (Figure 4.13(a)). This was lost after exposure to both the cone calorimeter ( $75\text{kWm}^{-2}$  for 600s, Figure 4.13(b)) and propane burner ( $116\text{kWm}^{-2}$  for 5min, Figure 4.13(c)). In Figure 4.13(b) the fibre had an oval shape, where oxidation had occurred predominantly along one side of the fibre, most likely this was the side facing the cone's heater. While that from P1, T1 in Figure 4.13(c) had oxidised in multiple places around the fibre perimeter, giving the cross-section a rippled effect. Figure 4.13(d-f) of fibre removed from P1, T1 after exposure to the propane burner for 10min showed hollowing of the core, this was not present after 5min exposure. This hollow core and internal voids were

not present for fibres removed from other sections of the same CC (Figure 4.13(g) P1, T2 (h) P1 T3 and (i) P8, T1)), indicating that this was due to being in direct contact with the flame.

The flame zone comprises of molecules, atoms, free radicals and ions and these high energy species can penetrate the graphitic structure of the carbon fibre. Simmons [12] measured the radicals in a premixed 92.5% oxygen/propane flame in the flame zone. Simmons' results for hydrogen and oxygen free radicals, along with a digital image of the oxygen/propane flame used in the experiments reported, are given in Figure 4.14(a-b). No oxygen or hydrogen radicals were detected in the luminous zone. However, at the end of the luminous zone, the concentration of both oxygen and hydrogen radicals increased rapidly to a maximum and then slowly decreased with distance in the non-luminous zone. The propane burner was positioned 350mm from CC in the graphite plate, placing CC P1, T1 in the non-luminous zone.

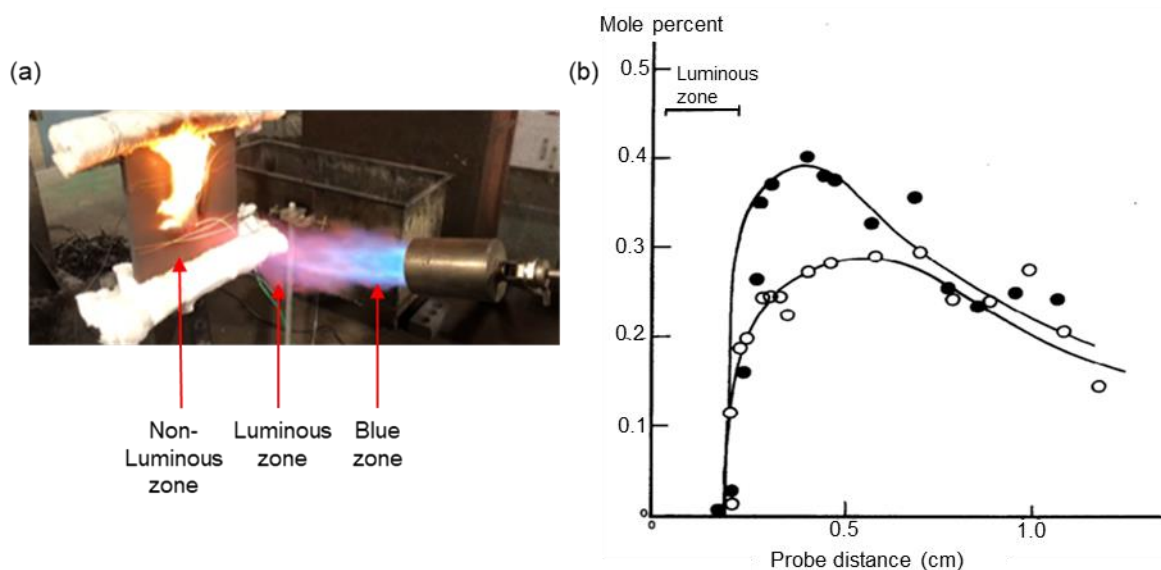


Figure 4.14. (a) Digital image of the propane/oxygen flame used in this work and (b) concentration of oxygen (o) and hydrogen (●) radicals at distance from the flame source, taken from [12].

As carbon fibres at P1, T1 are in contact with the flame at the non-luminous zone, they were the only fibres to show the results of the effect of attacking oxygen and hydrogen radicals. These radicals were not present outside this area of the flame zone, and above carbon fibre plies



protected those underneath. Furthermore, it may be concluded that 5min time was not sufficient for the radials to penetrate into the fibre core as this was only seen after 10min.

#### **4.4 Carbon fibre-reinforced composites with flame retardants and nano-additives**

Flame retardants and nano-additives were added to the resin of the CCs in order to increase the cross-linking during resin decomposition when exposed to heat/fire, with the aim of increasing char formation and its adhesion to the carbon fibres. In this way, it was assumed the carbon fibres would be encapsulated by char and so reduce their exposure to the environment.

##### **4.4.1 TGA studies (thermal stability) of CCs containing flame retardants and nano-additives**

APP, DOPO and RDP are all phosphorus-containing flame retardants (see Section 2.2.3). These are particularly popular nowadays as they are claimed to be more environmentally friendly than halogen-containing flame retardants which are often considered to be toxic to the environment [13]. The choice of these FR was driven by two factors; firstly, they have shown to be compatible with and have good dispersion in epoxy resins [14]. This is important so that the mechanical properties of the CC are minimally affected. Secondly, their flame retarding mechanisms in epoxy resins vary. APP is synthesised from inorganic salt of polyphosphoric acid and ammonia and works in the condensed phase [15]. At high temperatures APP degrades to release acidic hydroxyl groups and makes ultraphosphate and polyphosphoric acid, which catalyse the dehydration reaction of epoxy resin and help in char residue formation [15]. RDP on the other hand, is a low volatile flame retardant which acts predominantly in the gas phase to inhibit flames at the start of degradation [16]. On decomposition,  $\text{PO}\cdot$  and similar radicals are released, which by a free-radical scavenging mechanism react with and remove the highly reactive  $\text{H}\cdot$  and  $\text{OH}\cdot$  radicals from the combustion process. DOPO reacts with the epoxy monomer via its reaction of its P-H group and also works in the gas phases, again via the  $\text{PO}\cdot$  radical leading to flame inhibition. But unlike RDP, it has also been shown to be active in the condensed phase, increasing char production during combustion [17,18]. Their chemical formulae are shown in Figure 4.15.

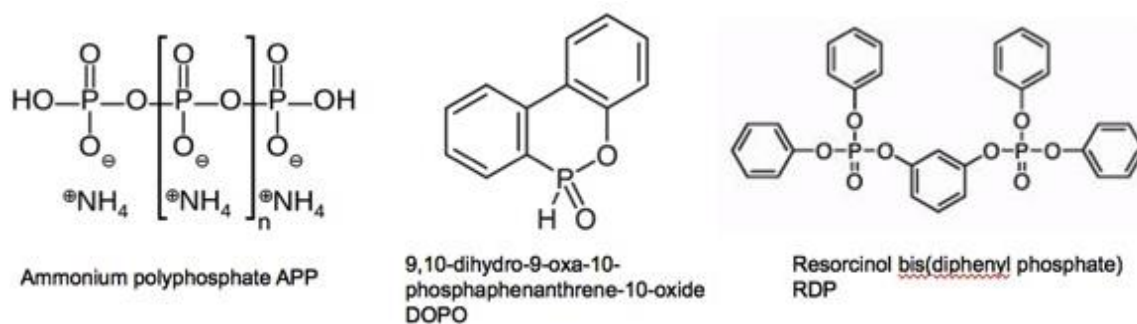


Figure 4.15. Chemical structures of the flame retardants.

Sections of similar mass to that used for the TGA of the CC in Figure 4.2 above were removed from the composites with 15wt% APP (CC\_APP), 15wt% DOPO (CC\_DOPO) and 15wt% RDP (CC\_RDP) and TGA was carried out under similar conditions (Figure 4.16). Important parameters derived from these TGA curves are given in Table 4.6.

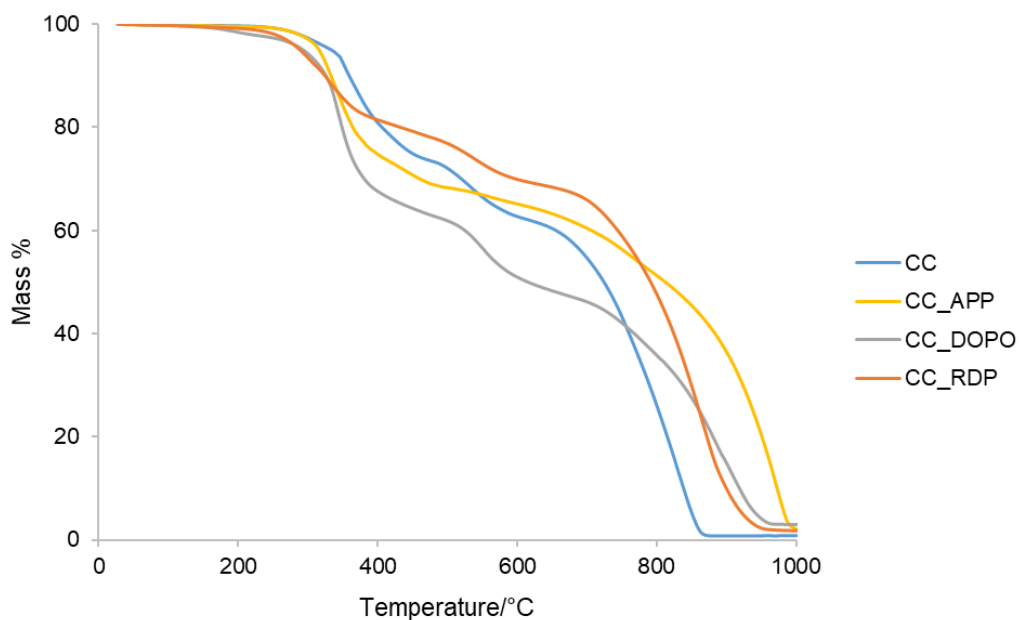


Figure 4.16. TGA of CC, CC\_APP, CC\_DOPO, CC\_RDP.

Table 4.6. TGA data for samples shown in Figure 4.16 in air.

Sample	T <sub>Onset</sub> , °C	T <sub>Max</sub> , °C	Mass remaining at 900°C, wt%
CC	334	895	0.7
CC_APP	225	984	36.6
CC_DOPO	148	951	15.0
CC_RDP	145	954	10.0

Note: T<sub>Onset</sub> = Temperature at which 5% mass loss occurs; T<sub>Max</sub> = Temperature at which all the mass has been lost and the residual mass is uniform.

Table 4.6 also shows that CC\_DOPO and CC\_RDP began to decompose at significantly lower temperatures than CC, this was expected as both DOPO and RDP break down at lower temperatures than pure epoxy (Table 4.1) [14]. In CC\_DOPO the P-O-C bond is less stable when heated than the -C-C bond [19]. CC\_APP also began decomposing before CC as expected since Levchik et al [20] found that in air, APP broke down into polyphosphoric acid over the range 260 to 420°C, and this corresponds to the rapid mass loss between these temperatures shown in Figure 4.16. The polyphosphoric acid then may react with the OH groups in the cured epoxy resin and form a phosphorus-rich layer as the temperature increased to 500°C [21], hence the rate of mass loss was reduced. All composites with phosphorus-based flame retardants retained more mass at 900°C than CC, indicating they all formed char. CC\_APP had the greatest mass as APP because of its known char-promoting properties, while CC\_RDP had the least.

#### 4.4.2 CCs containing flame retardants/nano-additives exposed to radiant heat and the effects on carbon fibre: cone calorimetric experiments

CCs with and without FR additives were tested with the cone calorimeter with spark ignition at 75kWm<sup>-2</sup> for 600s. The relevant cone data including residual masses of each sample are given in Table 4.7.

Table 4.7. Residual mass of CC exposed to 75kWm<sup>-2</sup>.

Sample	Composition, wt%			TTI/s	FO/s	Residual Mass after 600s, wt%	Normalised Residual w.r.t. 34.3 wt% resin content*, wt%
	CF	Resin	FR				
CC	65.7	34.3	0	23	93	39.9	39.9
CC_APP	53.9	39.2	6.9	17	74	58.0	66.3
CC_DOPO	57.2	36.4	6.4	12	71	42.9	45.5
CC_RDP	59.1	34.8	6.1	14	56	63.2	64.1
Nano-clay 5% (CC_NC)	65.0	33.3	1.7	20	78	51.7	50.2
LDH 5% (CC_LDH)	63.0	35.2	1.8	19	75	52.4	53.8

$$* \left( \frac{\text{resin wt\% of sample}}{\text{resin wt\% CC}} \right) * \text{residual mass}$$

Since the control CC with a resin content of 34.3wt% yields a residue after 600s of 39.3wt%, all other residue values were normalised to this same resin content. However, this normalisation process takes no effect of the reduced carbon fibre content that is a consequence of the flame retardant/additive content or any reduction in mass of the latter during cone exposure.

Bearing in mind the above, Table 4.7 shows that relative to the CC control, all the composites with FR and nano-additives had a greater normalised residual mass percentage even after compensating for the nano-particular content in the latter's residues. As APP works in the condensed phase, it promotes char formation which would have accounted for an increase in residual mass. While RDP works principally in the vapour phase by extinguishing the flame earlier, its inclusion has resulted in reduced FO, as well as the greatest residual mass, which could indicate incomplete combustion of the resin. However, while RDP is not a char promoter, as seen from TGA results (Table 4.6), because the vapour phase activity slows down the decomposition reactions of the resin, the slower char-forming reactions become significant and the increased char formation following cone exposure may also be a consequence. In contrast,

DOPO, which also works mainly in vapour phase has also shown some condensed phase activity and increased TGA-derived char above 800°C (see Figure 4.16), did not have a significantly shorter FO compared to the other composites, it also produced the least char during cone experiments.

CC\_NC and CC\_LDH have similar residual masses. In the case of CC\_NC, inorganic nanoparticles may have migrated to the top surface and formed a physical shield during thermal decomposition [3, 22]. This barrier would reduce the migration of the volatiles from decomposing polymer to the surface and diffusion of oxygen from the atmosphere to the polymer. It also acts as a heat shield to radiate heat from an external heat source away from the underlying polymer. Hence the slower char-forming reactions now become significant and could have accounted for the extra remaining mass. LDH works in a similar way but has the added benefit of releasing water when it breaks down; it is also known to leave a metal oxide residue [22].

After testing, the composites were left to cool at room temperature. Carbon fibres were carefully extracted using tweezers from different plies within the composites. Twenty fibres were examined under SEM and measured. Table 4.8 gives the mean carbon fibre diameters from plies – P1, P4 and P8 of CC, CC-APP, CC-DOPO and CC-RDP composites. CCs containing NC and LDH consisted of 10 plies instead of 8 plies and so fibres were taken from plies P1 (surface ply), P5 (middle ply) and P10 (underneath ply) of these composites.

Table 4.8. Mean fibre diameters after exposure to  $75\text{kWm}^{-2}$  for 600s.

Sample	Mean fibre diameter, $\mu\text{m}$		
	CF: $7.68 \pm 0.23\mu\text{m}$		
	P1	P4	P8
CC	$5.89 \pm 0.11$	$6.69 \pm 0.09$	$6.65 \pm 0.11$
CC_APP	$6.85 \pm 0.06$	$6.91 \pm 0.06$	$7.15 \pm 0.11$
CC_DOPO	$6.15 \pm 0.22$	$6.44 \pm 0.21$	$6.73 \pm 0.17$
CC_RDP	$6.22 \pm 0.11$	$6.41 \pm 0.23$	$6.63 \pm 0.11$
	P1	P5	P10
CC_NC	$6.72 \pm 0.13$	$7.09 \pm 0.10$	$6.81 \pm 0.13$
CC_LDH	$7.10 \pm 0.10$	$7.17 \pm 0.10$	$6.99 \pm 0.12$

SEM analysis of the fibre surfaces removed from P1 and P8/P10 of the composites after cone exposure are given in Figure 4.17, along with an image of the original fibre within the composite. SEM images were all taken at a similar magnification (x6-x7K). Images of the ordinal fibres were obtained by mechanically opening the composite and imaging the exposed fibres. On some of the raw fibres within the composites the striations were not as apparent as in others, even though the same fibre type and grade were used in all composites.

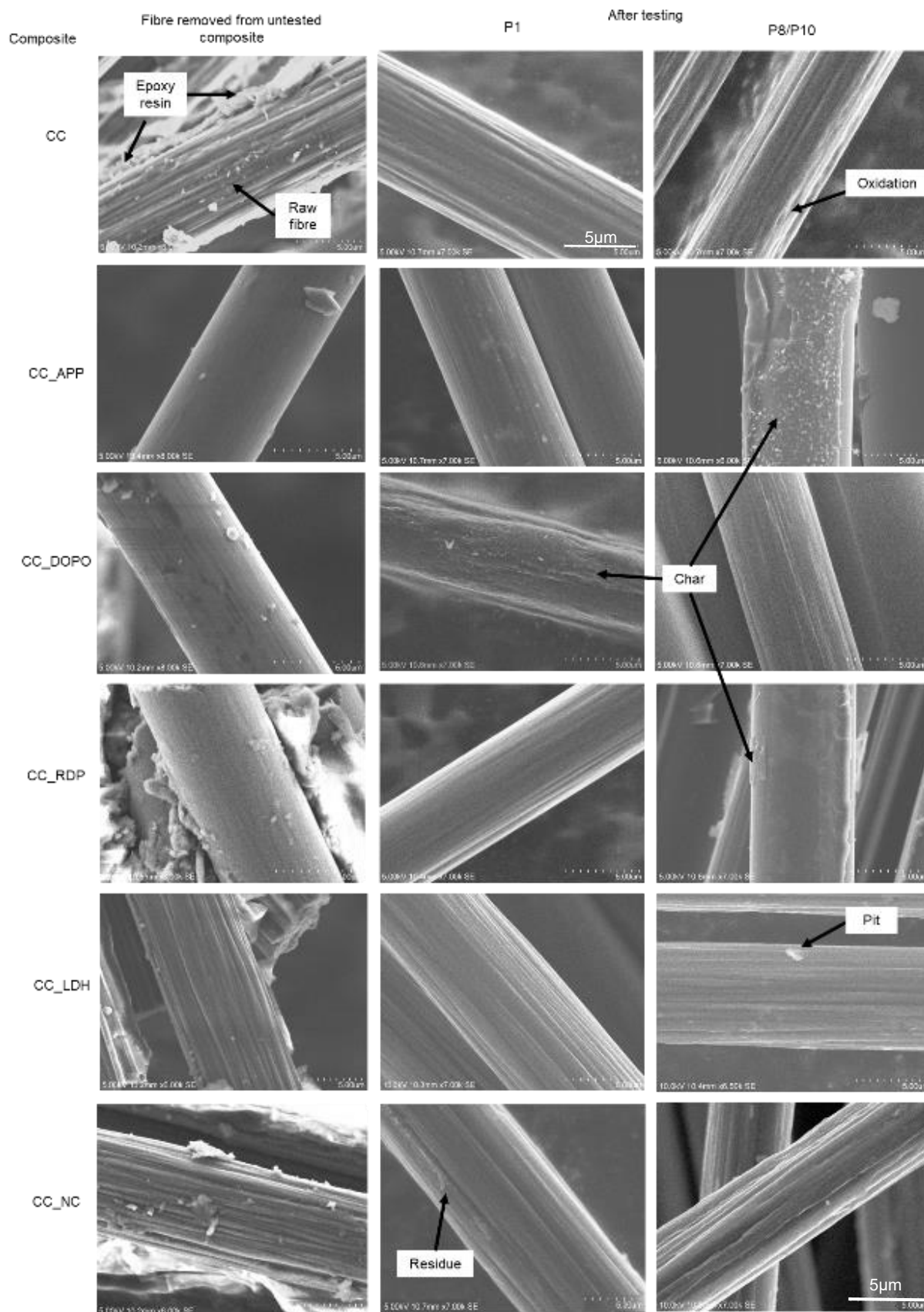


Figure 4.17. SEM images of fibres removed from the composite and of P1 and P8/10 after exposure to  $75\text{kWm}^{-2}$  for 600s.

As discussed in Section 4.3.1, fibres removed from P1 CC lost their original striated surface morphologies and the fibre surfaces appeared much smoother due to uniform surface oxidative ablation. On P8 fibres, areas of localised oxidation were seen, along with no residue or char. Fibres removed from CC\_APP before exposure to the cone calorimeter showed smooth surface textures most likely a consequence of a surface coating of APP. Fibres from P1 CC\_APP after heat exposure had a mottled surface, presumably due to APP residues still present on the fibre. Underlying faint surface striations were apparent, which could be indicators that any APP char had been removed coupled with some general oxidation although signs of localised oxidation were absent (such as pitting). Fibres removed from P8 CC\_APP showed large amounts of char encapsulating the fibre.

The raw fibres within CC\_DOPO also had less defined striations than those within the CC control before exposure. After heat exposure, char surface deposits were found adhering to P1 of CC\_DOPO. However, unlike APP, which works in the condensed phase during combustion yielding char, DOPO is reported to work predominantly in the gas phase, although as evidenced here, some condensed phase activity has been reported [18]. However, why it has not been oxidised as observed in CC\_APP sample P1 layer is not clear. CC\_RDP, on the other hand, a flame retardant generally considered to function mainly in the gas phase, had significantly less char-like deposits attached to fibres and especially on ply P8. EDX analysis of the above chars is given Figure 4.18. In the char present on fibres removed from ply P8 of CC\_APP, CC\_DOPO and CC\_RDP exposed composites, results show that phosphorus was detected in all samples, although at very low levels in the CC\_RDP sample.



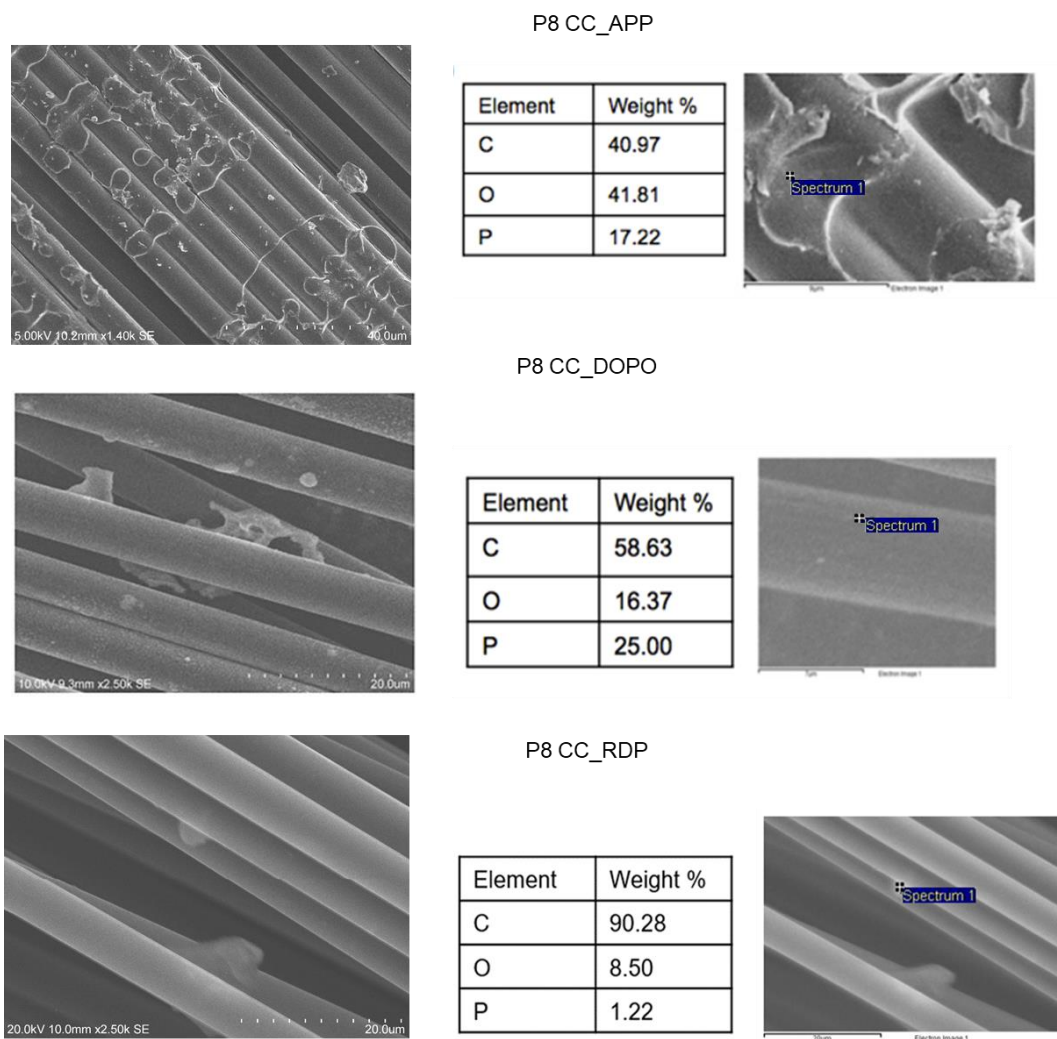


Figure 4.18. EDX analysis of char adhered on P8 of CC\_APP, CC\_DOPO and CC\_RDP.

Both LDH and nano-clay work in a similar way in that their particles can create a barrier on the surface, which prevents the flow of combustible products leaving the pyrolysing resin component and acts as a heat barrier to protect the unpyrolysed material underneath [23]. LDH has both a chemical and physical effect, however, as it begins to break down, it releases water and CO<sub>2</sub>, which dilute the combustible gases. Meanwhile the formation of a metal oxide residue creates a thermal barrier and restricts the flow of incoming oxygen as well as reflecting away incident radiant heat. As decomposition of the metal hydroxide is endothermic it also removes heat from the composite [24,25]. The raw fibres in these composites showed striations which remained on both P1 and P10 plies after exposure to the cone calorimeter (Figure 4.17). Small amounts of char were also observed on exposed P1 CC\_NC. On P10 of CC\_LDH a few pits

could also be identified, but these areas of localised oxidation were much smaller than on the P8 CC control.

TGA was carried out on retrieved fibres from P1 and P8/P10 of the tested composites, in order to examine the effects of char formation arising from different flame retardants and its resulting effect on the oxidation resistance of the carbon fibres. TGA was performed at 20°C/min from room temperature to 1050°C in air, at flow rate of 100ml/min. The results are given in Figures 4.19(a-b) for all exposed composite plies and in Figure 4.20(a-f) for the individual exposed composite plies.

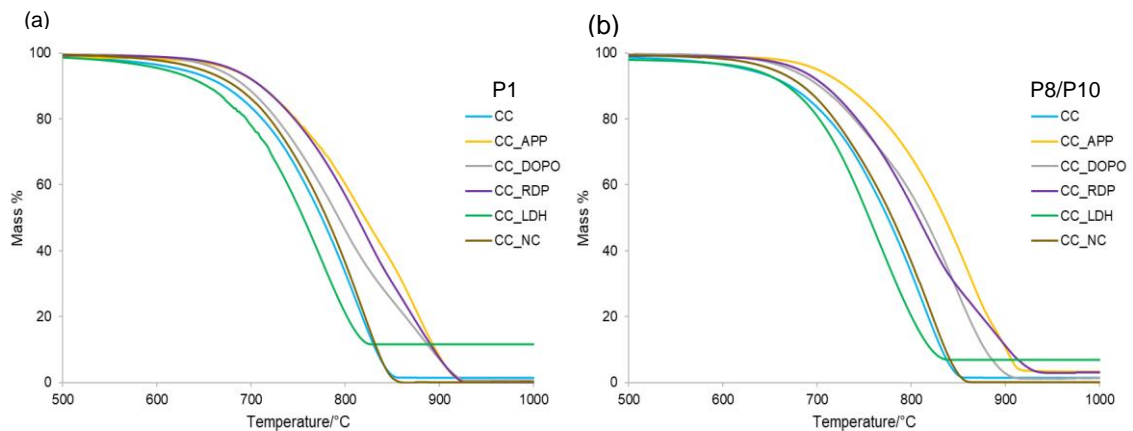


Figure 4.19. TGA responses of residual fibres removed from (a) P1 and (b) P8/10 plies from all exposed composites.

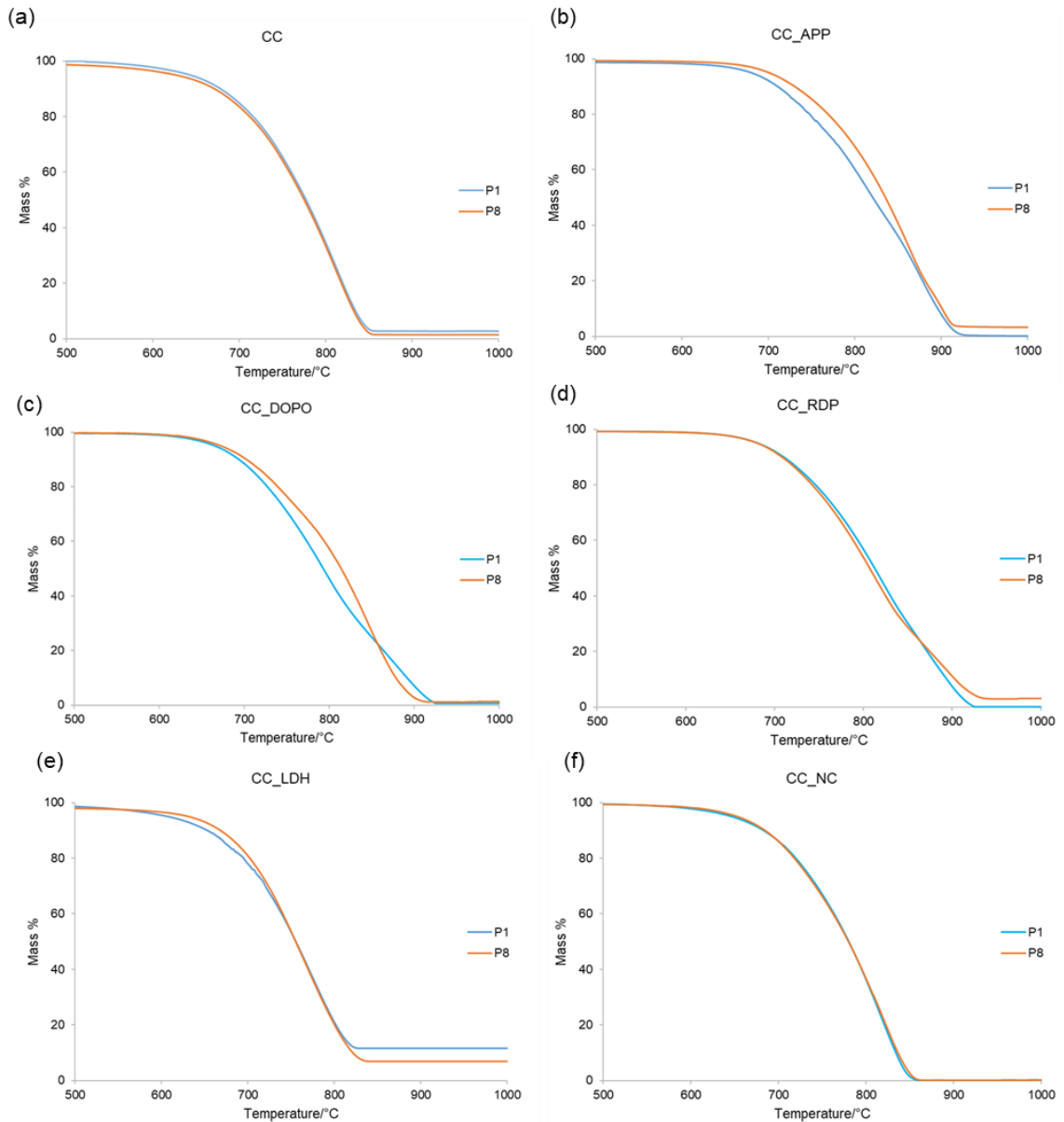


Figure 4.20. TGA responses of residual fibres removed from P1 and P8/10 of composites for (a) CC control, (b) CC\_APP, (c) CC\_DOPO, (d) CC\_RDP, (e) CC\_LDH, (f) CC\_NC

Fibres removed from P1 and P8 of CC showed almost identical TGA responses (Figure 4.20(a)), further confirming the lack of char on fibres from CC P8. With the exception of CC\_LDH, the TGA curves shifted to higher temperatures compared with respective ply P1 or P8 fibres extracted from CC as Figure 4.19 shows.

Further analysis shows that fibres from P1 and P8 of CC\_APP had the least mass loss at higher temperatures, most likely due the thermal barrier effect of char adhering to the carbon fibres, particularly from those of P8 (Figure 4.20(b)). DOPO (Figure 4.20(c)) is also observed to promote char formation during decomposition but did not provide as much protection as the effect of including APP. Until 881°C thermal decomposition for P8 was slower than for fibres from P1. For P1, CC\_RDP samples (Figure 4.20(d)), TGA showed results similar to those for P1 CC\_APP fibres. Early inhibition of the flame has led to the fibre being less damaged, reducing the number of oxidation sites introduced into the fibre (see Figure 4.17). Hence the TGA shifted to higher temperatures for both CC\_RDP P1 and P8, with both curves following a similar trend. These results also indicated that phosphorus-containing chars appear to be more thermally stable than those without it.

Fibres from P1 CC\_LDHD showed greater mass losses than those from P1 CC up to 800°C (Figure 4.19(a)). Furthermore, 11.6wt% from CC\_LDHD remained after 828°C, and 6.9wt% for those on P10. This difference in decomposition compared to the other TGA curves is due to the inorganic residues (MgO and Al<sub>2</sub>O<sub>3</sub>) on the carbon fibre surfaces. These results suggest that the presence of these oxides initially promotes surface oxidation of the carbon fibre. Furthermore, above 800°C more residue remained on P1 ply fibres than for P10 (Figure 4.20(e)). Again, this is most likely a consequence of greater oxidation of the carbon fibres promoted by the LDHD oxides and loss of LDHD decomposition, which is also evident by the surface pitting after on ply P10 in Figure 4.17.

For CC\_NC both TGA graphs (P1 and P10) the curves followed that of CC, indicating the nano-clay had not formed an effective protective thermal barrier on the carbon fibre. However, the thermal barrier effect is seen in bulk samples (Figure 4.17), when there is time for nano-clay particles to diffuse to the composite surface. In the TGA experiments only low mass samples were used (5-10mg) in which this flame retarding mechanism was not apparently observed. TGA curves for P1 and P10 were almost identical with no mass remaining (Figure 4.20(f)) and fibres from CC\_NC lost mass more rapidly than those with phosphorus-containing flame retardants present.

#### 4.4.3 Electrical conductivity of CCs before and after exposure to radiant heat

##### 4.4.3.1 Electrical conductivity of composites with flame retardants/nano additives

Before conducting any heat testing on the composites with additives, their electrical conductivities were measured. Electrical conductivity has been used in this section so these experimental results could be compared to the literature and Figure 4.21 from [29]. In Section 3.3 the electrical conductivity of the CF PAN-based TR30S was determined from single fibre resistivity testing as  $(4.81 \pm 0.30) \times 10^4$  S/m. The conductivity measured using strips of epoxy resin was  $(1.28 \pm 0.21) \times 10^{-13}$  S/m. As epoxy resins cure, OH groups are formed and cross-linking occurs, removing free electrons, which decrease the flow of electrical current. As curing processes vary between resins so does the electrical conductivity. Johari [26] found the electrical conductivity of resins to be in the range  $10^{-12}$  to  $10^{-19}$  S/m, Monti et al [27] measured for an epoxy resin as  $10^{-15}$  S/m, while Wajid et al [28] recorded a value of  $10^{-12}$  S/m. All these values put epoxy resins firmly in the region of insulators. Figure 4.21 from [29] shows electrical conductivity of different materials and where epoxy, carbon fibre and carbon fibre/epoxy lie on the chart.

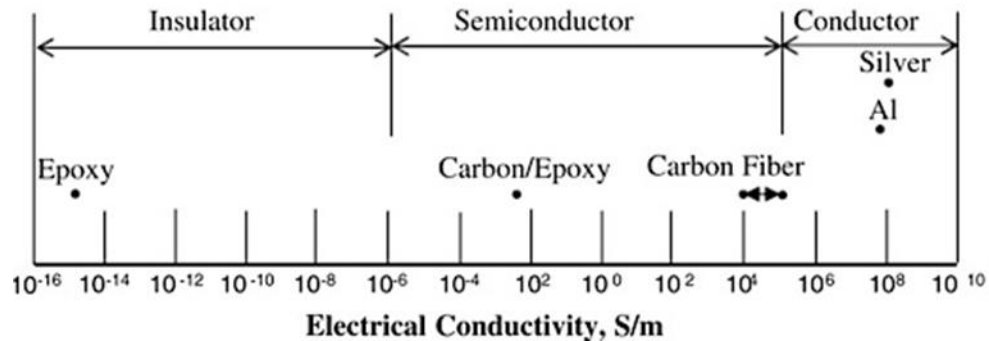


Figure 4.21. Electrical conductivity guide of components in CCs [29].

In this project 2x2 twill TR30S carbon fibre weave was used to make the composites. These fibres are in bundles which are woven bi-directionally; this means they are not always straight but crimped with many fibre/fibre contact points allowing the current to flow from one fibre to another. The bi-directional nature also means the current should flow equally in both the longitudinal and transverse directions. If unidirectional fibres were used (fibres all in one

direction) to make CCs, it would be expected that current flowed only in the fibre direction and not in the direction perpendicular to the fibre. However, this is not always what happens in practice due to the contact points between adjacent fibres allowing current to move between them. However, the out-of-plane electrical conductivities of the composites were not measured here. Conductivity in this direction is fully dependent on carbon fibre contact and given the nature of CCs, highly insulating epoxy resin lies between the layers, which restricts the direct contact between them and makes the electrical conductivity negligible compared to in the fibre direction.

Table 4.9 gives the conductivity values of each of the composites. The set-up for the test is given in Section 2.5.3.2. Measurements were repeated five times and a mean taken. Large errors arose due to the anisotropic nature of CCs. Furthermore, while efforts were taken to negate any current loss at contact points within the composites, by using a thin layer of silver loaded epoxy to even conductivity across the surface, the introduction of a small error remained here.

Table 4.9. Electrical conductivities of composites with additives.

Sample	Conductivity x10, S/m
CC	$19.7 \pm 1.8$
CC_APP	$2.0 \pm 0.5$
CC_DOPO	$7.5 \pm 1.6$
CC_RDP	$16.2 \pm 1.2$
CC_NC	$18.6 \pm 2.9$
CC_LDH	$3.5 \pm 1.4$

The inclusion of phosphorus-containing flame retardants APP, DOPO and RDP reduced CC electrical conductivity. CC\_APP had the lowest electrical conductivity (reduced by a factor of 10 compared to CC). APP was added to the composite in its solid state (8-12 $\mu$ m particle size)

and although APP is an inorganic salt of polyphosphoric acid and ammonia, solid-state inorganic salts do not conduct electricity, as ions are not mobile. The differences in particle size may be why including APP and DOPO led to greater reductions in their composite electrical conductivities compared with RDP, which is introduced as a liquid.

The introduction of 5wt% nano-clay had little effect on the conductivity. Rajini et al [30] studied the effect of nano-clay concentration on the properties of unsaturated polyester nanocomposites and reported that electrical conductivity increased with the addition of nano-clay up to 3wt%. But above 3wt% electrical conductivity began to decrease. This decrease was attributed to a greater number of immobile nano-layers at levels of 5 and 7wt%. However, nano-clay additives also reduced the cross-linking density of the resin, resulting in more free electrons in the resin to carry current, which would increase conductivity. This current study showed that 5wt% does not have an effect on the conductivity of the CC but it could be that these two mechanisms have balanced each other out. Furthermore, as the nano-clay is a layered silicate, any conductive positive ions would be trapped between the layers.

LDH was also added to the resin at 5wt% but unlike the nano-clay it notably reduced the CC conductivity. LDHs consist of positively charged cationic brucite-like layers (e.g.  $\text{Mg}(\text{OH})_2$ ) with interlayered hydroxide ions which are negatively charged [31] with overall poor conductivity in the solid state.

#### **4.4.3.2 Electrical resistivity of carbon fibres after cone calorimetric exposure**

After irradiance testing at  $75\text{kWm}^{-2}$  with spark ignition for 600s, single fibre electrical conductivity tests were carried out on five fibres taken from different tows within the same ply from all composites. The electrical resistivity results are given in Table 4.10.

Table 4.10. Mean electrical resistivity of CF from different plies of composites exposed to  $75\text{kWm}^{-2}$ .

Sample	Resistivity, $\Omega\text{m } 10^{-5}$		
CF	$2.08 \pm 0.13$		
	P1	P4	P8
CC	$2.20 \pm 0.16$	$1.94 \pm 0.11$	$2.27 \pm 0.07$
CC_APP	$1.43 \pm 0.23$	$1.68 \pm 0.12$	$1.69 \pm 0.31$
CC_DOPO	$1.68 \pm 0.22$	$2.01 \pm 0.23$	$1.46 \pm 0.11$
CC_RDP	$1.70 \pm 0.07$	$1.59 \pm 0.15$	$1.95 \pm 0.05$
	P1		P10
CC_NC	$2.56 \pm 0.41$		$2.20 \pm 0.08$
CC_LDH	$1.97 \pm 0.15$		$2.07 \pm 0.03$

Resistivity values for fibres removed from P1 and P8 of CC are higher than that of the CF. This was expected as they had experienced oxidation and damage was observed (Figure 4.17). P4 had a reduction in resistivity which was not predicted but could be related to the general variations in carbon fibre diameter. However, all these values were within error of the CF.

PAN-based fibres typically have a carbon content  $<94\%$  (Section 2.2.1, Table 2.1). Carbon fibre's electrical conductivity depends on both carbon content and level of carbonisation [32]. During the irradiance testing, the high temperature and contact with the surface flame, may have vaporised less conductive contaminating particles, such as alkali metals [33], resulting in only the more conductive carbon remaining. Chávez-Gómez et al. [33] investigated the role of impurities under exposure to flames for several PAN-based carbon fibres. They credited the resulting pitting on the fibres to the catalytic oxidation of alkali metals, such as sodium (Na), as well as channelling due to mobile impurities. Figure 4.22 from [33] gives the impurity concentration of the PAN-based fibres used: Hexcel AS4, IM7 and HM63. Given that the carbon fibre (TR30S) used in this project is a standard modulus PAN-based carbon fibre, like AS4, a similar concentration of elements may be expected.



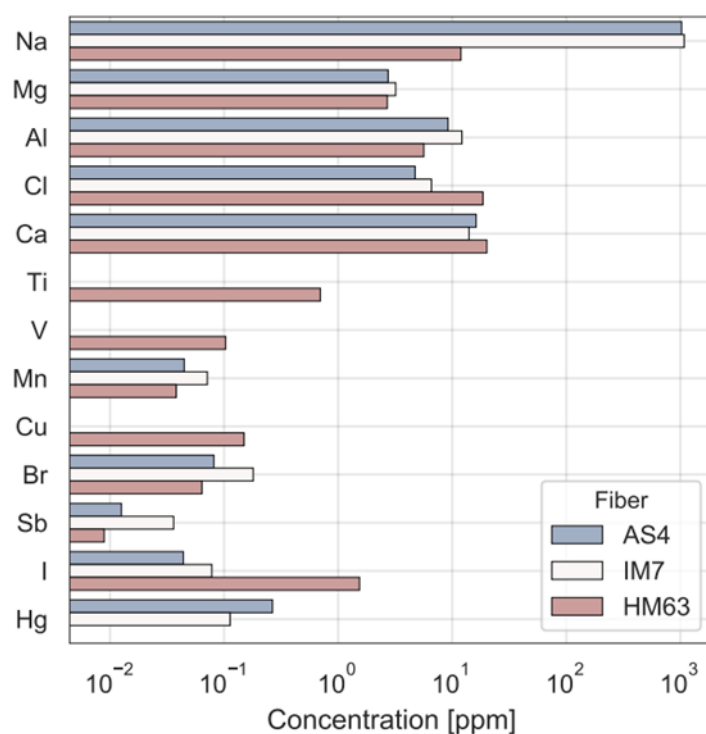


Figure 4.22. Impurity concentration of the PAN-based fibres used Hexcel AS4, IM7 and HM63 detected with Neutron Activation Analysis [33].

Chávez-Gómez et al. [33] also traced the cause of the presence of sodium to the polymerisation stage of PAN-based carbon fibre, whereby the precursor is dissolved with sodium thiocyanate (NaSCN) from which residues can then remain. Carbon fibres with a higher modulus (such as the HM63) had undergone further graphitisation that can vaporise these impurities.

The lower resistivity values of fibres from CC\_APP, compared to CC in Table 4.10, may be linked to the char residue remaining on the fibres (seen in Figure 4.17). After cone testing, APP was no longer in its insulating solid particulate form which previously had impeded the flow of electrons in the untested CC\_APP. During combustion a phosphorus-containing char residue formed on the fibre surfaces (see EDX results in Figure 4.18), affecting the conductivity of the fibres. Sogancioglu et. al [34] studied the effect of char (from pyrolysis) on the electrical conductivity of epoxy composites. They found that by replacing the weight percentage of epoxy resin in the composite with char, the electrical conductivity of the composite increased. The phosphorus in the char is typically in P-O-C [35], O=P-O- [35] and P=EN from carbon and

nitrogen residue [36]. Zhang et al. [37] found that in a phosphorus-carbon composite, adding a P-O-C bond, maintained the connection between P and C enhancing electron transport in the composite. Furthermore, such P-containing chars having conjugative structures (e.g.  $\text{-C=P-N=C-}$ ) [35] which will facilitate the flow of electrons. Char observed on ply P8 CC did not contain any phosphorus-containing species and hence had a higher resistivity than ply P8 in CC\_APP.

This also explains why fibres from P8 CC\_DOPO had a lower resistivity than plies P1 and P4. Char was seen on this ply P8 and like CC\_APP, this char also contained phosphorus-containing species (Figure 4.18). Moreover, the larger fibre diameter indicates less fibre oxidation had occurred on this underlying ply and so electrons were not as impeded. Yet for the CC\_DOPO composite, the high resistivity value for P4 (even above that on P4 CC and within error of the CF) stands out as an anomaly. As the fibres had experienced oxidation it was expected that the damage would increase their resistivity above that of the CF, but the presence of char would reduce it.

As RDP works mainly in the gas phase, the CC\_RDP composite had a shorter flame-out time than the CC control (Table 4.7), thus reducing the time the flame was in contact with the fibres and hence damage caused to P1 fibre. Both resistivity values for plies P1 and P4 are within error of each other. Fibres from P8 CC\_RDP had the same mean diameter as those from P8 CC\_DOPO yet the resistivity for P8 CC\_RDP was significantly higher than for that of CC\_DOPO. This could again be linked to more char attached to ply P8 in CC\_DOPO compared to CC\_RDP, as observed by SEM in Figure 4.18.

The electrical resistivity of fibres from ply P1 of CC\_NC was the highest for all fibres measured. In Figure 4.17 residue was seen attached for P1 fibres after heat exposure. A surface layer of nano-particles formed during the test which most likely would have contained  $\text{SiO}_2$ , an insulator. No such residue was detected on ply P10 of CC\_NC which is probably why its resistivity was within error of P8 CC. Both P1 and P10 of CC\_LDH had resistivity values within error of the CF. The slightly lower value of fibres from P1 of this composite could be due to the volatilisation of non-carbon particles, indicated by the pitting seen with SEM (Figure 4.17).

In this research, focus has been on surface oxidation and defects caused by the cone calorimeter's irradiation character; internal defects in the carbon fibre's crystalline structure have not been assessed and would need to be before further conclusions can be made.

#### 4.4.4 Mechanical properties of carbon fibres after cone exposure ( $75\text{kWm}^{-2}$ , 600s)

Single fibre tensile tests were carried out on carbon fibres removed from ply P1 of composites tested with the cone calorimeter. In Table 4.11 are the results along with the tensile strength and modulus percentage reductions with respect to the CF [38], and fibre diameter versus tensile strength is plotted in Figure 4.23.

Table 4.11. Mean tensile strength and modulus for carbon fibre from ply P1, removed from composites, exposed to  $75\text{kWm}^{-2}$ .

Sample	Tensile Strength, MPa	Modulus, GPa	Tensile strength reduction w.r.t CF), %	Modulus reduction w.r.t CF, %
CC	$2389 \pm 135$	$211 \pm 8$	$43 \pm 3$	$10 \pm 3$
CC_APP	$4175 \pm 234$	$218 \pm 7$	$-1 \pm 6$	$7 \pm 3$
CC_DOPO	$2695 \pm 181$	$199 \pm 14$	$35 \pm 4$	$15 \pm 6$
CC_RDP	$3811 \pm 316$	$231 \pm 26$	$8 \pm 7$	$1 \pm 11$
CC_LDH	$1978 \pm 101$	$175 \pm 6$	$52 \pm 2$	$25 \pm 3$
CC_NC	$2180 \pm 160$	$207 \pm 6$	$47 \pm 4$	$12 \pm 3$

\* '-' denotes an increase in tensile strength w.r.t CF

With the exception of fibres recovered from CC\_APP, all other fibres from the composites after cone testing ( $75\text{kWm}^{-2}$ , 600s) have reduced tensile strengths compared to the CF (= x MPa).

Residual fibres from exposed CC\_APP were within error of the CF and those from CC\_RDP showed only a small reduction in strength, indicating that the P1 fibres in these composites, experienced surface oxidation but no damage such as nano-flaws.

The residual fibres from exposed ply P1 CC had a reduced tensile strength of 43%. The reduction in strength is attributed to localised areas of oxidation, such as the volatilisation of contaminate particles, causing stress concentration sites, hence, increasing the chance of breakage at lower stresses. Less reduction was seen in those removed from CC\_DOPO (34%) indicating that the inclusion of DOPO did not make the carbon fibre significantly less likely to break. The tensile strength for residual fibres removed from exposed CC\_NC were within error of CC, this was not surprising as both these fibres had resistivity values within error of each other. Fibres from CC\_LDH have the lowest tensile strength. As seen in Figure 4.17, pits ( $\sim 0.5\mu\text{m}$ ) were found on the fibre surfaces, which could be linked to the metal oxides produced when LDH thermally decomposes. These would create localised stress concentrators on the fibre surface. No simple relationship between fibre diameter and tensile strength was observed however (Figure 4.23).

For all exposed fibres the modulus also decreased compared to the CF value, although to a lesser degree than the tensile strengths. However, those values from CC\_RDP were still within error that of the CF, again indicating that the mechanical properties of these fibres were largely unchanged during cone calorimeter testing. Feih and Mouritz [39] credited the decrease in carbon fibre modulus with increasing temperature to the oxidation of higher stiffness layers in the near-surface fibre region. The results in Table 4.11 also confirmed that this has most likely happened. With the exception of CC\_NC, the greater the decrease in tensile strength, the greater the decrease in modulus. It is also likely that other factors affecting the modulus occurred, which could include the removal of contaminate particles and potential graphitisation of the carbon fibres during heat testing.

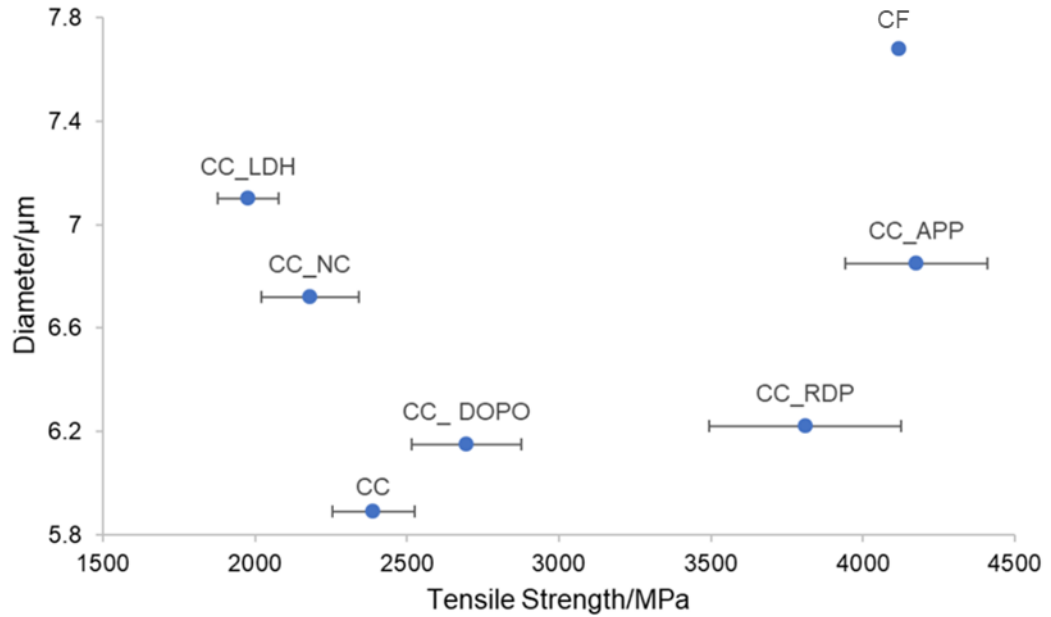


Figure 4.23. Fibre diameter vs tensile strength for fibres removed from ply P1 after cone testing at  $75\text{kWm}^{-2}$  for 600s.

#### 4.4.5 Analysis of char residue adhered on carbon fibres from cone exposed CC\_APP composites

The above results indicate that in CCs exposed to the cone heater ( $75\text{kWm}^{-2}$ , 600s), flame retardants and nano-additives in general help in improving the retention of tensile strength of the carbon fibres compared to those from control CC. However, the electrical resistivity results of individual fibres retrieved from cone-exposed composites indicated that the char attached to the carbon fibres has most likely affected their electrical resistivity. Further investigation was carried out on exposed fibres to determine whether the attached char residue had become part of its structure and hence a more permanent effect or if the char is loosely deposited on fibre surfaces and so easily removed by the intensity of the heat flux. For this study carbon fibres from ply P8 of cone exposed CC\_APP were investigated. These were chosen as they had the greatest amount of char adhering to them, as well as the greatest overall reduction in resistivity (see Figure 4.17 and Table 4.10).

EDX was first carried out during SEM examination of fibres removed from P8 CC\_APP (Figure 4.24 (a-d)). Carbon, oxygen and phosphorus were detected, with carbon dominating and oxygen

and phosphorus in much smaller amounts, mainly located where char was visually observed in the SEM images.

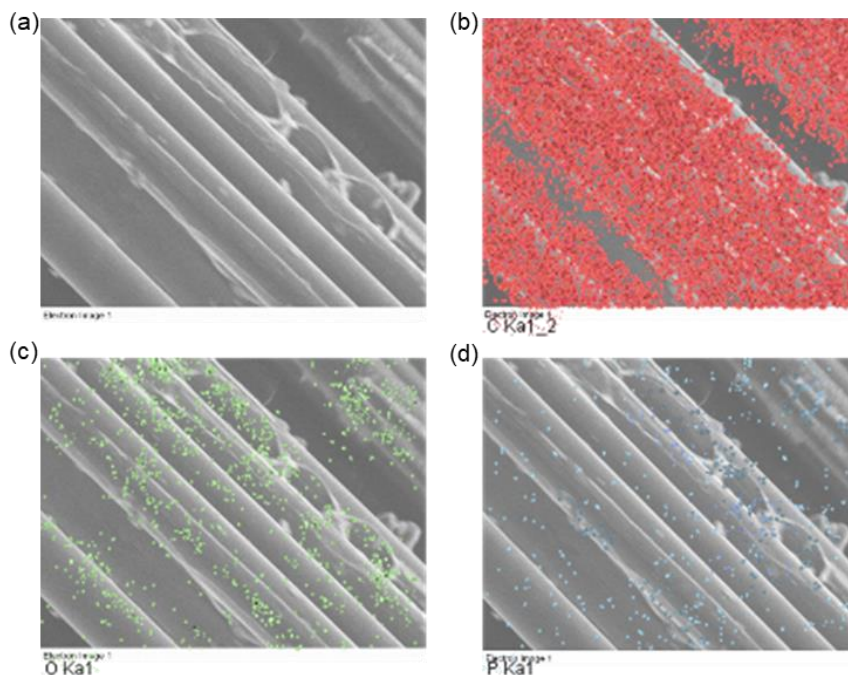


Figure 4.24. (a) SEM image and EDX maps showing the elements (b) carbon, (c) oxygen and (d) phosphorus on fibres from P8 CC\_APP after cone testing at  $75\text{kWm}^{-2}$ .

EDX mapping was also carried out on a loose piece of char attached to the underside of the CC\_APP composite after cone testing as a reference for analysis of the char adhered on the fibres. Results given in Figure 4.25(a-d) showed a high concentration of carbon, oxygen and phosphorus, indicating that mainly phosphorus-containing species were formed. Given the high levels of oxygen observed, it is most likely that some or all is combined with phosphorus as oxy-anions typical of the phosphate ion present in APP-derived chars [40].

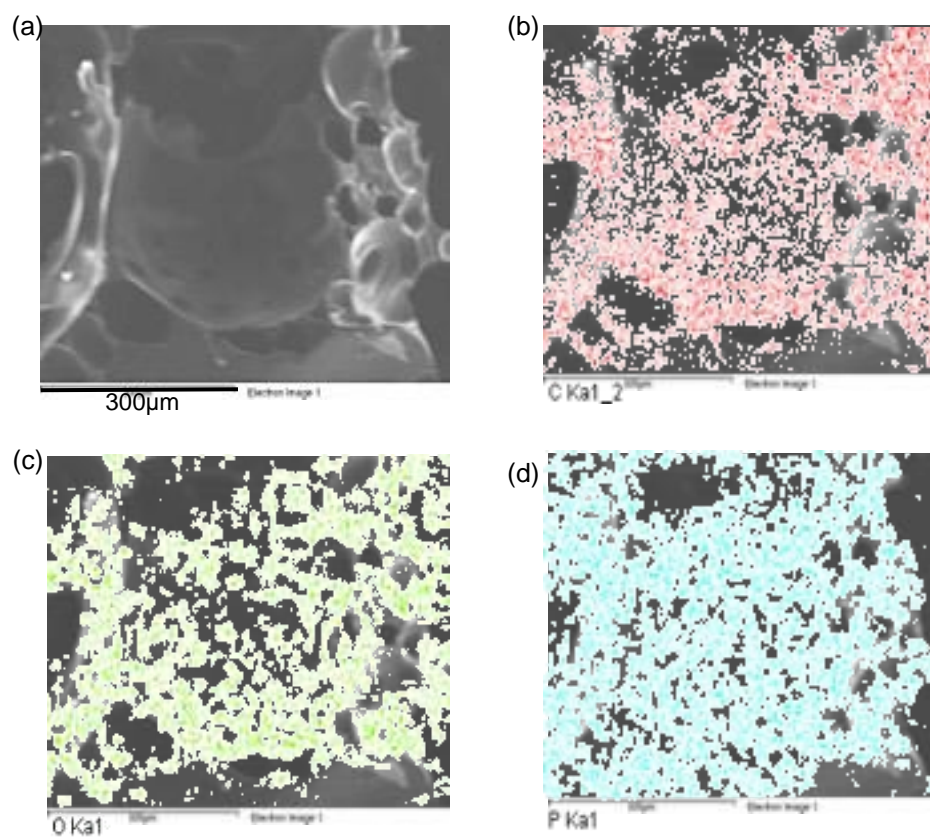


Figure 4.25. (a) SEM image and EDX maps showing the elements (b) carbon, (c) oxygen and (d) phosphorus in the loose char previously attached to P8 CC\_APP after cone testing at  $75\text{kWm}^{-2}$ .

In order to investigate the adherence of the char on carbon fibres from P8, the following possible extractive techniques were used:

#### 4.4.5.1 Use of solvents to remove residue

To attempt to remove the residue adhering to carbon fibres from P8 CC\_APP, fibres were placed in an ultrasound bath for 2h with different solvents; these are given in Table 4.12 along with their densities.

Table 4.12. Density of solvents used in ultrasound bath.

Solvent	Density, kg/m <sup>3</sup>
Distilled water	997
Toluene	873
Xylene	864
Acetone	784

After the ultrasound bath treatment, the fibres were removed, rinsed with distilled water and dried at 80°C for 4h. Figure 4.26 shows the SEM images of the resulting fibres, along with those from untreated P8 CC\_APP.

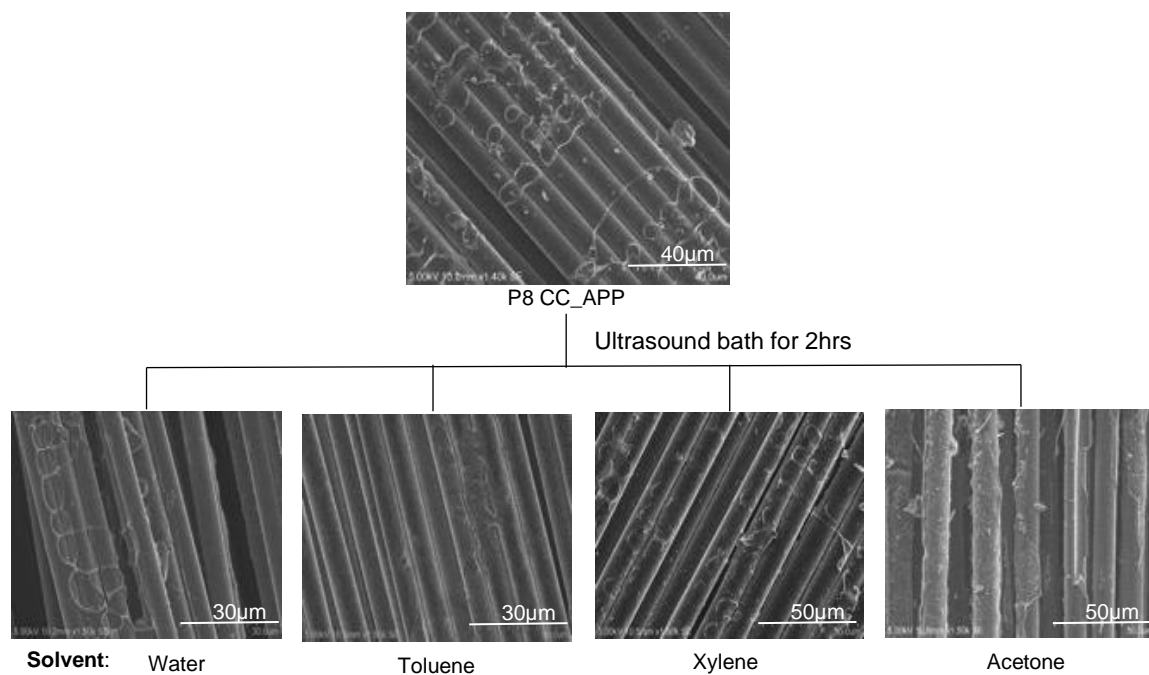


Figure 4.26. SEM images of CF from P8 CC\_APP after ultrasound cleaning with different solvents.

Carbonaceous residues were observed on all fibres after ultrasound cleaning. Cross-sections were also examined to identify any residues bonding the fibres together (Figure 4.27).



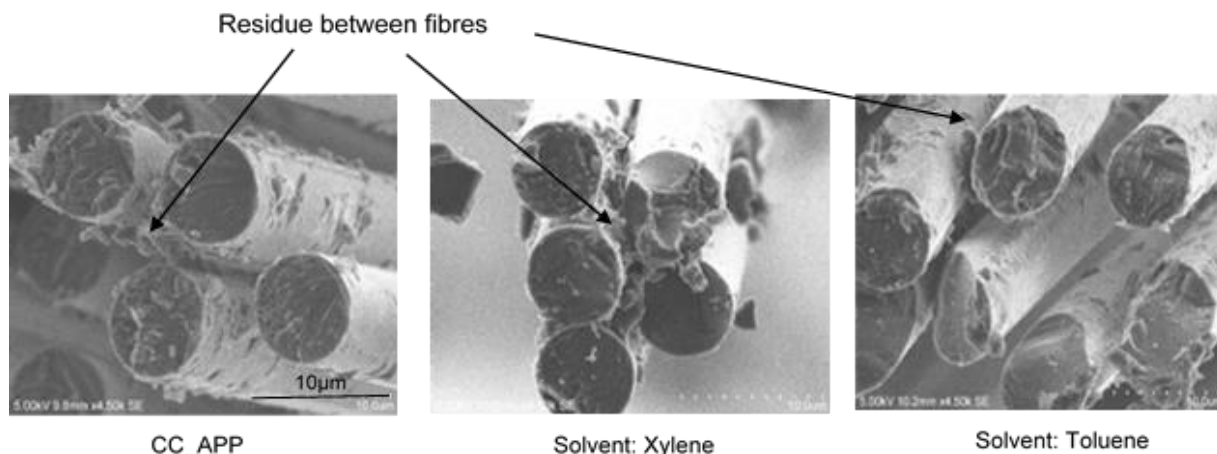


Figure 4.27. Cross-sections of fibres from Figure 4.26.

EDX was carried out on the resulting solvent-treated fibres to see if phosphorus remained in the residue. Below are EDX maps of the fibres cleaned with toluene, where the EDX element maps are overlaid on the respective SEM image (Figures 4.28(a-c)). As carbon tape was used to attach the fibre to the metal stub, carbon was found in all areas over the fibres and surroundings. While only a small amount of phosphorus was detected, it was most dense and coincided with areas of oxygen where there were visible areas of char. This showed that the presence of phosphorus is part of the fibre surface structure and may be able to affect fibre properties, such as electrical resistivity. These results were similar to the solvent-untreated fibres from P8 CC\_APP in Figures 4.24(b-d).

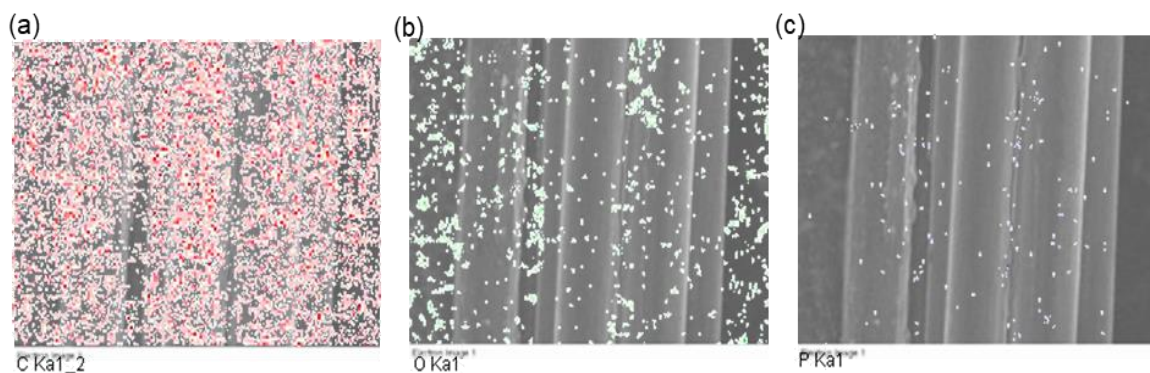


Figure 4.28. EDX maps showing the elements (a) carbon (b) oxygen and (c) phosphorus after cleaning fibres from P8 of CC\_APP with toluene.

#### 4.4.5.2 Use of alkali solution to remove residue

The use of NaOH solution was made since it is known to react with phosphorus, if present as the element, to give phosphine as in equation:



The aim was for this reaction to remove the phosphorus if present as the element from the carbonaceous residue. Residual fibres from P8 CC\_APP were removed and placed in 5wt% aqueous sodium hydroxide (NaOH) for 30min, then rinsed with distilled water and dried at 80°C. EDX was carried out and in Figure 4.29(a-e) the EDX-derived elemental maps are overlaid on the respective SEM images.

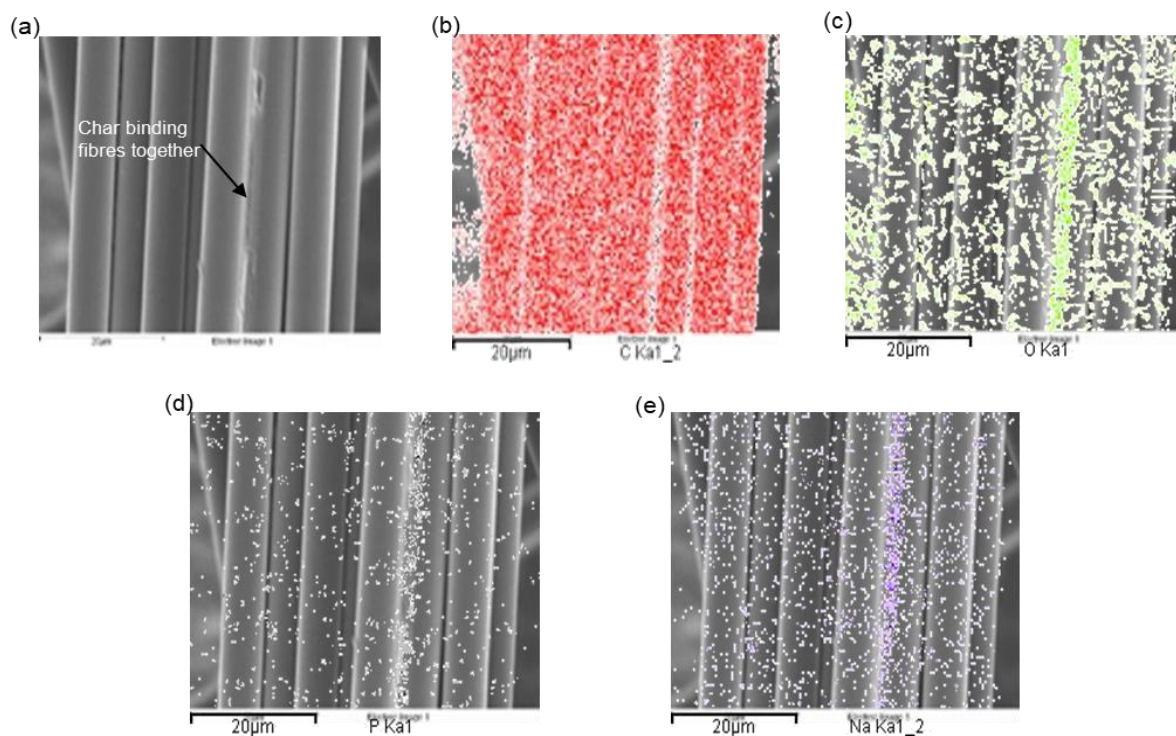


Figure 4.29. (a) SEM image, EDX maps showing the elements (b) carbon, (c) oxygen (d) phosphorus and (e) sodium after cleaning fibres from P8 CC\_APP with 5wt% NaOH.

These maps show again that carbon is the main element, as expected. Oxygen was also present on the fibres, with large concentrations over the residue areas which were binding together the carbon fibres. However, it was also seen that phosphorus combined with oxygen (Figure 4.29(d)) still remained in the carbonaceous along with sodium, most likely as the sodium salt with phosphate entities (Figure 4.29(e)).

#### 4.4.5.3 Use of strong acid to remove residue

Further attempts to remove the residue from the fibre included the use of nitric acid (69w/v% concentration). In a separate experiment, epoxy resin with 15wt% APP was charred by holding it at 400°C in a nitrogen atmosphere for 10s. This was then immersed in the nitric acid at 80°C, in order to see if it would chemically breakdown the char. In Figure 4.30 it is seen that after 30min in the acid the charred epoxy partially dissolved, while after 2h no solid residue was visually observed.

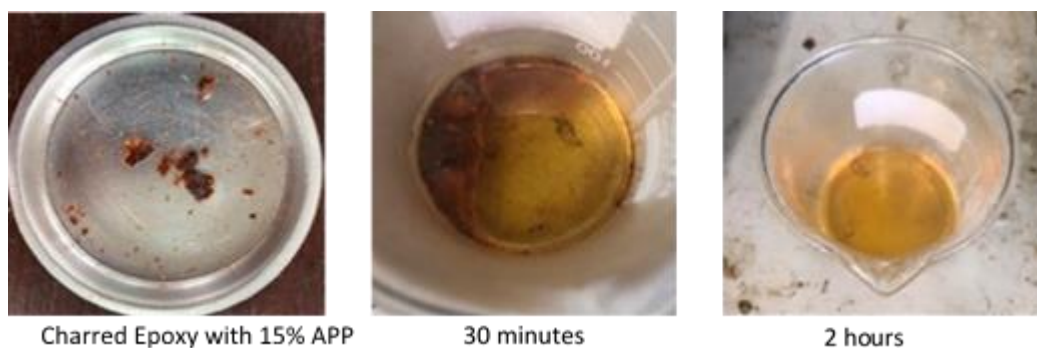


Figure 4.30. Images showing the breakdown of solid epoxy char with 15wt% APP over 2h.

Next the residual fibres from P8 CC\_APP were placed in nitric acid at 80°C for 2h. The fibres were removed from the acid, rinsed with distilled water and dried at 80°C for 4h. An SEM image of the resulting fibres is shown in Figure 4.31 indicating that residues remained on the fibres.

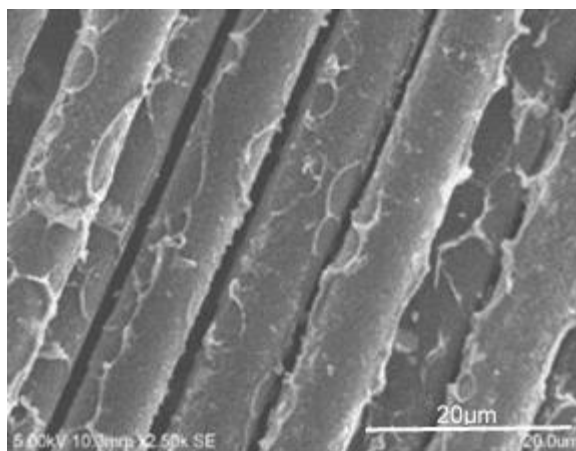


Figure 4.31. Residue covered CF from P8 CC\_APP after cone testing and 2 hours in 80°C nitric acid.

As nitric acid is a strong oxidising agent, it could have probably reacted with the carbon within the charred epoxy to form carbon dioxide, nitrogen dioxide and water. Furthermore, the phosphorus bonded into the char could also have been oxidised to either a soluble oxide or phosphorus oxyacid and hence removed by the nitric acid. The EDX results are presented in Figure 4.32, of an area where fibres were enclosed together by char residue from P8 CC\_APP.

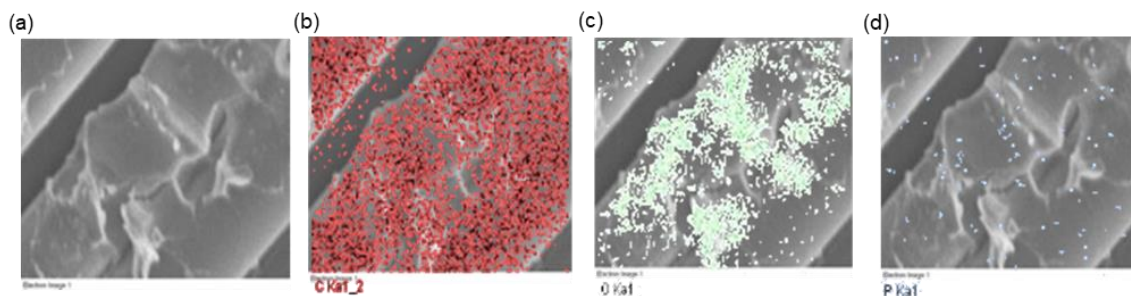


Figure 4.32. (a) SEM image, EDX maps showing the elements (b) carbon (c) oxygen and (d) phosphorus after 2 hours in 80°C nitric acid.

Carbon was detected over the fibres as expected, with oxygen shown overlaying the aggregates of residue. However, unlike those treated with toluene and sodium hydroxide, no large areas of phosphorus were found coinciding with the oxygen concentrations. This would suggest that there are significant areas of oxidised carbon carbonaceous char regions from which all phosphorus entities have been removed. In order to quantify the residue remaining on the fibres TGA was carried out in air (100m/min) at 20°C/min on the acid-treated and untreated residual

fibres from P8 CC\_APP, along with a residual fibre from P8 CC for comparison. These results are shown in Figure 4.33 with the solvent/acid used to treat the fibres labelled.

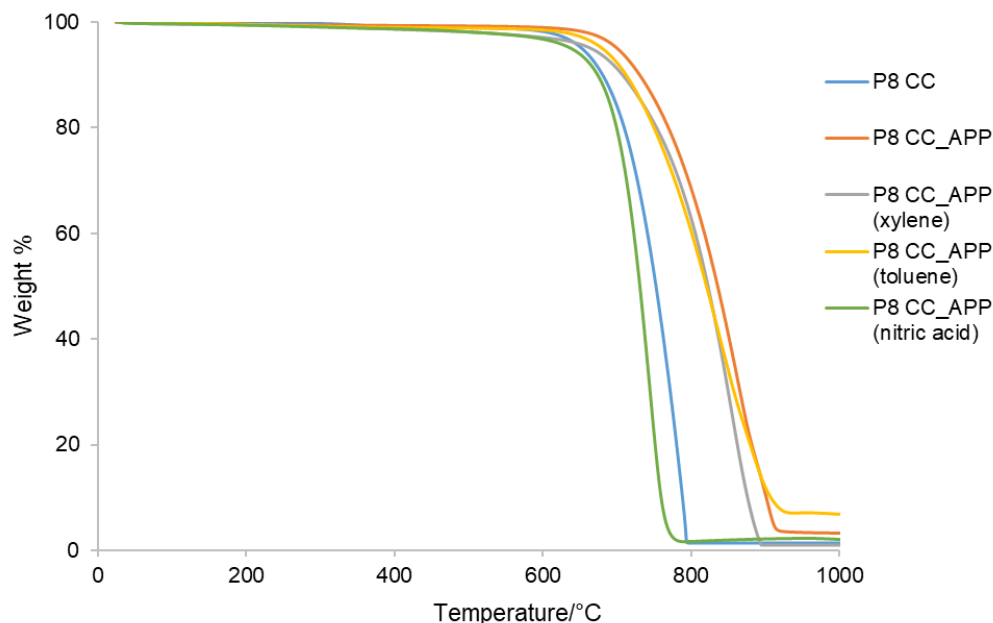


Figure 4.33. TGA in air of residual carbon fibres from P8 CC\_APP after various cleaning processes.

Both fibres treated with toluene and xylene followed the same curve as that of the untreated P8\_APP fibres suggesting that the use of dense solvents and the mechanical action of an ultra sound bath were not enough to remove the char bound to the fibres. The fibres treated with nitric acid began to oxidise at a lower temperature than those removed from the P8 CC (which had very little residue attached) also had a higher rate of oxidation. From this it was concluded that the char, containing phosphorus species on the carbon fibres in CC\_APP after exposure to the cone calorimeter at  $75\text{kWm}^{-2}$  was more thermally stable than both carbon fibre and char without these species. Furthermore, this stable char is not easily removed unless an oxidising acid is used and the TGA curve shows a faster tendency to oxidise than the control P8\_CC fibres. Therefore, not only is this faster oxidation a consequence of the removal of otherwise stabilising phosphorus species by nitric acid but also the associated oxidised char and carbon fibre surface species have sensitised further air oxidation.

#### 4.4.6 Effect of char residue on carbon fibre's electrical conductivity

As stated before, the electrical conductivity of these residual fibres after exposure to the cone calorimeter is also of interest. It was found in Section 4.5.2 that residual carbon fibres removed from composites containing phosphorus-containing flame retardants which work primarily in the condensed phase (e.g. APP and DOPO), had increased conductivity compared to fibres removed from the CC control. In Table 4.13 are the resistivity values measured from single fibres removed from P8 CC\_APP, along with those from P8 CC\_APP after cleaning in an ultrasound bath with different solvents. The resistivity of the CF and that of P8 of CC are also given.

Table 4.13. Mean electrical resistivity of carbon fibre after ultrasound cleaning with different solvents.

P8 of composite residual fibre removed from	Solvent	Resistivity, $\times 10^{-5}$
CF	None	$2.08 \pm 0.13$
CC	None	$2.27 \pm 0.07$
CC_APP	None	$1.46 \pm 0.11$
CC_APP	Xylene	$1.31 \pm 0.09$
CC_APP	Toluene	$1.96 \pm 0.15$

The higher electrical resistivity of the fibre removed from ply P8 CC than that of the CF was attributed to defects on the fibre surface occurring during heat exposure. Both CC\_APP and that cleaned with xylene had resistivity values within error of each other. While those exposed to toluene had a higher resistivity, it was still below that of the CF and CC. This indicated that the char adhering to the fibre decreased fibre resistivity, hence making it more conductive and potentially hazardous. These resistivity values and similar TGA curves, indicated that it is not possible to mechanically remove the char from the fibre without damaging it. Therefore, after



heat exposure the char, which appeared to be firmly adhered to the underlying carbon fibre surface, could be understood to be effectively part of the fibre's surface structure.

#### 4.5 Effect of jet fire on CCs with additives: Propane burner experiments

##### 4.5.1 Effects of exposure time on damage to carbon fibres within CC with added flame retardants and nano-additives

All composites were exposed to the propane flame for 1, 3 and 5min. After 1min all composites were intact and it was not possible to remove single fibres as they were still bound by epoxy resin. However, fibres were easily removed from the residual composites after 3 and 5min. Below in Figure 4.34 are digital photographs of the composites after exposure to the propane flame for 5min. CC\_APP and CC\_DOPO composites showed higher apparent char residues on P1 at thermocouple T3, as opposed to P1 at T1 which was the part of the composite in contact with the propane flame.

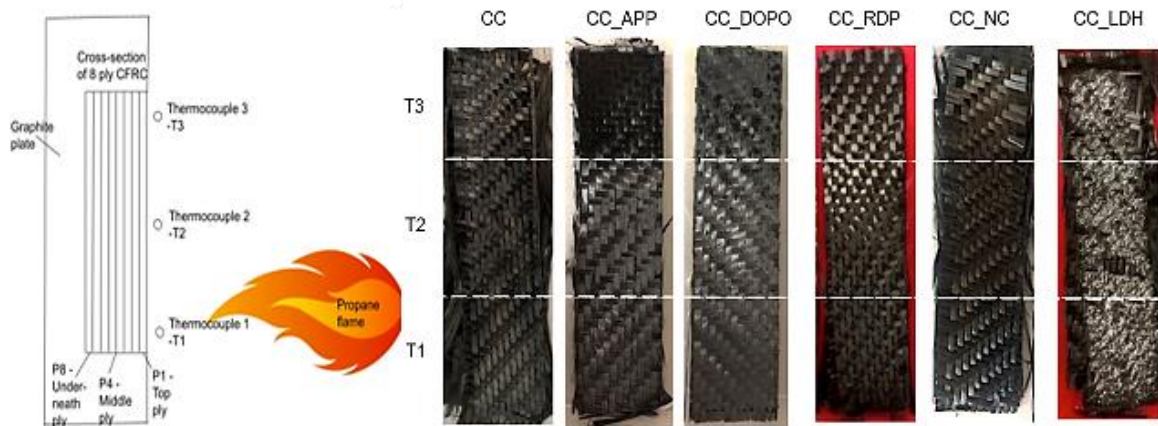


Figure 4.34. Digital photographs of composites after exposure to propane flame for 5min.

##### 4.5.2 Effects of propane flame on carbon fibres within CC with added flame retardants and nano-additives

Along with the composites used in the cone calorimeter experiments (Table 4.7) CC containing 0.5wt% graphene oxide (CC\_GO) and 1wt% nano-tubes (CC\_NT) were also exposed to the

propane burner for 5min. Table 4.14 gives the flame-out time and residual mass of CC and each of these composites, for varying exposure times to the propane flame. Increasing the exposure time, increased each sample's mass loss. During the first 1min, CC lost the least mass while CC\_APP lost more mass than other samples, indicating that APP catalysed the decomposition of the resin. Between 1 and 3min exposure major mass losses occurred as the epoxy resin pyrolysed. However, between 3 and 5min the mass did not reduce significantly and further, indicating most of the resin had completely decomposed within the first 3min.

Table 4.14. FO and residual mass of composites exposed to  $116\text{kWm}^{-2}$  300s.

Sample	Flame-out times at exposure time/min		Residual mass, % at exposure time, min			
	3	5	1	3	5	10
CC	160	153	89.3	65.6	61.3	46.6
CC_APP	175	182	69.1	57.5	55.8	-
CC_DOPO	181	200	81.6	67.4	66.2	-
CC_RDP	89	80	72.7	70.6	69.2	-
CC_NC	138	142	83.3	67.1	64.6	-
CC_LDH	165	102	81.5	66.6	62.1	-
CC_GO	-	153	-	-	71.1	-
CC_CNT	-	145	-	-	65.1	-

'-' = test not performed.

Composites CC, CC\_GO and CC\_CNT had similar flame-out times. It has been proposed that due to the hydroxyl and carboxyl functional groups on the surface of GO, it can dilute combustible gas produced during the resin decomposition, therefore slowing burning [41]. CNT particles, similarly to NC, can migrate to the surface and form an interlocking char barrier, thus stopping volatiles escaping to fuel combustion while also reflecting heat [42]. However, the inclusion of these did not affect the flame-out time, which potentially was due to the low mass percentages present and their presence on the surface.



The addition of both APP and DOPO increased the flame-out time. With the exception of CC\_LDH, flame-out values for the other composites for 3 and 5min exposures were fairly close, as were the percentage mass losses at these exposure times. As expected, CC\_RDP had a significantly reduced flame-out time compared to the other composites. However, this did not translate to a notable decrease in mass loss. While CC\_DOPO also works in the gas phase, a reduction in flame-out time was not seen.

The CC\_APP composite showed the greatest mass loss at each exposure time (1, 3 and 5min), which was surprising, as APP had shown excellent char-forming ability during cone calorimeter tests. Only the CC control was exposed for 10min. The total mass loss was 53.4wt%, this was less than the 60.1wt% lost under the cone calorimeter at  $75\text{kWm}^{-2}$  with spark ignition, indicating that high heat fluxes (above  $60\text{kWm}^{-2}$ ) cause CC to combust and loses a similar amount of mass.

#### **4.5.3 Identification of damage to carbon fibres within composites with additives exposed to a propane flame for 5 minutes**

Fibres from different distances from the flame (T) and plies (P) were removed from the composites exposed to the propane flame for 5min (outlined in Section 2.4.4, see also Figure 4.11). The mean diameter of fibres was taken from measuring twenty single fibres using an SEM. These are given in Table 4.15 along with the average temperature measured by the thermocouples over the 5min period.

Table 4.15. Mean CF diameters removed from different plies within the composites after exposure to propane flame for 5min.

Sample	Thermo -couple	Average temp recorded by thermocouple, °C	Mean Diameter, $\mu\text{m}$		
			P1	P4	P8
CC	T1	993	$6.79 \pm 0.14$	$6.98 \pm 0.22$	$6.96 \pm 0.14$
	T2	866	$7.38 \pm 0.13$	$7.27 \pm 0.13$	$7.28 \pm 0.12$
	T3	785	$7.27 \pm 0.13$	$7.32 \pm 0.16$	$7.43 \pm 0.15$
CC_APP	T1	1001	$5.92 \pm 0.15$	$7.03 \pm 0.04$	$7.04 \pm 0.08$
	T2	870	$6.65 \pm 0.12$	$7.27 \pm 0.10$	$7.34 \pm 0.07$
	T3	772	$7.22 \pm 0.10$	$7.46 \pm 0.12$	$7.50 \pm 0.14$
CC_DOPO	T1	986	$6.85 \pm 0.07$	$7.00 \pm 0.05$	$7.16 \pm 0.07$
	T2	880	$6.92 \pm 0.06$	$7.20 \pm 0.08$	$7.31 \pm 0.07$
	T3	779	$7.37 \pm 0.06$	$7.30 \pm 0.11$	$7.38 \pm 0.06$
CC_RDP	T1	1001	$6.82 \pm 0.07$	$6.51 \pm 0.12$	$6.89 \pm 0.02$
	T2	871	$7.16 \pm 0.04$	$7.01 \pm 0.08$	$6.81 \pm 0.04$
	T3	781	$7.02 \pm 0.09$	$7.27 \pm 0.07$	$7.02 \pm 0.04$
			P1	P5	P10
CC_NC	T1	970	$7.01 \pm 0.14$	$7.32 \pm 0.08$	$7.04 \pm 0.12$
	T2	846	$7.00 \pm 0.11$	$7.33 \pm 0.16$	$7.39 \pm 0.13$
	T3	777	$7.10 \pm 0.13$	$7.43 \pm 0.11$	$7.29 \pm 0.15$
CC_LDH	T1	1003	$7.04 \pm 0.11$	$7.12 \pm 0.09$	$7.12 \pm 0.13$
	T2	896	$7.24 \pm 0.09$	$7.36 \pm 0.10$	$7.16 \pm 0.14$
	T3	791	$7.31 \pm 0.11$	$7.57 \pm 0.10$	$7.42 \pm 0.13$
CC_GO	T1	997	$7.07 \pm 0.10$	$7.14 \pm 0.13$	$7.00 \pm 0.14$
	T2	869	$7.23 \pm 0.10$	$7.34 \pm 0.13$	$7.33 \pm 0.10$
	T3	780	$7.31 \pm 0.12$	$7.34 \pm 0.11$	$7.40 \pm 0.09$
CC_CNT	T1	983	$6.14 \pm 0.12$	$6.90 \pm 0.11$	$7.25 \pm 0.11$
	T2	865	$6.52 \pm 0.17$	$7.16 \pm 0.10$	$7.23 \pm 0.13$
	T3	775	$7.25 \pm 0.08$	$7.45 \pm 0.10$	$7.47 \pm 0.09$

\*‘Average’ temperature was taken over 5min from the temperatures recorded by each thermocouple

The general trend for all fibre diameters for all composites was that fibres in direct contact with the flame (ply P1 at temperature T1) had the greatest reductions in fibre diameter, while those furthest from the flame, on the underneath of the composite (P8/P10 at T3), showed the least reductions. Given that all the temperatures in Table 4.15 are well above the onset of oxidation temperature for the TR30S carbon fibres (538°C) and the resin’s decomposition temperature of 232°C (TGA in Figure 4.1), it is surprising what a significant difference between exposure to (approximately) 780°C and 1000°C, had on the degree of oxidation in terms of changes in diameter, of fibres removed from composites CC, CC\_APP, CC\_DOPO, CC\_GO and CC\_CNT.

As seen in Section 4.3.3 for CC, fibres from ply P8 at T3 had the least reduction in fibre diameter. As the composites were mounted in a graphite plate, the above plies impeded the flow of oxygen, therefore reducing the rate of fibre oxidation. With the exception of CC\_RDP and CC\_NC, all fibres measured from underneath the composite (P8/P10) at T3, had a similar diameter within error of the CF ( $7.68 \pm 0.23\mu\text{m}$ ). The mean diameter results for fibres removed from P1 of the CC\_APP were unexpected in terms of their apparent extreme reduction. In previous cone calorimeter testing at  $75\text{kWm}^{-2}$ , the addition of 15wt% APP (Section 4.2.2) resulted in a protective phosphorus-containing char forming on the fibres, preventing heat damage and oxidation of the fibres. Yet during the 5min exposure to the propane flame (heat flux of  $116\text{kWm}^{-2}$ ) fibres from P1 experienced more surface damage and oxidation than those from CC. SEM images of fibres removed from P1 at T1, T2, and T3 of composites with flame retardants are given in Figure 4.35.

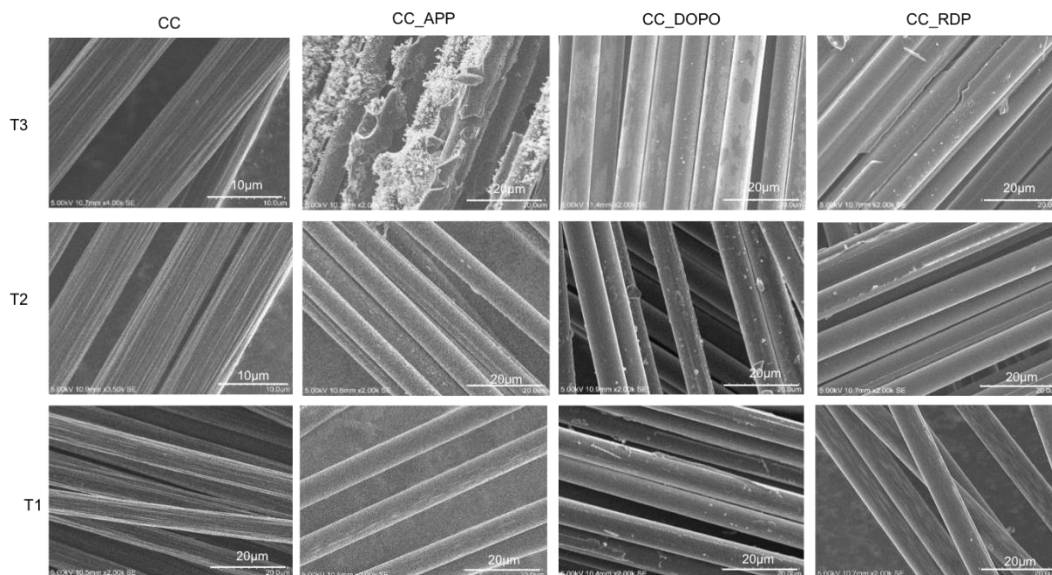


Figure 4.35. SEM images of fibres removed from P1 at T1, T2, and T3 of composites with phosphorus-containing flame retardants after 5min.

Char residue was not observed on any section of P1 CC fibres. However, on CC\_APP fibres a large amount of char had formed at P1, T3. Given that thermocouple T1 recorded an average temperature of 1001°C, while T3 recorded an average of 772°C, the lack of char on the lower half of CC\_APP indicated that at temperatures above 800°C the char residue had begun to oxidise and had been entirely oxidised at 1000°C. However, there was also a secondary factor attached to these tests. During cone calorimetric testing, heat is applied from the cone's heater on one side of the composite, and there were no additional forces applied. But with the propane burner set up, there is the pressure of gas directed at the composite (gas pressure of 2.2 bar located at 1m away) which could have blown away large pieces of char residue, thereby exposing the fibres during the 5min test. Furthermore, the additional oxidation of the carbon fibres in ply P1 at T1 of CC\_APP may also indicate a reaction between the APP char residue and carbon fibres at temperature ~1000°C. Traces of phosphorus oxides, such as phosphorus pentoxide could sensitise the carbon fibre to oxidation [40]. This did not occur in CC\_DOPO and CC\_RDP, which retained a greater fibre diameter, as these FRs are gas phase active.

CC\_DOPO performed better than CC\_APP in the propane burner tests. Fibres from P1, T1 were the only fibres to show speckles of what appears to be char residue and char was only found on

fibres removed from P1 T2 and T3 positions. SEM images showed residue almost bonding fibres together at P1, T3 of CC\_RDP. EDX was carried out on these fibres and confirmed the presence of phosphorus in the char (Figure 4.36). While this char appeared to have encased the individual fibres, it did not bind them together.

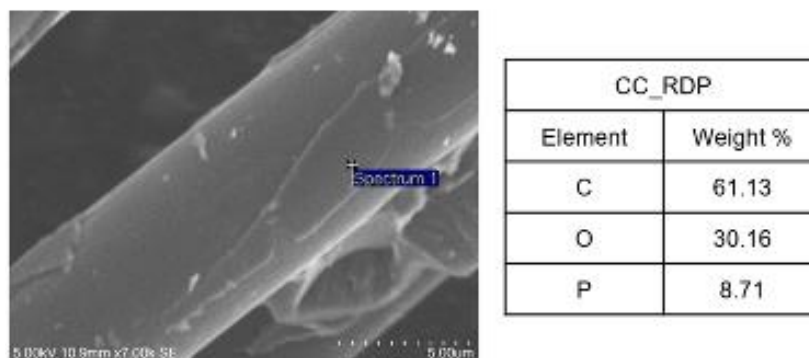


Figure 4.36. SEM and EDX of CC\_RDP from P1, T3.

In order to further understand the char formation, fibres were removed from P8 of the composites at T1 and T3 positions (Figure 4.37). Char was attached to all fibres removed from P8, with the least attached to that of CC at T1. The char on P8 of CC did not bind any carbon fibres together. On P8, T3 of CC\_APP, char had covered all fibres and bound them together. Similarly larger aggregates of char were found on CC\_DOPO (P8 T3 and T1) fibre surfaces, which suggested that DOPO was also effective at working in the condensed phase during the 5min propane burner test as noted previously (see Tables 4.6 (TGA) and 4.7 (cone calorimetry)) as might be expected from its gas phase activity and previous TGA results (Table 4.6) although cone calorimetric residue results suggest otherwise (Table 4.7). While char was seen on ply P8 of CC\_RDP, this did not appear to be more than on CC. The fibre diameters from P8 of CC\_RDP were less than that of CC and the other composites indicating that the lack of protective char meant increased fibre oxidation.

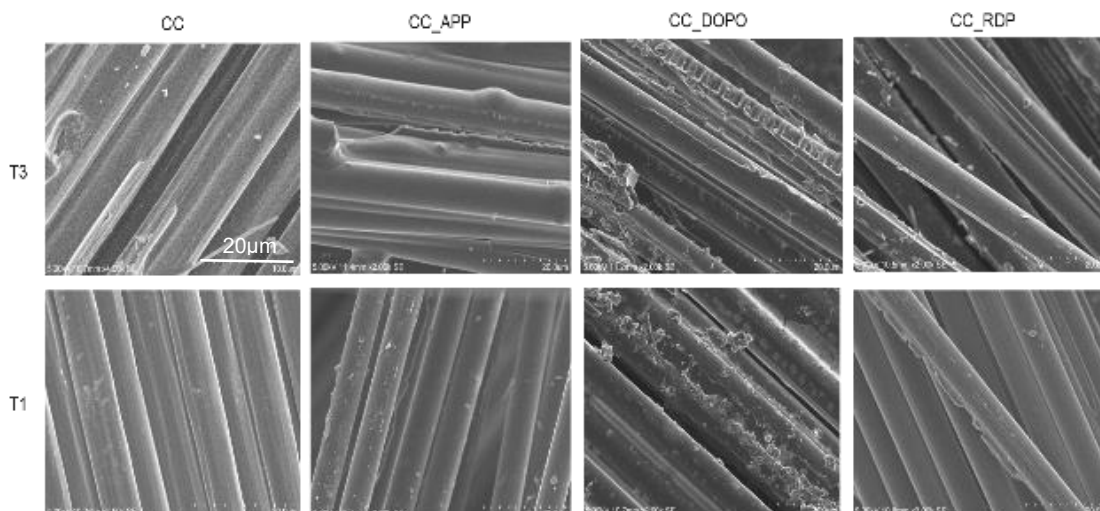


Figure 4.37. Fibres removed from P8 of CC and CC with phosphorus-containing flame retardants after 5min.

CC\_LD<sub>H</sub> was covered in a white powder residue, most likely from the residual inorganic LDH, composed of C, O, Mg, Al and trace amounts of Zn and Si [22], as well as MgO and Al<sub>2</sub>O<sub>3</sub>, which are white powders when pure. EDX was carried out on fibres from P1 and these images are presented next to a digital photo of exposed CC\_LD<sub>H</sub> in Figure 4.38(a). EDX identified the presence of carbon, oxygen and magnesium Figure 4.38(b). The magnesium may be in the form of MgO, as this can be formed at temperatures as low as 700°C to 1000°C. EDX of char from CC\_NC is also given in Figure 4.38(c) for comparison that contained only carbon and oxygen.

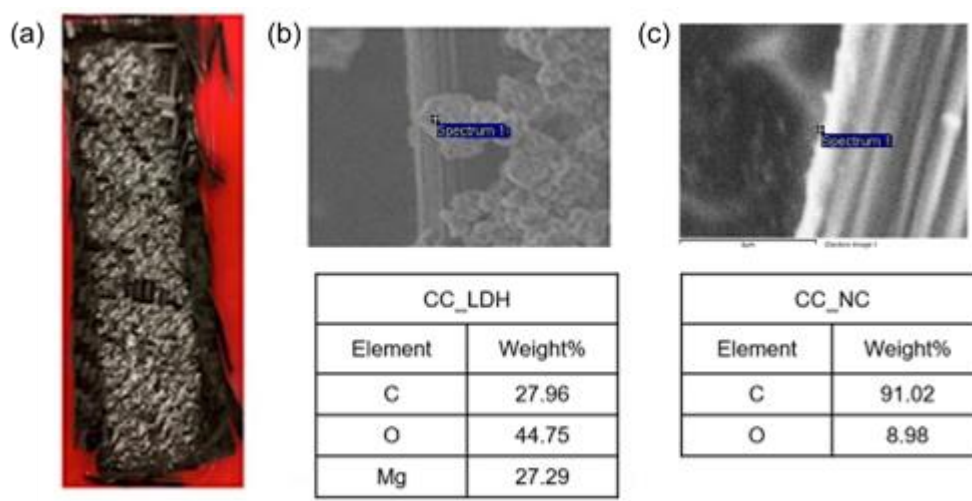


Figure 4.38. (a) Digital image, EDX from Ply P1 of (b) CC\_LD<sub>H</sub> (c) CC\_NC.

This residue did not seem to bind the fibres together, as char had in the SEM images for ply 8 T3 of CC\_APP and CC\_DOPO fibres. But a potential benefit of including LDH is that MgO is not conductive and would reduce the overall electrical conductivity of the heat-damaged CC. This does not remain true for CC\_GO and CC\_CNT. Carbon containing nano-additives are often included to increase the composites' electrical conductivity, for example in the aviation industry where there is the threat of lightning strikes [43].

All P1 fibres from CC\_LDH and CC\_NC exposed samples had significantly reduced diameters compared to those from ply P5. In Figure 4.39, are SEM images of fibres from the different plies at position T1 (in direct contact with the flame) for CC\_NC, CC\_LDH and CC\_GO, along with fibres furthest from the flame at P10, T3. Fibres at P1, T1 from CC\_LDH showed pitting (Figure 4.17). This was not seen in CC or CC composites with phosphorus-containing flame retardants. However, this pitting did not lead to a greater reduction in fibre diameter, instead it was localised and only on the fibres in direct contact with the flame. It is likely due to the volatilisation of contaminant particles or the catalytic effect of MgO, that sensitise local carbon oxidation. Fragments of residue and oxide particles were seen on fibres removed from P5, T1. For P10 T3, fibres furthest from the flame, extremely large amounts of residue were found. In CC\_LDH this char was mixed with what appear to be metal oxide deposits. The inclusion of GO at 0.5wt% resulted in an increased amount of char on P10, T3 compared to P8, T3 CC (Figure 4.37). Combined with having the greatest residual mass after 5min exposure (Table 4.14), the apparently high level of char present was effective at providing oxidation protection to the underlying carbon fibres.

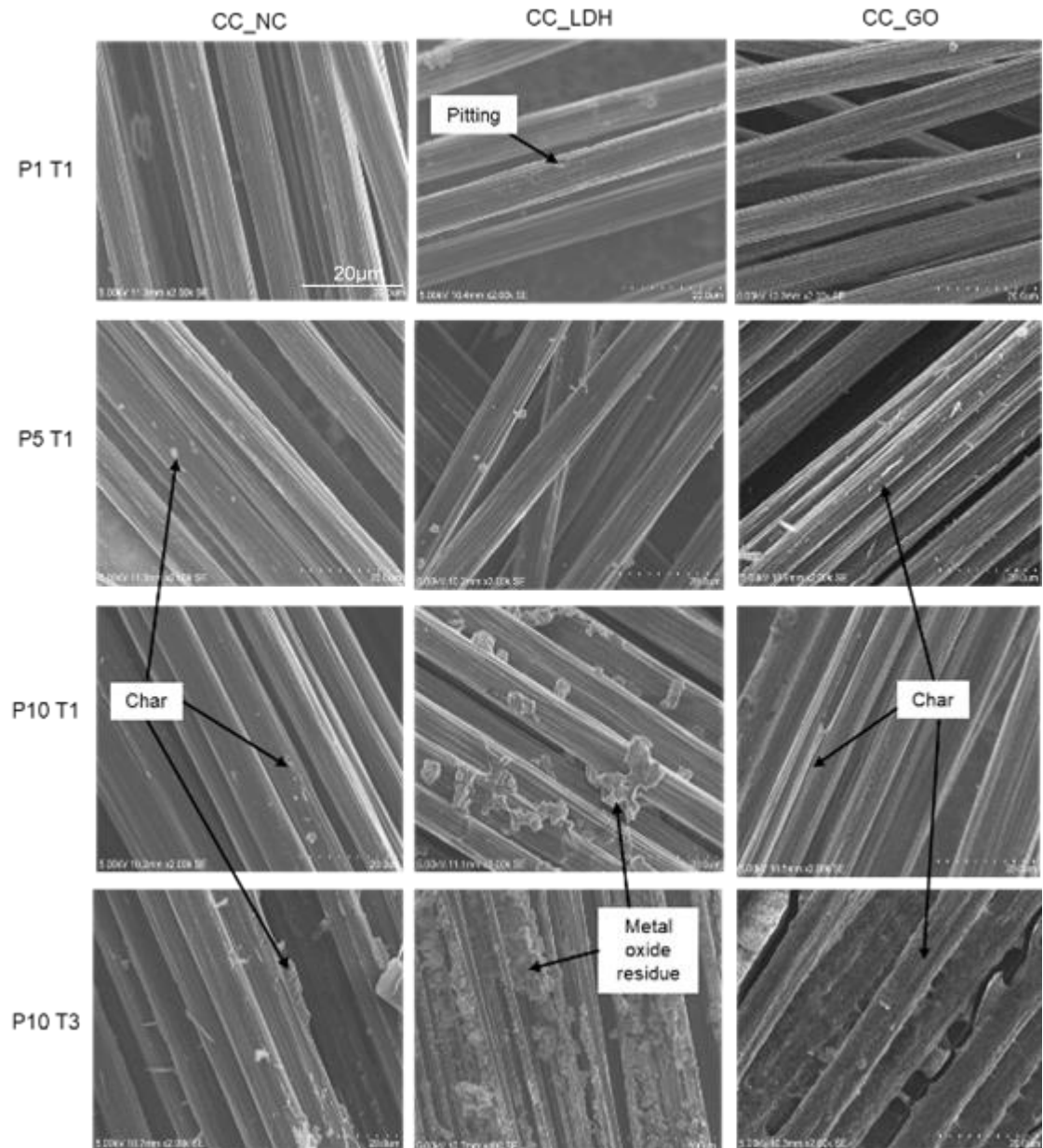


Figure 4.39. SEM images of fibres from the difference piles at position T1 for CC\_NC, CC\_LDH and CC\_GO, along with fibres furthest from the flame at P10, T3.

Similarly exposed CC\_CNT composite had 6wt% less residual mass than CC\_GO (Table 4.14) and fibres removed from ply P1 had reduced diameters compared to those from the control CC. Yet fibres removed from P10, T3 had the second largest average fibre diameter of composites tested (Table 4.15). Figure 4.40 shows SEM images of fibres removed from P1, T1 and P10, T3. The high number of pits on fibres from the former condition and which were in contact with the flames suggested it was not only due to volatilisation of contaminant particles but also



probably to localised oxidation promoted or catalysed by the CNT particles present. Pitting was seen on parts of the fibres that were in contact with the non-luminous zone of the flame, where there was a high concentration of oxygen and hydrogen radicals [12]. While a significant amount of protective char was formed on sections of CC\_CNT away from the flame (P10, T3), the extent of damage to P1 possibly negates any benefit of using it as a potential flame retardant.

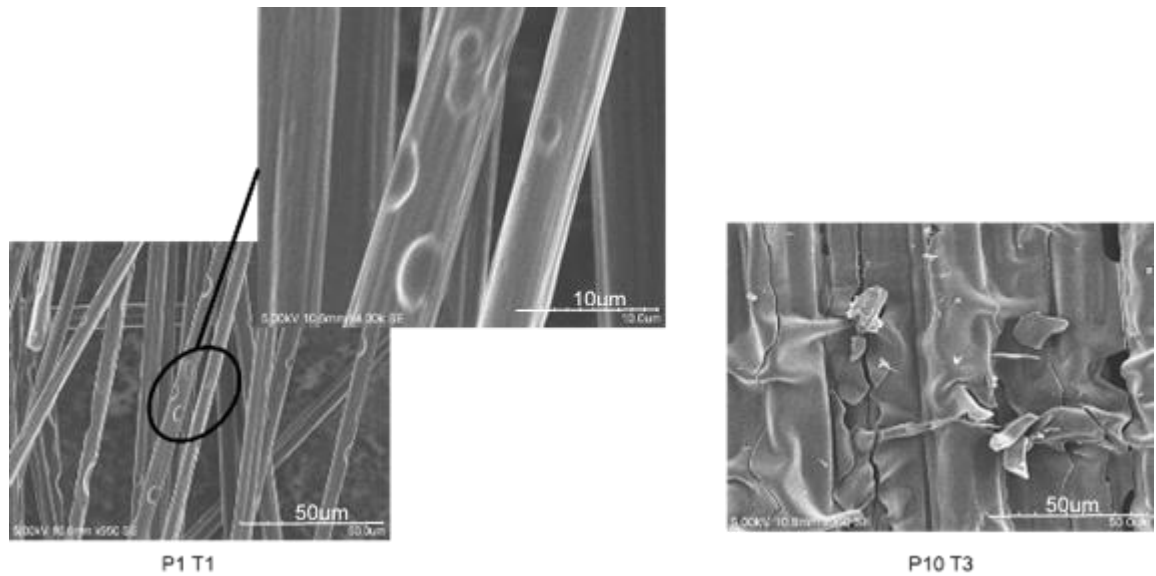


Figure 4.40. SEM images of fibres from CC\_CNT at P1, T1 and P10, T3.

#### 4.5.4 Electrical resistivity of carbon fibres after propane burner testing ( $116\text{kWm}^{-2}$ , 300s)

After exposure to the propane burner, fibres were removed from ply P1, T1 of the composites and their electrical resistivity measured (as in Section 4.4.3.2) and are given in Table 4.16. These fibres were tested as they were in direct contact with the propane flame and in the flame zone having the greatest number of hydrogen and oxygen free radicals. After 10min exposure fibres from CC resistivity had increased by 17.1% while after 5min it has only increased by 6.3% compared to the CF. This larger increase was attributed to the hollowing of the carbon fibre core after 10min expose, as seen in Figure 4.13.

Table 4.16. Mean electrical resistivity of CF at T1, from different plies of composites exposed to 116Wm<sup>-2</sup>.

Exposure time, min	Sample	Resistivity, $\Omega\text{m } 10^{-5}$
10	CC	$2.51 \pm 0.17$
5	CC	$2.22 \pm 0.29$
	CC_APP	$1.00 \pm 0.04$
	CC_DOPO	$1.75 \pm 0.15$
	CC_RDP	$1.54 \pm 0.06$
	CC_LDH	$2.54 \pm 0.26$
	CC_NC	$2.09 \pm 0.18$
	CC_CNT	$2.07 \pm 0.23$
	CC_GO	$1.94 \pm 0.29$
CF		$2.08 \pm 0.13$

The results in Table 4.16 show a similar trend to those given in Table 4.10, whereby after heat testing, fibres removed from P1 of the composites containing flame retardants had a notable decrease in resistivity. This was again attributed to the phosphorus-containing species in the char attached to the fibres (seen in Figure 4.35) and identified by EDX.

For fibres removed from exposed CC\_NC, CC\_CNT and CC\_GO composites had values that were within error that of the CF. While pits were observed on the surface of the fibres removed from CC\_CNT (Figure 4.40), these did not translate into a change in electrical resistivity, suggesting they are only a surface feature. Unlike when CC\_NC was exposed to the cone calorimeter, the residual fibres removed from after the propane burner did not have an increase in resistivity. This is most likely due to the physical force of the flame/propane gas displacing any insulating residue which may have formed on fibre surfaces. CC\_LDH, however, had an increase in resistivity. In Figure 4.38, the metal oxide aggregate particles are visible on the top surface ply P1 fibres. Unlike the nano-size particles in CC\_NC, as LDH first dehydrates, it

leaves behind a residue consisting of complex networks of metal hydroxides/oxides which were too large to be displaced by the propane flame.

#### 4.5.5 Mechanical properties of carbon fibres from composites after propane burner testing ( $116\text{kWm}^{-2}$ , 300s)

Single fibre tensile tests were carried out on carbon fibres removed from ply P1 of composites exposed to the propane burner test and the results are given in Table 4.17. Fibres removed from CC, after exposure to the propane burner ( $116\text{kWm}^{-2}$ , 300s), tensile strength decreased by 18%. The reduction in strength was attributed to localised areas of oxidation, as outlined in Section 4.4.4.

Table 4.17. Mean tensile strength and modulus for P1 carbon fibres removed from composites after heat testing ( $116\text{kWm}^{-2}$ , 300s).

Sample	Tensile Strength, MPa	Modulus, GPa	Tensile strength reduction w.r.t CF*, %	Modulus reduction w.r.t CF**, %
CC	$3364 \pm 376$	$219 \pm 13$	$18 \pm 9$	$6 \pm 6$
CC_APP	$3428 \pm 374$	$264 \pm 6$	$16 \pm 9$	$-13 \pm 3$
CC_DOPO	$3576 \pm 245$	$228 \pm 6$	$13 \pm 6$	$3 \pm 3$
CC_RDP	$4021 \pm 288$	$231 \pm 15$	$2 \pm 7$	$1 \pm 6$
CC_LDH	$2259 \pm 375$	$212 \pm 8$	$45 \pm 9$	$9 \pm 3$
CC_NC	$2980 \pm 154$	$243 \pm 8$	$28 \pm 4$	$-4 \pm 3$
CC_CNT	$2339 \pm 489$	$267 \pm 31$	$43 \pm 12$	$-14 \pm 13$
CC_GO	$2682 \pm 385$	$220 \pm 21$	$35 \pm 9$	

\*with respect to as-received control carbon fibre

\*\* '-' denotes an increase in modulus w.r.t CF

Residual fibres from P1 CC\_RDP had a tensile strength and modulus values within error of those of the CF. This was similar to the result found after cone calorimetric exposure ( $75\text{kWm}^{-2}$ , 600s). However, residual fibres from exposed CC\_APP did not perform as well, with a reduction in strength now within error of CC. In [39] they found that the tensile strength of T700 carbon fibres reduced when exposed to the temperature range  $400\text{--}700^{\circ}\text{C}$  in both air and inert atmospheres. They concluded that fibre strength was unaffected by oxygen content of the atmosphere during fire. Therefore, it is unlikely that the oxygen content in the propane burner flame (compared to the radiant heat source of the cone) was the reason for the CC\_APP reduced strength. It is more likely due to the physical force of the flame removing surface charring particles during the test, thereby preventing formation of the protective char barrier seen when testing with the cone calorimeter. The exposed fibres from CC\_APP therefore behaved more like those from CC, hence their similar reduction in strength.

Composites with nano-additives showed a decrease in carbon fibre tensile strength compared to the CC value. Residual fibres from CC\_NC were just out of error of the CC value (as also seen in Table 4.11, Section 4.4.4). Those from CC\_GO also had a lower tensile strength than CC fibre values and this was surprising as these fibres had the least fibre diameter reduction of those exposed to the propane flame and showed little evidence of surface damage. P1 residual fibres from both CC\_LDH and CC\_CNT had the lowest tensile strengths. These fibres also showed the greatest amount of surface damage in the form of pits. In Figure 4.40, some fibres from CC\_CNT were more heavily damaged than others; this was reflected in the large tensile strength error associated with these fibres, indicating that the surface damage was the cause of reduced tensile strength.

Figure 4.41 shows a plot of fibre diameter versus tensile strength. As seen in Section 4.4.4, Figure 4.23, no relationship was found between fibre diameter and tensile strength.

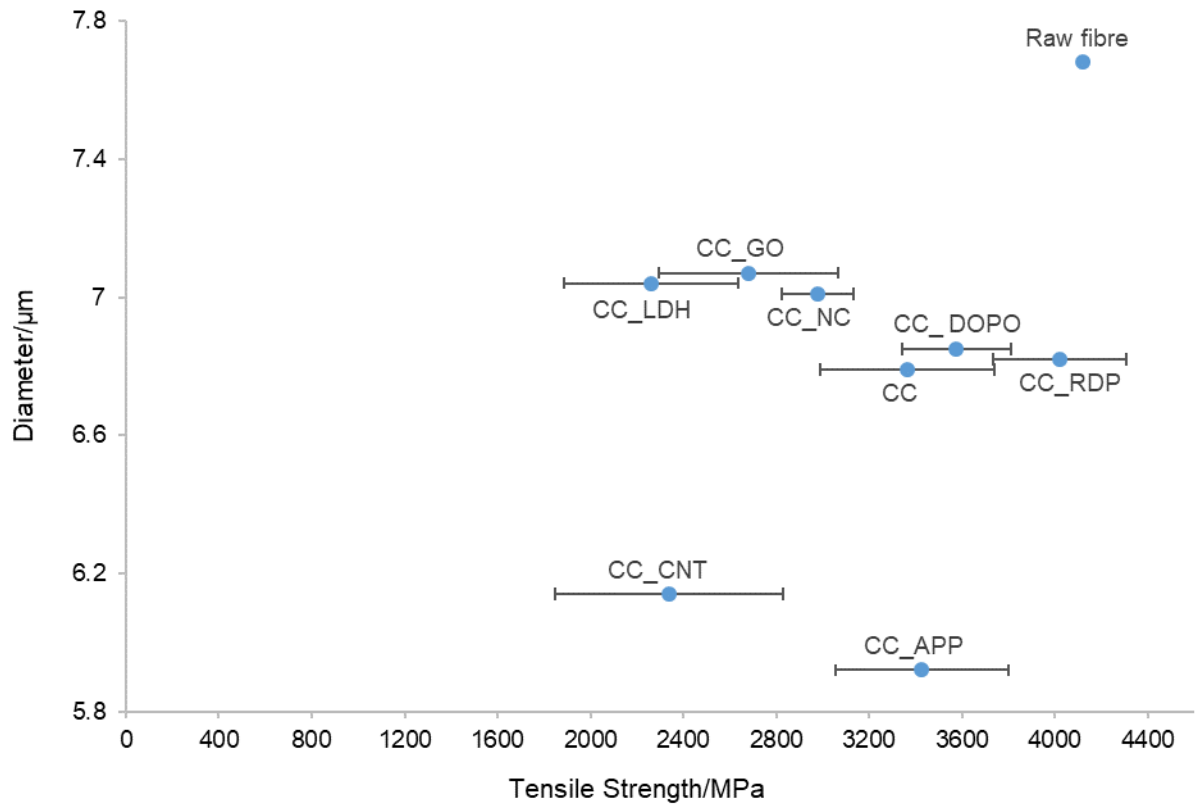


Figure 4.41. Fibre diameter vs tensile strength for fibres removed from P1 after propane burner testing at  $116\text{kWm}^{-2}$  for 300s.

Interestingly, with the exception of CC\_APP and CC\_LDH, the modulus values of the residual fibres (Table 4.17) were almost within error of the CF average value. As the propane burner test was half the length of time as exposure to the cone calorimeter, potential graphitisation of the carbon fibres during heat testing did not have time to occur. Fibres from CC\_APP and CC\_CNT showed similar increases in fibre modulus.

## 4.6 Conclusions

- The control CC composite auto-ignites when exposed to a heat flux of  $35\text{kWm}^{-2}$  and above. However, over a period of 600s, the minimum heat flux required to cause oxidation to the component carbon fibres is  $60\text{kWm}^{-2}$ .

- At a heat flux of  $75\text{kWm}^{-2}$  for 600s only surface oxidation was seen on the fibres and no internal voiding.
- Cone calorimeter testing at  $75\text{kWm}^{-2}$  showed that the addition of 15wt% APP resulted in large char formation and adherence to fibres in the underlying plies which results in less oxidation to these carbon fibres.
- Inclusion of phosphorus-containing flame retardants in CCs, reduces their overall electrical conductivity generally. However, after combustion of these composites, phosphorus-containing species within the char adhering to the carbon fibre appear to be the cause of the observed increased electrical conductivity.
- During testing with a propane burner ( $116\text{kWm}^{-2}$ ), the CC control lost mass within the first minute due to resin decomposition. During the next two minutes, most mass loss observed occurred during this period and between 3 and 5min exposure, only a small additional amount of mass was lost. However, after 10min there was significant loss of mass due to oxidation of the char and fibres. As well as, internal oxidation of fibres at P1, T1 which was credited to the high concentration of oxygen and hydrogen radicals in the flame.
- After 5min exposure to the propane flame, significantly less char was observed on ply P1 (in direct contact with the flame) than on the part of the composites on the flames edge. This was attributed to two things:
  - 1) The increased temperature (approximately  $1000^{\circ}\text{C}$  directly in the flame, as opposed to  $780^{\circ}\text{C}$  on the edge of the flame) led to oxidation of the char residue.
  - 2) The physical force of the flame/propane gas displaced any char residue formed.
- Additional oxidation of the carbon fibres in ply P1 at T1 of CC\_APP may indicate a reaction between the APP char residue and carbon fibres at higher than  $1000^{\circ}\text{C}$ . Potentially phosphorus

oxides could sensitise the carbon fibre to oxidation. Further work is required to identify if these oxides were present.

- Exposure of CC\_LDH and CC\_CNT to the propane flame for 5min resulted in pitting and localised oxidation of the carbon fibre. For CC\_LDH this was linked to the oxides produced when LDH thermally decomposes. While for CNT it was due to the additionally carbon content. The residual P1 fibres also showed the greatest reduction in tensile strength due to pits acting as stress concentrators.

## 4.7 References

- [1] Liu, Q., Wang, D., Li, Z., Li, Z., Peng, X., Liu, C., Zhang, Y., Zheng, P., Recent Developments in the Flame-Retardant System of Epoxy Resin. *Materials*, 13, 2145, (2020).
- [2] Zhang, W., He, X., Song, T., Jiao, Q., Yang, R., The influence of the phosphorus-based flame retardant on the flame retardancy of the epoxy resins, *Polymer Degradation and Stability*, Volume 109, Pages 209-217, (2014).
- [3] Katsoulis, C., Kandare, E., Kandola, B. K., The combined effect of epoxy nanocomposites and phosphorus flame retardant additives on thermal and fire reaction properties of fiber-reinforced composites. *Journal of Fire Sciences*. 29(4):361-383, (2011).
- [4] Chapple, R., Effect of Simultaneous impact and heat/Fire on carbon fibre reinforced composites containing nano-additives, PhD thesis, University of Bolton, UK, (2021).
- [5] Mouritz, A. P., *Fire Properties of Polymer Composite Materials*, Volume 143, ISBN: 978-1-4020-5355-9, (2006).
- [6] *Flammability Properties of Aircraft Carbon-Fiber Structural Composite*, DOT/FAA/AR-07/57, Federal Aviation Administration, October (2007).
- [7] Filipczak R., Lyon. R. E., The correlation of Heat Release Calorimetry Measurements DOT/FAA/AR-TN02/104 Federal Aviation Administration, November (2002).
- [8] Gibson, A. G., Wan-Jusoh, W. N. B., Kotsikos, G. A., Propane burner test for passive fire protection (PFP) formulations containing added halloysite, carbon nanotubes and graphene, *Polymer Degradation and Stability*, Vol 148, (2018).
- [9] Brown, A. L., Dodd, A. B., Pickett, B. M., *Proceedings of the ASME International Mechanical Engineering Congress & Exposition IMECE2011* November 11-17, (2011).
- [10] Su, W. C., and Cheng, Y. S., Deposition of fiber in the human nasal airway. *Aerosol Science and Technology*, 39, 888–901, (2005).
- [11] Inthavong, K., Mouritz, A. P., Dong, J., Tu, J. Y., Inhalation and deposition of carbon and glass composite fibre in the respiratory airway. *Journal of Aerosol Science*, 65, pp. 58–68 (2013).
- [12] Simmons E. L., ESR Measurements of Free Radical Concentration Profiles in the Propane-Oxygen Flame, *Journal of magnetic resonance* 16, 130-135, (1974).



- [13] Hull, T. R., Law, R. J., Bergman, A., Chapter 4 - Environmental Drivers for Replacement of Halogenated Flame Retardants, Editor(s): Constantine D. Papaspyrides, Pantelis Kiliaris, Polymer Green Flame Retardants, Elsevier, Pages 119-179, (2014).
- [14] Kandola, B. K., Magnoni, F., Ebdon, J. R., Flame retardants for epoxy resins: Application-related challenges and solutions, Vinyl and Additive Technology, Volume 28, Issue 1, (2022).
- [15] Kishore, K. and Mohandas, K., Mechanistic studies on the action of ammonium phosphate on polymer fire retardancy, Combustion and Flame, Volume 43, (1981).
- [16] Pomázi, Á., Szolnoki, B., Toldy, A., Flame Retardancy of Low-Viscosity Epoxy Resins and Their Carbon Fibre Reinforced Composites via a Combined Solid and Gas Phase Mechanism. Polymers, 10(10), 1081, (2018).
- [17] Scharrel, B., Balabanovich, A.I., Braun, U., Knoll, U., Artner, J., Ciesielski, M., Döring, M., Perez, R., Sandler, J. K. W., Altstädt, V., Hoffmann, T. and Pospiech, D., Pyrolysis of epoxy resins and fire behavior of epoxy resin composites flame-retarded with 9,10-dihydro-9-oxa-10-phosphaphenanthrene-10-oxide additives. J. Appl. Polym. Sci, (2007).
- [18] Perret, B., Scharrel, B., Stöß, K., Ciesielski, M., Diederichs, J., Döring, M., Krämer, J., Altstädt, V., Novel DOPO-based flame retardants in high-performance carbon fibre epoxy composites for aviation, European Polymer Journal, Volume 47, Issue 5, (2011).
- [19] Wei, Z., Gu, X., Wu, J., Wei, M., Yu, Q., Xiujuan, T., Wang, Z., Performance comparison of epoxy resins modified with diphenylphosphine oxide and DOPO, Materials Behaviour in Fire. Vol 43, Issue 7, pp 892-902, (2019).
- [20] Levchik, S. V., Costa, L., Camino, G., Effect of the fire-retardant, ammonium polyphosphate, on the thermal decomposition of aliphatic polyamides. I. Polyamides 11 and 12, Polymer Degradation and Stability, Volume 36, Issue 1, Pages 31-41, (1992).
- [21] Wang, J. S., Wang, D., Liu, Y., Ge. X., Wang, Y., Polyamide-enhanced flame retardancy of ammonium polyphosphate on epoxy resin, Applied Polymer, Vol 108, Issue 4, (2008).
- [22] Zhu, K., Wang, Y., Tang, D., Wang, Q., Li, H., Huang, Y., Huang, Z., Wu, K., Flame-Retardant Mechanism of Layered Double Hydroxides in Asphalt Binder. Materials (Basel). 12(5):801. doi: 10.3390/ma12050801. PMID: 30857152; PMCID: PMC6427306, (2019).
- [23] Zhang, J., Hereid, J., Hagen, M., Bakirtzis, D., Delichatsios, M. A., Fina, A., Castrovinci, A., Camino, G., Samyn, F., Bourbigot, S., Effects of nanoclay and fire retardants on fire

retardancy of a polymer blend of EVA and LDPE, *Fire Safety Journal*, Volume 44, Issue 4,, Pages 504-513, (2009).

[24] Kang, N-J., Wang, D-Y., Kutlu, B., Zhao, P-C., Leuteritz, A., Wagenknecht, U., A new approach to reducing the flammability of layered double hydroxide (LDH)-based polymer composites: preparation and characterization of dye structure-intercalated LDH and its effect on the flammability of polypropylene-grafted maleic anhydride/d-LDH composites. *ACS applied materials & interfaces*. 5(18):8991-7, (2013).

[25] Babu, H. V., Coluccini, C., Wang D. Y., 8- Functional layered double hydroxides and their use in fire-retardant polymeric materials, *Novel Fire Retardant Polymers and Composite Materials*, p201-238, (2017).

[26] Johari G. P., Electrical properties of epoxy resins. In: Ellis B. (eds) *Chemistry and Technology of Epoxy Resins*. Springer, Dordrecht, (1993).

[27] Monti, M., Rallini, M., Puglia, D., Morphology and electrical properties of graphene-epoxy nanocomposites obtained by different solvent assisted processing methods. *Compos Part A*; 46: 166–172, (2013).

[28] Wajid, A. S., Ahmed, H. S. T., Das, S., High-performance pristine graphene/epoxy composites with enhanced mechanical and electrical properties. *Macromol Mater Eng*; 298: 339–347, (2013).

[29] Imran, K. A., and Shivakumar, K. N., Enhancement of electrical conductivity of epoxy using graphene and determination of their thermo-mechanical properties, *Journal of Reinforced Plastic and Composites*, *Journal of Reinforced Plastics and Composites*, 37(2):118-133, (2018).

[30] Rajini, N., Winnowlin Jappes, J. T., Rajakarunakaran, S., Poornanand, P., Electrical properties of montmorillonite nanoclay reinforced unsaturated polyester nanocomposite, *IEEE-International Conference On Advances In Engineering, Science And Management (ICAESM - 2012)*, Nagapattinam, Tamil Nadu, pp. 141-145, (2012).

[31] Akram, M. W., Fakhar-e-Alam, M., Atif, M. et al. In vitro evaluation of the toxic effects of MgO nanostructure in Hela cell line. *Sci Rep* 8, 4576, (2018).

[32] Alarifi, I. M., Investigation the conductivity of carbon fiber composites focusing on measurement techniques under dynamic and static loads, *Journal of Materials Research and Technology*, Volume 8, Issue 5, Pages 4863-4893, (2019).

- [33] Chávez-Gómez, P., Pelzmann, T., Hall, D. R., Chilian, C., Lebel, L. L., Robert, É., Carbon fiber damage evolution under flame attack and the role of impurities. *Fire and Materials*, Vol 47, issue 2, p 226-240, (2022).
- [34] Sogancioglu, M., Yucel, A., Yel, E., Ahmetli, G., Production of Epoxy Composite from the Pyrolysis Char of Washed PET Wastes, *Energy Procedia*, Volume 118, pages 216-220, (2017).
- [35] Yuan, Y., Yu, B., Shi, Y., Mao, L., Xie, J., Pan, H., Liu, Y., Wang, W., Insight into Hyper-Branched Aluminum Phosphonate in Combination with Multiple Phosphorus Synergies for Fire-Safe Epoxy Resin Composites. *Polymers (Basel)*, Volume 12, Issue 1, 64, (2020).
- [36] Markwart, J. C., Battig, A., Zimmermann, L., Wagner, M., Fischer, J., Schartel, B., Wurm, F. R., Systematically Controlled Decomposition Mechanism in Phosphorus Flame Retardants by Precise Molecular Architecture: P–O vs P–N. *ACS Applied Polymer Materials*, 1, 5, 1118–1128, (2019).
- [37] Zhang, Y., Tao, H., Li, J., Yang, X., Achieving a high-performance P/C anode through P–O–C bond for sodium ion batteries. *Ionics* 26, 3377–3385, (2020).
- [38] Mitsubishi Pyrofil datasheet, accessible here: [https://www.m-chemical.co.jp/en/products/departments/mcc/cfcm/product/\\_icsFiles/afieldfile/2020/01/15/CFtow\\_Jan2020en.pdf](https://www.m-chemical.co.jp/en/products/departments/mcc/cfcm/product/_icsFiles/afieldfile/2020/01/15/CFtow_Jan2020en.pdf)
- [39] Feih, S. and Mouritz, A. P., Tensile properties of carbon fibres and carbon fibre–polymer composites in fire, *Composites Part A: Applied Science and Manufacturing*, Volume 43, Issue 5, Pages 765-77, (2012).
- [40] Camino, G., Costa, L., Trossarelli, L., Study of the mechanism of intumescence in fire retardant polymers: Part I—Thermal degradation of ammonium polyphosphate-pentaerythritol mixtures. *Polymer Degradation and Stability*, Volume 6, Issue 4, Pages 243-252, (1985).
- [41] Liu, Q., Zhao, Y., Gao, S., Yang, X., Fan, R., Zhi, M., Fu, M., Recent advances in the flame retardancy role of graphene and its derivatives in epoxy resin materials, *Composites Part A: Applied Science and Manufacturing*, Volume 149, 106539, (2021).
- [42] Meng, F., Liu, H., Xu, B., Li, S., Liu, J., Liu, L., Gu, T., Xiang, H., CNT film supported MXene/Co<sub>3</sub>O<sub>4</sub> composite interlayers for high performance Li–S batteries. *Applied Physics Letters* 121:12, pages 123901, (2022).

[43] Alemour B, Lim, H. N., Yaacob, M. H., Badran, O., Hassan, M. R., Improving the electrical conductivity of carbon fiber reinforced epoxy composites using reduced graphene oxide. *Materials Res, Express* 6 065607, (2019).

## **Chapter 5. Effects of high performance fibre inclusion in composites on thermal stability of carbon fibres**

### **5.1 Introduction**

The chapter continues to explore methods to improve the structural retention of carbon fibres in CCs when exposed to heat/fire. In the previous chapter flame retardants were added to the resin matrix in order to form protective residue and char barriers on the carbon fibres. In this chapter, additional layer(s) of fibrous non-woven or woven veils made of high temperature resistant materials were added to the composite as layers both at the surface and within in order to provide a heat barrier to the underlying carbon fibres.

Previous work has been carried out by Kandola et al. [1,2] on hybrid glass/carbon and glass/aramid epoxy laminates exposed to the cone calorimeter, which studied the effect of fibre type on its burning behaviour. However, in the present work, fire properties of the composites are secondary to the protection of the residual carbon fibres. Hybrid composites containing either aramid, basalt, E-glass and PPS fibrous veils were exposed to the cone calorimeter at  $75\text{kWm}^{-2}$  and the residual carbon fibres removed from the underlying plies. SEM was used to measure the change in fibre diameter and to study fibre surface damage, along with EDX to determine the chemical composition of any residue adhering to the fibres. Electrical conductivity was also measured. To understand the behaviours of these veils at high temperatures, TGA and TGA-FTIR were used. TGA-FTIR identified the volatiles produced during their thermal decomposition and the potential for interactions between the respective thermal degradation chemistries and adjacent carbon fibres. Short beam shear test was carried out to gain insight to the effect of including hybrid layers on the overall shear strength of the composite.

### **5.2 Characterisation of veils**

#### **5.2.1 Physical properties of veil material**

The mass or area densities of the veils were kept as low as possible so that the mechanical properties of the composites were minimally affected. As well as the selected lightweight veils, a satin 2x2 twill weave Kevlar® cloth with a thickness of 0.47mm and area density of 300gm<sup>-2</sup> was used to provide a comparison with the low mass density veils, particularly the aramid veil which shares a similar chemical structure. In addition, two E-glass veils were used to investigate if the structure (1x1 plain woven or fibrous non-woven) had an effect on the protective properties. The properties of the veils and Kevlar fabric are listed in Table 5.1, including their respective component fibre diameters and approximate melting points taken from the literature.

Table 5.1. Veil densities and approximate melting points.

Veil/fabric	Mass density, gm <sup>-2</sup>	Fibre diameter, µm	Approximate melting point, °C [ref]
Aramid	14	12.11 ± 0.17	500 [3]
Basalt	15	13.38 ± 0.45	1200 [4]
E-glass	17	11.19 ± 0.44	1600 [5]
Woven E-glass	25	4.95 ± 0.07	1600 [5]
Polyphenylene Sulphide	20	10.63 ± 0.33	280 [6]
Kevlar	300	12.12 ± 0.25	426 [7]

The non-woven veils, sourced from a commercial source (TechnoFire, Technical Fibres Ltd) were produced from short chopped fibres in a wet-laid manufacturing process, making them highly porous but with an even fibre distribution and uniformity across the material. The woven E-glass did not contain any chemical binders and is typically used for laminating thin skins, for example on the wings of a drone. Both basalt and E-glass have extremely high melting points. They soften, beginning to lose their structure and physical properties, at 840°C and 960°C respectively [8], thus making them excellent barrier materials in the CCs. Aramid and PPS also have high temperature resistance although they start to decompose at 560°C [9] and around 450 °C [10] respectively. The fibrous non-woven PPS veil was designed to increase the inter-laminar fracture toughness in fibre reinforced composites, making the laminate more resistant to delamination or crack propagation. The veils/fabric selected also have poor electrical

conductivity so will not increase the CC's electrical conductivity. SEM images of the structures of the veils/fabric are given in Figure 5.1.

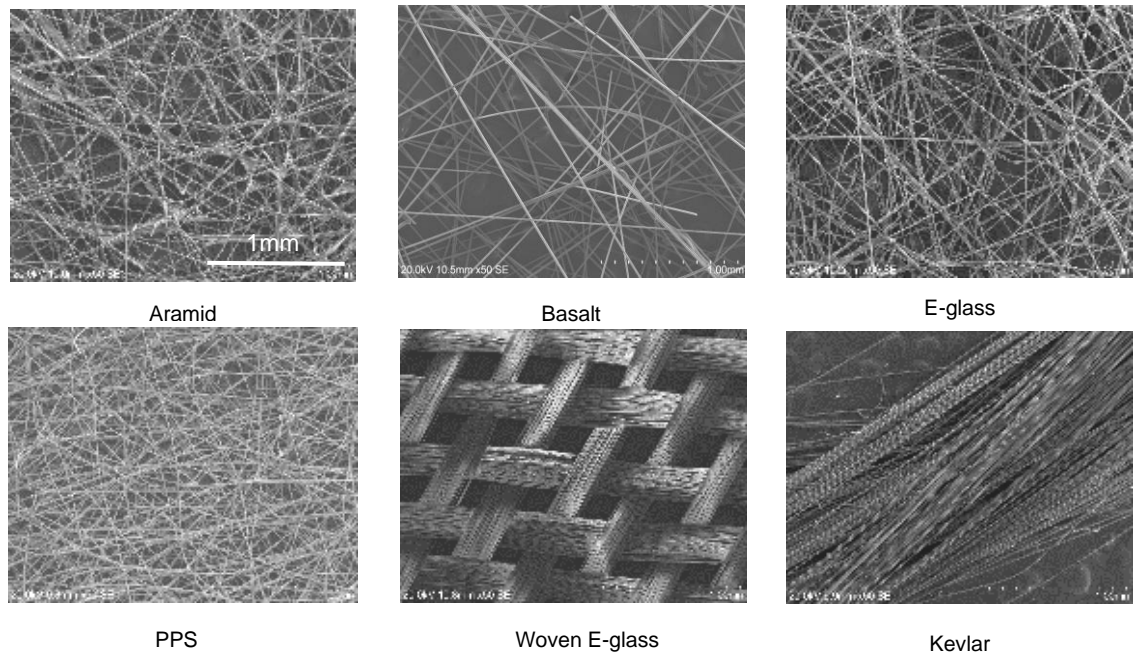


Figure 5.1. SEM images of veils/fabrics taken at the same magnification.

The elemental compositions of these veils/fabric measured using EDX are given in Table 5.2. Where aramid and Kevlar, and both E-glasses, showed very similar element compositions.

Table 5.2. EDX element composition.

Veil/fabric	Weight %											
	C	O	Na	Mg	Al	Si	K	Ca	Cu	Fe	S	Zn
Aramid	75.65	23.59	0.61						0.01			0.23
Basalt	15.58	45.62	1.35	1.62	6.46	18.53	1.04	4.46	0.10	5.23		
E-glass	8.90	50.38	0.48	0.47	5.94	20.71	0.08	12.99	0.03			
Woven E-glass	7.61	56.07	0.26	2.20	5.95	19.67	8.24	7.61				
PPS	77.15										22.85	
Kevlar	73.93	24.77	0.75			0.04					0.50	

### 5.2.2 Thermal stability of veil/fabric materials

TGA was carried on the aramid, Kevlar and PPS veils/fabric in order to study their thermal stability. The TGA responses in air (100ml/min) at a heating rate of 20°C/min are given in Figure 5.2(a), with the DTG responses for these in Figure 5.3. TGAs of E-glass and basalt were not carried out as at high temperatures they melt, sticking to the platinum pan and make it unusable for other TGAs, hence TGA results for E-glass and basalt were taken from the literature. These showed very little mass loss until up to 1200°C [1,11] and are illustrated in Figure 5.2(b) taken from [11].

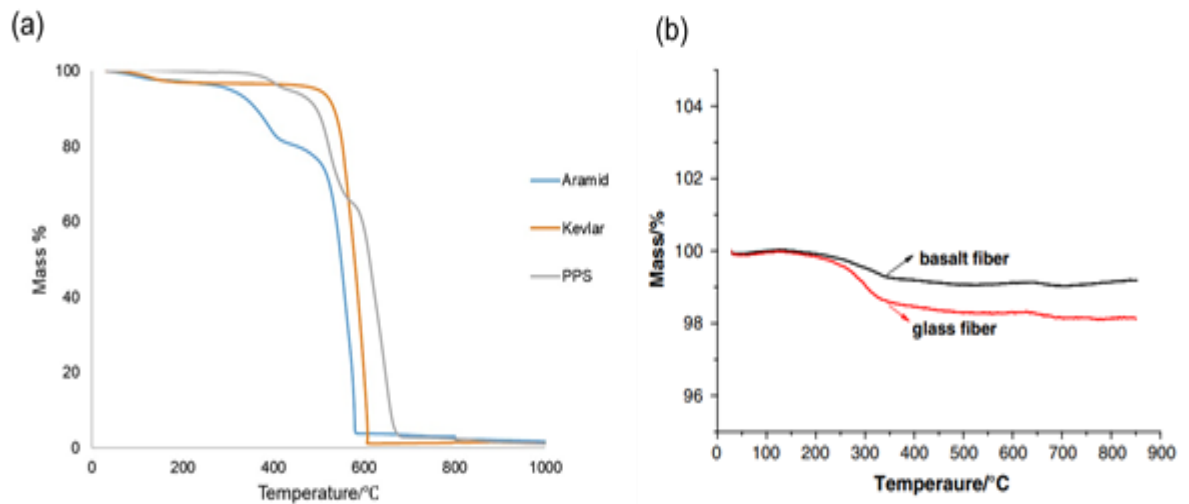


Figure 5.2. TGA responses of (a) aramid, Kevlar and PPS under air 100ml/s at 20°C/min, and (b) basalt and glass fibre taken from [11].

The initial 5wt% loss up to 120°C for both the aramid and Kevlar was due to the evaporation of water, as both materials have 5% moisture content at room temperature [7]. Data from the TGA curves is shown in Table 5.3 and the TGA and DTG are plotted in Figure 5.3, showing the temperature where the maximum mass losses occur.



Table 5.3. Characteristic parameters of the thermal decomposition from TGA curves.

Veil/fabric	T <sub>0t</sub> , °C	T <sub>DTG</sub> , °C	T <sub>res</sub> , °C	Wt% of residue at T <sub>res</sub>
Aramid	305	393; 557; 576	581	3.8
Kevlar	499	603	607	1.2
PPS	431	411; 526; 620(s); 662	685	2.7
E glass [11]	163	-	850	99.3
Basalt [11]	205	-	796	98.2

Where T stands for the temperature at which:

T<sub>0t</sub> = temperature at which 5wt% occurred.

T<sub>DTG</sub>= maximum mass loss occurs (DTG peak).

T<sub>res</sub>= stable residue formed.

‘-‘ data unavailable.

S = small shoulder peak.

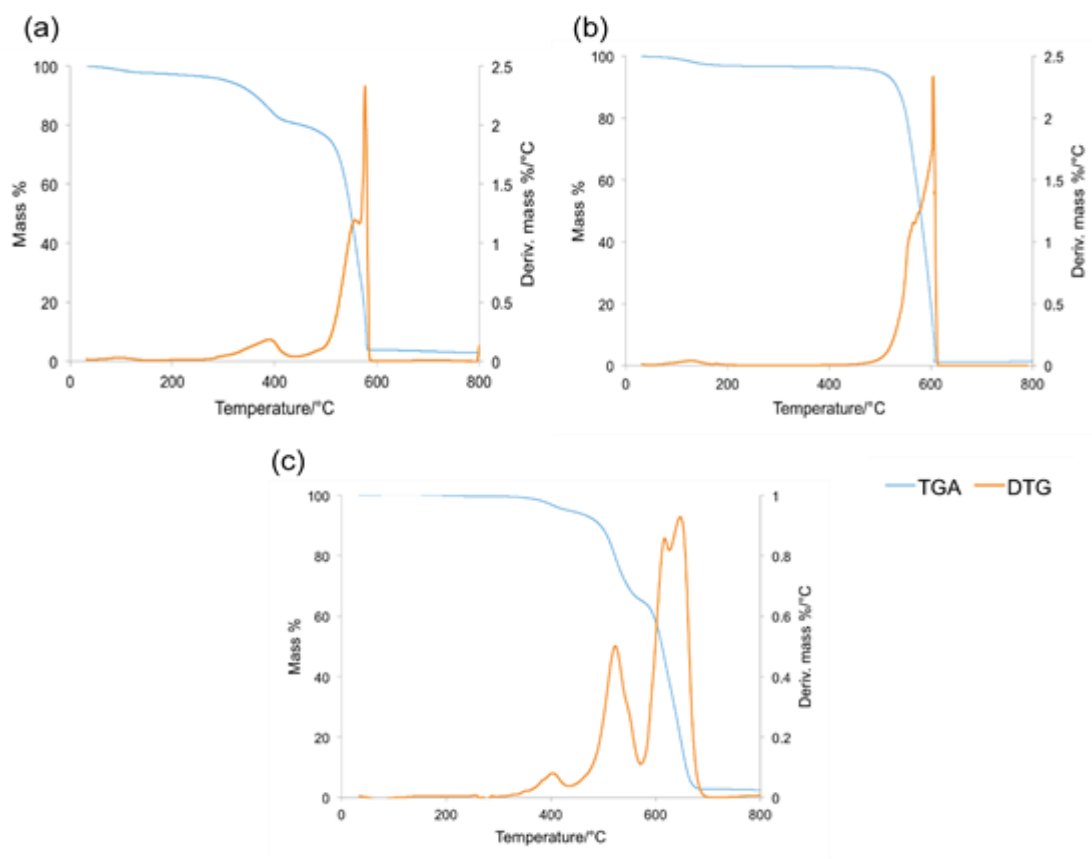


Figure 5.3. TGA and DTG curves of (a) aramid (b) Kevlar and (c) PPS, in air 100ml/s at 20°C/min.

The aramid fibres started losing mass ( $T_{0t}$ ) at 305°C and then showed a two-step degradation where after the first step of decomposition between 355°C and 439°C, fibres started charring. This thermal response is typical of a poly(m-phenylene terephthalamide) fibre such as Nomex [12]. As Kevlar is a poly(p-phenylene terephthalamide) (PPTA) fibre, degradation occurred in one step with a start temperature ( $T_{0t}$ ) of 499°C, similar to that reported in [13]. PPS on the other hand had a three-step degradation and unlike aramid and Kevlar, there was no initial mass reduction due to water loss (seen as no mass loss up to 120°). From Table 5.3,  $T_{0t}$  was 431°C, which coincided with the first stage of decomposition (from 328°C to 438°C) with a maximum mass loss at 411°C. Montaudo et al [14] attributed this to the evolution of cyclic oligomers caused either by the –SH end groups or the movement of sulphur atoms in the polymer chain. The second stage, from 438°C to 572°C had a maximum mass loss at 526°C due to the formation of aromatic linear thiols, followed shortly by dehydrogenation reactions resulting in thiodibenzofuran units. And finally, the third stage with maximum mass loss at 662°C the removal of the remaining sulphur occurred. Above 690°C, 3.5wt% residue remained, which has been referred to as having a cross linked, graphite-like structure [14].

### 5.2.3 TGA-FTIR of the aramid, Kevlar and PPS

TGA-FTIR was carried out for aramid, PPS and Kevlar fibres in order to identify evolved volatiles during thermal decomposition. These were conducted in an air atmosphere as this study was interested in gaseous decomposition products that could affect the oxidation of carbon fibre which requires oxygen. The same conditions (air 100ml/s and heat rate of 20°C/min) as in section 5.2.2 were used. The FTIR spectra were taken at the temperatures corresponding to the DTG peaks in Figure 5.3(a-c).

Figure 5.4 shows the FTIR spectrum for aramid at 576°C, superimposed over that of Kevlar at 600°C, the temperatures at which the greatest mass loss occurred (seen on the DTG of Figures 5.3(a) and (b)). Both spectra showed N-H stretching absorptions at 3300, 1500 and 1300cm<sup>-1</sup> due the vibrations in secondary amide groups present in the volatiles derived from each aramid fibre [15,16]. The effect of meta-phenylene groups in the former and para-phenylene in the latter does not appear to have influenced the spectra.

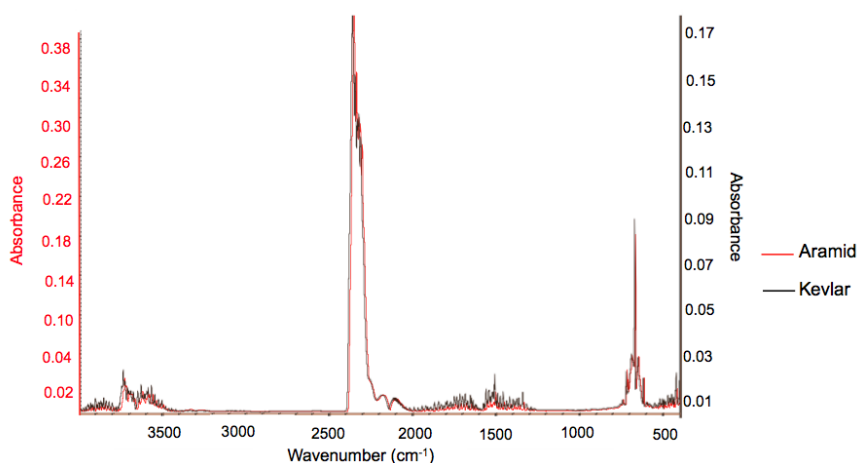


Figure 5.4. FTIR spectra of evolved gases during TGA experiments of aramid and Kevlar at 576°C and 600°C, respectively.

The DTG for PPS (Figure 5.3(c)) identified three peaks at 392°C, 524°C and 642°C. The FTIR spectra corresponding to these temperatures are given in Figure 5.5.

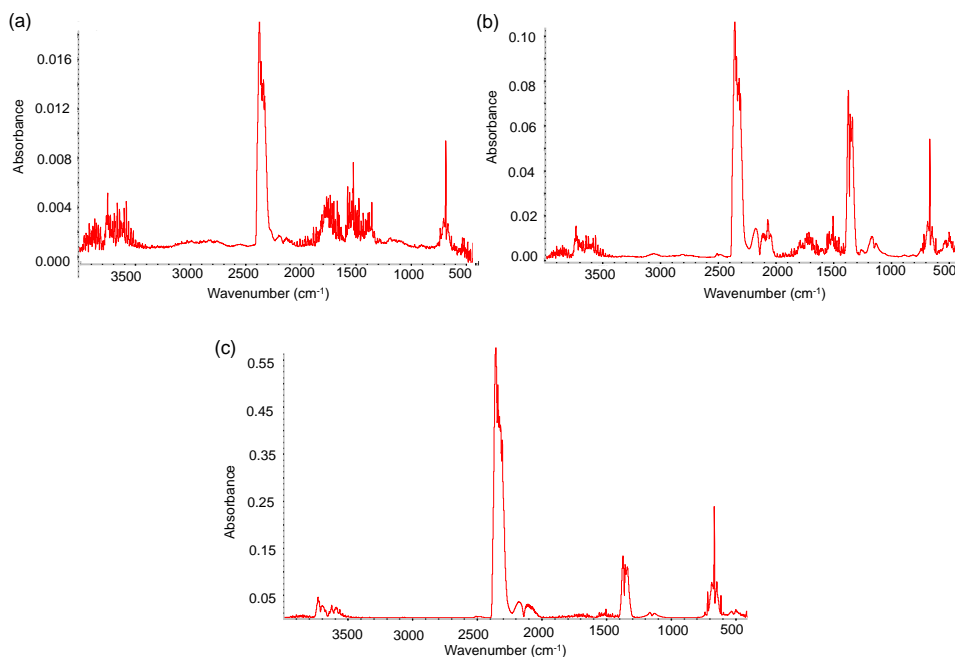


Figure 5.5. FTIR spectra of evolved gases during TGA experiments of PPS in air at temperatures (a) 392°C, (b) 524°C and (c) 642°C.

Common peaks were seen at all three temperatures, including O-H stretching (alcohol) at 3700-3584 $\text{cm}^{-1}$ , as well as a strong peak at 2349 $\text{cm}^{-1}$  for O=C=O stretching (carbon dioxide). The peaks around 710-630 $\text{cm}^{-1}$  may be due to C-H bending vibrations. Further peaks in these regions at 705-570 $\text{cm}^{-1}$  and 620-600 $\text{cm}^{-1}$  correspond with mono- and disulfides (C-S and S-S stretch respectively) [17]. TGA-FTIR experiments at the Sandia National Laboratory [18] found that major decomposition products were potential phenylene sulphides, including diphenyl disulphide and diphenyl sulphide.

Only PPS samples heated at 392°C showed identifiable FTIR peaks in the region 1415-1389 $\text{cm}^{-1}$  from S=O stretching (e.g. as in sulphate or sulphonate) [17]. For samples heated at both 392°C and 524°C FTIR spectra had peaks in the region of 1600-1300 $\text{cm}^{-1}$ . Lv et al [19] attributed those observed at 1570 $\text{cm}^{-1}$  and 1469  $\text{cm}^{-1}$  to nonsymmetric phenyl ring sulphide (C<sub>6</sub>H<sub>6</sub>-S) stretching and the peak at 1382 $\text{cm}^{-1}$  to the C-S stretching vibration. Also, at 524°C there was a peak in the 2175-2140 $\text{cm}^{-1}$  region potentially caused by S-C≡N stretching (thiocyanate) [17]. Peaks were also observed for sulphur dioxide (SO<sub>2</sub>) at 1200-1000 $\text{cm}^{-1}$  and a sharp peak between 1500-1300 $\text{cm}^{-1}$ , which could be a consequence of further oxidation of SO<sub>2</sub> to SO<sub>3</sub>. This was also seen at 642°C, where the remaining sulphur was removed. Finally, it may be noted that aramid and Kevlar had different phenylene groups (para- and meta-) none of the evolved gases identified were commonly known to react with carbon fibre. The spectra for thermally degraded PPS, however, which identified sulphur-containing species, including sulphur dioxide and possibly trioxide as oxidizing agents could interfere with the oxidation of carbon fibre at temperatures above 328°C.

#### **5.2.4 TGA of 50/50 wt% of carbon and veil fibres**

To study potential interactions between carbon fibre and the veils/fabric fibres at high temperatures, TGA was carried out on 50/50wt% mixtures of the carbon fibre and each veils/fabric, and compared to an average TGA curve calculated from the weighted TGA responses of the individual components.

Carbon fibre and the aramid, Kevlar and PPS veils were grounded with a Wiley mill and then each powdered fibre was individually mixed with ground carbon fibre at a mass ratio 50/50wt%. The glass and basalt fibres were not included as these would not grind easily to powder forms. TGA curves for the individual components, the 50/50wt% mixtures, and the calculated average curves are given in Figure 5.6(a-c), the corresponding DTG responses are given in Figure 5.7(a-c), and the data derived from these charts is in Table 5.4. All experimental curves for each mixture differed from the respective calculated curves.

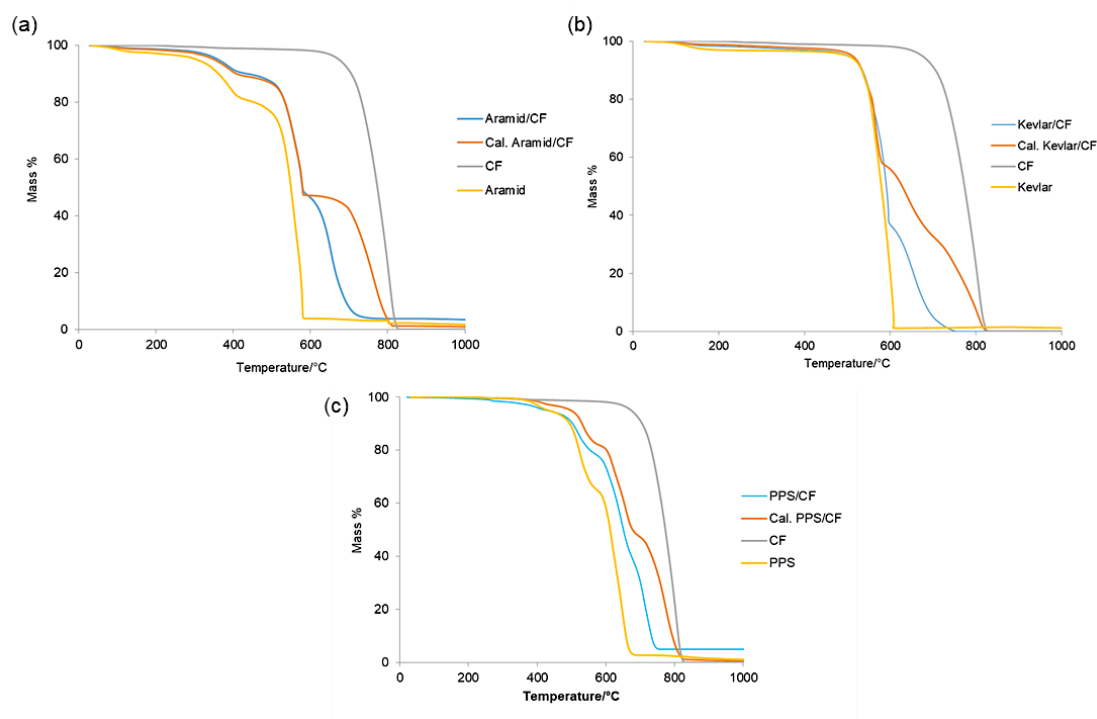


Figure 5.6. TGA curves in air of fibres from veils, carbon fibre (CF), 50/50wt% mixtures and calculated average 50/50wt% curve from the individual components. Fibres from veils used were (a) aramid, (b) Kevlar (c) PPS.

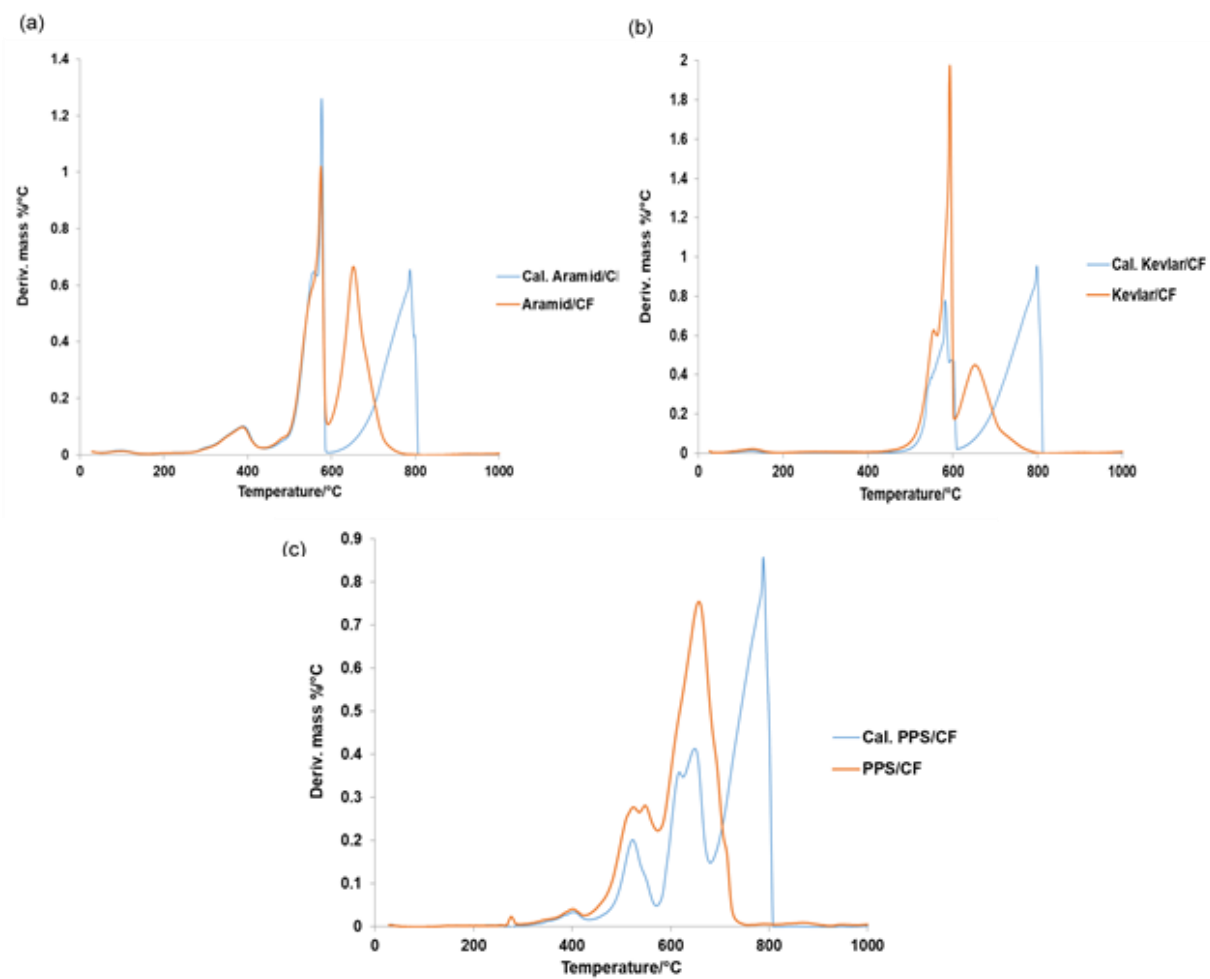


Figure 5.7. DTG in air of fibres from veil fibre/carbon fibre (CF), 50/50wt% mixtures and calculated average 50/50wt% curve from the individual components. Fibres from veils used were (a) aramid, (b) Kevlar, (c) PPS.

Table 5.4. Characteristic parameters of the thermal decomposition from TGA and DTG curves.

Curve	T <sub>0t</sub> , °C	T <sub>DTG</sub> , °C	T <sub>res</sub> , °C	Wt% of residue at T <sub>res</sub>
Aramid/CF	360	382; 575; 656	763	3.8
Cal. Aramid/CF	349	382; 575; 788	800	2.9
Kevlar/CF	503	566(s); 592; 662	740	0.7
Cal. Kevlar/CF	512	574; 600(s); 796	819	0.7
PPS/CF	463	407; 519(s); 550(s); 658	759	5.0
Cal. PPS/CF	487	408; 526; 618(s); 651; 789	824	0.8

Where T stands for the temperature at which:

T<sub>0t</sub> = temperature at which 5% mass loss occurred.

T<sub>DTG</sub> = maximum mass loss occurs (DTG peak).

T<sub>res</sub> = stable residue formed.

S = small shoulder peak.

All calculated DTG from the individual components had peaks under 700°C coinciding with the decomposition of the fibres removed from the veils. The DTG peaks calculated for mixtures with maxima over the range 788-796°C however, are due to the mass loss of the carbon fibre due to oxidation, as seen in Chapter 3, Figure 3.4.

Table 5.4 shows that for the actual aramid/CF mixture and the calculated TGA curves, the onset of decomposition temperatures were within 11°C of each other. Given a heating rate of 20°C/min, it can be surmised that T<sub>0t</sub> values are within error almost the same and so the decomposition of aramid was independent of the carbon fibre. The experimental and calculated curves of aramid/CF mixture were identical up to 592°C. By this temperature the aramid had fully decomposed and products volatilised (with 3.8wt% remaining, Table 5.3). It is now assumed that solely the carbon fibre would be oxidising, however the experimental curve is shifted to lower temperatures than the calculated curve (Figure 5.6(a)). Further analysis of the

DTG graph in Figure 5.7(a) reveals two peaks at 379°C and 576°C which are identical in both the experimental and calculated curves and are attributed to the decomposition of only the aramid. At these temperatures the carbon fibre had not begun its rapid oxidation. However, the third DTG peak (associated with carbon fibre oxidation) has shifted to a lower temperature of 656°C (experimental) compared to the predicted 788°C. These results indicate that the gaseous decomposition products of the aramid (Figure 5.5) may have sensitised the oxidation of carbon fibre.

The DTG response for the Kevlar/CF mixture in Figure 5.7(b) shows two major peaks. For both the experimental and calculated curves, the first peak occurring at 592°C. However, for the Kevlar/CF (experimental), this peak was significantly higher at 600°C. At this temperature the Kevlar had not yet fully decomposed and volatilised (see Table 5.3, Kevlar reached a stable residue at 607°C). As Kevlar is still decomposing at this temperature, there were more gaseous products available to sensitise the oxidation of carbon fibre, resulting in the carbon fibre oxidising at lower temperatures. This is also seen by the rapid mass loss (drop in the curve Figure 5.6(b)) of the Kevlar/CF (experimental) TGA curve at around this temperature leading to a DTG peak. Furthermore, the peak of the calculated Kevlar/CF mixture at 792°C did not occur, which was very similar to that with the aramid/CF mixture, and is not surprisingly given both aramid and Kevlar fibres produce similar volatiles (Figure 5.4).

Unlike the TGA responses for aramid/CF and Kevlar/CF mixtures, the experimental and calculated PPS/CF mixture curves did not begin to decompose at the same temperature. The experimental TGA curve showed mass loss began ( $T_{0i}$ ) 71°C before the PPS/CF calculated curve (Table 5.4). From the DTG of PPS in Figure 5.3 there was a small peak at 392°C, and TGA-FTIR in Figure 5.5(a) detected S=O stretching (as sulphate) is given off at this temperature. While carbon fibre does not oxidise at temperatures below 500°C, the presence of these sulphur-containing species may have sensitised the carbon fibre for oxidation, causing it to oxidise at a much lower temperature. Hence, the decomposition of PPS and carbon fibre were not independent of each other. Furthermore, at 524°C and 642°C sulphur dioxide and sulphur trioxide were detected from decomposing PPS (see Figure 5.5), which appeared to have also



increased the rate of carbon fibre oxidation in air compared see Figure 5.6(c) with the calculated DTG PPS/CF peak at 789°C completely removed.

**5.2.5 Hybrid composite geometries and shear strengths**

Two different hybrid composite configurations were constructed. The veils/fabric were added to the 8-ply CCs used in the previous chapter. These configurations are given in Figure 5.8. The first consisted of a single veil on the top layer of the composite. This was to see if the fibrous layer would act as a barrier to protect the underlying composite from an incident heat flux, as well as reduce the flow of oxygen to the carbon fibre plies underneath.

The second configuration consisted of three fibrous layers within the now hybrid composite, one again on the top layer but with two more placed within the composite. This was so that a comparison could be made between the configurations and to identify if the additional layers provided extra oxidation protection and to see if there was a protective residue on the carbon fibres directly beneath each one. The physical properties of the hybrid composites are given in Table 5.5.

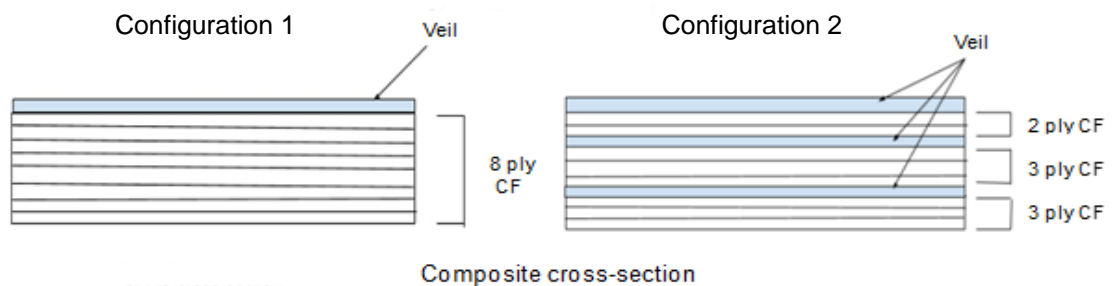


Figure 5.8. The two configurations of hybrid layers in CCs.

Table 5.5. Physical properties of composites.

Composite	Veil/fabric	No. Added veils	Mass fraction %			Thickness, mm
			Veil/fabric	Carbon fibre	Resin	
CC	-	-	-	65.7	34.3	2.08
CC_Ar_1	Aramid	1	0.4	46.4	53.3	1.79
CC_Ar_3	Aramid	3	1.3	54.0	44.6	2.05
CC_Bs_1	Basalt	1	0.8	62.2	37.0	1.88
CC_Bs_3	Basalt	3	2.1	53.8	44.1	1.97
CC_Gl_1	E-glass	1	0.6	66.5	32.9	1.79
CC_Gl_3	E-glass	3	1.6	58.4	40.0	2.05
CC_Wo-G_1	E-glass	1	0.9	59.5	39.6	1.91
CC_Wo-Gl_3	E-glass	3	3.7	52.1	44.2	2.19
CC_PPS_1	PPS	1	0.6	48.2	51.2	2.55
CC_PPS_3	PPS	3	1.8	57.2	41.0	2.07
CC_Kv_1	Kevlar	1	-	-	-	2.49

Note: Wo-Gl is woven E-glass

‘-‘ not recorded

The inclusion of fibrous layer/s increased the resin content of the composites with the exception of the CC\_Gl\_1. Including basalt and non-woven glass veils, the weight percentage of the epoxy only significantly increased after inclusion of three veils and not for the presence of one only. The inclusion of the 1x1 plain woven glass increased the resin content, this was attributed to it having a lower permeability than 2x2 twill weave of the carbon fibre.

Short beam shear tests were carried out in line with ASTM D2344 [20] to determine the interlaminar shear strength of the composites. The thickness and width of five samples of each composite were measured and then placed in a horizontal shear test fixture with the fibres parallel to the loading nose. The nose flexed the specimen at 0.05 inches (1.27mm) per minute until the composite broke, with the force recorded and the shear strength calculated using the equation:

$$\text{Shear strength} = (0.75 \times \text{breaking load}) / (\text{width} \times \text{thickness}) \quad [5.1]$$

The shear strength is given in Table 5.6.

Table 5.6. Shear strength of composites from short beam shear tests.

Composite	Shear strength, MPa
CC	$44.9 \pm 0.6$
CC_Ar_1	$40.9 \pm 2.3$
CC_Ar_3	$38.4 \pm 2.7$
CC_Bs_1	N/A
CC_Bs_3	$30.9 \pm 3.5$
CC_Gl_1	$38.7 \pm 1.4$
CC_Gl_3	$42.3 \pm 6.3$
CC_Wo-Gl_1	$35.8 \pm 1.6$
CC_Wo-Gl_3	$44.7 \pm 2.7$
CC_PPS_1	$42.5 \pm 5.3$
CC_PPS_3	$34.4 \pm 2.3$
CC_Kv_1	$41.0 \pm 3.5$

‘N/A’ = test failed, data unavailable

With the exception of the composites containing E-glass veils, the addition of one veil did not reduce the shear strength significantly below that of CC. However, the inclusion of three veils was detrimental to the overall composite shear strength and means that the veils had weaker adhesion to the polymer matrix. The inclusion of E-glass veils showed the opposite results with the shear strength of CC\_Gl\_1 and CC\_Wo-Gl\_1 below those of CC\_Gl\_3 and CC\_Wo-Gl\_3 respectively (which were within error of CC). The inclusion of two additional veils has partly restored the respective shear strengths, which was attributed to the higher resin content in composites when three E-glass veils were included (Table 5.5).

### 5.3 Cone calorimetric testing of composites at $75\text{kWm}^{-2}$

All composites were exposed to the cone calorimeter at  $75\text{kWm}^{-2}$  for 600s. It was seen in Chapter 4 that this test condition caused oxidation to carbon fibres in all plies of CC.

#### 5.3.1 Effect on structural coherence and morphological properties

Digital images of the hybrid composites in configuration 1 after testing are given in Figure 5.9. No surface veil residues were observed on CC\_Ar\_1. Composite CC\_Bs\_1 had a partly intact basalt veil on the surface. E-glass remained on the surface of the both CC\_Gl\_1 and CC\_Wo-Gl\_1 samples. However, only the woven glass remained fully intact. Disintegration of the non-woven glass veils suggests there may have been a binder holding the short-chopped glass strands together in a mat which decomposed at a lower temperature than the E-glass. As with CC\_Ar\_1 no surface veil residues were observed on CC\_Kv\_1 and CC\_PPS\_1 composites. This was expected as these veils/fabric were organic in nature and the heat from the cone calorimeter exceeded that which these materials could withstand (as seen in Table 5.1).

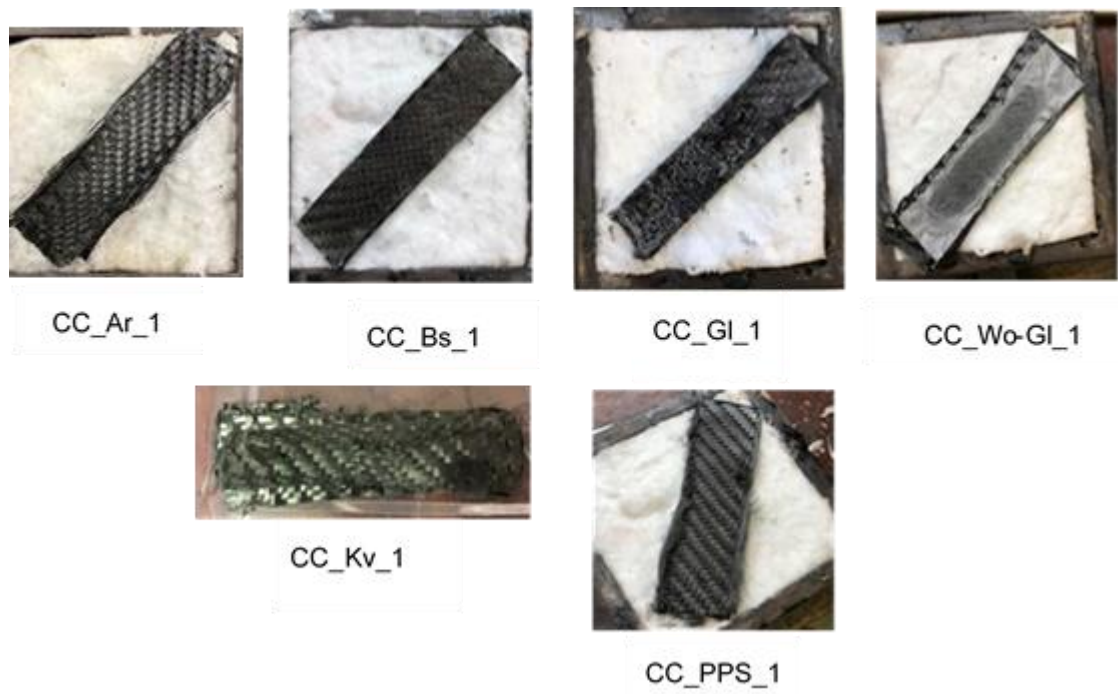


Figure 5.9. Digital images of composites from configuration 1 after testing at  $75\text{kWm}^{-2}$ .

The composites containing three hybrid layers were also examined in order to see if the veil interlayers remained after heat exposure. Both optical microscopy and SEM were used on interlayers removed from the delaminated residues of the exposed composites.

From CC\_Ar\_3, no traces of veil 1 (surface veil) or veil 2 (underneath ply 5 of configuration 2, Figure 5.8) were found using SEM. However, the third veil (underneath ply P5 of configuration 2, Figure 5.8) was recovered. A comparison with the untested aramid is shown in Figure 5.10. In the third layer, fibres remained separate and there was a slight increase in the aramid fibre diameter from  $12.1 \pm 0.3\mu\text{m}$  to  $13.8 \pm 0.2\mu\text{m}$  most likely the consequence of expansion and no damage was found on the individual aramid fibres. Under the cone calorimeter at  $75\text{kWm}^{-2}$ , the composite's top surface temperature was measured using a thermocouple as  $680 \pm 2^\circ\text{C}$ . From the TGA response in Figure 5.6(a), the aramid veil had fully decomposed by  $581^\circ\text{C}$ , almost  $100^\circ\text{C}$  below that recorded by the thermocouple. Thus it was expected that the aramid veils would not withstand this heat testing environment. However, the third veil remained intact suggesting that the carbon fibre plies above and below this veil restricted the flow of air. It has been reported that under nitrogen atmosphere (no oxygen) a significant mass percentage of aramid can remain at  $800^\circ\text{C}$  [21].

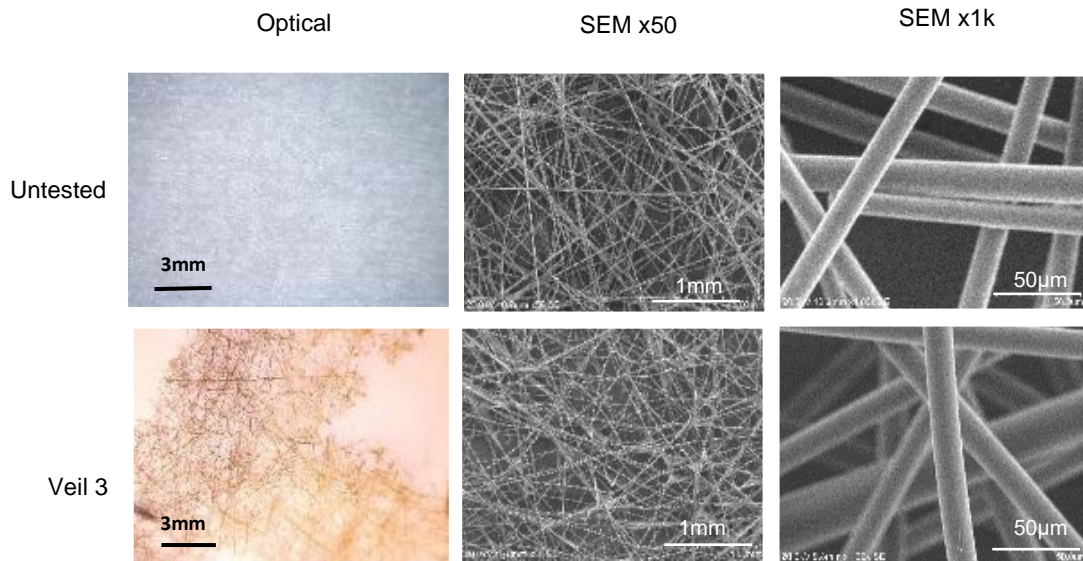


Figure 5.10. Comparisons of untested and the third aramid layer in CC\_Ar\_3 after cone calorimeter testing.

All three basalt veils were recovered from CC\_Bs\_3. From the TGA in the literature, Figure 5.2(b) very little mass loss occurred up to 1000°C so they were expected to remain intact. A comparison of the untested basalt veil and those removed from the exposed CC\_Bs\_3 composite is given in Figure 5.11. Basalt fibres removed from the surface veil 1 remained as individual entities, whereas those from the second veils (veil 2) showed signs of adhering to each other and had developed an uneven surface structure. By veil 3 the fibres had aggregated or fused together at fibre cross-over points.

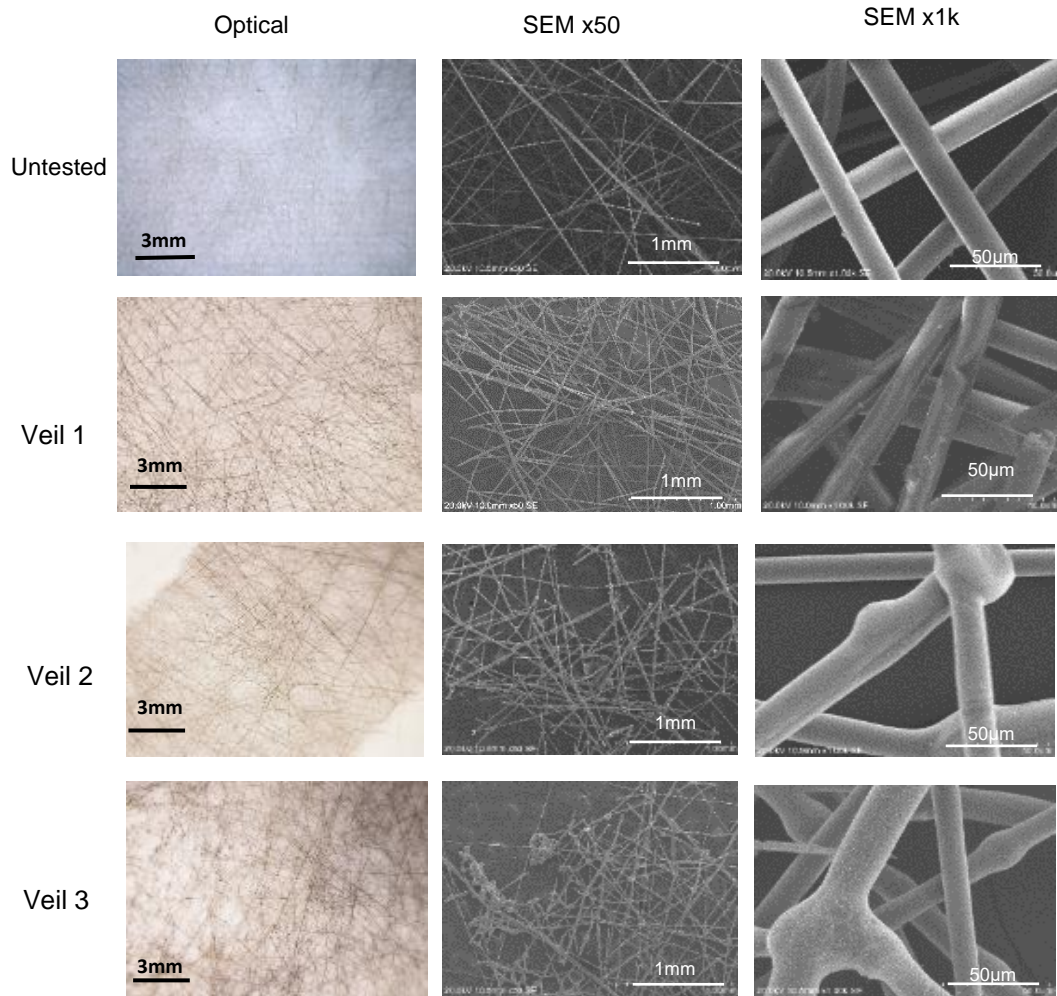


Figure 5.11. Comparisons of untested and layers of basalt in CC\_Bs\_3 after cone calorimeter testing.



The residual E-glass veils were examined from composite CC\_GI\_3. A comparison of the untested E-glass veil and those removed from CC\_GI\_3 is given in Figure 5.12. The top surface layers remained as clearly identifiable individual fibres, while the second and third layers showed signs of softening and aggregation and/or fusion, suggesting that the temperature within the composites is higher than on the surface during the 600s exposure to the cone. In addition all three layers of removed E-glass layers showed signs of gas bubble formation with the third layer remaining intact and evidence of molten glass nodules present on the E-glass fibres.

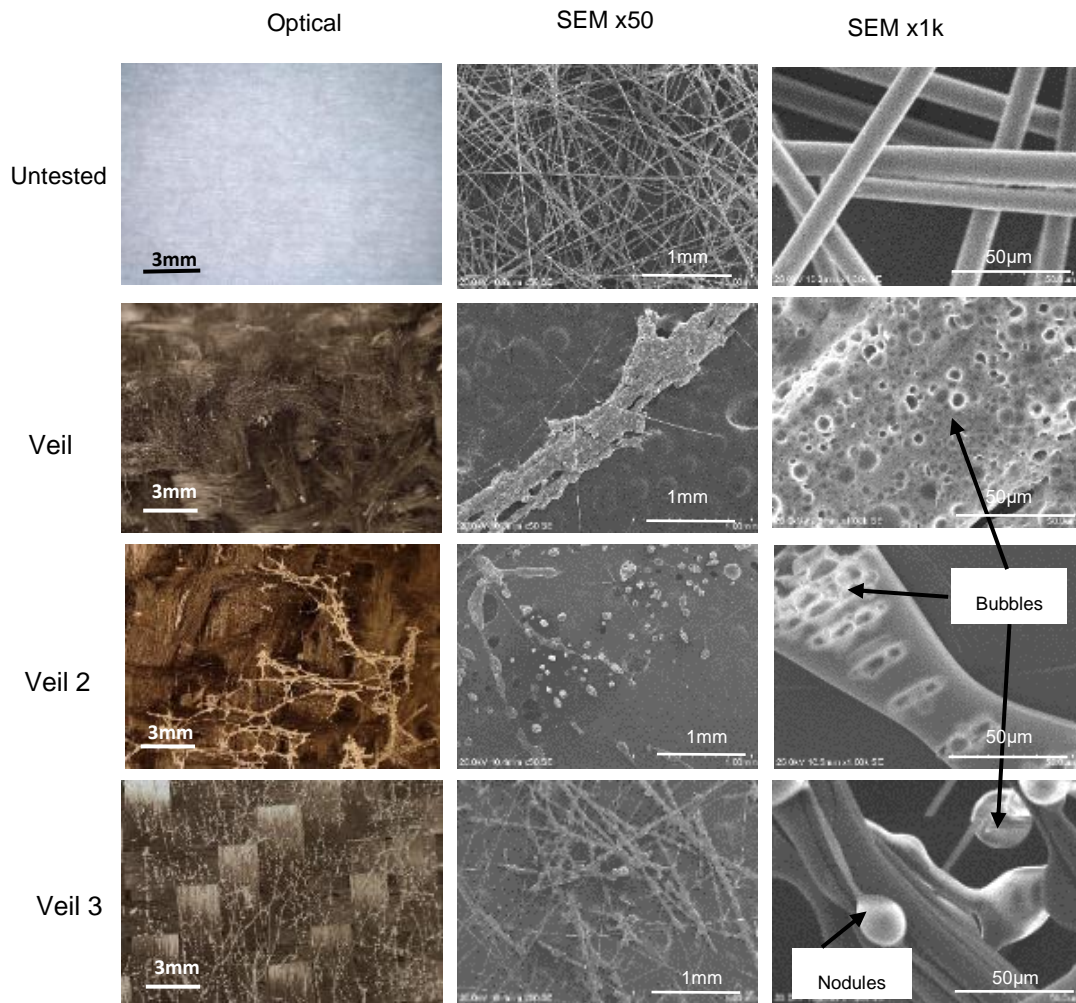


Figure 5.12. Comparisons of untested and layers of E-glass in CC\_GI\_3 after cone calorimeter testing.

To investigate this interesting effect further, residual veils were removed from CC\_Wo-GI\_3. Figure 5.13 shows a comparison of the untested woven E-glass and layers removed from CC\_Wo-GI\_3. The original untested E-glass was a tight weave flexible fabric, which after testing the top layer became brittle and showed signs of fracture at yarn cross-over points. Component fibres remained separately observable and had the same apparent diameters as unexposed original fibres. However, within veil 2, the individual fibres were no longer evident and appeared to have fused together. This behaviour was also found on veil 3.

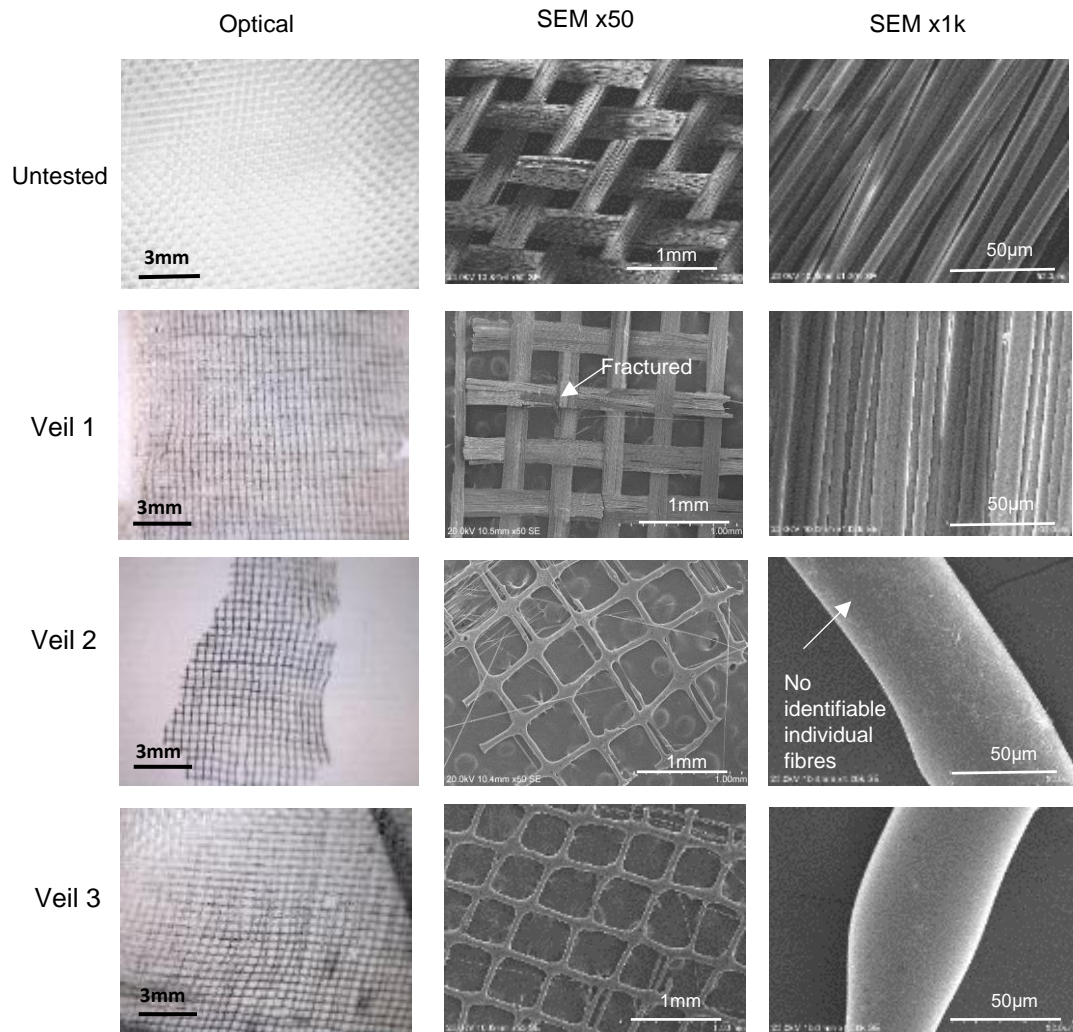


Figure 5.13. Comparisons of unexposed and layers of woven E-glass in CC\_Wo-GI\_3 after cone calorimeter testing.

Further SEM examination shown in Figure 5.14 of yarn cross-over areas, indicated that indeed aggregation and fusion of the fibres had occurred, with evidence of larger voids in the second



layer and smaller voids in the third. The E-glass fibres did not adhere to the carbon fibre and remained completely separate.

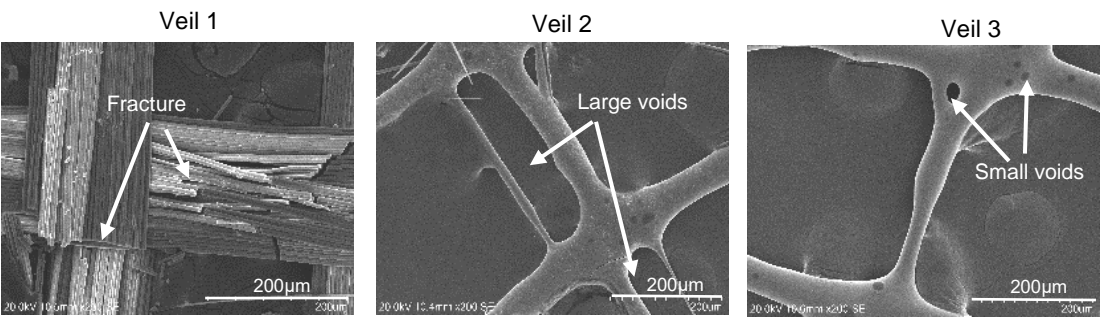
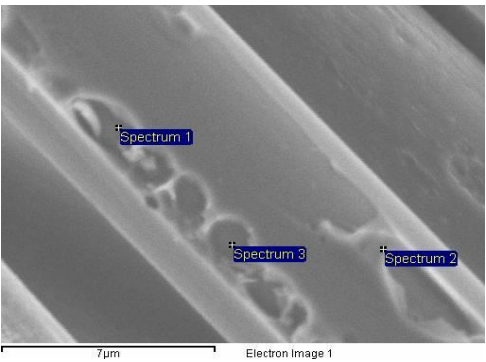


Figure 5.14. SEM images of where the weave crosses over in each hybrid layer.

The temperature of the cone calorimeter at a heat flux of  $75\text{kWm}^{-2}$  was insufficient to soften or melt either glass or basalt fibres while underlying layers did show such evidence as noted above, thereby suggesting an internal temperature in excess of  $700^{\circ}\text{C}$  or so. This unexpected observation suggests therefore that some exothermic reaction may be occurring within the composite as the otherwise inert glass or basalt fibres are surrounded by pyrolysing epoxy resin and adjacent carbon fibre surfaces.

The above SEM images (Figure 5.14) showed that the veils had not adhered to the carbon fibres during cone calorimetric testing. In order to confirm this, EDX examination was carried out and presents the results from carbon fibres removed from ply 6 (P6) of the CC\_Wo-GI\_3 Figure 5.15.



Element		C	O	Al	Si
Weight %	Spectrum 1	92.32	1.23	-	6.45
	Spectrum 2	100	-	-	-
	Spectrum 3	96.21	-	3.79	-

Figure 5.15. EDX analysis of carbon fibres removed from ply P6 (P6) of CC\_Wo-GI\_3.

These show that the presence of carbon dominates and that fibres removed from CC\_Wo-GI\_3 had trace amounts of silicon and aluminium present, presumably from the adjacent glass fibres, although there was no evidence of glass-carbon fibre adhesion as noted above.

Under SEM no visible signs of the PPS veils were observed in CC\_PPS\_3. From the TGA in Figure 5.2 it was seen that the PPS veil had decomposed and volatilised by 685°C, given that the top surface temperature of the CC\_PPS\_3 under the cone calorimeter (75kWm<sup>-2</sup>) was recorded by a thermocouple as 680±2°C, although residue of the PPS veils might remain. However and in contrast, the third veil which was intact in CC\_Ar\_3, where the aramid veil had a lower decomposition temperature. EDX was carried out on carbon fibres removed from ply P6 for CC\_PPS\_3 and results are given in Figure 5.16. No signs of sulphur were detected which meant that the PPS veils had not melted and left a residue adhering to the carbon fibre. Furthermore, this showed there was no obvious PPS-carbon interaction although the higher percentage of oxygen on these carbon fibres might suggest oxidation from generated sulphur oxidising species such as SO<sub>3</sub>. The earlier reported TGA results in Table 5.4 support this observation.

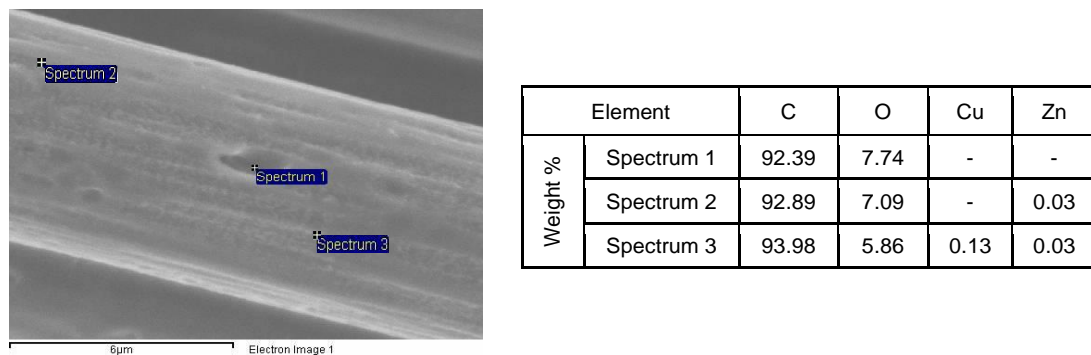


Figure 5.16. EDX analysis of carbon fibres removed from ply P6 of CC\_PPS\_3.

### 5.3.2 Effect on burning parameters: time-to-ignition, flame-out time and residual mass

The burning parameters time-to-ignition, TTI, and flame-out time, FO, were also recorded during the cone calorimeter tests and are given in Table 5.7. However, the purpose of these tests was not to investigate the burning behaviour of composites but to use the cone calorimeter as constant heat source and examine the damage to the residual carbon fibres. All TTI values were

within experimental error similar, with the composites containing aramid veils being slightly higher, most likely due to the barrier effect of the aramid fibre. The samples were weighed before and after exposure to the cone calorimeter to determine the residual mass. To calculate the percentage of carbon fibre oxidised, values listed in Table 5.7, the following assumption were made: firstly, that no resin remained after cone calorimeter testing at  $75\text{kWm}^{-2}$ , and secondly, that the inorganic fibres E-glass and basalt remained unchanged.

Table 5.7. Composition of composites and resulting cone calorimeter results after  $75\text{kWm}^{-2}$  for 600s.

Composite	Cone results			Derived results	
	TTI, s	FO, s	Residual mass, %	Composite oxidised, wt%*	% of carbon fibre oxidised**
CC	20	71	38.5	27.2	41.4
CC_Ar_1	28	78	28.2	18.5	39.1
CC_Ar_3	27	67	31.5	23.9	41.7
CC_Bs_1	17	51	43.3	18.9	30.3
CC_Bs_3	22	56	34.0	19.8	36.9
CC_Gl_1	16	48	30.7	35.8	53.9
CC_Gl_3	23	66	33.4	25.1	42.9
CC_Wo-Gl_1	17	52	47.7	11.8	20.0
CC_Wo-Gl_3	25	66	45.7	6.4	12.2
CC_PPS_1	22	75	29.6	19.1	38.5
CC_PPS_3	23	67	27.7	21.3	34.0
CC_Kv_1	22	66	42.1	-	-

\* Carbon fibre oxidised wt% =  $100 - (\text{residual mass wt\%} - \text{original resin (Table 5.5)wt\%})$

\*\*% of carbon fibre oxidised =  $\frac{\text{Carbon fibre oxidised}}{\text{Original carbon fibre}} \text{wt\%}$

‘-‘ not recorded

The inclusion of aramid veils only resulted in a small change in the apparent amount of carbon fibre oxidised as might be expected if their presence has a slight flame retarding effect. Composites containing basalt and PPS veils resulted in decreases in the apparent percentages of carbon fibre oxidised. This was particularly surprising for CC\_PPS\_1 and CC\_PPS\_3, as TGA results in Figure 5.7(c) indicated accelerated carbon fibre oxidation. However, the results in Table 5.7 suggest the barrier effect of including PPS veils (thermal and restricting flow of volatiles) outweighed this. Interestingly, for those containing basalt, the inclusion of one veil resulted in less carbon fibre oxidation than the inclusion of three. Conversely, both glass fibre-containing composites, CC\_Gl\_1 and CC\_Gl\_3, had greater apparent amounts of carbon fibre oxidation compared to CC, while CC\_Wo-Gl\_1 and CC\_Wo-Gl\_3 composites showed a similar but lower effect. This difference between veil and woven fabric presence could be because, as Figure 5.13 showed, the woven E-glass had remained intact on the first layer and then formed a web-like structure within the exposed CC\_Wo-Gl\_3 composite, which had created a barrier and low oxygen environment inside CC\_Wo-Gl\_3 resulting in less carbon fibre oxidation. In order to confirm this repeats of the samples would need to be carried out and the residual masses calculated.

### **5.3.3 Effect of veils on properties of residual carbon fibres**

Carbon fibres were removed from the plies P1, P4 and P8 from all exposed composites. Fibres from P1 were of particular interest as these were in direct contact with the surface veil/fabric layer and could indicate if there were any interactions between this and underlying carbon fibres during the exposure to the heat flux from the cone calorimeter. For the same reason fibres from composites with three veils were removed from P3 and P6 (directly under the veils).

Removed carbon fibres were examined for surface damage, diameter reduction and change in electrical conductivity. Single fibre tensile tests were not carried out as many of the residual P1 fibres were too fragile to undertake testing and accurate results could not be obtained. Carbon fibre diameters from fibre removed from the composites after cone calorimeter testing at  $75\text{kWm}^{-2}$  for 600s are given in Table 5.8.

Table 5.8. Carbon fibre diameters measured after exposure to  $75\text{kWm}^{-2}$  for 600s.

Composite	Carbon fibre diameter, $\mu\text{m}$				
	P1	P3	P4	P6	P8
CC	$5.89 \pm 0.11$	-	$6.69 \pm 0.09$	-	$6.65 \pm 0.11$
CC_Ar_1	$6.24 \pm 0.09$	-	$6.94 \pm 0.11$	-	$6.64 \pm 0.11$
CC_Ar_3	$5.53 \pm 0.13$	$7.12 \pm 0.10$	$6.80 \pm 0.13$	$7.07 \pm 0.14$	$6.81 \pm 0.13$
CC_Bs_1	$5.32 \pm 0.13$	-	$6.80 \pm 0.14$	-	$7.22 \pm 0.11$
CC_Bs_3	$4.03 \pm 0.13$	$6.69 \pm 0.10$	$6.39 \pm 0.13$	$5.80 \pm 0.20$	$6.16 \pm 0.14$
CC_GI_1	$3.37 \pm 0.15$	-	$6.74 \pm 0.05$	-	$6.45 \pm 0.05$
CC_GI_3	$2.90 \pm 0.08$	$6.51 \pm 0.05$	$6.52 \pm 0.06$	$6.66 \pm 0.04$	$6.14 \pm 0.11$
CC_Wo-GI_1	$6.18 \pm 0.11$	-	$6.11 \pm 0.10$	-	$6.96 \pm 0.09$
CC_Wo-GI_3	$6.76 \pm 0.09$	$6.22 \pm 0.11$	$6.38 \pm 0.11$	$7.18 \pm 0.08$	$6.88 \pm 0.14$
CC_PPS_1	$5.91 \pm 0.11$	-	$7.02 \pm 0.09$	-	$6.72 \pm 0.11$
CC_PPS_3	$5.76 \pm 0.13$	$6.84 \pm 0.08$	$7.04 \pm 0.11$	$6.94 \pm 0.11$	$6.47 \pm 0.09$
CC_Kv_1	$2.22 \pm 0.10$	-	$6.84 \pm 0.06$	-	$5.66 \pm 0.10$

‘-’ not recorded

Carbon fibre diameters as functions of sampled ply are also plotted in Figures 5.17(a-g). With the exception of CC\_Wo-GI\_3, for all other composites the greatest carbon fibre diameter reductions were for those in P1. Carbon fibres removed from P4 and P8 of CC were within error of each other, with P8 having a slightly decreased diameter compared to P4. Many of the plots in Figure 5.17 showed the general trend whereby fibres from P3 to P6 have a larger diameter than those from P8. Initial predictions were that the above plies would impede the flow of oxygen to underlying plies and therefore P8 would retain more of its original diameter compared to the above plies. However, as seen in Table 5.5, the composites used in these tests may be considered to be thermally thin laminates (1.79 to 2.55mm) where there is a negligible thermal gradient across the composite and so the reverse surface temperature may be approximately the same as the top surface temperature with free access to oxygen. During combustion and as the

epoxy burnt and released volatiles, these caused the distance between plies to expand, allowing airflow underneath the composite, hence oxidation of P8.

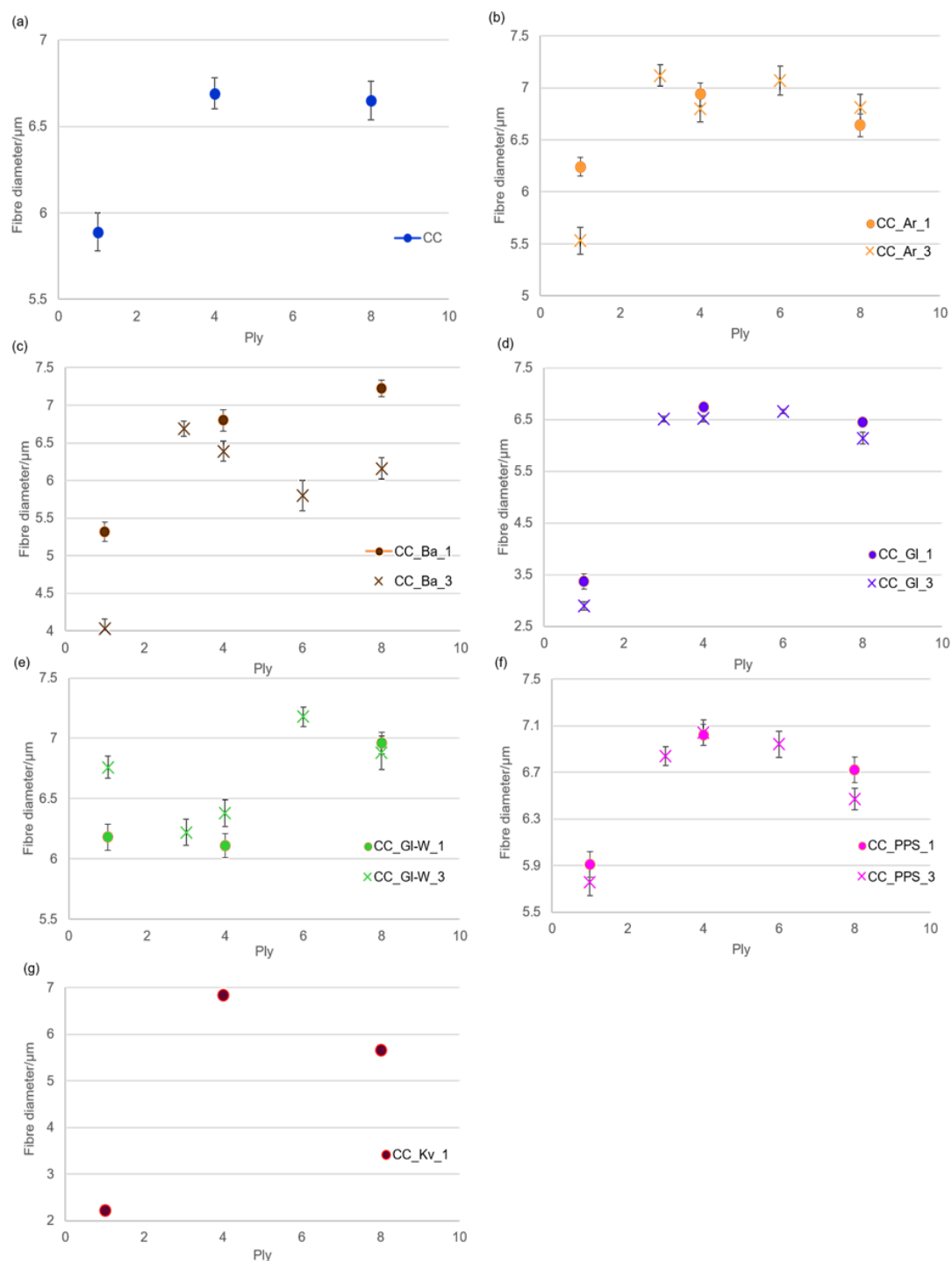


Figure 5.17. (a-g) Graphs of carbon fibre diameters removed from different plies versus ply number.

SEM images of carbon fibres removed from plies P1 and P8 from exposed hybrid composites were recorded and shown in Figures 5.18 and 5.19 respectively. The results of fibre diameter changes and related surface morphologies are analysed below in terms of the possible effects that each veil/fabric fibre type may have on the adjacent carbon fibres.

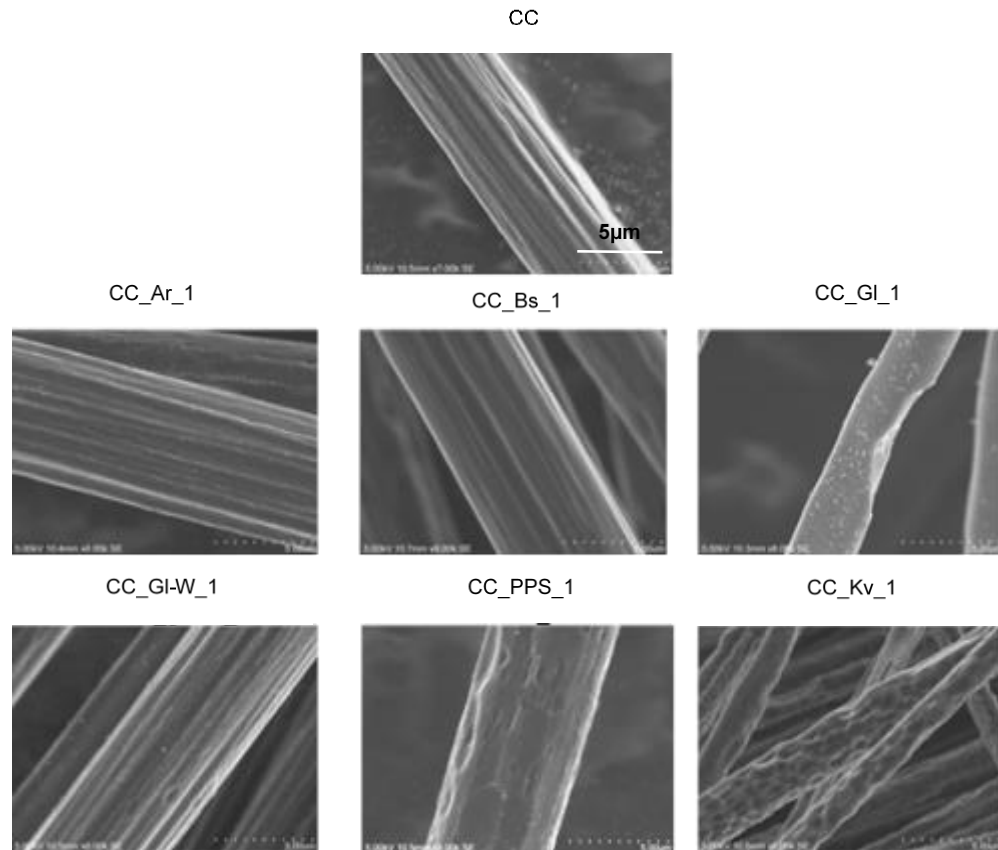


Figure 5.18. SEM images of carbon fibres removed from ply P1 after heat testing.

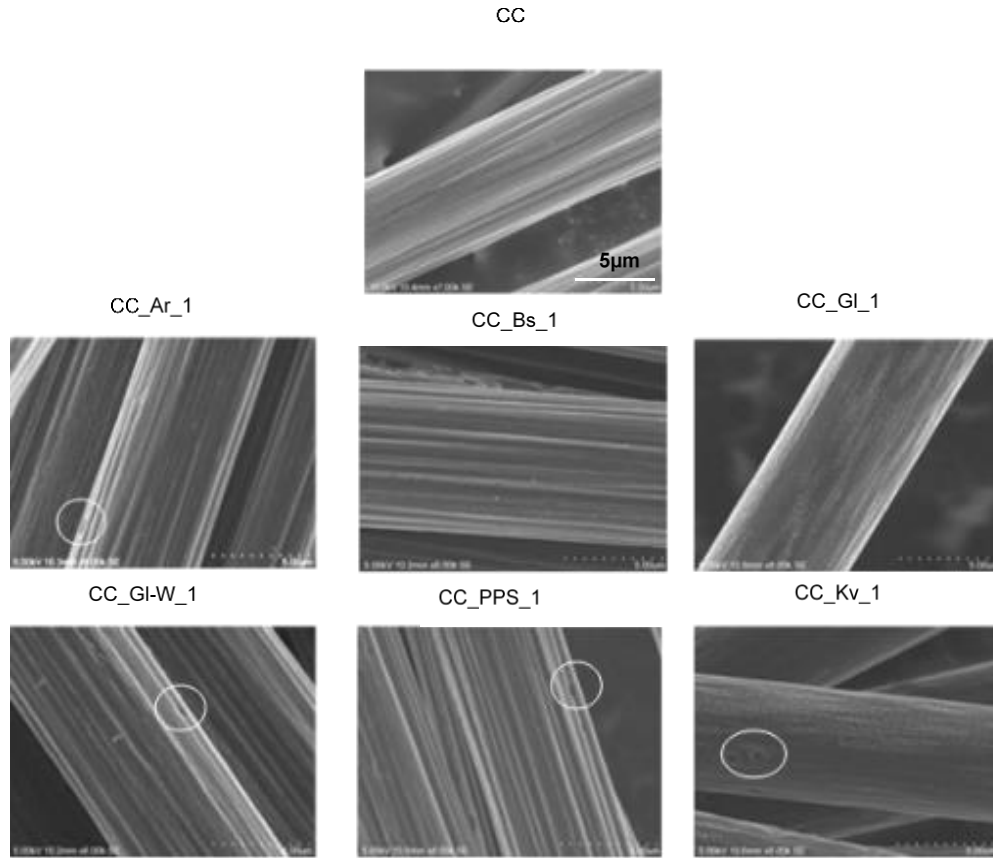


Figure 5.19. SEM images of carbon fibres removed from ply P8 after heat testing. Pits circled.

Generally, a greater fibre diameter reduction of P1 fibres from most composites with three veils (CC\_Ar\_3, CC\_Bs\_3, CC\_Gl\_3 and CC\_PPS\_3) compared to the same composite but with only a surface veil (CC\_Ar\_1, CC\_Bs\_1, CC\_Gl\_1 and CC\_PPS\_1) was seen (see Table 5.8). This result implied there might have been a thermal feedback process occurring, whereby the internal inclusion of veils two and three, caused a higher temperature within the composite. This proposal also supports the idea of ‘hotspots’ within the composites which resulted in the melting of basalt and glass veils (Figures 5.11 to 5.14). In order to confirm this, tests under the cone calorimeter would need to be repeated with a thermocouple placed inside the composite to record its internal temperature.

#### *Aramid*

The carbon fibre diameter within P1 for CC\_Ar\_3 (Table 5.8) was reduced below those from the corresponding plies in CC and CC\_Ar\_1. However, on examining the carbon fibres removed



from P4 and P8, the diameters were within error of each other for both composites, as well as greater than that of CC. Furthermore, carbon fibres from plies P3 and P6 of CC\_Ar\_3 (which were in contact with the aramid veil) retained a diameter of over 7µm. These results suggest that the significantly reduced diameter in P1 of CC\_Ar\_3 required an oxygen rich atmosphere such as would exist on the surface, for an aramid-carbon interaction.

### *Basalt*

As with aramid, carbon fibre removed from ply P1 of CC\_Bs\_1 had a more reduced fibre diameter than CC\_Bs\_3. Both these fibre diameters were less than those from the corresponding ply in CC. Overall CC\_Bs\_3 had an apparent greater amount of carbon fibre oxidation than CC\_Bs\_1 (Table 5.7) as well as, further reduced diameters (seen in Figure 5.17(c)). No areas of pitting or localised oxidation were observed on fibres removed from plies P1 and P8 of CC\_Bs\_1; this was also true for plies P3 and P6 of CC\_Bs\_3. The reduced diameters of residual carbon fibres from CC\_Bs\_3 suggested either, a possible basalt-carbon interaction or an interaction between the veils' binder and the carbon fibre.

### *E-glass (non-woven)*

Residual fibres from ply P1 of both CC\_Gl\_1 and CC\_Gl\_3 were significantly reduced in diameter. The graph in Figure 5.17(d) showed that the carbon fibre diameters of both composites followed the same trend, whereby the most significant damage was done to ply P1. With the exception of fibres from P4 of CC\_Gl\_1, all other measured carbon fibres had smaller diameters than from the corresponding ply in CC. Furthermore, the SEM image of a carbon fibre removed from P1 of CC\_Gl\_1 showed large areas of localised oxidation. No signs of the fibres' inherent surface striations were observable on the P1 or P8 plies, where the surface had become smooth on the latter due to uniform surface oxidation on ply P8 (Figure 5.19). The extent of surface oxidation on ply P1 suggested that inclusion of the non-woven E-glass increased oxidation of the carbon fibres.

### *E-glass (woven)*

Fibre diameter values of those removed from plies P1 and P8 of CC\_Wo-Gl\_1 and CC\_Wo-Gl\_3 were greater than those removed from the same plies of CC. The inclusion of three fabric

layers also resulted in greater carbon fibre diameters compared to that beneath just one surface layer; this effect is seen in the graph in Figure 5.17(f).

It is also seen for CC\_Wo-GI\_3 that fibres from plies P3 and P4 had reduced diameters compared to those in plies P1 and P8. This meant that while the E-glass web had remained intact, it did not form a barrier to reduce the oxygen concentration uniformly inside the composite. Furthermore, as highlighted in Section 5.3.1, there may be ‘hotspots’ generated within the composites, particularly in the CC\_Wo-GI\_3 sample which resulted in increased oxidation to these fibres. However, unlike the other composites, P1 fibres from CC\_Wo-GI\_3 were greater in diameter than those from CC\_Wo-GI\_1 indicating that the intact web may have acted as a heat barrier from any internal heat generation.

### *PPS*

Fibres from ply P1 of the exposed CC\_PPS\_1 and CC\_PPS\_3 composites had average diameters within error of each other. Fibres removed from ply P4 were found to have a larger average diameter compared with the corresponding ply in all composites tested. This suggests that the inclusion of the PPS layer had reduced the oxygen concentration within the composite. However, SEM images of ply P1 fibres from CC\_PPS\_1, in Figure 5.18, showed a loss of the original surface striations with localised oxidation and pitting, whereas, ply P8 CC\_PPS\_1 fibres, in Figure 5.19, showed evidence of retention of the original fibre structure with only a few nano-pits observable. This indicates that during heat exposure of the PPS its decomposition products reacted with the carbon fibre, which was also found in the TGA response in Figure 5.6(c).

In order to confirm this, carbon fibres were removed from plies P1, P3 and P6 of the CC\_PPS\_3 composite, since these fibres were in contact with the PPS veils, and examined using SEM. These SEM images are given in Figure 5.20. All fibres showed significant surface damage and pitting. TGA-FTIR of PPS (Figure 5.5) revealed that during the thermal decomposition of PPS, sulphur dioxide is produced. Sulphur dioxide can react with carbon to give carbon disulphide at elevated temperatures (700 to 1000°C) [22, 23], hence could react with the surface carbon fibre to form pits. Additionally, during combustion carbon disulphide reacts with oxygen to give

sulphur dioxide and carbon dioxide [24]. This would explain why EDX did not detect any sulphur remaining on the residual fibres from CC\_PPS\_1 and CC\_PPS\_3 as noted in Figure 5.16 above.

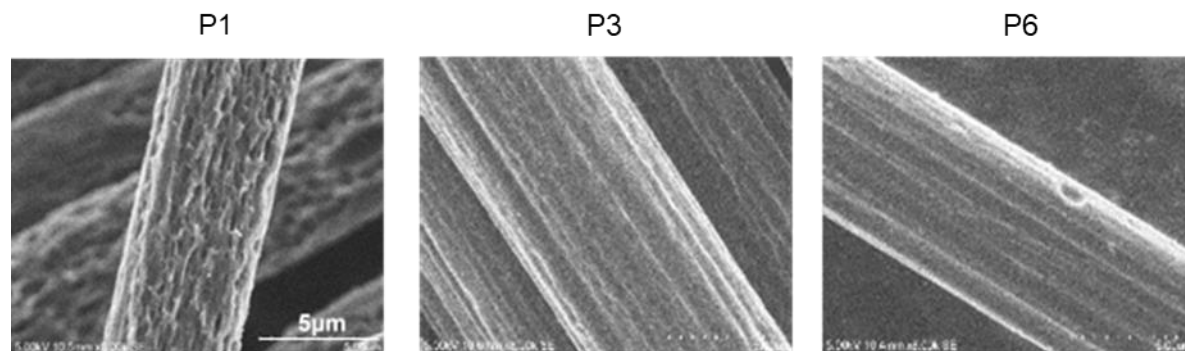


Figure 5.20. SEM images of carbon fibres removed from P1, P3 and P6 of CC\_PPS\_3.

### *Kevlar*

Kevlar was included in only one composite as a top surface layer. Carbon fibres removed from ply P1 of CC\_Kv\_1 showed major signs of oxidation, including diameter reduction (62% less than that of CC) and large pits along the length of the fibre (Figure 5.18). Carbon fibres from P8 also showed signs of pitting but with an overall much smoother surface structure. This evidence pointed to the inclusion of Kevlar as the reason for the additional damage to the carbon fibres as those closest to the Kevlar are more likely to react with its oxidising combustion products. While this damage to carbon fibres was not seen for an inclusion of the aramid veils, which had a similar FTIR spectrum (Figure 5.4), aramid was included in a much lower mass percentage than Kevlar, which was around 21 times greater in mass, hence the decomposition product were in a larger quantity.

Single fibre electrical conductivity tests were carried out (outlined in Section 2.5.3.1) and are given in Table 5.9. Fibres were removed from ply P1 as these had the greatest fibre diameter reduction and were the most oxidised. Furthermore, these fibres were in contact with the veils so any potential effect of residue or interaction with them on its electrical conductivity could be measured. Due to the extent of the damage to fibres from P1 of CC\_PPS\_1 and CC\_Kv\_1, single fibres could not be removed from these composite without breakage, so were not included here.

For CC\_Ar\_1 there is a decrease in resistivity of fibres from ply P1 compared to those from CC indicating that the fibre was not significantly damaged and residue may have been attached to the fibres (even though this was not detected with SEM). Fibres from CC\_Bs\_1 were within error of CC, with those from CC\_Wo-Gl\_1 showing only a slight increase in resistivity. However, carbon fibres from CC\_Gl\_1 had a significant increase in resistivity. This was expected as large areas of localised oxidation were seen in Figure 5.18. These defects introduced during oxidation of the carbon fibre can impeded the flow of electrons, thus increasing its resistivity.

Table 5.9. Electrical resistivity results for carbon fibres removed from P1.

P1 from composite	Resistivity, $\Omega\text{m} \times 10^{-5}$
CC	$2.20 \pm 0.05$
CC_Ar_1	$1.71 \pm 0.10$
CC_Bs_1	$2.24 \pm 0.04$
CC_Gl_1	$2.87 \pm 0.28$
CC_Wo-Gl_1	$2.28 \pm 0.08$

#### 5.4 Discussion on inclusion of veils in CC

TGA curves (Figure 5.6 (a) and (b)) showed that carbon fibre began to oxidise at lower temperatures when mixed with aramid or Kevlar fibres. However, both CC\_Ar\_1 and CC\_Ar\_3 had a similar apparent percentage of carbon fibre oxidised after exposure to cone calorimetry (Table 5.7). Furthermore, with the exception of ply P1 of CC\_Ar\_3, all other measured carbon fibre diameters were either within error or greater than those from the corresponding ply in CC (Table 5.8). While TGA-FTIR results (Figure 5.4) showed that aramid and Kevlar produced similar volatiles during decomposition, the inclusion of Kevlar fabric resulted in negative effects to carbon fibre morphologies in CC\_Kv\_1; these included significantly reduced ply P1 fibre diameter, as well as many areas of pitting (Figure 5.18). As the Kevlar was included in a 2x2 twill weave Kevlar cloth ( $300\text{gm}^{-2}$ ), compared to the fibrous aramid veil ( $14\text{gm}^{-2}$ ), it amplified the amount of volatiles produced during decomposition. In a large enough quantity, these

volatiles have sensitised the carbon fibre for oxidation. Due to this, the inclusion of an aramid-based material cannot be recommended in the heat protection of carbon fibre in CC.

Carbon fibre from ply P1 from both CC\_Bs\_1 and CC\_Bs\_3 composites had diameters reduced below those of CC. Given that the basalt veils remained intact during cone heat exposure ( $75\text{kWm}^{-2}$ , 600s), it was expected that they would provide some heat protection to the underlying carbon fibres. However, in the oxygen-rich surface ply region, the binder holding the short-chopped basalt fibres in a veil, has increased carbon fibre oxidation. Furthermore, for CC\_Bs\_3, melting of the second and third basalt veils occurred. This was attributed to ‘hotspots’ generated within the composite, this also explained the increased oxidation to the carbon fibres (seen by the decreased fibre diameter result for P6 of CC\_Bs\_3 Table 5.8).

The inclusion of E-glass veils (woven and non-woven) in CC produced different results on the residual carbon fibre morphologies. Carbon fibres removed from ply P1 of both CC\_Gl\_1 and CC\_Gl\_3 had a significantly reduced diameter. The E-glass veil also contained a binder (as did the basalt veil) and carbon fibres in P1 had large areas of localised oxidation (Figure 5.18) which were not seen from those removed from CC\_Bs\_1 and CC\_Bs\_3. This confirmed that it was the presence of E-glass veil that caused this damage to the carbon fibre and not the binder. Figure 5.12 showed that the veil did not stay as individual chopped fibres but after heat testing formed agglomeration of E-glass fibres from their melting and fusing together. Given that the surface temperature was recorded with a thermocouple as  $680\pm 2^\circ\text{C}$ , this temperature is not sufficient to cause E-glass normally to melt. This suggests that like CC\_Bs\_3, there were areas of higher temperature which also increased carbon fibre oxidation.

The inclusion of woven E-glass veil (CC\_Wo-Gl\_1 and CC\_Wo-Gl\_3) on the other hand, provided protection to the underlying carbon fibres; this was seen by its retaining more of its diameter with less surface damage. Unlike CC\_Gl\_3, the surface fabric remained intact in the composite CC\_Wo-Gl\_3 after heat testing (Figure 5.13). The woven E-glass then formed a web-like structure within the exposed CC\_Wo-Gl\_3 composite which created a barrier and low oxygen environment inside CC\_Wo-Gl\_3 resulting in less carbon fibre oxidation. Further

evidence of this is the reduced apparent percentage of carbon fibre oxidised derived in Table 5.7, (12.2% compared to 41.4% in CC).

The inclusion of the PPS veils resulted in large areas of localised oxidation and pitting on ply P1 carbon fibres (Figure 5.18), similar to that seen in CC\_Kv\_1. However unlike CC\_Kv\_1, this did not translate into a reduced fibre diameter, as they were still within error of CC (Table 5.8). However, fibre diameters from ply P4 in composites CC\_PPS\_1 and CC\_PPS\_3 had the least reductions in diameter compared to the other composites. This suggests that a low oxygen environment was created in the composite, due to carbon fibre plies impeding air flow, in which some of the gaseous products seen in the FTIR (Figure 5.5) were not produced in the same quantity as they would in an oxygen rich atmosphere, for example, the oxidation of the sulphur to either SO<sub>2</sub> or SO<sub>3</sub> does not occur.

From the percentage of carbon fibre oxidised derived in Table 5.7 and the carbon fibre diameters in Table 5.8, with the exception of the composite with woven E-glass, the inclusion of three veils did not significantly result in greater carbon fibre protection when exposed to a high heat flux (75kWm<sup>-2</sup>, 600s). The inclusion of veils/fabric also increased the resin content (Table 5.5), as well as a slight reduction in composite shear strength. However, CC\_Wo-Gl\_3 did not fit this trend. This composite had a shear strength within error of CC. Also, the composite's residual carbon fibre had larger fibre diameters, as well as an overall apparent lower percentage of carbon fibre oxidised compared to CC\_Wo-Gl\_1. This increased oxidation protection to carbon fibres was attributed to the melting of the woven E-glass fibres into a web-like structure which acted as an oxygen barrier to the carbon fibre.

## 5.5 Conclusions

High temperature resistant materials as fibrous non-woven or woven veils, or fabric, were successfully incorporated into the composite CC in two configurations, both at the surface and also within the structure, in order to provide a heat barrier to the underlying carbon fibres. Heat testing of the composites was carried out with the cone calorimeter at 75kWm<sup>-2</sup> for 600s and the

remaining components examined – the inorganic veils and residual carbon fibres. The following conclusions were made:

- In CC\_Bs\_3, CC\_Gl\_3 and CC\_Wo-Gl\_3, melting of the veil layers 2 and 3 were observed and this was attributed to ‘hotspots’ generated within the composites.
- EDX confirmed that a protective residue from the veils/fabric did not adhere to the carbon fibres directly beneath the veil.
- With the exception of CC\_Wo-Gl\_3, for all other composites the surface carbon fibres (P1) had the largest fibre diameter decrease.
- The inclusion of aramid veils in CC\_Ar\_1 and CC\_Ar\_3, provided some protection to the underlying carbon fibres, with most of their residual carbon fibre diameters being greater than those from the corresponding ply in CC.
- CC\_Wo-Gl\_1 and CC\_Wo-Gl\_3 showed notable reductions in the percentage of carbon fibre oxidised. However, CC\_Wo-Gl\_3 showed better protection to carbon fibres from oxidation with larger residual carbon fibre diameters, particularly for ply P1.
- Kevlar and PPS produced volatiles during decomposition which sensitised the carbon fibre for oxidation, resulting in the carbon fibre oxidising at a lower temperature and more rapidly.

## 5.6 References

- [1] Kandola, B. K., Horrocks, A. R., Rashid, M. R., Effect of Reinforcing Element on Burning Behaviour of Fibre-Reinforced Epoxy Composites, Recent Advances of Flame Retardancy of Polymeric Materials, Ed. M.Lewin; proceedings of the 17th conference, Business Communication Company, Stamford, Conn. (2006).
- [2] Kandola, B. K., Myler, P., Kandare, E., Herbert, K., Rashid, M. R., Fire and Mechanical Behaviour of Hybrid Composite Laminates, 8th International Conference on Textile Composites (TEXCOMP-8), Nottingham, UK, 16-18 Oct (2006).
- [3] Hutten, M. I., CHAPTER 4 - Raw Materials for Nonwoven Filter Media, Editor(s): Irwin M. Hutten, Handbook of Nonwoven Filter Media, Butterworth-Heinemann, (2007).
- [4] Chen, X., Zhang, Y., Hui, D., Chen, M., Wu, Z., Study of melting properties of basalt based on their mineral components, Composites Part B: Engineering, Volume 116, Pages 53-60, (2017).
- [5] Bourbigot, S., and Flambard, X., Heat resistance and flammability of high-performance fibres: A review. Fire Mater. 26: 155-168, (2002).
- [6] Kemmish, D., J., Practical Guide to High Performance Engineering Plastics, Smithers Rapra Technology, (2011).
- [7] Technical Guide for Kevlar® Aramid Fiber, DuPont, p12
- [8] Hao, L.C., and Yu, W.D. Evaluation of thermal protective performance of basalt fiber nonwoven fabrics. J Therm Anal Calorim 100, 551–555, (2010).
- [9] Liu, W., Wang, M., Xu, L., Zhang, W., Xing, Z., Hu, J., Yu, M., Li, J., Wu, G., Chapter Two - Radiation Technology Application in High-Performance Fibers and Functional Textiles, Editor(s): Guozhong Wu, Maolin Zhai, Mozhen Wang, Radiation Technology for Advanced Materials, Academic Press, , Pages 13-73, (2019).
- [10] Gao, Y., Zhou, X., Zhang, M., Lyu, L., Li, Z.. Polyphenylene Sulfide-Based Membranes: Recent Progress and Future Perspectives. Membranes (Basel), 12(10):924. (2022).
- [11] Fiore, V., Scalici, T., Bella, G., Valenza, A., A review on basalt fibre and its composites, Composites Part B: Engineering, Volume 74, Pages 74-94, (2015).



- [12] Genç, G., Alp, B., Balköse, D., Ulku, S., Akşit, A., Moisture sorption and thermal characteristics of polyaramide blend fabrics. *Journal of Applied Polymer Science*. 102. 29 – 38, (2006).
- [13] Bourbigot, S., Flambard, X. and Duquesne, S. Thermal degradation of poly(*p*-phenylenebenzobisoxazole) and poly(*p*-phenylenediamine terephthalamide) fibres. *Polym. Int.*, 50: 157-164, (2001).
- [14] Montaudo, G., Puglisi, C., Samperi, F., Primary thermal degradation processes occurring in poly(phenylenesulfide) investigated by direct pyrolysis–mass spectrometry. *J. Polym. Sci. A Polym. Chem.*, 32: 1807-1815, (1994).
- [15] Giraldo, L., Ladino, Y., Piraján, J. C., Rodríguez, M., Synthesis and characterization of activated carbon fibers from Kevlar. *Eclética Química*. 32. 55-62, (2006).
- [16] Mukherjee, M., Kumar, S., Bose, S, Das, C. K., Kharitonov, A. P., Study on the Mechanical, Rheological, and Morphological Properties of Short Kevlar™ Fiber/s-PS Composites. *Polymer-Plastics Technology and Engineering*. 47. 623-629, (2008).
- [17] Coates, J., Interpretation of infrared spectra, a practical approach. *Encyclopedia of analytical chemistry*, 12, 10815-10837, (2000).
- [18] Erickson, K. L., Thermal Decomposition Mechanisms Associated with Functional Groups in Selected Polymers, Sandia National Laboratories, <https://www.osti.gov/servlets/purl/1266194> last accessed 09/03/23
- [19] Lv, Y., He, H., Chen, F., Yu, J., Ning, X., Zhou, R., Polyphenylene sulfide (PPS) fibrous felt coated with conductive polyaniline via in situ polymerization for smart high temperature bag-filter. *Materials Research Express*, 6(7), 075706, (2019).
- [20] ASTM D2344/D2344M-22, Standard Test Method for Short-Beam Strength of Polymer Matrix Composite Materials and Their Laminates, Aug (2022).
- [21] Hu, C., Chen, L., Gu, R., Yu, J., Zhu, J., Hu, Z., Thermal Decomposition Behavior of a Heterocyclic Aramid Fiber. *Journal of Macromolecular Science*. 52. 10.1080/00222348.2012.725641, (2013).
- [22] Humeres, E., Moreira, R., Peruch, M. G. B., Reduction of SO<sub>2</sub> on different carbons, *Carbon*, Volume 40, Issue 5, Pages 751-760, (2002).
- [23] Blackwood, J. D., and McCarthy, D. J., The kinetically effective stoichiometry of reactions in the carbon-sulphur dioxide system, *Australian Journal of Chemistry*, 26(4) 723-731, (1973).

[24] Rich, A. L., and Patel, J. T., Carbon Disulfide ( $\text{CS}_2$ ) Mechanisms in Formation of Atmospheric Carbon Dioxide ( $\text{CO}_2$ ) Formation from Unconventional Shale Gas Extraction and Processing Operations and Global Climate Change, *Environmental Health Insights*, 9(Suppl 1), 35-39, (2015).

## **Chapter 6. Surface modification of carbon fibres for improved structural retention on exposure to fire**

### **6.1 Introduction**

In the previous chapters methods to protect the carbon fibres within CC during exposure to high heat or fire were discussed. These included the addition of nano-particles and phosphorus-based flame retardants to the resin matrix to aid the formation of char barriers on the fibre surfaces, as well as the inclusion of high temperature fibrous non-woven and woven veils within CCs to provide a heat barrier. After exposing these composites with FR additives to both the cone calorimeter ( $75\text{kWm}^{-2}$ , 600s) and propane burner ( $116\text{kWm}^{-2}$ , 300s) it was found that carbon fibres on the surface ply P1 and those in direct contact with the flame underwent the most oxidation with the largest reduced diameters, with those removed from the underneath ply P8 being the least oxidised.

The introduction of high temperature veils had mixed results with regards to carbon fibre oxidation protection. Veils were included as both a surface layer and also within CCs, and then exposed to the cone calorimeter ( $75\text{kWm}^{-2}$ , 600s). The addition of woven glass veils in CC significantly reduced the overall percentage of carbon fibre oxidised. However, the addition of non-woven fibrous PPS, and Kevlar fabrics resulted in pitting on the residual carbon fibre surfaces.

This chapter covers the application of selected high temperature chemical coatings on individual carbon fibres prior to making the composites with a view that all fibres within them can be protected in this manner. Ceramic compounds were chosen as coating materials because of their stability at high temperatures. These included nitrides, oxides and metal oxides, which have melting points well above  $1,000^{\circ}\text{C}$ , e.g. BN ( $2,973^{\circ}\text{C}$ ) [1] and  $\text{SiO}_2$  ( $1,710^{\circ}\text{C}$ ) [2]. This is challenging because as well as being resistant to high temperatures, the coating must completely cover and adhere to individual carbon fibres without aggregating on fibre surfaces and also not adding too much additional weight. Furthermore, coatings must be applied using an economical method. In the literature, chemical vapour deposition (CVD) had been used to coat carbon fibres

but this can use hazardous and expensive materials, as well as require extremely high temperatures [3]. This makes it not viable for large scale use. Hence in this study, the use of less expensive approaches were used, including dip coatings and plasma treatments.

## 6.2 Characterisation of activated carbon fibre surface prior to coating

As discussed in Chapter 3, Section 3.2, when carrying out TGA in nitrogen on the as-received carbon fibres (CF), a mass loss of 1.2% was observed up to 450°C. This was credited to the removal of the polymer sizing applied to the carbon fibres at the final manufacturing stage which prevents damage to the fibres if later woven. Typically in industry, electrochemical processes are used to ‘activate’ the CF surfaces before introducing fibres to the sizing materials. Given the low temperature at which the sizings typically begin to degrade, it can and must be removed thermally prior to coating the CF without damaging them (especially if done in an oxygen-free atmosphere). Furthermore, surface functional groups can be subsequently introduced to the un-sized fibre surface to improve the interfacial adhesion with the chemical coatings.

To remove the sizing from the CF a tow was placed in a tube furnace at 450°C in a nitrogen atmosphere for 1h (Chapter 2, Section 2.4.2). EDX was used in order to determine if the sizing had been removed. While the chemical formula of the size present was not known, EDX analysis of the (sized) CF identified oxygen on the surface apart from carbon (Figure 6.1(a)). After removal of the sizing this was not detected (Figure 6.1(b)).

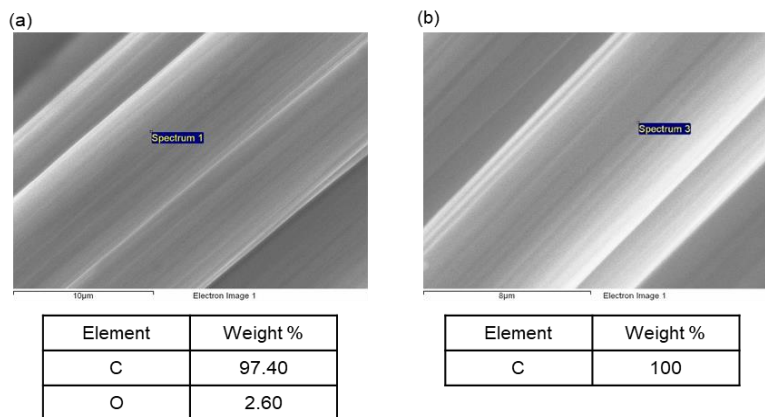


Figure 6.1. EDX of (a) CF (b) desized CF.

Once the CF were desized, functional groups were introduced. Carbon fibre is predominantly carbon ( $\geq 92\text{wt}\%$ ) and as such, displays non-polar characteristics. Hence, functional groups such as hydroxyls, carboxyls and carbonyls, needed to be created on the carbon fibre surface for chemical bonding with the coating. Two oxidative methods were chosen in order to introduce functional groups: the use of nitric acid and plasma. Nitric acid ( $\text{HNO}_3$ ) treatment was selected as it had been shown to not only convert hydroxyl type oxygen into carboxyl functions but also increase the surface roughness of the fibre [4, 5]; this is desirable as it leads to a larger specific surface area and helps to produce mechanical interlocking of the coating with the fibres. Li-Xiang et al. [6] used  $68\text{wt}\%$   $\text{HNO}_3$  at  $140^\circ\text{C}$  for 4.5h which resulted in significantly more carbonyl and carboxyl groups than from air oxidation, a treatment which introduced hydroxyl groups together with only very small amount of carbonyl and carboxyl groups. Alternatively, plasma uses an ionized gas containing electrons, radicals, ions or molecules to create active sites and attach functional groups on the surface of carbon fibres. Typical gases used for plasma treatment on carbon fibres include air, oxygen, nitrogen and argon. For this project argon plasma treatment was selected as it has been seen to make the carbon fibre surface hydrophilic in nature with a measurable increase of oxygen groups on the carbon fibre surface [7, 8]. While argon gas does not directly place oxygen-containing functional groups on the surface, because it is used at atmospheric pressure, it mixes with the oxygen in the air and hence, interacts with the fibre surface.

For acid oxidation, after removing sizing in the tube furnace, the CF surfaces were activated with  $\text{HNO}_3$  (Chapter 2, Section 2.6.1.1). The fibre diameters were measured from SEM images to make sure that uniform oxidation of the fibre surface had occurred. The CF had a mean diameter of  $7.68 \pm 0.23\mu\text{m}$ , whereas after  $\text{HNO}_3$  treatment it was  $7.58 \pm 0.06\mu\text{m}$ . This was within error of the original CF.

Prior to plasma treatment (Chapter 2, Section 2.6.1.2) the polymer sizing was again removed from CF in the tube furnace. Argon plasma exposure removes surface contaminants while indicating no significant ablation of the CF in terms of reduction in fibre diameter. An argon and oxygen/air mixture could have been more effective but due to the conductivity of carbon fibre, using a system like dielectric-barrier discharge (DBD) was not possible in which such a

mixture could be used. The fibre tows were kept a 10mm distance from the end of the quartz tube which constantly swept along the tows for a total of 10min.

In Figure 6.2(a-b) are SEM images of the desized CF after HNO<sub>3</sub> or plasma treatment. Figure 6.2(a) showed clear striations along the fibre with a slightly mottled texture. After plasma treatment as seen in Figure 6.2(b) (along with higher magnification image of surface) the fibre showed a more etched surface texture. EDX analysis results of these activated CF are given in Figure 6.2(c-d), showing a higher concentration of oxygen (wt%) on the CF surfaces after both treatments.

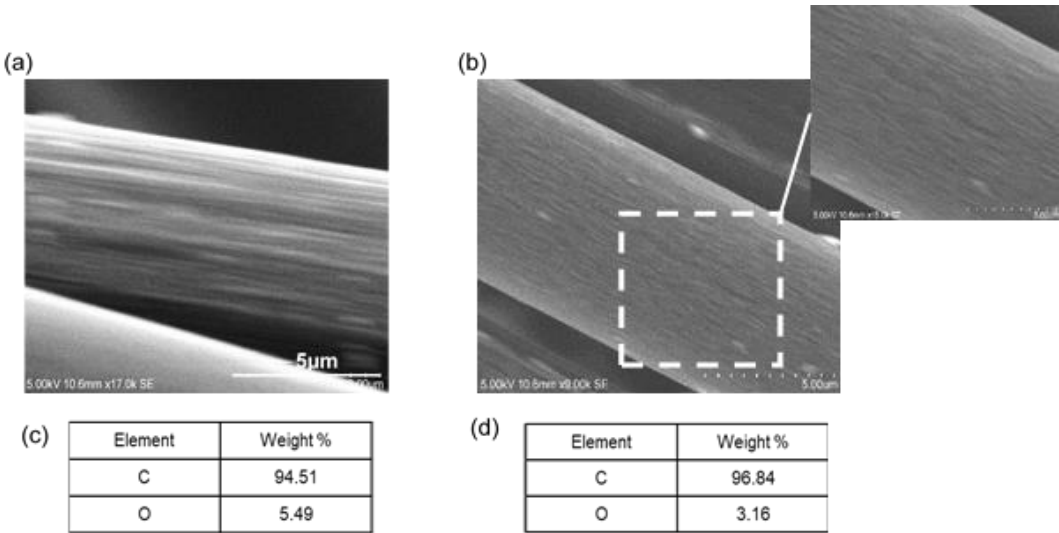


Figure 6.2. SEM images of desized CF followed by (a) HNO<sub>3</sub> or (b) plasma treatment, (c-d) EDX analysis of fibre in (b) and (c).

However, oxygen concentration was almost double on the CF after HNO<sub>3</sub> treatment compared to the plasma treatment suggesting this was more effective in introducing oxygen-containing functional groups. Hence going forward, HNO<sub>3</sub> was used to activate the carbon fibre surface prior to coating.

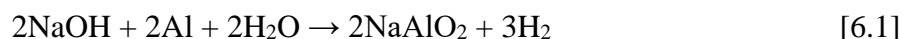
### 6.3 Characterisation of carbon fibre surfaces, modified by thermal barrier coatings

In this section carbon fibres modified by high temperature resistant inorganic compounds, deposited as chemical coatings and different coating methods were characterised in order to identify the most viable ones for evenly coating individual carbon fibres.

### 6.3.1. Inorganic coatings deposited by dip coating

#### 6.3.1.1 Sodium aluminate ( $\text{NaAlO}_2$ )

$\text{NaAlO}_2$  was chosen as a coating material as it has a melting point of  $1,650^\circ\text{C}$  [9]. The sodium aluminate solution was prepared from sodium hydroxide  $\text{NaOH}$ , deionized water and aluminium metal (Chapter 2, Section 2.6.2.) at room temperature for 2hr, according to followed equation [6.1]:



SEM images of the resulting  $\text{NaAlO}_2$  coated fibres ( $\text{CF-NaAlO}_2$ ) and EDX (Figure 6.3(a-b)) indicated that the CF was coated, however, there were cracks evident in the coating, so a further heat treatment in a tube furnace in a nitrogen atmosphere for 3h at  $900^\circ\text{C}$  was carried out to remove any excess solvent. An SEM image of  $\text{CF-NaAlO}_2$  is shown in (Figure 6.3(c)) where the coating has a smoother and more intact structure following this heat treatment. After these heat treatments the coating was present at 14.3wt%.

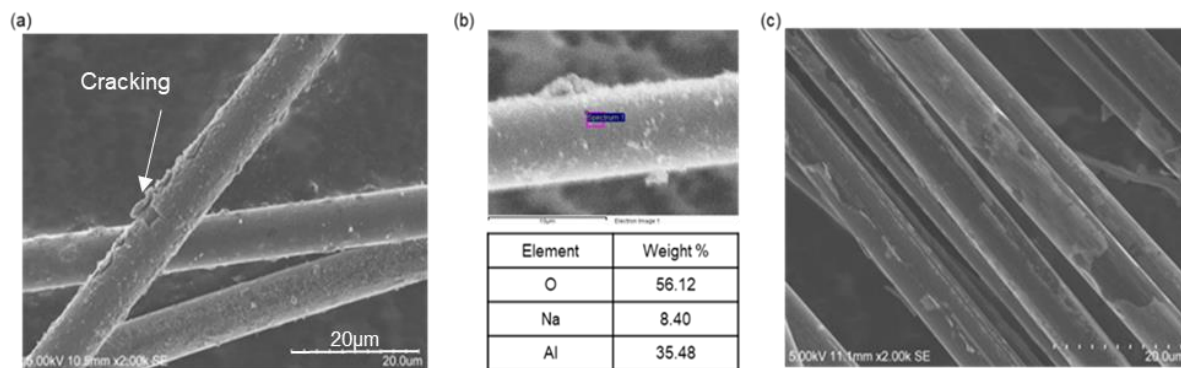


Figure 6.3. SEM images of  $\text{CF-NaAlO}_2$  (a) after oven drying at  $80^\circ\text{C}$  for 12h, (b) EDX of fibre in (a), (c) fibres from (a) after 3.5h in nitrogen at  $900^\circ\text{C}$ .

In order to test if  $\text{CF-NaAlO}_2$  surfaces were fully coated, TGA was carried out on the CF and  $\text{CF-NaAlO}_2$  in air (100ml/s) at  $20^\circ\text{C}/\text{min}$  up to  $1000^\circ\text{C}$  (Figure 6.4(a)). These are given along with the DTG (Figure 6.4(b)), with the characteristic parameters given in Table 6.1. TGA results showed that the temperature at which 5% mass loss occurred,  $T_{0t}$ , as  $246^\circ\text{C}$  for the  $\text{CF-NaAlO}_2$ . Furthermore, carbon fibre only had one DTG maximum peak at  $789^\circ\text{C}$  corresponding to mass

loss due to oxidation, whereas for the  $\text{NaAlO}_2$  coated carbon fibres there were two DTG peaks (246°C and 776°C). The first DTG peaks corresponds to first stage of mass loss (5.2wt% between 153°C-269°C) due to the decomposition of the coating or potentially loss of  $\text{NaAlO}_2$  aggregates adhering to the fibre surface, as seen in Figure 6.3(c).

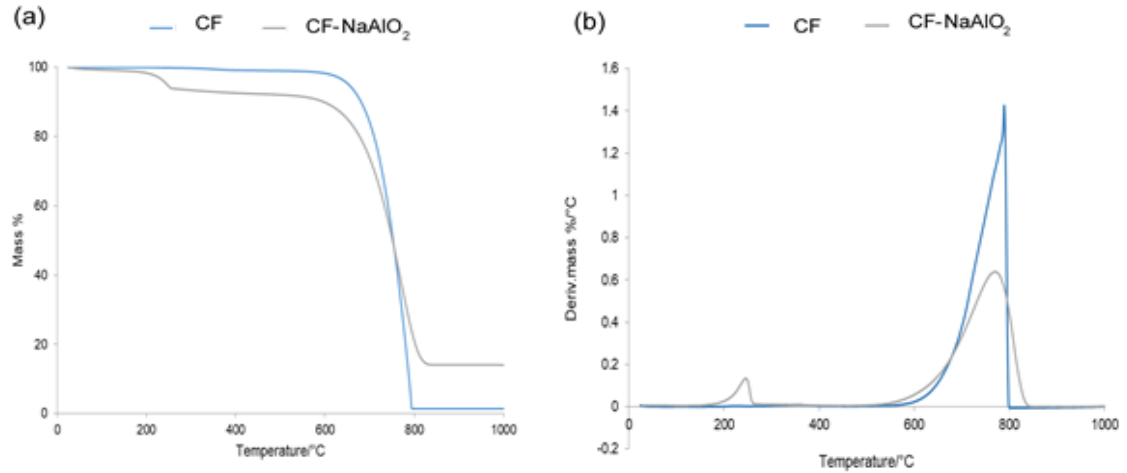


Figure 6.4. (a) TGA curves for the CF and CF- $\text{NaAlO}_2$ , (b) DTG responses for the fibres in (a).

Table 6.1. Characteristic parameters of the thermal decomposition from TGA and DTG curves.

Curve	$T_{0t}$ , °C	$T_{DTG}$ , °C	$T_{res}$ , °C	Wt% of residue at $T_{res}$
CF	652	789	798	1.3
CF- $\text{NaAlO}_2$	246	246; 778	877	14.1

Where T stands for the temperature at which:

$T_{0t}$  = temperature at which 5% mass loss occurred.

$T_{DTG}$  = maximum mass loss occurs (DTG peak).

$T_{res}$  = stable residue formed.

### 6.3.1.2 Boron nitride (BN)

Boron nitride has a high melting point of 2,973°C [1] and is also extremely chemically resistant, which makes it a good choice for a protective coating. As before the carbon fibre sizing was



removed from tows and the surface activated with HNO<sub>3</sub>. Boric acid (H<sub>3</sub>BO<sub>3</sub>) was used as a precursor with a nitrogen atmosphere, used for nitridation (Chapter 2, Section 2.6.2.2). An SEM image of the resulting fibre is given in Figure 6.5(a). The striations on the BN-coated CF (CF-BN) were more defined, most likely due to further etching by the boric acid or boron nitride building up on the high points of the fibre striations. Speckles were on the surface, potentially oxynitrides (BO<sub>x</sub>N<sub>y</sub>) or B<sub>2</sub>O<sub>3</sub> species. Nitridation is typically carried out at temperatures over 1,200°C [10, 11], but the experiments in this work were limited to a temperature of 900°C. However, both Wei et al. [12] and Fu et al. [13] reported coating PAN-based carbon fibres using urea (as an additional source of nitrogen) and boric acid. This resulted in nitridation occurring at 850°C in a nitrogen atmosphere, with the urea improving the purity of the coating and reducing oxide content. The reaction for boric acid and urea is given in equation [6.2]. Excess moisture is then removed as the temperature increases, with the excess urea solidifying. At above around 320°C boric acid dehydrates to boron oxide (equation 6.3) with urea breaking down into NH<sub>3</sub> and CO<sub>2</sub>, and B atoms can then bond directly with N atoms at this temperature. Furthermore, NH<sub>3</sub> can react with B<sub>2</sub>O<sub>3</sub> in the presence of N<sub>2</sub>, (equations [6.4] and [6.5]) and at higher temperatures these can convert into BN [14, 15]



After a subsequent urea treatment (see Section 2.6.2.2), a resulting BN and urea-coated CF (CF-BN-U) SEM image is given in Figure 6.5(b) where a rougher surface texture is seen, implying that the fibre is obviously coated. However, EDX could not confirm the presence of a BN coating because nitrogen has a low-Z number, overlapping with the carbon and oxygen K-alpha making it difficult to detect nitrogen with EDX.

TGA was carried out on, CF, CF-BN and CF-BN-U fibre samples as shown in Figure 6.5(c). While both the CF and CF-BN fibre samples began to oxidise at the same temperature, the CF-BN sample lost mass at a slower rate, forming a stable mass at 926°C of 8.5wt%. This indicated

that a surface residue had formed but oxygen was still able to penetrate through to the carbon fibre. For CF-BN-U, the initial mass loss ( $T_{0t}$ ) occurred at 598°C (compared to 652°C for carbon fibre). Up to a 50.3wt% mass loss had occurred by 750°C and this CF-BN-U sample also lost mass at lower temperatures than the CF. This was most likely due to the removal of the excess products which had not formed during the nitration process. After 750°C the TGA curve showed a shift to higher temperatures, similar to that of the CF-BN curve, indicating that there was a barrier present to slow the diffusion of oxygen, yet unlike CF-BN, only 1.1wt% residue remained above 918°C; this might be due to the early removal of coating at lower temperatures, leaving only a negligible amount of protective coating.

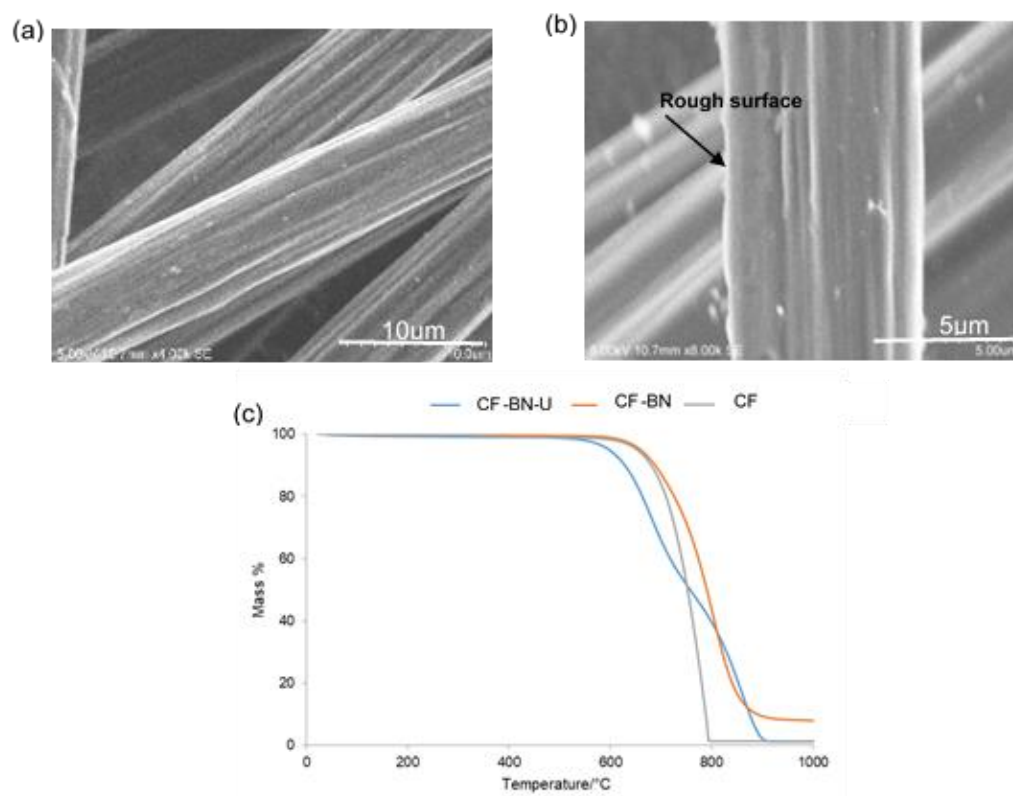


Figure 6.5. SEM images (a) CF-BN, (b) CF-BN-U and (c) TGA of CF and coated fibres in air.

### 6.3.2 Inorganic coatings deposited by sol-gel technology

The next fibre coating method was via the formation of gel coatings. The sol-gel process involves two reactions – hydrolysis of the precursor, and polycondensation of the hydrolysed

products to a ceramic-based structure (depending on the precursor used). The metal precursor undergoes hydrolysis to produce a metal hydroxide solution, followed by condensation leading to the formation of three-dimensional gels, and then a final drying process. Metal oxide nanoparticles  $\text{SiO}_2$ ,  $\text{Al}_2\text{O}_3$  and  $\text{ZrO}_2$  were synthesised using this method, which is outlined in Chapter 2, Section 2.6.3. Individual carbon fibre tows were coated with the ‘gels’ and underwent a subsequent heat treatment to remove any excess solvents. The masses of the tows before and after treatment were recorded.

### 6.3.2.1 Silica ( $\text{SiO}_2$ )

Silica has a very high melting point of  $1,710^\circ\text{C}$  [2] due to its strong covalent bonds, making it useful as a thermal coating. The sol-gel process involves two reactions which are given in Figure 6.6 – hydrolysis of the precursor (TESO for  $\text{SiO}_2$ ) and polycondensation of the hydrolysed products to a  $\text{SiO}_2$ -based structure. These reactions are given in Figure 6.6, where the alkyl group  $\text{R} = \text{C}_2\text{H}_5$ .

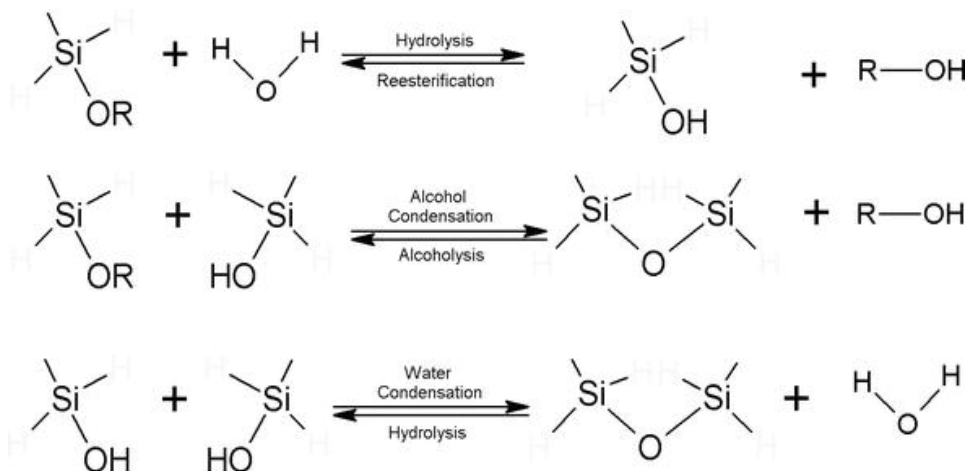


Figure 6.6. Schematic of the reaction during sol-gel process to form  $\text{SiO}_2$  [16].

As described in Section 6.2, Sizing was first removed from CF and the surfaces activated with  $\text{HNO}_3$ . In order to see what difference these surface preparations made to the quality of a coating, both desized and sized CF (were dipped in the  $\text{SiO}_2$  solution (preparation as in Section 2.6.3.1) and then underwent the same drying procedure.

SEM images in Figure 6.7(a) showed an uneven  $\text{SiO}_2$  coating on the sized CF which was most likely due to any active sites on the fibre surfaces being blocked by the sizing. However, on the activated CF, the  $\text{SiO}_2$  gel coating ( $\text{CF-SiO}_2$ ) appeared smoother on the fibre surface with none of the underneath carbon fibre striations visible (Figure 6.7(b)). This showed that removal of sizing and surface activation were required to produce a coherent coating. In order to confirm that the  $\text{SiO}_2$  coating was present, EDX analysis was carried out, and only silicon and oxygen were detected (Figure 6.7(c)). The carbon fibre tows were weighed before and after coating, which enabled the calculated the  $\text{SiO}_2$  coating to be  $20.6 \pm 1.6\text{wt}\%$  add-on. This large increase in mass suggests that  $\text{SiO}_2$  aggregates may have also been formed which adhered to the tow as evidenced by the raised surface sections in Figures 6.7(b) and (c).

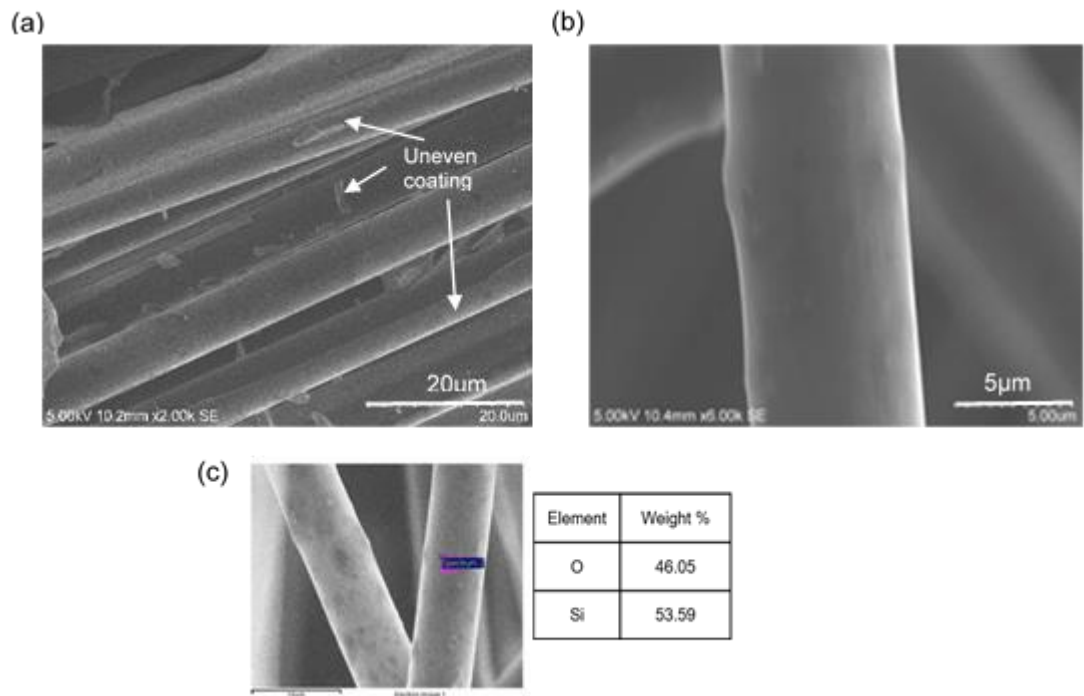


Figure 6.7.  $\text{SiO}_2$  coated (a) sized CF, (b) de-sized and treated with  $\text{HNO}_3$  CF, (c) EDX of the coated fibre in (b).

TGA was not undertaken as EDX was sufficient to confirm the presence of the coating.

### 6.3.3.2 Alumina ( $\text{Al}_2\text{O}_3$ )

Alumina has an even higher melting point than silica at  $2,072^\circ\text{C}$  [17]. The  $\text{Al}_2\text{O}_3$  sol was formed using the same reactions as in Figure 6.6, with aluminium isopropoxide as the precursor and the

alkyl group  $R = \text{CH}(\text{CH}_3)_2$ . Here the gel coating was applied only to unsized, activated fibres. Preparation of the dip coating is outlined in Chapter 2, Section 2.6.3.2.

The coating add-on was  $8.5 \pm 1.5\text{wt}\%$ . As with the  $\text{SiO}_2$  gel coating, a visible coating was observed with SEM. A cross-section of an  $\text{Al}_2\text{O}_3$  coated carbon fibre (CF- $\text{Al}_2\text{O}_3$ ) is shown in Figure 6.8(a), along with the EDX of the CF- $\text{Al}_2\text{O}_3$  in Figure 6.8(b) which gives the atomic Al/O ratio within  $\text{Al}_2\text{O}_3$  as aluminium 36.90 to oxygen 63.10 which is close to the 2:3 ratio expected.

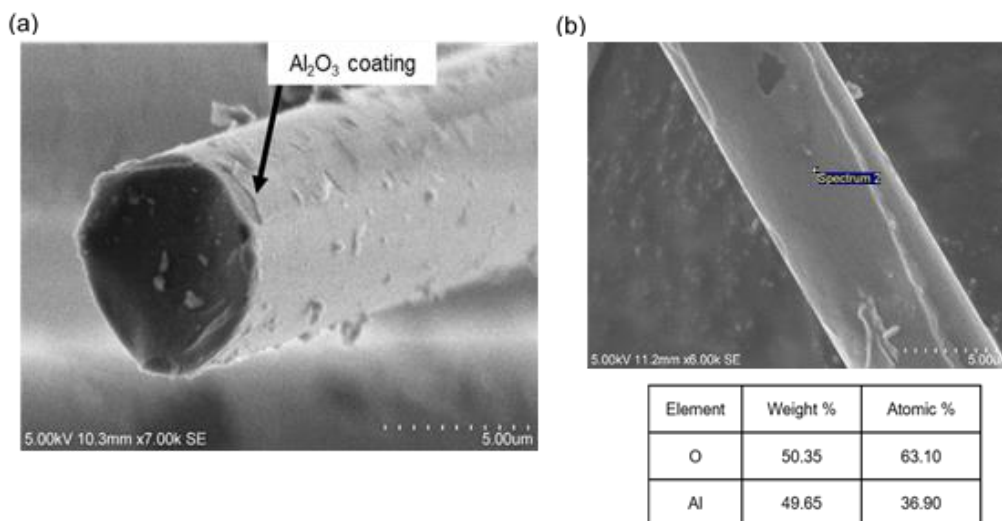
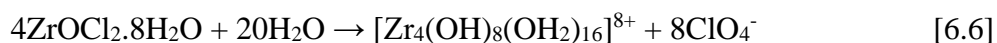


Figure 6.8. (a) Cross-section of CF- $\text{Al}_2\text{O}_3$  and (b) EDX analysis CF- $\text{Al}_2\text{O}_3$ .

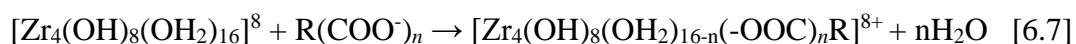
### 6.3.3.3 Zirconia ( $\text{ZrO}_2$ )

$\text{ZrO}_2$  was also synthesised using the sol-gel process with zirconyl chloride octahydrate ( $\text{ZrOCl}_2 \cdot 8\text{H}_2\text{O}$ ) as a precursor, from reactions between  $\text{ZrOCl}_2 \cdot 8\text{H}_2\text{O}$  and the ionized complexing agent  $\text{R}(\text{COO}^-)_n$  (from acetylacetone).

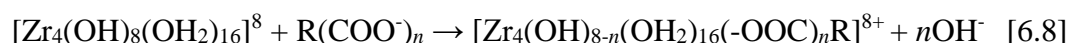
The hydrolysis of zirconyl chloride octahydrate is given as [18], following the equations [6.6] to [6.8]:



followed by the polymerisation reaction:



or



The resulting schematic structure is given in Figure 6.9, where the complex =  $R(\text{COO}^-)_n$ . The coated fibre was then held at 700°C for 2h in nitrogen in order to sinter the above  $\text{ZrO}_2$  complex compound to produce a  $\text{ZrO}_2$ -coated fibre (CF-  $\text{ZrO}_2$ ).

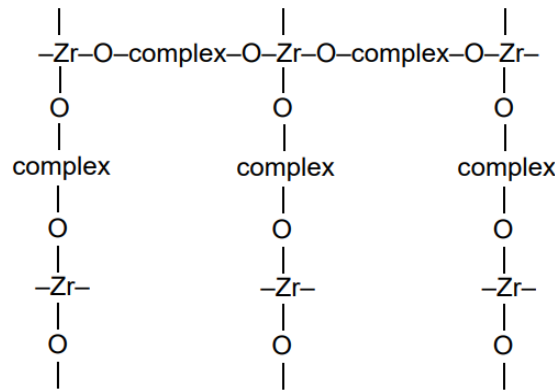


Figure 6.9. Structure of sol, where the complex =  $R(\text{COO}^-)_n$  [18].

The  $\text{ZrO}_2$  and complex coating formed crystals (Figure 6.10(a)) while the resulting reduced CF-  $\text{ZrO}_2$  had a more uniform coating (Figure 6.10(b)). However, EDX analysis (Figure 6.10(c)) detected large amounts of carbon on the surface, indicating that the fibre was not fully coated.

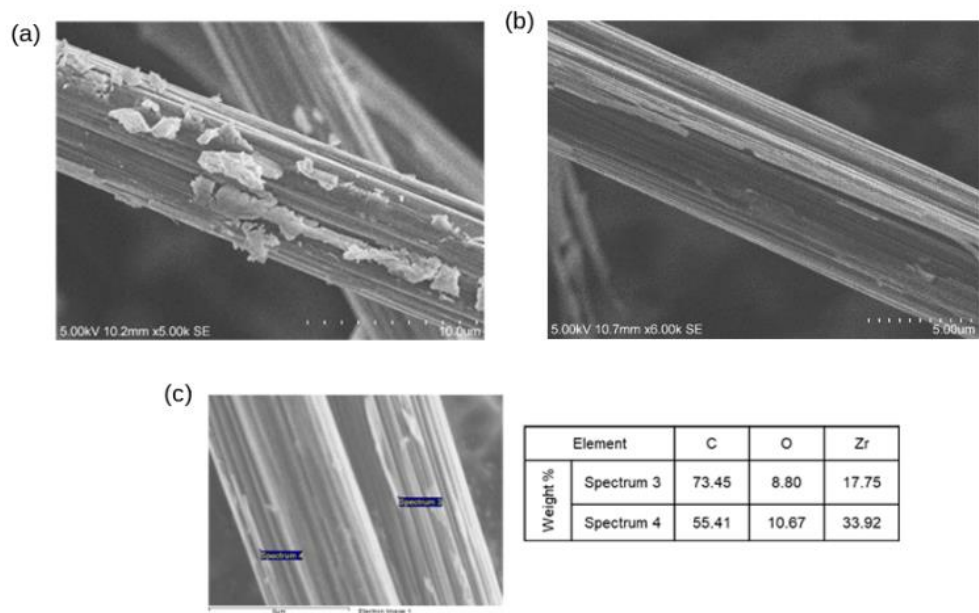


Figure 6.10. Carbon fibre coated with (a)  $\text{ZrO}_2$  and complex, (b)  $\text{ZrO}_2$  and (c) EDX analysis of carbon fibres from (b).

ZrO<sub>2</sub> crystals synthesised from the sol-gel method are typically on the nano-scale. Tyagiet et al. [19] found crystallite sizes to be 13-28nm, which was similar to Heshmatpour and Aghakhanpour's results [20], who recorded 10-30nm. However, as seen in Figure 6.10(b), the crystals synthesised here were significantly larger. Given that no chloride was found, this indicated that the zirconyl chloride octahydrate had been fully hydrolysed. The large crystals are most likely due to the processing parameters used. While ZrO<sub>2</sub> has several benefits over SiO<sub>2</sub> and Al<sub>2</sub>O<sub>3</sub>, such as its stability over a greater pH range and can withstand greater pressure, these are not requirements for a carbon fibre thermal coating. ZrO<sub>2</sub>'s higher sensitivity during its processing to pH value, type of anion and reaction temperature, makes it less ideal for a coating material compared to SiO<sub>2</sub> and Al<sub>2</sub>O<sub>3</sub>.

### **6.3.3 Silica nano-particles deposited as sizing**

In Chapter 3, Section 3.2 a polymer sizing presence on the TR30S carbon fibres used in this project was identified to comprise 1.2wt% of the fibre. Using the concept of a sizing, nano SiO<sub>2</sub> particles were pre-treated with a silane coupling agent and then dispersed in epoxy resin which had been diluted with butanone, with the aim of making a thermal barrier sizing.

The coating procedure is given in Chapter 2, Section 2.6.4. Two epoxy nano-SiO<sub>2</sub> sizings prepared, where one was emulsified. SEM images of activated CF coated in both sizings are given in Figures 6.11(a-b). On the CF coated with the un-emulsified sizing, aggregates of SiO<sub>2</sub> particles were seen and the inherent fibre striations were still identifiable. On the other hand, that of the emulsified sizing, generated smooth fibre surfaces, with only a few small aggregations of SiO<sub>2</sub> particles. The weight increase of this coated fibre tow was  $7.26 \pm 0.7\text{wt}\%$  and the mean diameter of these fibres was recorded at  $7.76 \pm 0.12\mu\text{m}$ , which was within error of the original CF. EDX analysis (Figure 6.11(c)) was carried out at points on the carbon fibre where no obvious clusters of SiO<sub>2</sub> particles were seen, in order to determine if the nano-SiO<sub>2</sub> particles were present. EDX detected low amounts of silicon ( $\sim 3.3\text{wt}\%$ ). The high weight percent of carbon could be identifying the uncoated carbon fibre or the carbon content of the epoxy sizing, which may be covering nano-SiO<sub>2</sub> particles. In order to investigate this further, X-ray photoelectron spectrometry (XPS) would need to be carried out to identify the exact

elemental composition. At this stage of the project, it was decided that the SiO<sub>2</sub> ‘gel’ coating (Section 6.3.3.1) provided a more coherent coating with no carbon detected and that this would be used in heat testing, and not the sized carbon fibres.

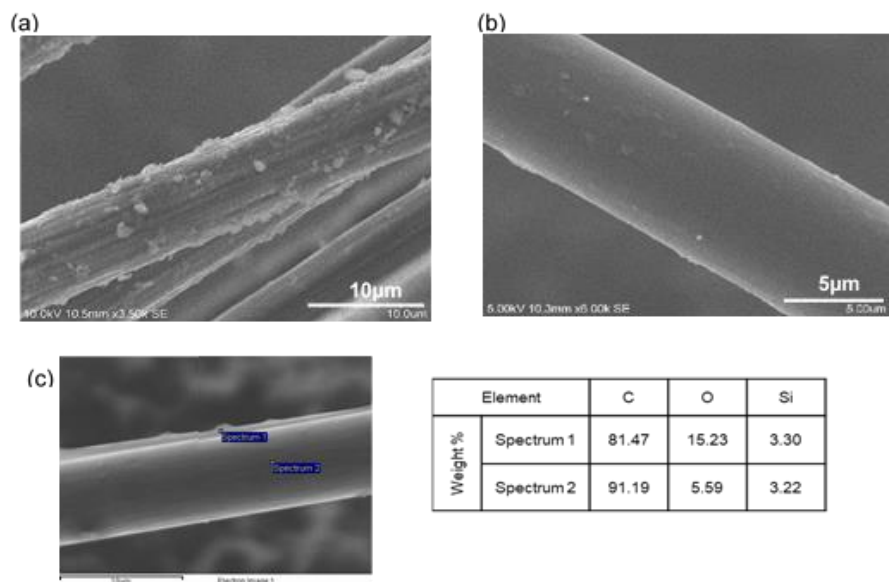


Figure 6.11. SEM images of coated CF with (a) sizing and (b) emulsified sizing, and (c) EDX of the carbon fibre coated with the emulsified epoxy nano-SiO<sub>2</sub>.

#### 6.3.4 Polysiloxane (PS) film, deposited by chemical vapour deposition of hexamethyldisiloxane (HMDSO)

As seen in Section 6.2, argon plasma can activate the carbon fibre surface. Furthermore, it can also be used as a carrier for HMDSO to deposit a polysiloxane film on to the activated carbon fibre surfaces. This is outlined in Chapter 2, Section 2.6.5 and further information is in [21]. Several carbon fibre tows were coated with polysiloxane using this jet plasma method and the coating added  $4.2 \pm 0.8\text{wt}\%$  to the fibre. SEM images of the coating showed spherical particles (ranging up to approximately  $0.5\mu\text{m}$  in diameter) adhering to the carbon fibre surface. Images of the coating and the corresponding EDX analysis are given in Figure 6.12. EDX of a spherical particle (Figure 6.12(a)) detected only silicon and oxygen having an approximate atomic % ratio of 1:2 which could indicate SiO<sub>2</sub>. However, on examining a larger area of the carbon fibre (Figure 6.12(b)), carbon was also detected. This suggests that either EDX is identifying carbon surface areas between particles if the fibre was not fully coated, or, more likely, that these are



other products of HMDSO's fragmentation, such as trapped liquid  $\text{Si}(\text{CH}_3)_4$  [22, 23] or solid SiOC [24].

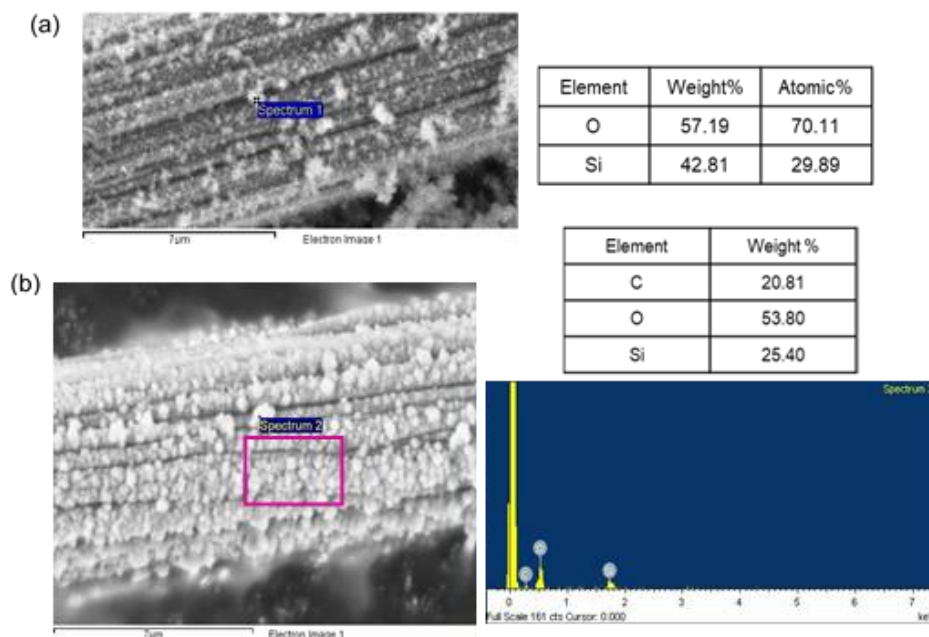


Figure 6.12. EDX analysis of (a) a single spherical particles and (b) over a larger area on the coated carbon fibre surface.

### 6.3.5 Discussion: thermal and oxygen barrier coatings on carbon fibres

Initially the inorganic dip-coating  $\text{NaAlO}_2$  was studied as a deposit on carbon fibre surfaces. While this salt dissolves readily in water, producing a strong alkaline solution, this was not deemed a problem as the carbon fibres present reinforced epoxy composites would not come into contact with water. Furthermore, the curing agent use for a typical epoxy resin is typically amine-based, which is alkaline and not acidic. However, problems arose with using this ionic compound since TGA results indicated that there might be defects in the crystalline structure which allowed oxygen to reach the underlying carbon fibre surface.

Nitrides, which can be formed by nitriding, were then studied for their coating properties. Nitriding is a heat treatment process that diffuses nitrogen into the surface of the metal. This can be done in several ways, including gas nitriding, salt bath nitriding or plasma nitriding. In this project gas nitriding with nitrogen gas was attempted. However, it was found that  $900^\circ\text{C}$  was

not high enough for the boric acid to absorb a sufficient amount of nitrogen, even with the addition of the nitrogen source of urea. For sufficient diffusion of nitrogen, temperatures over 1,200°C are most likely required. Furthermore, another consideration is how the coating affects the mechanical properties of the carbon fibre. Das et al. [10] also activated PAN-based carbon fibres with  $\text{HNO}_3$  and coated them using boric acid followed by nitriding under  $\text{N}_2$  to form a BN coating. They found a significant reduction in the tensile strength of BN-coated fibre comparable to the original CF and activated carbon fibres. This was attributed to a composite layer of BN and carbon together with some graphitic content like BCN (in the forms  $\text{B-N-C}$  and  $\text{B(N-C)}_3$ ) being formed on the coated fibre; these results are reproduced in Figure 6.13. Due to these reasons, BN and other nitride coatings, including aluminium nitride were deemed not to be feasible for this project.

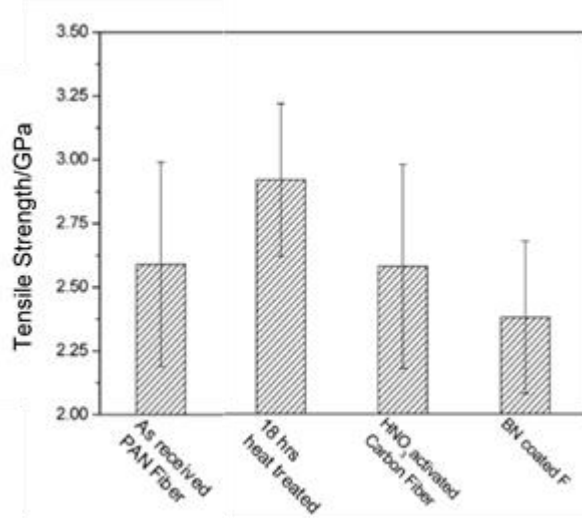


Figure 6.13. Tensile strength of carbon fibres after different surface treatments [10].

Because the previous tests of a coating with a purely crystalline structure ( $\text{NaAlO}_2$ ) resulted in defects which allowed oxygen to reach the carbon fibre surface, alternative three-dimensional gels were formed using a two stage reaction, sol-gel process from which nano-particulate metal oxides could be produced. The chosen metal oxide nanoparticles were -  $\text{SiO}_2$ ,  $\text{Al}_2\text{O}_3$  and  $\text{ZrO}_2$  as all three have extremely high melting points. A sized as well as unsized and activated CF sample was coated in  $\text{SiO}_2$  using the sol-gel process to observe the effect of the original size presence. Results showed that size removal and surface activation with  $\text{HNO}_3$  were required in order to form a smooth coating (Figures 6.6(a-b)). The  $\text{SiO}_2$  coating was confirmed by EDX on

the desized and activated carbon fibre which was considerably smoother than on original, sized CF. While sizing presence only accounts for 1.4wt% of the carbon fibre, this is enough to block any carboxyl groups which maybe on the fibre surface, where it is concentrated. Using the same sol-gel process,  $\text{Al}_2\text{O}_3$  was also successfully placed on the individual desized carbon fibres of a tow, as seen in Figure 6.8(a). However,  $\text{ZrO}_2$  coatings (Figure 6.10(b)) were unsuccessful as the  $\text{ZrO}_2$  agglomerated along the valleys and grooves of carbon fibre striations. The reason for this is not fully understood, however,  $\text{ZrO}_2$  is almost twice as dense as  $\text{Al}_2\text{O}_3$  and significantly denser than  $\text{SiO}_2$ , and so perhaps the increased density resulted in the  $\text{ZrO}_2$  not dispersing evenly in a three-dimensional gel. The preferential filling of valleys and grooves of striations could be the surface tension effect.

Using the idea of carbon fibre polymer sizing,  $\text{SiO}_2$  nano-particles were dispersed in an epoxy resin in order to make a ‘thermal barrier sizing’. It was found that by creating an emulsion in the epoxy, the nano- $\text{SiO}_2$  particles were distributed more uniformly. However, it was not established whether the nano- $\text{SiO}_2$  coating was distributed evenly enough to provide an oxygen barrier to the underlying carbon fibre (see Figure 6.11(b) and (c)). However, apart from this caveat, the  $\text{SiO}_2$  coating formed via the sol-gel process was more promising as a complete barrier coating.

Finally, plasma surface treatment was found to roughen the carbon fibre surfaces and in the literature it has shown to introduce surface functional groups. Along with HMDSO vapour in the plasma gas (argon), it was also used to deposit polysiloxane on to the carbon fibre surfaces, identified as evenly distributed spherical particles adhering to the underlying carbon fibre surface. This coating method also resulted in only a mean gain in mass of  $4.2 \pm 0.8\text{wt}\%$ .

From these result is was concluded that the  $\text{SiO}_2$  and  $\text{Al}_2\text{O}_3$  coated carbon fibres (formed via a sol-gel process) would be subjected to further heat testing. Unlike the  $\text{ZrO}_2$  coating, both  $\text{SiO}_2$  and  $\text{Al}_2\text{O}_3$  showed smooth surface coatings with EDX confirming their presence. While nitrides offered extremely high melting points and are generally chemically inert, the temperatures required for nitration are out the scope of this project and so deemed to be unsuitable for coating carbon fibres. Polysiloxane and organosilicon compounds from the plasma fragmentation of

HMDSO were successfully deposited. Furthermore, the use of plasma also has surface activation benefits, such as surface roughening, hence polysiloxane coating was also selected for further heat exposure testing. Along with heat testing, the mechanical and electrical properties of these selected coated fibres were also assessed and are discussed in the following sections.

#### 6.4 Evaluation of thermal and oxidation protection efficiency of coatings

In order to identify if the coatings provided heat resistance to carbon fibre, tows of individually coated fibres were placed in the tube furnace at varying temperatures in static air, as was done in Chapter 3, Section 3.3. The coated tows were selected from the most promising results in Section 6.3. TGA results in Figure 6.4(a) showed that oxidation of carbon fibres began around 550°C and they were fully oxidised after 800°C. From this, temperatures where the carbon fibres were susceptible to oxidation (500, 550 and 600°C) were selected and coated carbon fibre tows were held at these temperatures for between 0.5 to 2h. Five of each coated tows were weighed before and after, and the fibre diameters measure from SEM images. Results are given in Table 6.2 for the mass losses.

Table 6.2. wt% loss of CF and coated carbon fibres held in the tube furnace for varying temperatures and times.

Temp/°C	Time/h	Coating wt% loss			
		CF*	CF-SiO <sub>2</sub>	CF-Al <sub>2</sub> O <sub>3</sub>	CF-PS
500	0.5	4.3 ± 1.2 (3.1)	39.8 ± 2.3	0.7 ± 0.4	2.4 ± 0.6
500	1	14.2 ± 1.8 (13.0)	49.6 ± 2.8	11.1 ± 0.4	5.3 ± 0.3
500	2	20.4 ± 1.6 (19.2)	43.5 ± 1.5	15.1 ± 0.6	21.7 ± 0.7
550	0.5	7.3 ± 0.9 (6.1)	45.5 ± 2.1	7.5 ± 1.0	10.3 ± 1.1
550	1	18.3 ± 0.5 (17.1)	45.0 ± 3.3	21.3 ± 0.9	49.5 ± 3.2
600	0.5	33.8 ± 2.8 (32.6)	37.8 ± 1.3	33.0 ± 1.2	44.9 ± 4.4

\*The values in parentheses and italics represent wt% loss due to oxidation (after compensating for 1.2% wt loss due to removal of sizing). For coated samples, there is no sizing and assuming that the coating is stable, no further compensation required.

For CF, after 0.5h at 500°C, only a small mass loss was expected, which would include the sizing of the CF (1.2wt%) and slight uniform oxidation. The CF had a  $4.3 \pm 1.2$ wt% loss which is included with these. The CF-Al<sub>2</sub>O<sub>3</sub> and CF-PS lost less ( $0.7 \pm 0.4$  and  $2.4 \pm 0.6$ wt% respectively), indicating that the respective coatings have reduced the level of oxidation of the underlying carbon fibres. However, the CF-SiO<sub>2</sub> lost a significant amount of mass ( $39.8 \pm 2.3$ wt%), which was even greater than the weight of the original coating  $20.6 \pm 1.6$ wt%. SiO<sub>2</sub> is known to absorb water and during its coating, CF-SiO<sub>2</sub> fibres were heated in nitrogen at 700°C. It has been reported [25] that after heating above 400°C, the ability for SiO<sub>2</sub> to be rehydrated by water vapour via its surface hydroxyl sites is reduced. However, the results in Table 6.2 suggest that water had been absorbed after coating and a contributing factor to the mass loss was the condensation of surface silanol (Si-OH) [25]. The coated carbon fibres were stored in sealed container, but were removed for 2h for sample preparation before heat testing in the tube furnace and SEM analysis. Furthermore, unlike for the other fibres, the mass losses for CF-SiO<sub>2</sub> over the different temperature ranges and times, did not vary by more than ~10wt%. Indicating that this mass loss was not sensitive to temperatures changes above 500°C, such as carbon fibre oxidation, and hence is more likely the evaporation of water which occurs at a much lower temperature.

At 500°C for 1h both CF-Al<sub>2</sub>O<sub>3</sub> and CF-PS again had the least reductions in mass, indicating slightly improved oxidation resistance relative to CF. At higher temperatures CF-Al<sub>2</sub>O<sub>3</sub> showed very similar mass loss results to CF, however, this does not take into account for the mass of the coating ( $8.5 \pm 1.5$ wt%). At 550°C for 1h and 600°C for 0.5h the CF-PS fibre gave larger than expected mass losses ( $49.5 \pm 3.2$  and  $44.9 \pm 4.4$ wt% respectively) and significantly higher than for CF. Again, this may be due to the coatings containing trapped volatiles such as, Si(CH<sub>3</sub>)<sub>4</sub>, and these results indicate that mass loss alone is not sufficient to accurately determine the degree of underlying carbon fibre oxidation. Hence, SEM was used to measure the average carbon fibre diameters at each condition and examine the surface for damage. Diameter results are given in

Table 6.3 and plotted in Figure 6.14(a-b) in order to identify any trends with SEM images of the coated fibres (Figure 6.15(a-d)) and those from Table 6.3 (Figure 6.15(e-t)). All fibre diameters of the coated fibres were within error of the CF.

Table 6.3. Diameters of CF and coated carbon fibres after being held in the tube furnace for varying temperatures and times.

Temp/°C	Time/h	Diameter of carbon fibres, $\mu\text{m}$			
		CF	CF-SiO <sub>2</sub>	CF-Al <sub>2</sub> O <sub>3</sub>	CF-PS
Unexposed		$7.68 \pm 0.23$	$7.72 \pm 0.11$	$7.65 \pm 0.06$	$7.76 \pm 0.12$
500	0.5	$7.13 \pm 0.15$	$7.17 \pm 0.08$	$6.88 \pm 0.05$	$7.30 \pm 0.08$
500	1	$6.02 \pm 0.21$	$6.93 \pm 0.05$	$7.00 \pm 0.04$	$7.01 \pm 0.06$
500	2	$5.87 \pm 0.34$	$6.01 \pm 0.11$	$6.63 \pm 0.05$	$7.06 \pm 0.07$
550	0.5	$6.57 \pm 0.28$	$6.40 \pm 0.06$	$6.79 \pm 0.07$	$7.19 \pm 0.07$
550	1	$5.47 \pm 0.31$	$6.41 \pm 0.07$	$6.03 \pm 0.13$	$7.03 \pm 0.13$
600	0.5	$5.26 \pm 0.32$	$6.23 \pm 0.12$	$6.15 \pm 0.06$	$5.41 \pm 0.15$

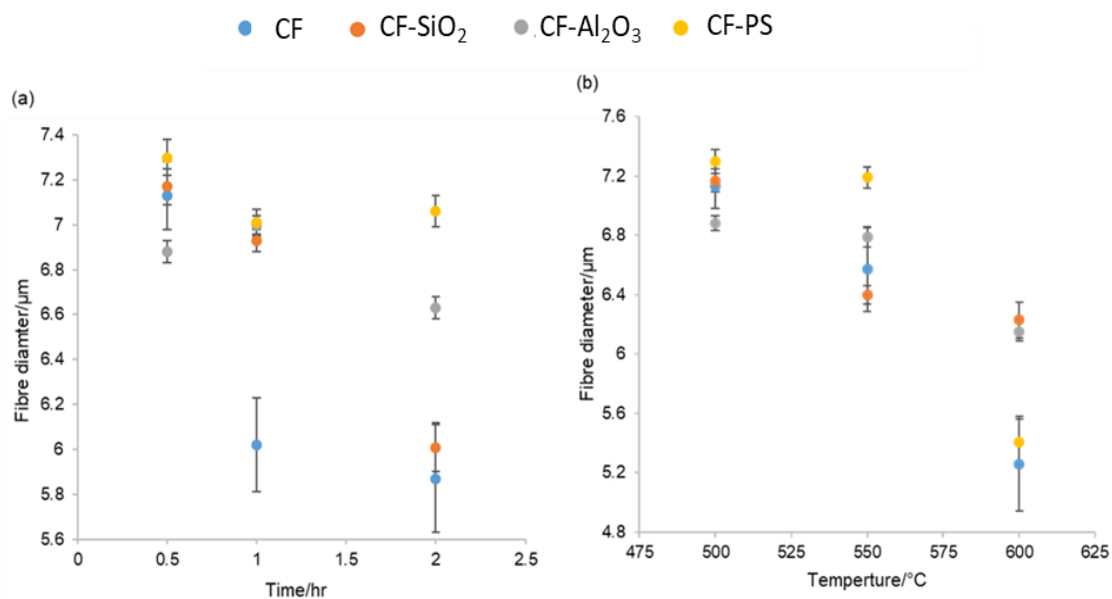


Figure 6.14. Coated carbon fibre diameters after being held for (a) Varying lengths of times at 500°C (b) Varying temperatures for 0.5h.

For fibres held at 500°C for 0.5h, with the exception of CF-Al<sub>2</sub>O<sub>3</sub>, respective fibre diameters were within error of each other and little reduction in diameter was seen. Figure 6.15(e-h) shows SEM images of the individual fibres where the coatings are visible. In Table 6.2 the CF-SiO<sub>2</sub> experienced a large mass loss but this did not translate into a reduced diameter in Table 6.3, therefore the mass loss was from the SiO<sub>2</sub> coating and not the carbon fibre.

After 1h at 500°C all the coated fibres had retained their diameters at around 7µm and were within error of each other, while CF was more oxidised losing over an extra 1µm in diameter, which indicated that the coatings had maintained a sufficient oxygen barrier. The SEM images in Figures 6.15(i-l) showed an intact SiO<sub>2</sub> coating  $7.68 \pm 0.23\mu\text{m}$  fibres with small areas of agglomeration while the Al<sub>2</sub>O<sub>3</sub> coating had lost some of its original smooth texture, and the polysiloxane coating still had spherical particles adhering to the surface, although much less in number.

After 2h exposure at 500°C CF-PS had an average diameter within error of that after 1h at the same temperature. CF-Al<sub>2</sub>O<sub>3</sub> on the other hand had reduced in diameter but were still significantly larger than similarly exposed CF and CF-SiO<sub>2</sub> which were now in error of each other at around 6µm. The reduction in CF-Al<sub>2</sub>O<sub>3</sub> may be linked to fine pore formation in the Al<sub>2</sub>O<sub>3</sub> coating as reported by Ramanathan et al., [26] which allowed the slow diffusion of oxygen through it in over the longer time. This effect was also seen at 550°C where the diameter of CF-Al<sub>2</sub>O<sub>3</sub> only slightly reduced on increasing the time from 0.5h to 1h heat exposure. CF-SiO<sub>2</sub> did maintain a slightly larger average diameter than CF but after 2h at 500°C oxygen had almost reached that of the carbon fibre control, most likely due to cracks in the SiO<sub>2</sub> coating. The precursor used to make the SiO<sub>2</sub> 'gel' was TEOS (Si(OC<sub>2</sub>H<sub>5</sub>)<sub>4</sub>, or Si(OR)<sub>4</sub>, where the alkyl group R= C<sub>2</sub>H<sub>5</sub>. As stated previously TEOS underwent hydrolysis of the Si-OR groups to silanol groups (Si-OH) which then condense to form Si-O-Si bonds through the loss of alcohol and/or water [27]. However, during this process intermediate species could potentially remain within the developing three-dimensional gel, such as H<sub>2</sub>O and R-O-H species if full polymerization had not occurred. While present in very small amounts may not be an issue for most applications, the loss of these over time may be the cause of formation of cracks or pores as they escape the

three-dimensional SiO<sub>2</sub> gel coating, thus allowing oxygen to enter and reach the underlying carbon fibre surfaces.

The plot of fibre diameters for the CF and coated fibres held at different temperatures for 0.5h given in Figure 6.14(b) show that when heated at 550°C for 0.5h, CF-SiO<sub>2</sub> and CF-Al<sub>2</sub>O<sub>3</sub> average diameters were both within error of that of CF and Figure 6.15(n and o) shows the surface coating to be largely intact.

Also, after exposing at 600°C for 0.5h, CF-SiO<sub>2</sub> and CF-Al<sub>2</sub>O<sub>3</sub> average diameters were within error of each other with values almost 1 µm larger than the similarly exposed CF control. This suggests that 0.5h was not long enough time for the diffusion of any remaining intermediate species within the SiO<sub>2</sub> coating to rupture the coating shown in Figure 6.15(r) (as also noted with the fibre held for 1h at 500°C (Figure 6.15(i)). While CF-PS had both superior oxidation protection results at 500°C for up to 2h, and at 550°C for 0.5h, after exposure at 600°C for 0.5h, its fibre diameter was within error that of the similarly exposed CF with a severely oxidised surface as shown in Figure 6.15(t). Both the CF and CF-PS fibres showed oxidatively formed cavities along the fibres' striations. Figures 6.15(r) and (s) shows at 600°C the carbon fibres coated with SiO<sub>2</sub> and Al<sub>2</sub>O<sub>3</sub> respectively had less obvious signs of surface oxidation. In order to investigate this surface oxidation further more CF-PS samples were examined with SEM to identify any damage to the coating (see Figures 6.16(a)-(c)). These results may be correlated with the surprising mass loss results shown in Table 6.2 for the CF-PS fibre samples after exposing at 550°C for 1h and 600°C for 0.5h, which were  $49.5 \pm 5.8$  and  $44.9 \pm 4.7$ wt% respectively.



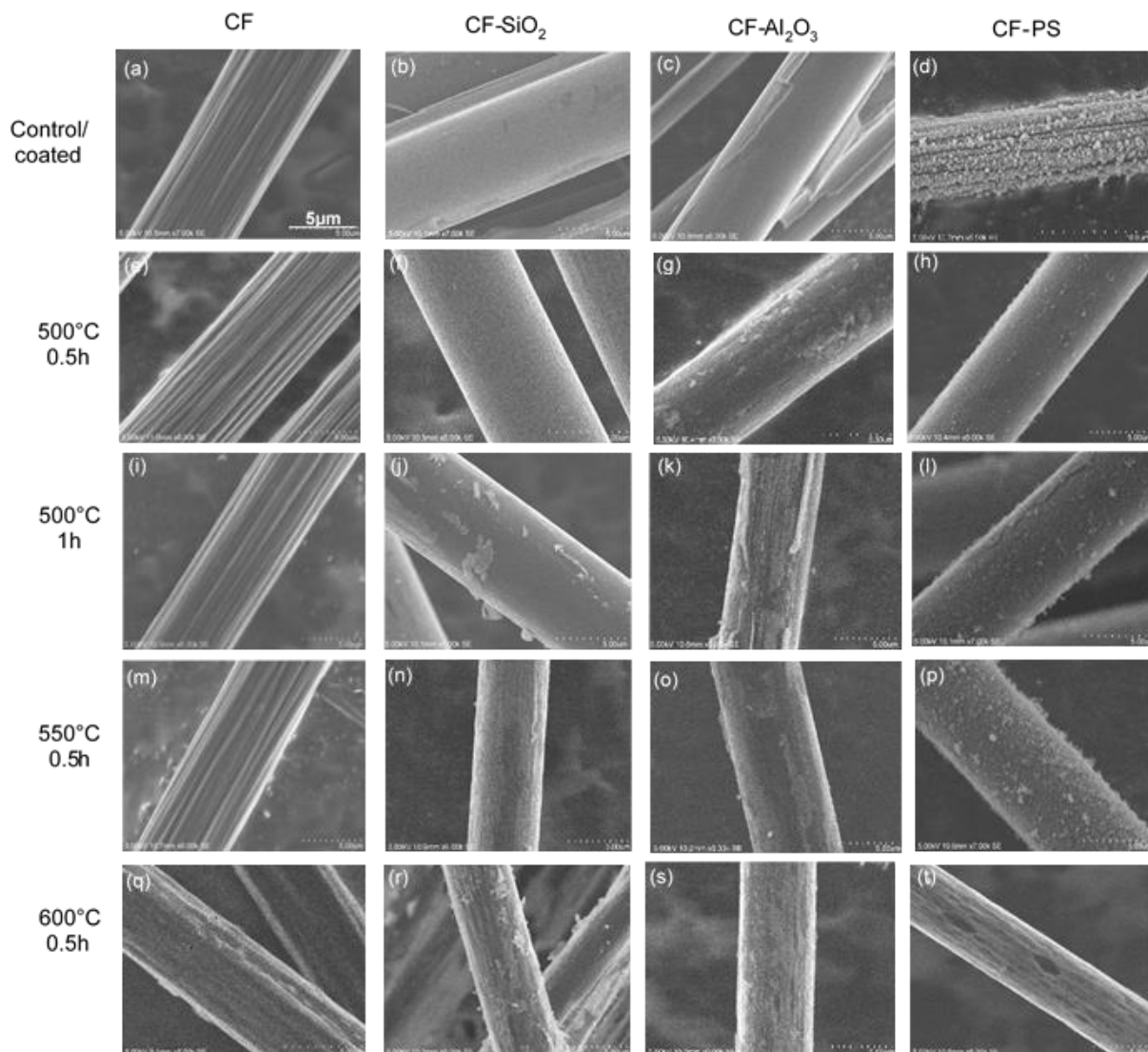


Figure 6.15. SEM images of the CF and coated fibres held a different temperatures for varying times.

Given that the coating only accounted for  $4.2 \pm 0.8\text{wt}\%$  of the sample, these weight losses indicated there was also some considerable oxidation of the carbon fibre. Polysiloxane is a hydrophobic polymer hence it is unlikely to absorb moisture so no mass loss due to the evaporation of water was expected. After the  $550^\circ\text{C}$  for 1h and  $600^\circ\text{C}$  for 0.5h exposures, cracking of the polysiloxane coating was found on some fibres as shown in Figures 6.16(a) and (b), leading to fully exposed carbon fibres. These exposed carbon fibres thus showed large areas of localised oxidation (Figure 6.16(c)) which therefore accounts for the mass losses and reductions in fibre diameter. This cracking of the polysiloxane coating may be linked to the

thermomechanical mismatch of the coating and the carbon fibre as carbon fibres have a slight negative thermal expansion. Similar findings were also reported by Chaiwong et al. [28] where they found that the difference in mechanical properties of a polysiloxane coating, also applied via argon plasma, on a polylactic acid substrate resulted in intrinsic stress within the coating, leading to its cracking.

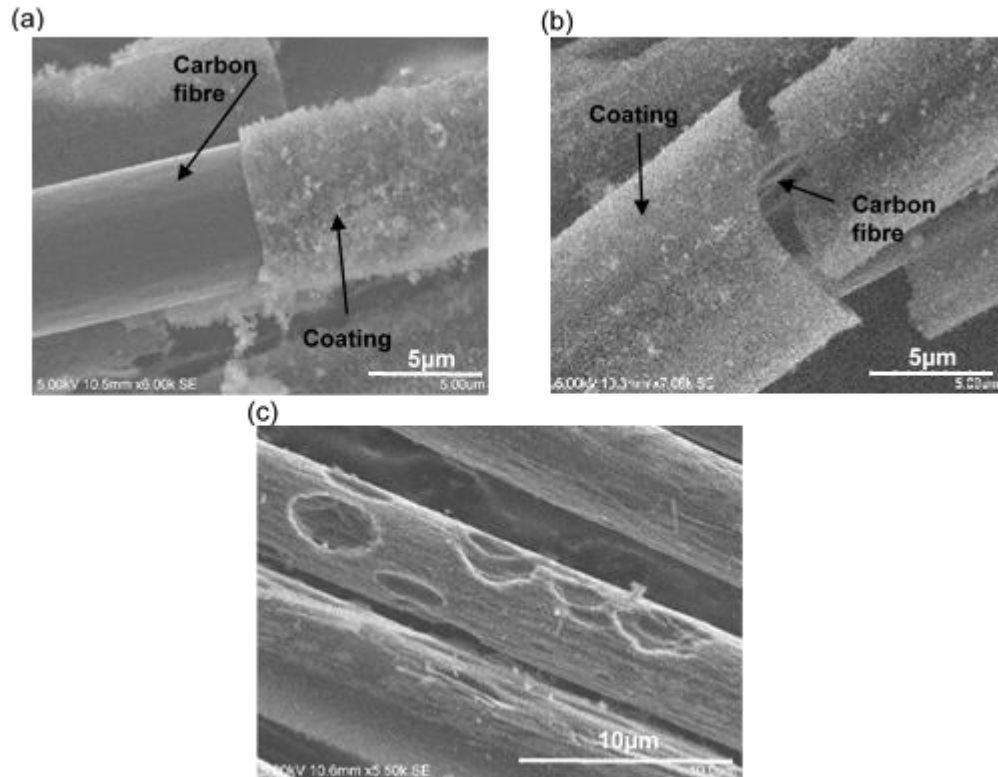


Figure 6.16. SEM images of CF-PS after exposing at (a) 550°C 1h and (b-c) 600°C 0.5h.

## 6.5 Mechanical properties of the coated fibres after exposure to heat

In order to assess whether the coated carbon fibres had improved heat and fire resistance, single fibres were removed from tows exposed in the tube furnace for tensile testing as in Chapter 2, Section 2.5.4. Fibres held at 500°C for 0.5h were not selected for tensile testing as little change in fibre diameter was found. After 600°C for 0.5h both CF and CF-PS were too fragile for single fibre tensile tests, so these were also not included. Assuming uniform circular cross-section and

using the diameters in Table 6.3, the results for tensile strength and modulus are given in Table 6.4.

Table 6.4. Tensile strength and modulus of CF and coated carbon fibres after heat testing in the tube furnace.

Temp, °C	Time, h	Coating							
		CF		CF-SiO <sub>2</sub>		CF-Al <sub>2</sub> O <sub>3</sub>		CF-PS	
		Strength, MPa	Modulus, GPa	Strength, MPa	Modulus, GPa	Strength, MPa	Modulus, GPa	Strength, MPa	Modulus, GPa
Control/coated fibre		3877 ± 136	237 ± 4	3518 ± 125	200 ± 8	3204 ± 137	179 ± 4	3412 ± 98	201 ± 11
500	1	2852 ± 183	211 ± 5	2325 ± 229	249 ± 14	1807 ± 91	194 ± 3	2685 ± 188	198 ± 9
500	2	1504 ± 254	174 ± 11	1351 ± 150	215 ± 15	1512 ± 184	211 ± 7	1796 ± 163	190 ± 7
550	1	2180 ± 130	167 ± 9	1962 ± 114	273 ± 10	1592 ± 159	150 ± 9	1869 ± 340	223 ± 15

Stress-strain curve of fibres close to the mean results in Table 6.4 are plotted in Figures 6.17(a)-(d). Due to the fragility of the extracted single carbon fibres, as well as a high signal to noise ratio, undulations in some curve were seen.

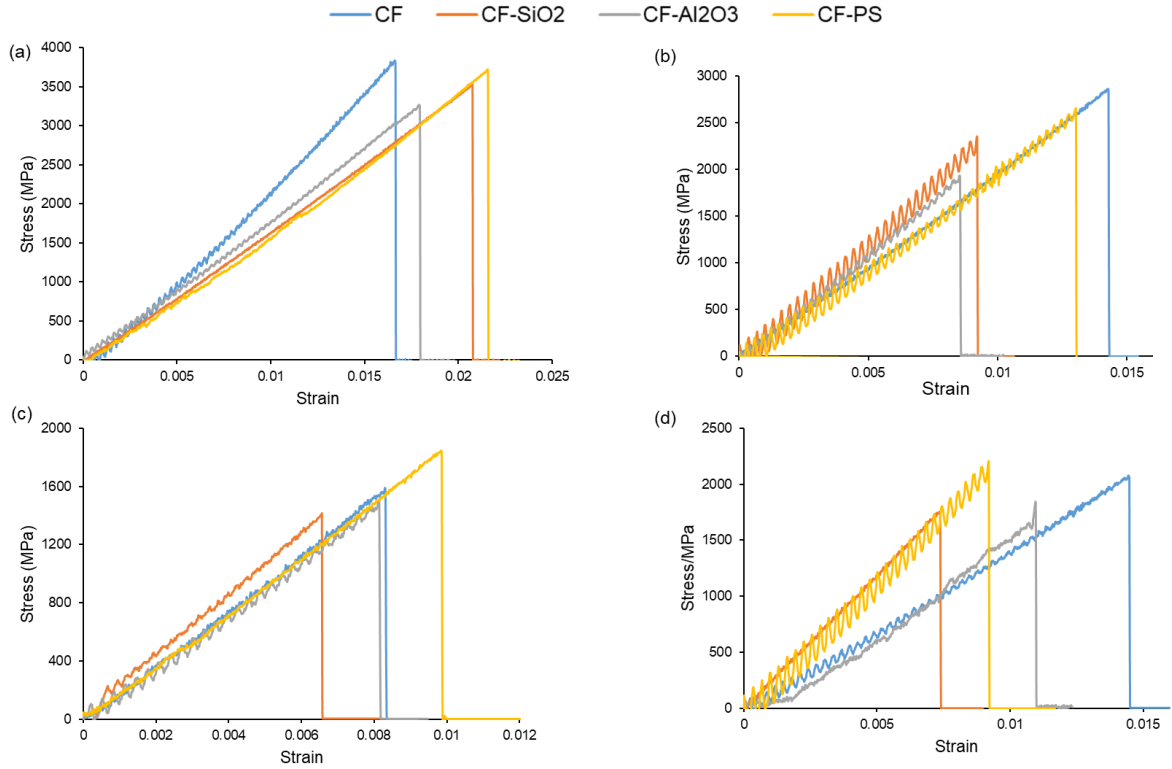


Figure 6.17. Stress-strain curves for (a) CF and coated fibres, after holding at (b) 500°C for 1h, (c) 500°C for 2h and (d) 550°C for 1h.

The tensile strength of the unexposed CF was greater than those which were coated. This is due to the surface activation treatments, 1.5h at 450°C in nitrogen atmosphere and 2h in concentrated  $\text{HNO}_3$  at 80°C. All unexposed coated fibres had tensile strengths and tensile modulus values within error of each other and both had decreased with respect to unexposed CF values most likely due to the volatilisation of non-carbon particles when undergoing surface activation treatments. Any resulting surface pits will then have acted as possible stress concentrators during tensile testing. Wu et al. [29] found a 15% fibre tensile strength loss after 1.5h in 70%  $\text{HNO}_3$ , which is very similar to those found here ( $\text{SiO}_2$  – 9.3%,  $\text{Al}_2\text{O}_3$  – 17.4% and PS 12%) and Nohara et al. [30] also noted a strength decrease after  $\text{HNO}_3$  treatment on Toray T300 carbon fibres, which have a similar modulus and strength to TR30S (Mitsubishi-Rayon Pyrofil) fibres. The use of the argon plasma appeared not to have reduced the strength of the carbon fibre, as CF-PS had a tensile strength within error of the CF- $\text{SiO}_2$  which were exposed only to  $\text{HNO}_3$ .

After holding the fibres at 500°C for 1h Figure 6.17(b), all the fibres showed reductions in strength, which followed the same relative positions as untested fibres in Figure 6.17(a) (with CF-Al<sub>2</sub>O<sub>3</sub> still being the weakest and CF the strongest). However, the fibre modulus showed a different trend in that while the CF modulus reduced, those of CF-SiO<sub>2</sub> and CF-Al<sub>2</sub>O<sub>3</sub>'s increased and CF-PS showed only a small change. Further reduction of the CF modulus occurred after 2h at 500°C and after 1h and 550°C, suggesting that oxidation was the cause. This was not seen for the coated fibres in that the CF-SiO<sub>2</sub> modulus increased after heat treatments, while that of CF-PS always remained within error, potentially indicating that these were less oxidised than CF.

Because surface activation treatment had resulted in a reduction in strength, by introducing possible pits, this had to be taken into account when more accurately comparing tensile strengths, hence in Table 6.5 the percentage tensile strength reduction with respect to the untested fibres are given.

Table 6.5. Percentage tensile strength loss of the fibres with respect to the untested fibres.

Temp, °C	Time, h	Tensile strength reduction w.r.t CF/coated fibre, %			
		CF	CF-SiO <sub>2</sub>	CF-Al <sub>2</sub> O <sub>3</sub>	CF-PS
500	1	22 ± 5	27 ± 6	41 ± 3	16 ± 5
500	2	54 ± 6	57 ± 4	46 ± 6	43 ± 5
550	1	40 ± 3	41 ± 3	45 ± 5	34 ± 9

CF experienced a 22 ± 5% loss in tensile strength after 1h at 500°C and after 1h at 550°C it had almost double (i.e. 40 ± 3)%, which showed that the strength of carbon fibre was very sensitive to temperatures at above 500°C. The greatest reduction in tensile strength however, occurred after 2h at 500°C (54 ± 7%). The coated fibres also showed this trend whereby the greatest reduction occurred after 2h at 500°C.

After exposure at 500°C for 1h, both CF and CF-SiO<sub>2</sub> were within error of each other, while CF-PS had a 6% increase in fibre strength compared to CF. However, CF-Al<sub>2</sub>O<sub>3</sub> lost considerably more strength than CF and other coated fibres. This was surprising as it had maintained over 1µm more in fibre diameter than CF, indicating that Al<sub>2</sub>O<sub>3</sub> had formed a barrier to stop the diffusion of oxygen. However, if excess aluminium remained in the Al<sub>2</sub>O<sub>3</sub> sol coating, the unstable brittle carbide Al<sub>4</sub>C<sub>3</sub> has been reported to form in aluminium-graphite systems at 500°C [31], which could have reduced the tensile strength of the fibre, similar to the results in Figure 6.11 when coating with boron nitride.

After exposing at 500°C for 2h, CF and CF-SiO<sub>2</sub> had tensile strength (%) losses again within error of each other. It was seen in Table 6.3 that these same fibres had diameters within error of each other and this was credited to unreacted species within the SiO<sub>2</sub> coating diffusing to the surface, resulting in micro-cracks. Hence the oxidation-protective character of the SiO<sub>2</sub> coating was impaired and the fibres had a similar loss in diameter and tensile strength. On the other hand CF- Al<sub>2</sub>O<sub>3</sub> showed a marked improvement in retaining its strength compared with CF and even if carbides had been formed, the oxidative protection afforded by the Al<sub>2</sub>O<sub>3</sub> coating (seen by its larger diameter) appears to have outweighed this. Of all coated samples, CF-PS had the least reduction in strength. While it had mass loss within error of the CF, it maintained a larger diameter, indicating that mass loss was most likely from the polysiloxane coating and not oxidation of the carbon fibre following a 500°C for 2h exposure.

On raising the temperature to 550°C for 1h, the CF, CF-SiO<sub>2</sub> and CF-Al<sub>2</sub>O<sub>3</sub> all had a similar reductions in tensile strength. The CF-PS also showed a large reduction in tensile strength ( $34 \pm 8$ )% compared to the CF ( $40 \pm 3$ )%. As seen in Table 6.3, these fibres also retained the largest fibre diameters. However, there is the possibility that the fibre had oxidised within the coating, as seen in Figure 6.16. If this had occurred then the fibre diameters measured in Table 6.3 would be greater than the actual carbon fibre diameter inside. Furthermore, some of the fibres with cracked coatings may have been oxidised more than others with coherent coatings (Figure 6.15), which would explain the large (9%) error associated with its percentage reduction in tensile strength.

## 6.6 Electrical properties of the coated fibres after exposure to heat

Single fibre electrical resistivity measurements were undertaken on the coated carbon fibres and those heated in the tube furnace. Unfortunately CF-PS fibres held at 600°C for 0.5h were too damaged to be tested. The results are given in Table 6.6.

Table 6.6. Electrical resistivity of CF and coated carbon fibres after heat treatments in the tube furnace.

Temp, °C	Time, h	Electrical resistivity, $\Omega\text{m} \times 10^{-5}$			
		CF	CF-SiO <sub>2</sub>	CF-Al <sub>2</sub> O <sub>3</sub>	CF-PS
Control/coated fibre		2.08 ± 0.13	2.19 ± 0.18	1.97 ± 0.18	2.24 ± 0.32
500	1	1.48 ± 0.05	2.31 ± 0.19	1.85 ± 0.15	2.27 ± 0.48
500	2	6.28 ± 0.30	2.04 ± 0.15	2.05 ± 0.47	2.00 ± 0.52
550	0.5	2.35 ± 0.22	1.77 ± 0.07	2.21 ± 0.05	1.62 ± 0.41
550	1	2.30 ± 0.38	1.85 ± 0.14	3.00 ± 0.60	2.10 ± 0.22
600	0.5	16.31 ± 0.71	2.49 ± 0.23	2.00 ± 0.07	-

‘-’ not tested

The electrical resistivities of the coated fibres were measured at room temperature (20°C). Both CF-SiO<sub>2</sub> and CF-Al<sub>2</sub>O<sub>3</sub> become more conductive through ion transport as the exposure temperature increased, but here the interest was in the potential hazards of residual fibres after exposure to heat. In general, the electrical resistivity of SiO<sub>2</sub> and Al<sub>2</sub>O<sub>3</sub> are in the region of 10<sup>12</sup>  $\Omega\text{m}$  [32, 33].

However, silica’s electrical conductivity can be increased by the absorption of water vapour [34], where the surface SiO<sub>2</sub> can be modified into silanol groups (Si-OH) that the results in Table 6.2 suggested had happened. The purity of SiO<sub>2</sub> and Al<sub>2</sub>O<sub>3</sub> can also affect its use as an electrical insulator, where the higher its purity, the more resistivity it has. The results in Table 6.6 showed an increase in the resistivity of the CF-SiO<sub>2</sub> which was expected due to the insulating coating. CF-Al<sub>2</sub>O<sub>3</sub> had lower electrical resistivity than the CF, while it was still within its error

the same up to and including temperatures of 550°C, which was surprising. Along with the results in Table 6.6, the electrical resistivity of a carbon fibre after surface activation (450°C for 1.5h and 2h in 80°C in HNO<sub>3</sub>) was recorded as  $2.06 \pm 0.05$ , which is very close to the CF indicating that removal of the insulating polymer sizing and addition of potentially conductive carboxyl groups on the surface had minimal effect of the overall electrical resistance of the fibre. This implied that even when coated, the carbon fibre's resistivity is not just a surface property but dominated by the cross-sectional morphology (in this case carbon).

The electrical resistivity of CF-PS increased after coating. The electrical properties of the polysiloxane coating were more difficult to determine as the coating contains many silicon-containing compounds (SiO<sub>2</sub>, Si(CH<sub>3</sub>)<sub>4</sub>, SiOC, etc.). Zajickova et al. [35] deposited coatings on polycarbonates from HMDSO and HMDSO/O<sub>2</sub> mixtures via plasma. Hydrogen and carbon were present in all films, even those mixed with a high oxygen flow rate where it was expected that all the molecular oxygen would have reacted with the HMDSO. Therefore, it can be assumed here, where argon gas was used, that the polysiloxane film still contained a relatively high hydrogen and carbon (up to 20% from EDX in Figure 6.12(b)) content. The presence of SiOC and particularly the C bonds within the SiO<sub>2</sub> network have been found to increase the electrical conductivity by several orders of magnitude compared to pure SiO<sub>2</sub> [36], but this would still be less than the conductivity of carbon fibre.

After 1h at 500°C only CF-SiO<sub>2</sub> had a noticeable increase in electrical resistivity. This might be due to the loss of any moisture contained in the coating. After 2h at 500°C all the coated fibres had similar resistivities.

At 550°C for 0.5h these resistivities were below that of the CF for the same condition. Both CF-SiO<sub>2</sub> and CF-PS showed a clear drop in resistivity, this also coincided with a large mass loss (Table 6.2). After exposure at 550°C for 1h, the most noticeable change in electrical resistivity was a significant increase for CF-Al<sub>2</sub>O<sub>3</sub>. Table 6.3 shows that this heat treatment also resulted in the largest reduction in fibre diameter, indicating that oxygen must have penetrated the Al<sub>2</sub>O<sub>3</sub> coating. After being held at 600°C for 0.5h, CF had significantly higher resistivity than the remaining and coherent coated fibres. The high electrical resistivities of CF was attributed to



large areas of surface oxidation impeding the continuous flow of electrons along the fibre. Furthermore, after exposures at 600°C for 0.5h, both CF-SiO<sub>2</sub> and CF-Al<sub>2</sub>O<sub>3</sub> retained larger diameters but showed considerably less surface damage in Figures 6.15(r) and (s) with no large obvious areas of oxidation, which were evident on exposed CF and CF-PS samples in Figure 6.15(q) and (t). This further showed that the SiO<sub>2</sub> and Al<sub>2</sub>O<sub>3</sub> coatings provide some oxidation protection to the carbon fibre at 600°C.

It was also noted that the CF-PS resistivities had large errors associated with them. These small changes could be due to the variations in the polysiloxane coating, as noted in Figure 6.15(a) where the coating consisted of non-uniform spherical particles adhering to the fibre, their level of contact and ability to form a continuous network of electrical conduction will determine its resistivity.

Overall, while measuring the resistivity of the heat-exposed coated fibres has given some insight into the oxidative protection that they may have provided, it was found that simply applying an insulating coating did not have a noticeable effect in reducing carbon fibre conductivity. The electrical properties of the underlying carbon fibre were dominant over those of the surface coating.

## 6.7 Conclusions

Carbon fibres tows were coated with several different, potentially high temperature-resistant coatings including included ionic compounds (NaAlO<sub>2</sub>), nitrides (BN), ceramics (SiO<sub>2</sub>, Al<sub>2</sub>O<sub>3</sub>, ZrO<sub>2</sub>), SiO<sub>2</sub>-nano-particles deposited as sizing and polysiloxane deposited during plasma exposure. From these coatings the most viable in terms of a coherent coating were selected for further heat testing. These were those comprising SiO<sub>2</sub> and Al<sub>2</sub>O<sub>3</sub> formed via the sol-gel process, as well as a polysiloxane polymerised *in situ* during plasma exposure. The following conclusions were made:

- Removal of the polymer sizing and activation of the surface with HNO<sub>3</sub> resulted in a smoother surface coating. However, these pre-treatments reduced the mechanical strength of the fibre.

- The coatings, while insulators, did not result in a significant increase in carbon fibre resistivity. This indicated that carbon fibre resistivity is not just a surface property but dominated by the underlying carbon cross-sectional morphology.

After heat testing in the tube furnace at different temperatures and times, for each coating it was found:

- $\text{SiO}_2$  coating:
  - Above  $500^\circ\text{C}$  a large mass loss occurred which was not reflected in loss of fibre diameter. This mass loss was attributed to desorption of water from the coating.
  - Over a long period at high heat ( $500^\circ\text{C}$  for 2h) deterioration of the  $\text{SiO}_2$  coating occurred. This is likely due to residual products from the sol-gel process diffusing through the coating and causing micro-cracks and pores which allowed oxygen to reach the underlying carbon fibre surface.
  - Application of the  $\text{SiO}_2$  coating did not result in any significant changes to its tensile strength.
- $\text{Al}_2\text{O}_3$  coating:
  - Fibres retained a larger diameter than the CF, indicating the alumina formed a potentially oxidation-resistant barrier.
  - The alumina coating resulted in a decrease of carbon fibre tensile strength which could be due to the formation of the brittle carbide,  $\text{Al}_4\text{C}_3$ , at above  $500^\circ\text{C}$ .
- Polysiloxane coating:
  - Using argon plasma as a carrier for HMDSO, a surface coating of silicon compounds including the derived polysiloxane was deposited on carbon fibre surface.
  - Up to  $600^\circ\text{C}$ , fibres coated with HMDSO retained the largest fibre diameters.
  - After exposure at  $550^\circ\text{C}$  for 1h some cracks in the coating were found; however, these became more frequent at  $600^\circ\text{C}$  and were linked to the mechanical mismatch of the coating and the carbon fibre.

As an overall conclusion it may be said that, coating individual carbon fibres has provided some oxidation protection, which was most evident with CF- $\text{Al}_2\text{O}_3$  as the coated fibres retained larger diameters than CF following heat exposure. However, because carbon fibre is extremely

susceptible to oxidation at above 500°C, any defects, such as pores and micro-cracks, which allow oxygen to reach the underlying fibre surface, resulted in oxidation. This was the case with CF-SiO<sub>2</sub> and CF-PS samples. It is evident that while further work is required in this area to develop more acceptable, high temperature-resistant, surface coatings which are compatible with carbon fibre, this study has provided a basis for such research.

## 6.8 References

- [1] Solozhenko., V. L., Turkevich, V. Z., Holzapfel, W. B., Refined phase diagram of boron nitride J. Phys. Chem.B 103 2903–5, (1999).
- [2] Belton, D. J., Deschaume, O., Perry, C. C., An overview of the fundamentals of the chemistry of silica with relevance to biosilicification and technological advances. FEBS J. May;279(10):1710-20, (2012).
- [3] Archer, N. J., Chemical Vapour Deposition, Physics in Technology, 10, 152, (1979).
- [4] Li, J., The effect of surface modification with nitric acid on the mechanical and tribological properties of carbon fiber-reinforced thermoplastic polyimide composite. Surface and Interface Analysis 41(9):759-63, (2019).
- [5] Tiwari, S., Bijwe, J., Panier, S., Tribological studies on polyetherimide composites based on carbon fabric with optimized oxidation treatment, Wear, Volume 271, Issues 9–10, Pages 2252-2260, (2011).
- [6] Li, L-X., and Li, F., The effect of carbonyl, carboxyl and hydroxyl groups on the capacitance of carbon nanotubes, New Carbon Materials, Volume 26, Issue 3,, Pages 224-228, (2011).
- [7] Vinodhini, J., Sudheendra, K., Balachandran, M., Bhowmik, S., Influence of argon plasma treatment on carbon fibre reinforced high performance thermoplastic composite. High Performance Polymers, 33(3):285-294, (2021).
- [8] K  ppler, I.,Hund, R., Cherif, C., Surface Modification of Carbon Fibres Using Plasma Technique, AUTEX Research Journal, Vol. 14, No 1, (2014).
- [9] National Center for Biotechnology Information, PubChem Compound Summary for CID 14766, Sodium aluminate, (2023).
- [10] Das, M., Basu, A. K., Ghatak, S., Joshi, A. G., Carbothermal synthesis of boron nitride coating on PAN carbon fiber, Journal of the European Ceramic Society, Volume 29, Issue 10, Pages 2129-2134, (2009).
- [11] Badakhsh, A., Han, W., Jung, S. C., An, K. H., Kim, B. J., Preparation of Boron Nitride-Coated Carbon Fibers and Synergistic Improvement of Thermal Conductivity in Their Polypropylene-Matrix Composites. Polymers (Basel).Dec 4;11(12): (2019).
- [12] Wei, Y-S., Huang, X-Z., Dub, Z-J., Chenga, Y., Synthesis of BN coatings on carbon fiber by dip coating, Surface and Interface Analysis, Volume 49, Issue 3, pages 117-181, (2016).

- [13] Fu, S., Wang, Y., Wang, Y., Qu, C., Niu, F., Liu., J, A study of boron nitride coatings on carbon fibers by the powder immersion reaction method, *Material Research Express*, Volume 5 Number 7, (2018).
- [14] Liu, J., Wang, S., Li, P., Feng, M., Yang, X., A modified dip-coating method to prepare BN coating on SiC fiber by introducing the sol–gel process, *Surface and Coatings Technology*, Volume 286, Pages 57-63, (2016).
- [15] Fu, S., Wang, Y., Wang, Y., Qu, C., Niu, F., Liu, J.,, A study of boron nitride coatings on carbon fibers by the powder immersion reaction method, *Material Research Express*, Volume 5 Number 7, (2018).
- [16] Chandra, U., (Ed.). *Recent Applications in Sol-Gel Synthesis*. doi: 10.5772/65824, (2017).
- [17] Doremus, R. H., Alumina. In: Shackelford, J.F., Doremus, R.H. (eds) *Ceramic and Glass Materials*. Springer, Boston, MA. (2008).
- [18] Wang, M-W., Liu, B-L., Ren, C-C., Shih, Z-W., Preparation of the Precursor of the Zirconium Oxide in EDTA–Ammonia Solution by the Sol–Gel Method, *Industrial & Engineering Chemistry Research*, 36 (6), 2149-2155, (1997).
- [19] Tyagi, B., Sidhpuria, K., Shaik, B.,Jasra, R., Synthesis of Nanocrystalline Zirconia Using Sol-gel and Precipitation Techniques, *Industrial & Engineering Chemistry Research* 45, 8643-8650, (2006).
- [20] Heshmatpour F. and Aghakhanpour, R. B., Synthesis and characterization of nanocrystalline zirconia powder by simple sol-gel method with glucose and fructose as organic additives, *Powder Technology* 205, 193-200, (2011).
- [21] Horrocks, A. R., Nazare, S., Masood, R.,Kandola, B., Price, D., Surface modification of fabrics for improved flash-fire resistance using atmospheric pressure plasma in the presence of a functionalized clay and polysiloxane, Volume 22, Issue 1 Special Issue: Selected papers presented at the 10th International Symposium on Polymers for Advanced Technologies, Pages 22-29, (2010).
- [22] Goujon, M., Belmonte, T., Henrion, G., OES and FTIR diagnostics of HMDSO/O<sub>2</sub> gas mixtures for SiO<sub>x</sub> deposition assisted by RF plasma, *Surface and Coatings Technology*, Volumes 188–189, Pages 756-761, (2004).
- [23] Ji, Y-Y., Hong, Y-C., Lee, S-H., Kim, S-D., Kim, S-S., Formation of super-hydrophobic and water-repellency surface with hexamethyldisiloxane (HMDSO) coating on

polyethyleneterephthalate fiber by atmospheric pressure plasma polymerization, *Surface and Coatings Technology*, Volume 202, Issues 22–23, Pages 5663–5667, (2008).

[24] Prado, M., Marski, S. R. D. S L., Pacheco, P., Barros, A. C., Gerardo, C. F., Prado, M. C., Marques, F. D., Lunz, J. N., Silva G. C., Archanjo, B. S., Lione, V. F., Achete, C. A., Simão, R. A., Hexamethyldisiloxane coating by plasma to create a superhydrophobic surface for fabric masks, *Journal of Materials Research and Technology*, Volume 17, Pages 913–924, (2022).

[25] Young, G. J., Interaction of Water Vapor with Silica Surfaces, *Journal of Colloid Science* 13, 67--85 (1958).

[26] Ramanathan, S., Bhat, R., Upadhyay, D. D., Roy, S. K., Alumina ceramics by sol-gel technique, *Bull. Mater. Sci.*, Vol. 17, No. 2, pp. 95–103, (1994).

[27] Schubert, U. and Hüsing, N., *Synthesis of Inorganic Materials*, 3rd edn, VCH-Wiley Verlag GmbH, Weinheim, ISBN 3-527-32714-1, (2012).

[28] Chaiwong, C., Rachtanapun, P., Sarapirom, S., Boonyawan, D., Plasma polymerization of hexamethyldisiloxane: Investigation of the effect of carrier gas related to the film properties, *Surface and Coatings Technology*, Volume 229, Pages 12–17, (2013).

[29] Wu, Z., Pittman, C. U., Gardner, S. D., Nitric acid oxidation of carbon fibers and the effects of subsequent treatment in refluxing aqueous NaOH, *Carbon*, Volume 33, Issue 5, Pages 597–605, (1995).

[30] Nohara, L. B., Filho, G. P., Nohara, E. L., Kleinke, M. U., Rzende, M. C., Evaluation of carbon fiber surface treated by chemical and cold plasma processes. *Mater Res*; 8(3): 281–286, (2005).

[31] Zeng, Q., Aluminium based composites reinforced with alumina coated carbon fibres, *Materials Science and Technology*, 14:12, 1266–1268, (1998).

[32] Braunger, M. L., Escanhoela, C. A., Fier, I., Walmsley, L., Ziemath, E. C., Electrical conductivity of silicate glasses with tetravalent cations substituting Si, *Journal of Non-Crystalline Solids*, Volume 358, Issue 21, Pages 2855–2861, (2012).

[33] Martin, M., Sedláček, J., Parchovianský, M., Micháľková, M., Galusek, D., Mechanical properties and electrical conductivity of alumina/MWCNT and alumina/zirconia/MWCNT composites. *Ceramics International*. Volume 40, Issue 1, Part B, Pages 1289–1295, (2014).

- [34] Voorthuyzen, J. A., Keskin, K., Bergveld, P., Investigations of the surface conductivity of silicon dioxide and methods to reduce it, *Surface Science*, Volume 187, Issue 1, Pages 201-211, (1987).
- [35] Zajickova, L., Bursikova, V., Perina, V., Mackova., Subedi, D., Janča, J., Smirnov, S., Plasma modification of polycarbonates, *Surface and Coatings Technology*, Volumes 142–144, Pages 449-454, (2001).
- [33] Renlund, G. M., Prochazka, S., Doremus, R. H., Silicon oxycarbide glasses: Part II. Structure and properties *J. Mater. Res.*, 6, pp. 2723-2734, (1991).

## Chapter 7. Conclusions

The purpose of this research was to improve the structural retention of carbon fibre-reinforced composites on exposure to heat/fire so that the carbon fibres maintained their structural coherence. While the fire performance of these composites has been previously studied by many researchers, usually with emphasis on the decomposition and flammability of the resin [1-3], little attention has been paid to the fate of the carbon fibres. This research is concerned with the effect of heat/fire on carbon fibres. At temperatures above 500°C in an oxidative environment, oxidation of the carbon fibres begins to occur [4] and on prolonged exposure to this environment >550°C, oxidised fibres start breaking into small fibres/fibrils [5]. The released broken fibres, which could be aeri ally transported given their low weight, pose several hazards. Firstly, they may interfere with surrounding electrical equipment and secondly, there are health concerns if inhaled. Studies on the residual component carbon fibres, especially in relation to these hazards, remain limited.

The aim of this research was to improve the structural retention of carbon fibre-reinforced composites on exposure to heat/fire so that the structural integrity is maintained and the carbon fibres are not exposed to the environment. To address this, the following objectives were set:

1. To develop a methodology to study and quantify structural damage to carbon fibres under a range of heat/fire conditions.
2. To develop carbon fibre-reinforced composites with improved structural retention.
3. To modify the carbon fibres prior to making the composites so that the carbon fibres will not defibrillate and oxidise when exposed to heat/fire.

To address Objective 1, a methodology was developed to expose carbon fibres (CF) and carbon fibre-reinforce composites (CCs) to different heat fluxes and temperatures, and as carbon fibre is sensitive to oxygen, to understand how heating in different atmospheres affected it. Then, techniques to measure change in fibre diameter, electrical resistivity and mechanical strength were established. Initially, carbon fibre tows were tested and examined to understand the damage caused by different temperatures and heat sources.



CCs were then modified with the aim of improving their structural retention on exposure to heat/fire. These included:

1. Modifying the CCs' resin with the addition of phosphorus flame retardants and nano-additives in order to: increase cross-linking, reduce carbon fibre exposure, and promote the formation of char and its adherence to the carbon fibres (Objective 2).
2. Introducing protective layers (woven, non-woven veils, fabric) of high temperature materials such as glass, basalt and thermoplastic (Objective 2).
3. Coating individual carbon fibres in high temperature chemicals, including nitrides and oxides, prior to incorporating them in CCs (Objective 3).

These are discussed in detail in the following sections.

## **7.1 Development of a methodology to study and quantify structural damage to carbon fibres under a range of heat/fire conditions (Chapter 3).**

### **7.1.1 Overall conclusions**

- Carbon fibre oxidation began at 550°C with rapid oxidation between 700 and 850°C. Above 850°C the fibre was fully oxidised.
- Below an exposure time of 1h, carbon fibre diameter was found to be directly proportional to temperature.
- On exposing carbon fibre to the cone calorimeter for 600s at 50kWm<sup>-2</sup>, there was no signs of fibre oxidation but at 75kWm<sup>-2</sup> there was significant oxidation.
- When exposed to higher heat flux of 116kWm<sup>-2</sup> and a direct flame, vaporisation of possible contaminant particles in the fibre created sites for localised oxidation.

### **7.1.2 Discussion**

A test methodology had to be established in order to quantify the damage to carbon fibres in various high heat situation. For this, a series of experimental techniques were used to simulate fires which radiate varying amounts of heat and temperatures, ranging from 400°C to 1100°C.

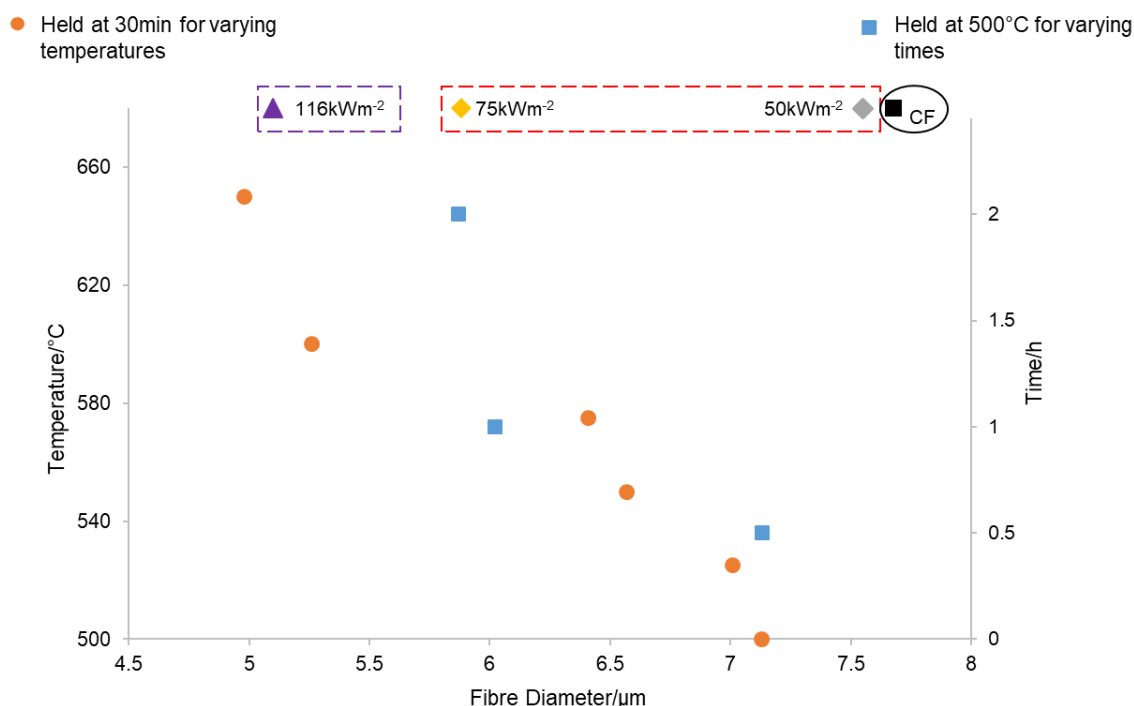
The effect of heat in a controlled environment was studied. Thermogravimetric analysis (TGA) is an extremely accurate and precise instrument to measure the mass loss of carbon fibre as temperature increases. This was performed in air or nitrogen, simulating environmental conditions where oxygen is present or absent, respectively. However, it is limited by the small sample sizes (under 10mg). Tube furnaces on the other hand, allow larger samples, such as fibre tows to be exposed to high temperatures in air or nitrogen. To replicate real fire conditions using radiant heat fluxes, the cone calorimeter was used from  $50\text{kWm}^{-2}$  to  $75\text{kWm}^{-2}$ , where a heat flux of  $50\text{kWm}^{-2}$  simulates a standard house fire and  $75\text{kWm}^{-2}$  the flashover condition. For situations where there is extremely high heat flux reaching  $116\text{kWm}^{-2}$  (close to what would be experienced in a jet fuel fire) a propane burner setup was used and the flame effects on carbon fibres studied.

TGA results showed that exposing carbon fibre to high temperatures in a nitrogen atmosphere did not reduce fibre diameter but did remove the polymer sizing (above  $450^{\circ}\text{C}$ ). While in air carbon fibre oxidation began at  $550^{\circ}\text{C}$  with rapid oxidation between 700 and  $850^{\circ}\text{C}$ . Above  $850^{\circ}\text{C}$  the fibre was fully oxidised.

A tube furnace was then used to expose carbon fibre tows to varying temperatures. Carbon fibre diameters measured using a scanning electron microscope (SEM) were found to be directly proportional to temperature when held at 30min from  $450^{\circ}\text{C}$  to  $650^{\circ}\text{C}$  (Figure 7.1). Furthermore, electrical resistivity had a linear relationship between the logarithm of the fibre resistivity with increasing temperature above  $525^{\circ}\text{C}$ . At  $650^{\circ}\text{C}$  not enough carbon fibre remained for electrical resistivity testing. It was noted that electrical resistivity did not increase significantly with heat exposure and remained within the range expected for carbon. When carbon fibres were then held at  $500^{\circ}\text{C}$  for varying length of times, results indicated an exponential relationship between fibre diameter and time (Figure 7.1).

Carbon fibre in a 2x2 twill weave fabric (as used in CCs) was exposed to the cone calorimeter at  $50\text{kWm}^{-2}$  and  $75\text{kWm}^{-2}$  for 600s. At  $50\text{kWm}^{-2}$  no notable fibre oxidation or change in electrical resistivity occurred. However, at  $75\text{kWm}^{-2}$  there was significant carbon fibre oxidation with the dominant mechanism being determined by the rate of diffusion of gases through pores and micro-structural defects. The carbon fibre fabric was then exposed to a higher heat flux

using an oxygen/propane gas flame ( $116\text{kWm}^{-2}$ ) in order to simulate jet fire conditions for 300s and 600s. Carbon fibres removed from the area in direct contact with the flame had nano-pits which were likely caused by vaporisation of possible contaminant particles, creating sites for localised oxidation. Fibre diameter for those exposed to the cone calorimeter at  $50\text{kWm}^{-2}$  and  $75\text{kWm}^{-2}$ , as well as to the oxygen/propane gas flame at  $116\text{kWm}^{-2}$  for 600s, are also given in Figure 7.1.



**7.2 Modification of the resin in the CCs with the addition of flame retardant additives in order to increase cross-linking, reduce carbon fibre exposure, and promote the formation of char and its adherence to carbon fibres when the CCs are subjected to heat/fire (Chapter 4).**

### **7.2.1 Overall conclusions**

- Over a period of 600s the minimum heat flux required to cause oxidation to the component carbon fibres was  $60\text{kWm}^{-2}$ .
- Cone calorimeter testing at  $75\text{kWm}^{-2}$  showed that the addition of 15wt% APP resulted in large char formation and adherence to fibres in the underlying plies. This resulted in less oxidation to these carbon fibres.
- Phosphorus-containing species within the char adhering to the carbon fibre appeared to cause an increase in the residual fibres' electrical conductivity.
- After 10min exposure to the propane burner ( $116\text{kWm}^{-2}$ ), fibres on the surface ply, in contact with the flame, oxidised internally.
- Exposure of composites containing LDH and CNT to the propane flame for 5min resulted in pitting and localised oxidation of the carbon fibre.

### **7.2.2 Discussion**

Carbon fibre is typically used in CCs as a reinforcement in a polymer matrix. In this research 8-ply thick CCs consisting of 2x2 twill weave 3K carbon fibre with an epoxy matrix were used. After heat and fire testing, residual fibres were removed from plies throughout the composite to assess the damage caused to its different parts. A schematic of CC is given in Figure 7.2.

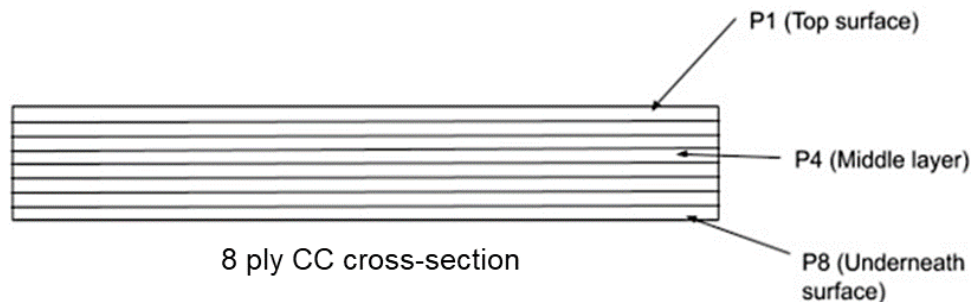


Figure 7.2. Schematic of CC.

CCs were exposed to the cone calorimeter for 600s at various heat fluxes. Auto-ignition occurred when exposed to heat fluxes of  $35\text{kWm}^{-2}$  and above. Over a period of 600s, the minimum heat flux required to cause oxidation to the component carbon fibres was  $60\text{kWm}^{-2}$ . After 20min (1200s) at  $75\text{kWm}^{-2}$  surface (ply 1, P1) carbon fibres were removed from CC and found to be between  $4\mu\text{m}$  and  $7\mu\text{m}$  in length, which are considered respirable particles [6, 7].

Next CCs were exposed to a propane burner ( $116\text{kWm}^{-2}$ ). CC lost mass within the first minute due to resin decomposition, followed by a large mass loss after 3min and only a small additional mass loss between 3 to 5min. However, after 10min there was significant decrease in mass due to oxidation of the char and carbon fibres, as well as internal oxidation of ply P1 fibres directly in contact with the flame. This was credited to the high concentration of oxygen and hydrogen radicals in the flame [8].

To fulfil the next objective of this research the CCs' resin was modified with flame retardants and nano-additives in order to:

- Increase cross-linking during resin decomposition.
- Promote the formation of char.
- Increase char adherence to carbon fibres.
- Reduce carbon fibre exposure by encapsulating within char.

Phosphorus flame retardants; APP, RDP and DOPO were added to the CCs' resin at 15wt% (CC\_APP, CC\_RDP, CC\_DOPO) and the nano-additives; nano-clay and LDH at 5wt%

(CC\_NC and CC\_LDH). Table 7.1 gives a comparison of the properties of ply P1 carbon fibres after heat and fire testing.

#### **7.2.2.1 CCs containing flame retardants/nano-additives exposed to radiant heat and the effects on carbon fibre: cone calorimetric experiments**

The cone calorimeters results ( $75\text{kWm}^{-2}$ , 600s) indicated that the addition of APP resulted in more char formation and adherence to fibres in the underlying plies. This resulted in less oxidation to these carbon fibres as seen by the larger fibre diameters and retained tensile strength (within error of the CF). Phosphorus-containing species were detected within the char using energy dispersive x-ray analysis (EDX). Attempts were made using different solvents, and alkali and acid solutions to remove this residue, but overall it was found to be extremely difficult to remove and could therefore be considered part of carbon fibres' structure.

RDP is gas phase reactive and not a char promotor, yet it still resulted in a high residual wt% and only a small reduction in P1 fibre tensile strength ( $8 \pm 7\%$ ). While DOPO is both condensed and gas phase active, its inclusion resulted in a much lower residual mass along with reduction in ply P1 carbon fibre tensile strength. EDX detected phosphorus species in the residue on ply P8 carbon fibre of composites CC\_APP, CC\_DOPO and CC\_RDP. These phosphorus-containing species within the char were found to increase the electrical conductivity of the residual fibres.

The inclusion of nano-clay had a barrier effect, seen by the larger ply P1 fibre diameter. The residue on the carbon fibres only contained carbon and oxygen. It was expected to be siliceous as this would have explained the slight increase in the residual fibres' electrical resistivity. LDH showed slightly less of a barrier effect than nano-clay, with visible metal oxide residue on the surface ply. This was attributed to decreasing its electrical conductivity.

#### 7.2.2.2 Effect of jet fire on CCs with additives: Propane burner experiments

The above composites, along with those including 0.5wt% graphene oxide (CC\_GO) and 1wt% nano-tubes (CC\_NT), were exposed to a propane burner ( $116\text{kWm}^{-2}$ ) for 1 to 5min. For all composites, after 5min there was significantly less char on ply P1 (in direct contact with the flame) than on the part of the composites on the flame's edge. This was attributed to two things:

- 1) The increased temperature (approximately  $1000^{\circ}\text{C}$  directly in the flame, as opposed to  $780^{\circ}\text{C}$  on the edge of the flame) led to oxidation of the char residue.
- 2) The physical force of the flame/propane gas displaced any char residue formed.

Unlike when CC\_APP was tested under the cone calorimeter ( $75\text{kWm}^{-2}$ , 600s), additional oxidation of the carbon fibres in ply P1 CC\_APP was found. This may indicate a reaction between the APP char residue and carbon fibres at higher than  $1000^{\circ}\text{C}$ . Potentially phosphorus oxides could sensitise the carbon fibre to oxidation. Further work is required to identify if these oxides were present.

Additionally, after 5min of exposure to the propane flame, pitting was seen on residual fibres from CC\_LDH and CC\_CNT. In CC\_LDH this was linked to the oxides produced when LDH thermally decomposed. While for CC\_CNT it was due to the additional carbon content. The residual P1 fibres from these composites also had the greatest reduction in tensile strength due to pits acting as stress concentrators. Hence the inclusion of these additives cannot be recommended.

Table 7.1. Comparison of the properties of ply P1 carbon fibres after heat and fire testing.

	Cone calorimeter, 75kWm <sup>-2</sup> , 600s				Propane burner, T1, 116kWm <sup>-2</sup> , 300s			
Flame retardant/ nano additive	Residual mass, %	Diameter, $\mu\text{m}$	Resistivity, $\Omega\text{m } 10^{-5}$	Tensile strength reduction w.r.t CF, %	Residual mass, %,	Diameter, $\mu\text{m}$	Resistivity, $\Omega\text{m } 10^{-5}$	Tensile strength reduction w.r.t CF, %
CF (untested)	-	$7.68 \pm 0.23$	$2.08 \pm 0.13$	0	-	$7.68 \pm 0.23$	$2.08 \pm 0.13$	0
Control	39.9	$5.89 \pm 0.11$	$2.20 \pm 0.16$	$43 \pm 3$	61.3	$6.79 \pm 0.14$	$2.22 \pm 0.29$	$18 \pm 9$
APP	66.3	$6.85 \pm 0.06$	$1.43 \pm 0.23$	$-1 \pm 6$	55.8	$5.92 \pm 0.15$	$1.00 \pm 0.04$	$16 \pm 9$
DOPO	45.5	$6.15 \pm 0.22$	$1.68 \pm 0.22$	$35 \pm 4$	66.2	$6.85 \pm 0.07$	$1.75 \pm 0.15$	$13 \pm 6$
RDP	64.1	$6.22 \pm 0.11$	$1.70 \pm 0.07$	$8 \pm 7$	69.2	$6.82 \pm 0.07$	$1.54 \pm 0.06$	$2 \pm 7$
NC	50.2	$6.72 \pm 0.13$	$2.56 \pm 0.41$	$52 \pm 2$	64.6	$7.01 \pm 0.14$	$2.54 \pm 0.26$	$45 \pm 9$
LDH	53.8	$7.10 \pm 0.10$	$1.97 \pm 0.15$	$47 \pm 4$	62.1	$7.04 \pm 0.11$	$2.09 \pm 0.18$	$28 \pm 4$
GO	-	-	-	-	71.1	$7.07 \pm 0.10$	$2.07 \pm 0.23$	$43 \pm 12$
CNT	-	-	-	-	65.1	$6.14 \pm 0.12$	$1.94 \pm 0.29$	$35 \pm 9$

Note: ‘-’ = Not tested



## 7.3 Introduction of high-temperature material layers within the carbon fibre plies to improve the structural retention of carbon fibres within CCs (Chapter 5)

### 7.3.1 Overall conclusions

After heat testing with the cone calorimeter at  $75\text{kWm}^{-2}$  for 600s:

- In composites containing basalt and E-glass, melting of the veil layers 2 and 3 were observed and this was attributed to ‘hotspots’ generated within the composites.
- The inclusion of aramid veils provided some protection to the underlying carbon fibres.
- The inclusion of woven E-glass showed a notable reduction in the percentage of carbon fibre oxidised.
- Kevlar and PPS produced volatiles during decomposition which sensitised the carbon fibre for oxidation, resulting in the carbon fibre oxidising at a lower temperature and more rapidly.

### 7.3.2 Discussion

In Chapter 5 high temperature resistant materials in fibrous non-woven or woven veils, or fabric, were successfully incorporated into the CC in two configurations, both at the surface and within, in order to provide a heat barrier to the underlying carbon fibres. A schematic of these configurations is given in Figure 7.3, with the composites’ physical properties in Table 7.2.

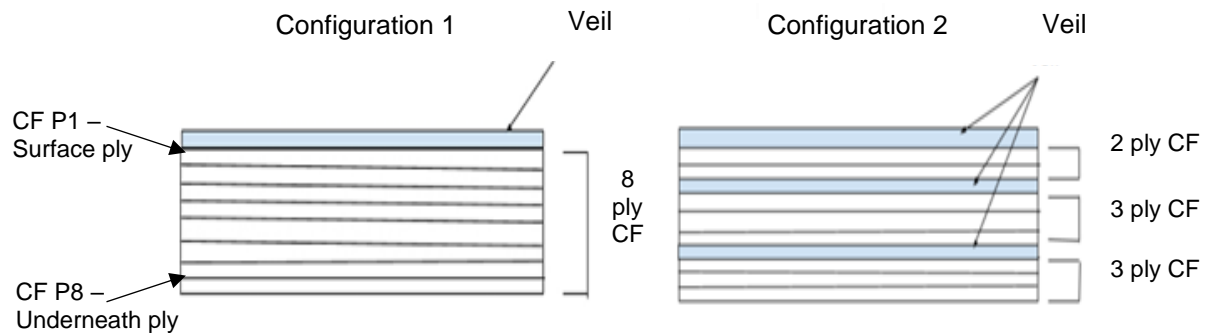


Figure 7.3. The two configurations of hybrid layers in CC.

Table 7.2. Physical properties of composites.

Composite	Veil/fabric	Veil mass density, $\text{gm}^{-2}$	No. Added veils	Mass fraction %			Thickness, mm
				Veil/fabric	Carbon fibre	Resin	
CC	-	-	-	-	65.7	34.3	2.08
CC_Ar_1	Aramid	14	1	0.4	46.4	53.3	1.79
CC_Ar_3			3	1.3	54.0	44.6	2.05
CC_Bs_1	Basalt	15	1	0.8	62.2	37.0	1.88
CC_Bs_3			3	2.1	53.8	44.1	1.97
CC_Gl_1	E-glass	17	1	0.6	66.5	32.9	1.79
CC_Gl_3			3	1.6	58.4	40.0	2.05
CC_Wo-G_1	E-glass (woven)	25	1	0.9	59.5	39.6	1.91
CC_Wo-Gl_3			3	3.7	52.1	44.2	2.19
CC_PPS_1	PPS	20	1	0.6	48.2	51.2	2.55
CC_PPS_3			3	1.8	57.2	41.0	2.07
CC_Kv_1	Kevlar	300	1	-	-	-	2.49

Note: '-' = Not available

Heat testing of the composites was carried out with the cone calorimeter at  $75\text{kWm}^{-2}$  for 600s and the remaining components examined – the inorganic veils and residual carbon fibres. EDX confirmed that a protective residue from the veils/fabric did not adhere to the carbon fibres directly beneath it. In Table 7.3 a summary of results for CC with additional veils/fabric layers after heat testing is presented.

With the exception of the woven glass containing composite CC\_Wo-Gl\_3, for all other composites the surface carbon fibres (ply P1) had the largest fibre diameter decrease. A trend was observed whereby the diameter of carbon fibres removed from plies within the composites (P3 to P6) were not as reduced compared to the surface ply P1 and underneath ply P8, indicating that during combustion, as the epoxy and veils burnt, they released volatiles causing the distance between plies to increase. This allowed air to flow under the composite during testing.

The inclusion of a surface aramid veil in CC\_Ar\_1 provided protection to the underlying carbon fibres. Larger residual carbon fibre diameters were recorded from plies P1 and P4. For CC\_Ar\_3, with the exception of ply P1, fibres removed from other plies had diameters larger than those from the corresponding ply in CC. Both aramid and Kevlar have similar structures. Kevlar was included in a 2x2 twill weave Kevlar cloth ( $300\text{gm}^{-2}$ ) as a surface veil to compare to the fibrous aramid veil ( $14\text{gm}^{-2}$ ). A large amount of fibre diameter reduction and pitting was observed on carbon fibres removed from ply P1 of CC\_Kv\_1. TGA-FTIR results also indicated that the aramid veil and Kevlar fabric produced similar volatiles during decomposition. It was believed that in a large enough quantity, these volatiles sensitised the carbon fibre for oxidation. Due to this, the inclusion of an aramid-based material could not be recommended in the heat protection of carbon fibre in CCs.

In composites containing basalt and non-woven E-glass, ply P1 residual carbon fibres had a diameter reduced below those from ply P1 of CC. This was believed to be due to the veil's binder reacting with the surface carbon fibres as it decomposed in the oxygen rich surface region. This was also indicated by the increased resistivity of carbon fibres removed from ply P1 CC\_Gl\_1. Furthermore, in CC\_Bs\_3 melting of the second and third basalt veil occurred. This was attributed to 'hotspots' generated within the composites resulting in increased oxidation to ply P6 carbon fibres which were directly below the third veil. Composites containing non-woven E-glass had similar detrimental results and these were credited to the same reasons. Therefore, the uses of non-woven fibrous basalt and E-glass veils were not recommended for heat protection in CCs.

The inclusion of PPS veils resulted in large areas of localised oxidation and pitting on ply P1 carbon fibres. This was believed to be due to the sulphur containing species sensitising the carbon fibre to oxidation. However, this localised damage did not translate into a significantly reduced fibre diameter or change in percentage of carbon fibre oxidised in the composite. But because of the localised damage to carbon fibres, the use of this PPS veil was also not recommended.

Both CC\_Wo-GI\_1 and CC\_Wo-GI\_3 had a notable reduction in the percentage of carbon fibre oxidised. However, CC\_Wo-GI\_3 exhibited better protection to carbon fibres from oxidation with larger residual carbon fibre diameters, particularly for ply P1. Furthermore, the woven E-glass also underwent melting of the second and third layer in CC\_Wo-GI\_3. Due to its woven construct this resulted in an intact web like structure which reduced the flow of volatiles and oxygen into the composite, hence reducing oxidation of the carbon fibre. It was therefore recommended that this veil be used for carbon fibre oxidation protection in CC.

Table 7.3. Summary of results for CC with additional veils/fabric layer after heat testing (75kWm<sup>-2</sup> for 600s).

Composite	Cone residue, wt% /% of oxidised fibre	Ply 1 fibre diameter, $\mu\text{m}$	P3	P4	P6	P8	Ply 1, Resistivity, $\Omega\text{m}$ $\times 10^{-5}$
CC	38.5 / 41.4	$5.89 \pm 0.11$	-	$6.69 \pm 0.09$	-	$6.65 \pm 0.11$	$2.20 \pm 0.05$
CC_Ar_1	28.3 / 39.1	$6.24 \pm 0.09$	-	$6.94 \pm 0.11$	-	$6.64 \pm 0.11$	$1.71 \pm 0.10$
CC_Ar_3	31.5 / 41.7	$5.53 \pm 0.13$	$7.12 \pm 0.10$	$6.80 \pm 0.13$	$7.07 \pm 0.14$	$6.81 \pm 0.13$	-
CC_Bs_1	43.3 / 30.3	$5.32 \pm 0.13$	-	$6.80 \pm 0.14$	-	$7.22 \pm 0.11$	$2.24 \pm 0.04$
CC_Bs_3	34.0 / 36.9	$4.03 \pm 0.13$	$6.69 \pm 0.10$	$6.39 \pm 0.13$	$5.80 \pm 0.20$	$6.16 \pm 0.14$	-
CC_Gl_1	30.7 / 53.9	$3.37 \pm 0.15$	-	$6.74 \pm 0.05$	-	$6.45 \pm 0.05$	$2.87 \pm 0.28$
CC_Gl_3	33.4 / 36.9	$2.90 \pm 0.08$	$6.51 \pm 0.05$	$6.52 \pm 0.06$	$6.66 \pm 0.04$	$6.14 \pm 0.11$	-
CC_Wo-Gl_1	47.4 / 20.0	$6.18 \pm 0.11$	-	$6.11 \pm 0.10$	-	$6.96 \pm 0.09$	$2.28 \pm 0.08$
CC_Wo-Gl_3	45.7 / 12.2	$6.76 \pm 0.09$	$6.22 \pm 0.11$	$6.38 \pm 0.11$	$7.18 \pm 0.08$	$6.88 \pm 0.14$	-
CC_PPS_1	29.6 / 38.5	$5.91 \pm 0.11$	-	$7.02 \pm 0.09$	-	$6.72 \pm 0.11$	-
CC_PPS_3	27.7 / 34.0	$5.76 \pm 0.13$	$6.84 \pm 0.08$	$7.04 \pm 0.11$	$6.94 \pm 0.11$	$6.47 \pm 0.09$	-
CC_Kv_1	42.1 / -	$2.22 \pm 0.10$	-	$6.84 \pm 0.06$	-	$5.66 \pm 0.10$	-

Note: '-' = Not tested

## **7.4 Modification of the carbon fibres prior to making the CCs so that the carbon fibres will not defibrillate and oxidise when exposed to heat/fire (Chapter 6)**

### **7.4.1 Overall conclusions**

- Carbon fibres coated in  $\text{Al}_2\text{O}_3$  formed via the sol-gel process retained the largest fibre diameters when heat tested.
- Over a long period at high heat ( $500^\circ\text{C}$  for 2h) deterioration of the  $\text{SiO}_2$  coating occurred.
- Polysiloxane coating provided oxidation protection up to  $600^\circ\text{C}$  but above this, cracks in the coating occurred.

### **7.4.2 Discussion**

In Chapter 6 high temperature chemical coatings were selected to individually coat carbon fibres prior to making the composites with a view that all fibres within them can be protected in this manner. Ceramic compounds were chosen as coating materials because of their stability at high temperatures. Challenges arose because as well as being resistant to high temperatures, the coating must completely cover and adhere to individual carbon fibres without aggregating on fibre surfaces and adding too much additional weight.

It was found that by removing the carbon fibre's polymer sizing and activating the surface with nitric acid it resulted in a smoother and more coherent coating. However, while the use of nitric acid increased surface roughening, which can aid in the coatings' adhesion, it also introduced nano-pits on the fibre surface which reduced the mechanical strength of the fibre.

Initially sodium aluminate was tested as a chemical coating. However, SEM and TGA results indicated the presence of micro-cracks, and its uneven surface coating resulted in oxygen reaching the fibre surface. Next, boron nitride was selected, but even with an additional nitrogen source (urea), nitridation of boric acid to boron nitride in a nitrogen atmosphere did not fully occur by  $900^\circ\text{C}$  and hence due to the high temperatures involved in forming this coating it was deemed not feasible for this project.

However, depositing inorganic coatings by the sol-gel process resulted in more successful surface coatings. Three inorganic coatings were deposited using this method; silica ( $\text{SiO}_2$ ), alumina ( $\text{Al}_2\text{O}_3$ ) and zirconia ( $\text{ZrO}_2$ ). While synthesis of  $\text{ZrO}_2$  crystals on the carbon fibre resulted in an uneven coating, attributed to zirconia's greater sensitivity to processing parameters (i.e. pH value, type of anion and reaction temperature), both  $\text{SiO}_2$  and  $\text{Al}_2\text{O}_3$  formed smooth coatings which completely covered the individual carbon fibres.

An alternative approach was also tested, which used the concept of a sizing to make a thermal barrier. Nano- $\text{SiO}_2$  particles were pre-treated with a silane coupling agent and then dispersed in epoxy resin which had been diluted with butanone and applied to the individual carbon fibres. Full dispersion of the nano- $\text{SiO}_2$  particles could not be confirmed and it was deemed that the  $\text{SiO}_2$  coating deposited by the sol-gel process provided a more complete coating.

The final coating method was to deposit a polysiloxane film by chemical vapour deposition of hexamethyldisiloxane (HMDSO). Argon plasma was used as a carrier for HMDSO, to coat carbon fibre tows with polysiloxane using jet plasma method. EDX confirmed a polysiloxane film on the fibre surface which coated the individual carbon fibres.

From the SEM and EDX analysis results, the coatings which exhibited the most potential were selected for further heat testing. These were;  $\text{SiO}_2$  and  $\text{Al}_2\text{O}_3$  deposited using the sol-gel process and polysiloxane from the chemical vapour deposition of HMDSO. Tows of individually coated fibres (CF- $\text{SiO}_2$ , CF- $\text{Al}_2\text{O}_3$ , and CF-PS) were placed in the tube furnace at varying temperatures (at which they would be susceptible to oxidation (500, 550 and 600°C)) for between 0.5 to 2h in static air. Five of each coated tows were weighed before and after, and the fibre diameters are given in (Table 7.4). All coated carbon fibres showed a level of protection to the CF at certain temperatures and over different lengths of time.

At above 500°C, the CF- $\text{SiO}_2$  lost a large amount of mass which was not reflected in the fibre diameter reduction. This mass loss was credited to desorption of water from the coating. It was only over longer periods at high heat (2h) that deterioration of the  $\text{SiO}_2$  coating occurred, which was attributed to the loss of intermediate species remaining within the  $\text{SiO}_2$  three-dimensional

gel resulting in small pores. Thus, allowing oxygen to enter and reach the underlying carbon fibre surfaces. Furthermore, application of the  $\text{SiO}_2$  coating did not result in any significant increase in fibre tensile strength compared to CC (Table 7.4). Conversely, the CF- $\text{Al}_2\text{O}_3$  had a significantly smaller mass loss and retained a larger diameter than CF (Table 7.4), indicating that the alumina formed an oxidation barrier. However, the  $\text{Al}_2\text{O}_3$  coating decreased the carbon fibre's tensile strength, which could have been due to the formation of brittle carbide  $\text{Al}_4\text{C}_3$  at above  $500^\circ\text{C}$  [9]. The CF-PS retained the largest fibre diameters up to  $600^\circ\text{C}$  and had the least reduction in tensile strength (with respect to the untested CF-PS). Yet unfortunately, after  $550^\circ\text{C}$  for 1h cracks in the coating were identified. These became more frequent at  $600^\circ\text{C}$  and was linked to the mechanical mismatch of the polysiloxane coating and the carbon fibre.

Furthermore, while the selected coatings were insulators, this did not result in a significant increase in the carbon fibre's resistivity and hence would not reduce the potential electrical hazards carbon fibres may pose.

This research highlighted the difficulties in fully coating individual carbon fibres. In Chapter 3 it was seen that at above  $500^\circ\text{C}$ , carbon fibre was very susceptible to oxidation, with this increasing as the temperature rose. Any micro-cracks or nano-pores resulted in oxygen penetrating the coating and leading to oxidation of the carbon fibre. However, the applications of  $\text{SiO}_2$ ,  $\text{Al}_2\text{O}_3$  and PS all acted to reduce the rate at which the carbon fibre oxidised.



Table 7.4. Summary of results for CF and coated fibres.

	Temp/°C	Time/h	Coating			
			CF	SiO <sub>2</sub>	Al <sub>2</sub> O <sub>3</sub>	PS
Fibre diameter, µm	500	0.5	7.13 ± 0.15	7.17 ± 0.08	6.88 ± 0.05	7.30 ± 0.08
Fibre diameter, µm	500	1	6.02 ± 0.21	6.93 ± 0.05	7.00 ± 0.04	7.01 ± 0.06
Tensile strength reduction w.r.t. CF/coated fibre, %			22 ± 5	27 ± 6	41 ± 3	16 ± 5
Electrical resistivity, x10 <sup>-5</sup> Ωm			1.48 ± 0.05	2.31 ± 0.19	1.85 ± 0.15	2.27 ± 0.48
	500	2	5.87 ± 0.34	6.01 ± 0.11	6.63 ± 0.05	7.06 ± 0.07
			54 ± 6	57 ± 4	46 ± 6	43 ± 5
			6.83 ± 0.30	2.04 ± 0.15	2.05 ± 0.47	2.00 ± 0.52
	550	0.5	6.57 ± 0.28	6.40 ± 0.06	6.79 ± 0.07	7.19 ± 0.07
			-	-	-	-
			2.35 ± 0.22	1.77 ± 0.07	2.21 ± 0.05	1.62 ± 0.41
	550	1	5.47 ± 0.31	6.41 ± 0.07	6.03 ± 0.13	7.03 ± 0.13
			40 ± 3	41 ± 3	45 ± 5	34 ± 9
			2.30 ± 0.38	1.85 ± 0.14	3.00 ± 0.60	2.10 ± 0.22
	600	0.5	5.26 ± 0.32	6.23 ± 0.12	6.15 ± 0.06	5.41 ± 0.15
			-	-	-	-
			16.31 ± 0.71	2.49 ± 0.23	2.00 ± 0.07	-

Note: '-' = Not tested

## **7.5 Limitations and recommendations for future research**

### **1) To study carbon fibres from alternative sources**

About 90% of the carbon fibres commercially used today are PAN-based [10] with the others being pitch and rayon-based. In this research the high strength PAN-based carbon fibre TR30S, Mitsubishi-Rayon Pyrofil was used in composites. While PAN-based carbon fibres from different grades and manufactures were also studied (Chapter 3, Section 3.6), these were also high strength carbon fibres and the study was limited compared to the full characterisation of the TR30S carbon fibres. Heat and fire testing of different strength carbon fibres, and those from alternative precursors, would lead to a greater understanding into the mechanics of carbon fibre oxidation in high temperature oxygenated environments.

### **2) Investigate the interaction between carbon fibre and E-glass, PPS and Kevlar**

Given the significant diameter reduction and areas of localised oxidation seen on ply P1 fibres from composites containing these veils/fabrics (Table 7.3), it is highly suggested that there was a reaction between these veils/fabrics and carbon fibre in an oxygenated environment. While TGA-FTIR was used to aid in the identification of thermal decomposition products of these materials, no definitive reactions between these products and carbon fibre could be determine. Clearly further study is required.

### **3) Understanding the thermal gradient in CCs**

It was seen that after exposure to the cone calorimeter ( $75\text{kWm}^{-2}$ , 600s), composites CC\_Bs\_3, CC\_Gl\_3 and CC\_Wo-Gl\_3 had melting of the second and third veil layer. This was unexpected as the thermocouple on the front surface of the composites recorded approximately  $680^{\circ}\text{C}$ , under the same heat flux and test conditions, which is below the melting points of basalt and E-glass. Further investigation is required to understand the thermal gradient in these thermally thin composites to identify areas or ‘hotspots’ within the composites and what generates these.

### **4) To incorporate inorganic metal oxide coated carbon fibres within a CC**

The interfacial adhesion between the carbon fibres and resin dominates the mechanical strength of the CC. To determine if coating the carbon fibre in inorganic metal oxides, such as silica or alumina, would reduce this adhesion, single coated fibres could undergo microdroplet test [11,12]. This would also identify if additional surface treatments, such as

attaching oxygen-containing functional groups, would be required to improve the interfacial adhesion.

## 7.6 References

- [1] Toldy, A., Szolnoki, B., Marosi, Gy. Flame retardancy of fibre-reinforced epoxy resin composites for aerospace applications, *Polymer Degradation and Stability*, Volume 96, Issue 3, Pages 371-376, (2011).
- [2] Braun, U., Balabanovich, A. I., Scharrel, B., Knoll, U., Artner, J., Ciesielski, M., et al. Influence of the oxidation state of phosphorus on the decomposition and fire behaviour of flame-retarded epoxy resin composites, *Polymer*, 47 (26), pp. 8495-8508, (2006).
- [3] Quang Dao, D., Luche, J., Richard, F., Rogaume, T., Bourhy-Weber, C., Ruban, S., Determination of characteristic parameters for the thermal decomposition of epoxy resin/carbon fibre composites in cone calorimeter, *International Journal of Hydrogen Energy*, Volume 38, Issue 19, Pages 8167-8178, (2013).
- [4] Yin, Y., Binner, G. P., Cross, T. E., Marshall, S. J., The oxidation behaviour of carbon fibres *J Mater Sci*, 29, pp. 2250-2254, (1994).
- [5] Chapple, R., Kandola, B., Myler, P., Ferry, L., Lopez-Cuesta, J., Chivas-joly, C., Erskineet, E., The effect of simultaneous heat/fire and impact on carbon fibril and particle release from carbon fiber-reinforced composites. *Polymer Composites*, 42 (11), pp.6127-6145, (2021).
- [6] Su, W. C., & Cheng, Y. S., Deposition of fiber in the human nasal airway. *Aerosol Science and Technology*, 39, 888–901, (2005).
- [7] Inthavong, K., Mouritz, A. P., Dong, J., Tu, J. Y., Inhalation and deposition of carbon and glass composite fibre in the respiratory airway. *Journal of Aerosol Science*, 65, pp. 58–68, (2013).
- [8] Simmons, E. L., ESR Measurements of Free Radical Concentration Profiles in the Propane-Oxygen Flame, *Journal of magnetic resonance* 16, 130-135, (1974).
- [9] Zeng, Q., Aluminium based composites reinforced with alumina coated carbon fibres, *Materials Science and Technology*, 14:12, 1266-1268, (1998).
- [10] Nunna, S., Blanchard, P., Buckmaster, D., Davis, S., Naebe, M., Development of a cost model for the production of carbon fibres, *Heliyon*, Volume 5, Issue 10, (2019).
- [11] Cai, G., Wada, M., Ohsawa, I., Kitaoka, S., Takahashi, J., Interfacial adhesion of recycled carbon fibers to polypropylene resin: Effect of superheated steam on the surface chemical state of carbon fiber, *Composites Part A: Applied Science and Manufacturing*, Volume 120, Pages 33-40, (2019).

[12] Sato, M., Imai, E., Koyanagi, J., Ishida, Y., Ogasawara, T., Evaluation of the interfacial strength of carbon-fiber-reinforced temperature-resistant polymer composites by the micro-droplet test, *Advanced Composite Materials*, 26:5, 465-476, (2017).